

Frequency Conversion of High-Intensity, Femtosecond Laser Pulses

Paul Stuart Banks
(Ph.D Thesis)

July 1997



Lawrence
Livermore
National
Laboratory

DISCLAIMER

This document was prepared as an account of work sponsored by an agency of the United States Government. Neither the United States Government nor the University of California nor any of their employees, makes any warranty, express or implied, or assumes any legal liability or responsibility for the accuracy, completeness, or usefulness of any information, apparatus, product, or process disclosed, or represents that its use would not infringe privately owned rights. Reference herein to any specific commercial product, process, or service by trade name, trademark, manufacturer, or otherwise, does not necessarily constitute or imply its endorsement, recommendation, or favoring by the United States Government or the University of California. The views and opinions of authors expressed herein do not necessarily state or reflect those of the United States Government or the University of California, and shall not be used for advertising or product endorsement purposes.

This report has been reproduced
directly from the best available copy.

Available to DOE and DOE contractors from the
Office of Scientific and Technical Information
P.O. Box 62, Oak Ridge, TN 37831
Prices available from (615) 576-8401, FTS 626-8401

Available to the public from the
National Technical Information Service
U.S. Department of Commerce
5285 Port Royal Rd.,
Springfield, VA 22161

Frequency Conversion of High-Intensity, Femtosecond Laser Pulses

**Paul Stuart Banks
(Ph.D Theis)**

July 1997



Frequency Conversion of High-Intensity, Femtosecond Laser Pulses

by

Paul Stuart Banks

B.S. (Brigham Young University) 1990
M.S. (University of California, Davis) 1991

DISSERTATION

Submitted in partial satisfaction of the requirements for the degree of

DOCTOR OF PHILOSOPHY

in

Engineering: Applied Science

in the

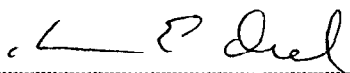
OFFICE OF GRADUATE STUDIES

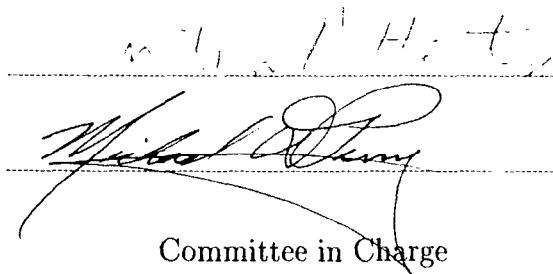
of the

UNIVERSITY of CALIFORNIA

DAVIS

Approved:





Committee in Charge

1997

Frequency Conversion of High-Intensity, Femtosecond Laser Pulses

Copyright 1997

by

Paul Stuart Banks

Frequency Conversion of High-Intensity, Femtosecond Laser Pulses

Abstract

Almost since the invention of the laser, frequency conversion of optical pulses via non-linear processes has been an area of active interest. However, third harmonic generation using $\chi^{(3)}$ (THG) in solids is an area that has not received much attention because of material damage limits. Recently, the short, high-intensity pulses possible with chirped-pulse amplification (CPA) laser systems allow the use of intensities on the order of 1 TW/cm² in thin solids without damage.

As a light source to examine single-crystal THG in solids and other high field interactions, the design and construction of a Ti:sapphire-based CPA laser system capable of ultimately producing peak powers of 100 TW is presented. Of special interest is a novel, all-reflective pulse stretcher design which can stretch a pulse temporally by a factor of 20,000. The stretcher design can also compensate for the added material dispersion due to propagation through the amplifier chain and produce transform-limited 45 fs pulses upon compression. A series of laser-pumped amplifiers brings the peak power up to the terawatt level at 10 Hz, and the design calls for additional amplifiers to bring the power level to the 100 TW level for single shot operation.

The theory for frequency conversion of these short pulses is presented, focusing on conversion to the third harmonic in single crystals of BBO, KD*P, and d-LAP (deuterated

l-arginine phosphate). Conversion efficiencies of up to 6% are obtained with 500 fs pulses at 1053 nm in a 3 mm thick BBO crystal at 200 GW/cm². Contributions to this process by unphasematched, cascaded second harmonic generation and sum frequency generation are shown to be very significant. The angular relationship between the two orders is used to measure the tensor elements of $C = \chi^{(3)}/4$ with $C_{10} = -1.8 \times 10^{-23} \text{ m}^2/\text{V}^2$ and $.15C_{11} + .54C_{16} = 4.0 \times 10^{-23} \text{ m}^2/\text{V}^2$. Conversion efficiency in d-LAP is about 20% that in BBO and conversion efficiency in KD*P is 1% that of BBO. It is calculated that conversion efficiencies of 30–40% are possible at intensities of 600–800 GW/cm², which is the operating level of the Petawatt laser at LLNL. The main limiting factors are phase modulation and material damage.

Acknowledgements

Now that I am at the end of this long adventure, I guess I would say that I am thankful to be done. It seems that I almost always ended up doing things the hard way, but I learned a lot along the way.

First and foremost, I need to say thanks to Lety, my wife, who has earned this as much as I have. It's always nice to have a good friend behind you and along side you all of the way.

Then there is everyone at SPLAT who have been a great group of people to work with and have helped a great deal. Mike Perry, my advisor, has provided a playroom full of wonderful toys that even work (most of the time) and an atmosphere of freedom that would have been perfect if such a thing as time did not exist. He has taught me a great deal about physics in the “real” world and provided many helpful suggestions. Jason Zweiback (Mr. YLF) built the pump laser and provided the needed comic relief during long days in the lab. I still want to see him pull a breadboard from underneath a pile of optics without moving the optics. Brent Stuart has given his sage advice as the occasion permits. Mike Feit has endured countless questions and discussions, and a solution was almost always found.

Turning to the larger world, the facilities available in the Laser Program at LLNL are to be envied by all graduate students. It again is just too bad that there is not more time to make use of all of the opportunities that I've had. Finally, I want to thank Roger Haas for instilling in me a solid understanding of the theory that makes up nonlinear optics.

Contents

List of Figures	viii
List of Tables	xii
1 Introduction	1
2 Design of 100 TW Laser System	6
2.1 Ti:sapphire MOPA Chain	12
2.1.1 Master Oscillator and Stretcher	13
2.1.2 Broadband Regenerative Amplifier	15
2.1.3 4-Pass Power Amplifier	26
2.1.4 Second 4-pass power amplifier	29
2.1.5 Final two Ti:sapphire amplifier stages	32
2.2 Hybrid Nd-doped YLF and glass pump system	33
2.2.1 Second harmonic generation of 1053 nm light	37
2.2.2 High energy amplifiers	39
2.3 Conclusion	40
3 All-Reflective Pulse Stretcher for Chirped-Pulse Amplification	41
3.1 Pulse Stretcher	45
3.1.1 Stretcher design	46
3.1.2 Design considerations	49
3.1.3 Alignment issues	52
3.1.4 Performance issues	54
3.2 Compressors	65
3.3 Conclusion	67
4 High intensity nonlinear optics	68
4.1 Preliminaries	70
4.1.1 Fourier transform pair	71
4.1.2 Coordinate systems	72
4.1.3 Derivation of wave equation	72
4.2 Coupled wave equations	80
4.2.1 Cascaded third harmonic generation	85
4.2.2 Effective nonlinear coupling	88
4.2.3 Self-phase modulation	90

4.2.4	Optimal input intensity	92
4.3	Biaxial crystals	98
4.4	Material considerations	102
4.5	Numerical solution of coupled wave equation	110
4.6	Conclusion	121
5	High intensity third harmonic generation	122
5.1	BBO	124
5.1.1	Type I phasematching	127
5.1.2	Type II phasematching in BBO	133
5.2	LAP	140
5.3	KD*P	143
5.4	Higher intensities and self-phase modulation	145
5.5	Damage and UV absorption	148
5.6	Conclusion	151
6	Conclusion and future directions	152
6.1	Future directions	153
A	Effects of residual phase on pulse shapes	156
A.1	Spectral-clipping and gain-narrowing effects	157
A.2	Second-order residual phase effects	160
A.3	Third-order residual phase effects	162
A.4	Fourth-order residual phase effects	165
A.5	Fifth-order residual phase effects	168
B	Phasematching loci of biaxial crystals	171
B.1	LBO	172
B.2	KTP	174
B.3	LAP	175
B.4	d-LAP	177
B.5	KLN	179
B.6	KCN	181
B.7	BMF	183
B.8	LFM	185
	Bibliography	187

List of Figures

2.1	Stimulated emission cross section σ_e of Ti:sapphire	10
2.2	Components of the 100 TW laser system	12
2.3	Schematic of Ti:sapphire portion of laser.	13
2.4	Ti:sapphire oscillator	14
2.5	Broadband regenerative amplifier design	16
2.6	Calculated waist of regenerative amplifier mode	22
2.7	Regenerative amplifier buildup	23
2.8	Energy stability of the regenerative amplifier	24
2.9	Spatial profile of beam output from regenerative amplifier.	25
2.10	Output spectrum of the regenerative amplifier	25
2.11	Polarizer transmission	26
2.12	Schematic of first four-pass amplifier	27
2.13	Beam waist in first amplifier	28
2.14	Spatial mode in first amplifier	29
2.15	Beam image in second amplifier	30
2.16	Beam propagation effects in second amplifier	31
2.17	Schematic of the second amplifier stage	31
2.18	Schematic of the YLF-based pump system.	33
2.19	Small signal, single pass gain of 9.5 mm Nd:YLF rod	34
2.20	The spatial profile of the 10 Hz 9mm amplifier head.	36
2.21	Second harmonic conversion efficiency	38
2.22	Spatial profile of second harmonic beam	39
3.1	Grating pair schematic	42
3.2	Stretcher design	47
3.3	Stretched pulse shape	50
3.4	Stretcher bandpass	51
3.5	Interferometric autocorrelation with parabolic mirror	55
3.6	Transverse spatial chirp for parabolic and french design	56
3.7	Deformed mirror shape	58
3.8	Transverse spatial chirp with deformed mirror	59
3.9	Transverse spatial chirp for spherical mirror	61
3.10	Residual phase and temporal delay	62
3.11	Interferometric autocorrelation using large spherical mirror	63
3.12	Autocorrelation of 45 fs pulse	64

3.13	Single grating compressor	65
3.14	Two grating compressor	66
4.1	The coordinate systems	71
4.2	Cascaded third harmonic generation	85
4.3	Principal axes for a biaxial crystal	98
4.4	Polarization eigendirection angle	99
4.5	The birefringence of a biaxial crystal	100
4.6	Small signal growth for THG	114
4.7	KD*P SHG conversion efficiency	116
4.8	BBO SHG conversion efficiency	116
4.9	Propagation distance for max. conversion	117
4.10	SHG of 100 fs pulses	117
4.11	Temporal profiles for Type I SHG in KD*P	118
4.12	SHG efficiency along prop. distance	119
5.1	Dependence of C_{eff}^2 for Type I phasematching	128
5.2	Experimental setup	129
5.3	Effective nonlinear coupling for internal azimuthal angle ϕ_{int}	130
5.4	Spatial profiles on input and output beams	132
5.5	Type II dependence of C_{eff}^2	133
5.6	Type II effective nonlinear coupling	134
5.7	Type I output energy	136
5.8	Type II output energy	136
5.9	Type I efficiency	137
5.10	Type II efficiency	137
5.11	Calculated longitudinal growth	138
5.12	Calculated Type I temporal profiles	139
5.13	Calculated Type II temporal profiles	139
5.14	LAP output energy	142
5.15	Predicted conversion efficiency	145
5.16	Calculated amplitude and phase w/o $\chi^{(2)}$ and SPM	146
5.17	Calculated amplitude and phase w/o SPM	147
5.18	Calculated amplitude and phase	147
6.1	Schematic for single-shot third-order autocorrelator	155
A.1	Pulse shape of input pulse	157
A.2	Autocorrelation of input pulse	157
A.3	Pulse shape of clipped pulse	158
A.4	Autocorrelation of clipped pulse	158
A.5	Pulse shape of narrowed pulse	158
A.6	Autocorrelation of narrowed pulse	159
A.7	Pulse shape of narrowed, clipped pulse	159
A.8	Autocorrelation of narrowed, clipped pulse	159
A.9	Pulse shape with 2nd order phase	160
A.10	Autocorrelation with 2nd order phase	160
A.11	Pulse shape with 2nd order phase	160
A.12	Autocorrelation with 2nd order phase	161

A.13	Pulse shape with 2nd order phase	161
A.14	Autocorrelation with 2nd order phase	161
A.15	Pulse shape with 3rd order phase	162
A.16	Autocorrelation with 3rd order phase	162
A.17	Pulse shape with 3rd order phase	162
A.18	Autocorrelation with 3rd order phase	163
A.19	Pulse shape with 3rd order phase	163
A.20	Autocorrelation with 3rd order phase	163
A.21	Pulse shape with 3rd order phase	164
A.22	Autocorrelation with 3rd order phase	164
A.23	Pulse shape with 4th order phase	165
A.24	Autocorrelation with 4th order phase	165
A.25	Pulse shape with 4th order phase	165
A.26	Autocorrelation with 4th order phase	166
A.27	Pulse shape with 4th order phase	166
A.28	Autocorrelation with 4th order phase	166
A.29	Pulse shape with 4th order phase	167
A.30	Autocorrelation with 4th order phase	167
A.31	Pulse shape with 5th order phase	168
A.32	Autocorrelation with 5th order phase	168
A.33	Pulse shape with 5th order phase	168
A.34	Autocorrelation with 5th order phase	169
A.35	Pulse shape with 5th order phase	169
A.36	Autocorrelation with 5th order phase	169
A.37	Pulse shape with 5th order phase	170
A.38	Autocorrelation with 5th order phase	170
B.1	Phasematching loci SHG in LBO at 820 nm	172
B.2	Phasematching loci SHG in LBO at 1053 nm	172
B.3	Phasematching loci THG in LBO at 1053 nm	173
B.4	Phasematching loci SHG in KTP at 820 nm	174
B.5	Phasematching loci SHG in KTP at 1053 nm	174
B.6	Phasematching loci SHG in LAP at 820 nm	175
B.7	Phasematching loci THG in LAP at 820 nm	175
B.8	Phasematching loci THG in LAP at 1053 nm	176
B.9	Phasematching loci THG in LAP at 1053 nm	176
B.10	Phasematching loci SHG in d-LAP at 820 nm	177
B.11	Phasematching loci THG in d-LAP at 820 nm	177
B.12	Phasematching loci SHG in d-LAP at 1053 nm	178
B.13	Phasematching loci THG in d-LAP at 1053 nm	178
B.14	Phasematching loci SHG in KLN at 820 nm	179
B.15	Phasematching loci SHG in KLN at 1053 nm	179
B.16	Phasematching loci THG in KLN at 1053 nm	180
B.17	Phasematching loci SHG in KCN at 820 nm	181
B.18	Phasematching loci SHG in KCN at 1053 nm	181
B.19	Phasematching loci THG in KCN at 1053 nm	182
B.20	Phasematching loci SHG in BMF at 820 nm	183
B.21	Phasematching loci SHG in BMF at 1053 nm	183

B.22 Phasematching loci THG in BMF at 1053 nm	184
B.23 Phasematching loci SHG in LFM at 820 nm	185
B.24 Phasematching loci THG in LFM at 820 nm	185
B.25 Phasematching loci SHG in LFM at 1053 nm	186
B.26 Phasematching loci THG in LFM at 1053 nm	186

List of Tables

2.1	Results of cavity calculations for several design parameters	21
2.2	Output energies for the second amplifier stage. Fluences are in J/cm ²	32
3.1	Sensitivity to alignment errors in stretcher	52
3.2	Material dispersion effects	60
3.3	Material phase terms	60
4.1	Coupling coefficients d_j and C_j	84
4.2	Coupling coefficients C_j^{SPM} and C_j^{XPM}	84
4.3	Possible interactions for THG	88
4.4	Relationship between subscripts of d_{ijk} and d_{im}	89
4.5	Relationship between subscripts of C_{ijkl} and C_{im}	89
4.6	ooo interactions	94
4.7	ooe interactions	94
4.8	occ interactions	94
4.9	eee interactions	95
4.10	oooo interactions	95
4.11	oooe interactions	96
4.12	ooee interactions	96
4.13	oeee interactions	97
4.14	eeee interactions	97
4.15	sss interactions	102
4.16	Type I SHG bandwidths for 820 nm	107
4.17	Type II SHG bandwidths for 820 nm	107
4.18	Type I SHG bandwidths for 1053 nm	107
4.19	Type II SHG bandwidths for 1053 nm	107
4.20	Type II SFG bandwidths for 820 nm	108
4.21	Type II SFG bandwidths for 1053 nm	108
4.22	Type I THG bandwidths for 820 nm	108
4.23	Type I THG bandwidths for 1053 nm	109
4.24	Type II THG bandwidths	109
4.25	Material parameters for uniaxial and biaxial crystals	109
5.1	Correct nonzero third-order tensor elements for crystal class 3m.	126

Chapter 1

Introduction

With the advent of the laser in the early 1960s,^{1,2} it became possible to produce electric fields whose magnitude is sufficient to readily probe nonlinear material response functions. Within a year, the generation of the second harmonic of the laser light was observed,³ and quickly thereafter, the theory behind such nonlinear interactions had been developed.^{4,5} Soon, several nonlinear optical phenomena had been discovered and studied in a large range of solids, liquids, and gases, thereby giving rise to the field of nonlinear optics. Second harmonic generation (SHG), third harmonic generation (THG), sum and difference frequency generation (SFG and DFG), self-phase-modulation (SPM), stimulated Raman scattering (SRS), and stimulated Brillouin scattering (SBS) are but a few of the many processes which have been observed.

Nonlinear optics is germane whenever high intensity electromagnetic radiation interacts with matter. In solid matter, while some interactions involving the third-order nonlinearity such as self-phase modulation and self-focusing are significant, frequency conversion processes have typically been limited to those involving the second-order nonlinearity, and so the nonlinear media has been required to be crystalline with no center of inversion. The

technique of using birefringence to match the phase velocities of the interacting waves^{6,7} requires that the crystal have significant birefringence. Higher order interactions in solids are not typically possible because very high intensities are needed, and solid media damage before efficient conversion can be achieved via higher-order nonlinearities. Early attempts at direct THG (a third-order process) met with very poor conversion efficiency,^{8–11} and the process has been mostly neglected since. Work has continued in the area of higher-order nonlinear processes in gases and liquids where material damage is not a concern.¹²

Recently, however, the development of the technique known as chirped-pulse amplification (CPA)^{13,14} has made possible the construction of terawatt and even petawatt (10^{15} W) class lasers.¹⁵ Such high powers have been used in focused beams to explore very high-order nonlinearities in gases. This same technology, though, can also be used to explore higher-order electronic responses in solids because the material intensity damage threshold increases as the pulse length decreases.^{16,17} With the subpicosecond pulse lengths that are typical of CPA lasers, intensities of over 1 TW/cm^2 can propagate short distances through solid media without damaging the material.

This increase in intensity and the correspondingly larger nonlinear interactions does not come without other difficulties being introduced. The short pulse lengths of CPA lasers and, as required by the uncertainty principle, the associated large bandwidths complicate the frequency conversion process. Because of the dispersion of the linear refractive indices of materials, only a single set of frequencies is phasematched for a given configuration. In order to obtain efficient conversion, we require that the phasematching properties of the interaction be relatively insensitive to frequency. This is the same as requiring that both the phase and group velocities match for the interacting waves.¹⁸ Otherwise the pulses will walk off from each other in time over a relatively short distance. There have been a

number of methodologies proposed for SHG^{18–23} to minimize this effect. In addition, the fact that the intensities are so high (in excess of 100 GW/cm²) that other, higher-order nonlinearities are efficiently excited, can result in reduced gain for the desired effect.

In spite of these difficulties, the high intensities available from CPA lasers open opportunities to investigate interactions which to this date had been relatively unexplored. One such effect is to generate the third harmonic (THG) directly from the fundamental frequency of a laser, combining three photons to create light at three times the frequency in one interaction. This mechanism of generating the third harmonic was explored within a few years of the creation of the laser, but with little success. The idea was abandoned in favor of using two crystals with the first phasematched for SHG followed by a second crystal phasematched for SFG of the fundamental and the second harmonic. For long pulses without the bandwidth problems mentioned above, very high conversion efficiencies (up to 80%)²⁴ to the third harmonic have been achieved. In fact, it is this two crystal process that has become to be denoted by THG today. In this work, when there is a possibility of confusion, single-crystal THG will refer to the direct conversion to the third harmonic in a single crystal, and two-crystal THG will refer to process involving SHG and SFG in two crystals.

The use of two crystals becomes more problematic for sub-picosecond pulse lengths due to the temporal walkoff due to group velocity mismatch (GVM) between the fundamental and its harmonics. Not only is the mismatch worse for the third harmonic wave, a delay device must be introduced between the crystals in order to have the fundamental and second harmonic wave overlap in time at the second crystal. This has resulted in conversion efficiencies to the third harmonic for sub-picosecond pulses to be limited to 10–20%.²⁵ Finally, there is a desire to be able to efficiently triple the Petawatt laser at LLNL, but

GVM coupled with self-focusing concerns prohibit the use of the standard, two-crystal tripler arrangement.

In the last twenty years, single-crystal THG has been tried every so often^{26–29} with somewhat better results as the pulse lengths became shorter and intensities increased, particularly in BBO. In the low-drive regime, the amount of third harmonic light generated will increase as the third power of the incident intensity so an increase in the input intensity by a factor of ten will increase the output intensity by three orders of magnitude. Thus one would expect that the large intensities made possible by CPA lasers might enable one to achieve relatively good production of tripled light using a single crystal.

The outline of this dissertation, then, is to first describe the design and operation of a CPA laser system ultimately capable of producing pulses with peak powers of 100 TW. To achieve powers of this magnitude with pulse energies achievable with a “tabletop” system, it is required that the temporal pulse length to be on the order of 50 femtoseconds which will influence several design considerations. In particular, a unique all-reflective stretcher design was developed in order to support the bandwidth while avoiding some of the aberrations present in most transmissive designs. This design allows for easy compensation of the material dispersion of the laser system, thereby permitting the use of a regenerative amplifier for ease of use and energy stability. Following this discussion on the construction of the laser system, the aspects of nonlinear optics pertinent to high intensity frequency conversion will be discussed. In particular, it has been postulated and calculated that unphasematched second-order interactions can significantly contribute to THG,^{28,30,31} but there is no conclusive experimental confirmation of this. Finally, the production of UV light via single-crystal THG will be experimentally investigated in three crystalline materials: KD*P, BBO, and d-LAP. Conclusive evidence for the relative contributions between

second- and third-order nonlinearities is obtained, and accurate measurements are made of the tensor elements of the third-order susceptibility $\chi^{(3)}$. Also, it should be noted that throughout this work, c and λ denote the speed of light and the wavelength, respectively, in vacuum.

Chapter 2

Design of 100 TW Laser System

Achievable peak powers in moderate-scale lasers have typically been limited to less than a few gigawatts because of material damage considerations. It is well known that at intensities on the order of $1\text{--}10\text{ GW/cm}^2$ laser pulses undergo self-focusing due to the intensity dependent nonlinear refractive index. This leads to a deterioration of the beam quality and can lead to catastrophic damage of the material through which the beam passes. To reach high powers without damage, it has been necessary to use large aperture beams as is common with the large fusion lasers. In fact, this problem is exacerbated as the temporal pulse length decreases because of the inverse proportionality of the laser intensity with the pulse length. For example, a 100 fs pulse will have a peak power of 10 GW with a pulse energy of only 1 mJ. However, for short pulse lasers, it is possible to make use of the associated large spectral bandwidths to expand the pulse in time prior to amplification as well as in space, thereby reducing the intensity while maintaining smaller amplifier apertures. This technique of expanding the pulse by imposing a large frequency chirp (a time-dependent frequency) is known as chirped-pulse amplification (CPA)^{13,14} and now has been used by many groups in the last few years to generate even tens of terawatts

of peak laser power in systems that are room-sized.^{32–37}

Recently, the peak powers achievable with CPA lasers systems has been raised yet again with 100 TW and 1 PW (1 petawatt equals 10^{15} Watts) being produced at LLNL.^{38,39} These tremendous peak powers were produced even though the final pulse length was relatively long, approximately 400 fs. Petawatt pulses were accomplished by using a section of one of the amplifier beam lines of the NOVA laser to generate over 600 J of energy in the amplified pulse. To avoid the use of large scale amplifiers to achieve 100 TW class pulses, efforts can be made to significantly decrease the final pulse duration and achieve the same peak powers with a fraction of the energy. The latter is the approach chosen for the laser considered here. The final goal will be produce pulses with peak powers of close to 100 TW with final pulse energies of approximately 5 J, thereby necessitating pulse lengths of 50 fs or less. Energies of this level can be achieved with a room-sized laser system. The laser system uses titanium-doped sapphire as the gain medium with several amplifier stages located in between a pulse stretcher and a pulse compressor. Both the amplifiers and the CPA stretcher/compressor have exacting design constraints for amplification of short pulses (sub-100 fs) and will be discussed separately: the overall laser system and amplification process in this chapter and the pulse stretcher/compressor in Chapter 3.

There are several aspects of amplification of a sub-50 fs laser pulse which are unique to CPA lasers which had to be taken into consideration in the design of this laser system. These include the nonlinear phase (the B-integral) acquired by the pulse as it traverses the laser system, additional chirp added to the pulse by group-velocity dispersion (GVD) and self-phase modulation, and most importantly, the spectral bandwidth supported by the entire system. All of these have an effect on the final pulse shape and duration.

It is essential to carefully control the phase effects produced by all of the elements of

the laser system. This includes the nonlinear phase introduced by the intensity-dependent refractive index $n_{\text{total}} = n + \gamma I$. As discussed by Perry *et al.*,⁴⁰ it is important to keep this at a minimum to avoid significant temporal pulse distortion upon recompression. The standard measure of the accumulated nonlinear phase over a length L is known as the B-integral, defined as

$$B = \frac{2\pi}{\lambda} \int_0^L \gamma I dz. \quad (2.1)$$

The total B summed over all components of the system should be less than $\cong 1$ in order to achieve Fourier transform limited pulses.

In addition to the effects of the nonlinear refractive index, the frequency dependence of the linear refractive index of the material traversed by the pulse also becomes significant. This frequency dispersion means that each frequency component of the pulse will be delayed by a slightly different amount as the pulse travels through the material, affecting the phase of the pulse in a frequency-dependent manner. Also, as will be discussed in Chapter 3, even the chirp imposed by material dispersion means that the compressor will need to be adjusted to compensate. This results in the compressor no longer identically matching the stretcher, meaning that there will be some chirp imposed by the stretcher and material that cannot be perfectly removed in the compressor. Because of this, some groups choose to design their system to minimize the amount of material through which the pulse propagates. Otherwise, the stretcher/compressor must be designed to account for this effect.

Spectral bandwidth is critically important in CPA lasers because femtosecond pulses have relative bandwidths on the order of a few percent. This is due to the fact that the uncertainty principle requires that the time-bandwidth product $\Delta\nu\Delta t$ be larger than approximately .5; the actual value depends on the actual pulse shape and the definition

used for Δt and $\Delta\nu$. For example, if one defines the widths in terms of the FWHM values, then for a gaussian temporal pulse shape ($I(t) = I_0 \exp(4 \ln 2 (t/\Delta t)^2)$), $\Delta\nu\Delta t = .441$ while for sech^2 pulses ($I(t) = I_0 \text{sech}^2(1.76t/\Delta t)$), $\Delta\nu\Delta t = .315$. In terms of wavelength, $\Delta t(\text{fs})\Delta\lambda(\mu\text{m}) = 1.47\lambda_0^2$ for gaussian pulses and $1.05\lambda_0^2$ for sech^2 pulses where λ_0 is the center wavelength of the pulse in microns. For a pulse whose spectrum is centered at 820 nm, $\Delta t\Delta\lambda = .99$ and $.71$, respectively. Thus even for a gaussian pulse of 50 fs FWHM, the associated spectral bandwidth will be 20 nm, and for a 20 fs pulse, the associated bandwidth will be 50 nm. These large bandwidths must be maintained as much as possible throughout the system since a narrowing of the spectrum directly corresponds to longer pulses at the end of the system. Effects that will narrow the spectrum include the finite gain bandwidth of the amplifying medium, the frequency-dependent reflectivity of dielectric mirrors and polarizers, and finite size of the optics in the pulse stretcher and compressor.

The bandwidth requirements limit the possible gain medium to very few materials, most notably titanium-doped sapphire (Ti:sapphire) and chromium-doped LiSrAlF_6 (LISAF), whose stimulated emission cross section σ_e are spectrally broad. Many CPA lasers have been built in recent years using both materials^{42–45,35,46} with the majority using Ti:sapphire. There are positive and negative aspects of both materials: LISAF has a large saturation fluence and a much longer upperstate lifetime enabling flashlamp pumping of the medium while Ti:sapphire has a much higher gain, a broader gain spectral profile, and much higher thermal diffusivity. Ti:sapphire is also typically available in crystals of higher optical quality than LISAF. The bandwidth supported is, however, the most critical aspect for amplification of 50 fs laser pulses. The pulse spectrum will be significantly narrowed for the enormous gain ($\sim 10^9$) required in CPA lasers, even for

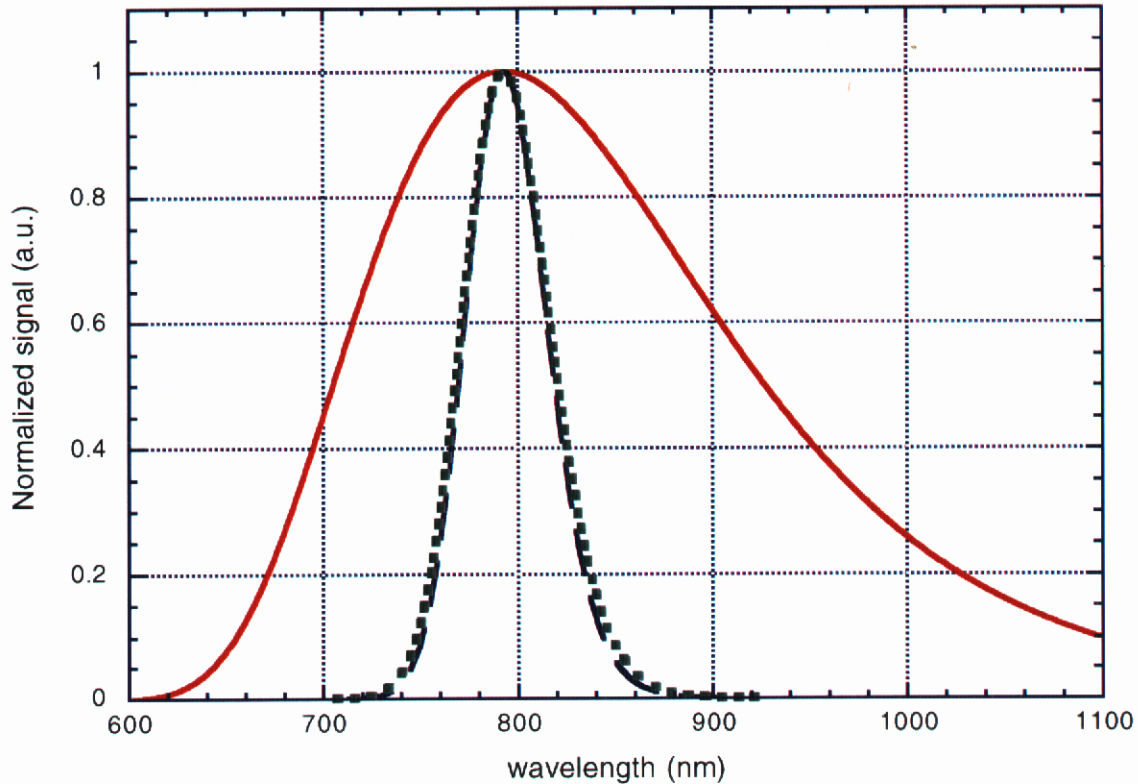


Figure 2.1: The normalized stimulated emission cross section σ_e of Ti:sapphire⁴¹ (solid line). The dotted and dashed lines are the resulting spectra after amplifying a flat spectrum by a total gain of 10^7 and 10^8 , respectively.

Ti:sapphire, for which $\sigma_e(\lambda)$ is 215 nm (FWHM, Fig. 2.1). Also shown in Fig. 2.1 is the final amplified spectra of an input pulse with a flat spectrum ($I(\omega) = I_0$) after a total gain of 10^7 or 10^8 . These output spectra are only 50 nm wide, indicating that even an infinitely short pulse will be broadened to 20 fs upon amplification. For a 66 nm wide gaussian pulse (15 fs), it will be narrowed to 41 nm (25 fs), and a 33 nm wide gaussian pulse (30 fs) will be narrowed to 28 nm (35 fs). LISAF, whose cross section spectral distribution is about half as wide, will be even worse and cannot be used for the high gain amplifiers with 50 fs pulses. Once the energy has been amplified to the millijoule level, the spectral gain narrowing will be less important, but LISAF amplifiers of the size needed at this stage typically cannot be fired more than every few seconds while Ti:sapphire can

be fired at tens of Hertz. Therefore, Ti:sapphire was chosen as the gain medium for our entire system.

However, the choice of Ti:sapphire, because of its short upperstate lifetime, requires that all of the amplifiers be pumped by the output of another laser systems. Since the peak of the absorption cross section of Ti:sapphire is approximately 500 nm⁴⁷, it is common to use the second harmonic of a Nd-doped laser medium such as YAG or glass. However, in order to both take advantage of large aperture Nd:phosphate rods which were available and simultaneously allow for higher repetition rates than is possible for glass at low energies, we selected Nd:YLF as the laser medium for part of the pump laser system. Fig. 2.2 shows a schematic block diagram of the various components of both Ti:sapphire and Nd:YLF/glass laser systems.

The limiting factor throughout the total system for both final pulse energies and the pulse repetition rates is that of the pump source. Small aperture YLF rods (less than 10 mm diameter) can be fired at 10 Hz and produce energies of around 1 J; therefore the laser system up to this level will operate at 10 Hz and produce pulse energies of about 200 mJ at 820 nm. The larger aperture 19 mm YLF rods can only be fired about once per second and so the next stage will operate at 1 Hz producing approximately 1.5 J at 820 nm. Finally, the glass based amplifiers can only be fired every 7 minutes requiring that the final, high energy stage be operated on a single shot basis producing $\cong 7$ J of 820 nm light.

The details of the design and modeling of the Ti:sapphire amplifier chain are presented in Section 2.1 as well as the performance characteristics of the parts now completed. The performance characteristics of the Nd:YLF pump system are given in Section 2.2.

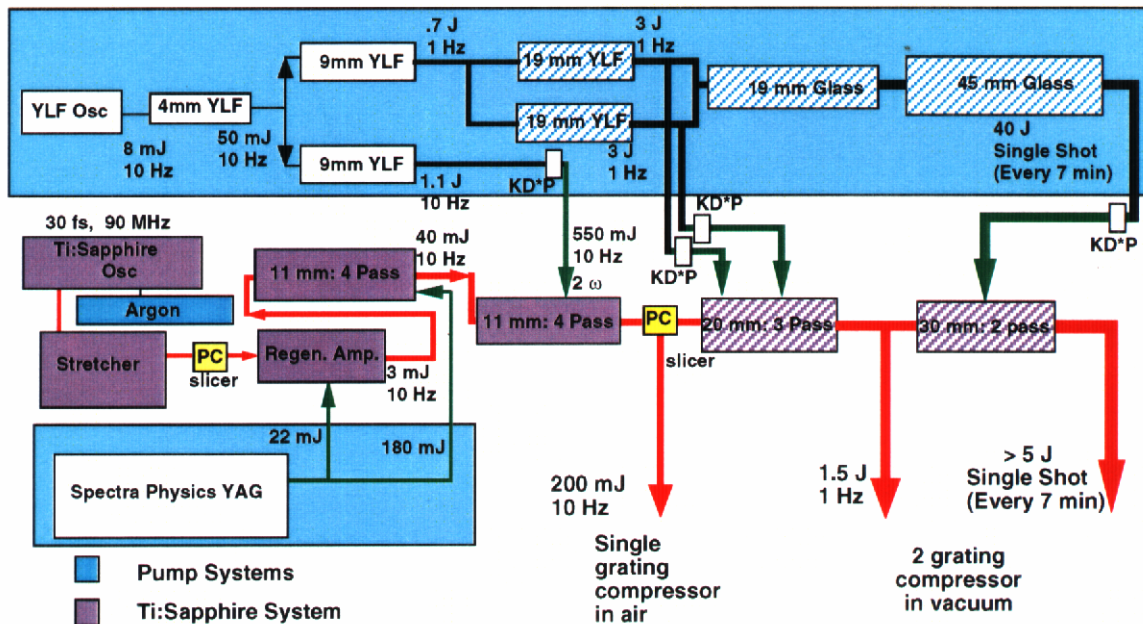


Figure 2.2: Block diagram indicating the components of the 100 TW laser system. The lighter blocks indicate the pump components.

2.1 Ti:sapphire MOPA Chain

A more detailed diagram of the components of the Ti:sapphire amplifier chain is presented in Fig. 2.3. It is composed of a 30 fs Kerr lens modelocked oscillator which provides the seed for the amplifier chain. The pulse is stretched in time using an all-reflective stretcher that is described in Chapter 3. Once stretched, a Pockels cell slicer creates a 10 Hz pulse train that is injected into a regenerative amplifier which gives a gain of 10^7 . Following this, there are two 4-pass amplifiers that bring the pulse energy up to 200 mJ in a flat-top or gaussian beam. The creation of the flat-top spatial profile using a serrated aperture requires that the remainder of the system be relay-imaged using vacuum spatial filters. This beam is then compressed using a single-grating compressor in air, giving about 2 TW of peak power at 10 Hz. Another Pockels cell can be used to slice out a 1 Hz pulse train from the 10 Hz for the seed for the next amplifier stage which will give 1.5 J. This can either be compressed using a 2 grating compressor at vacuum for 20 TW pulses at 1 Hz

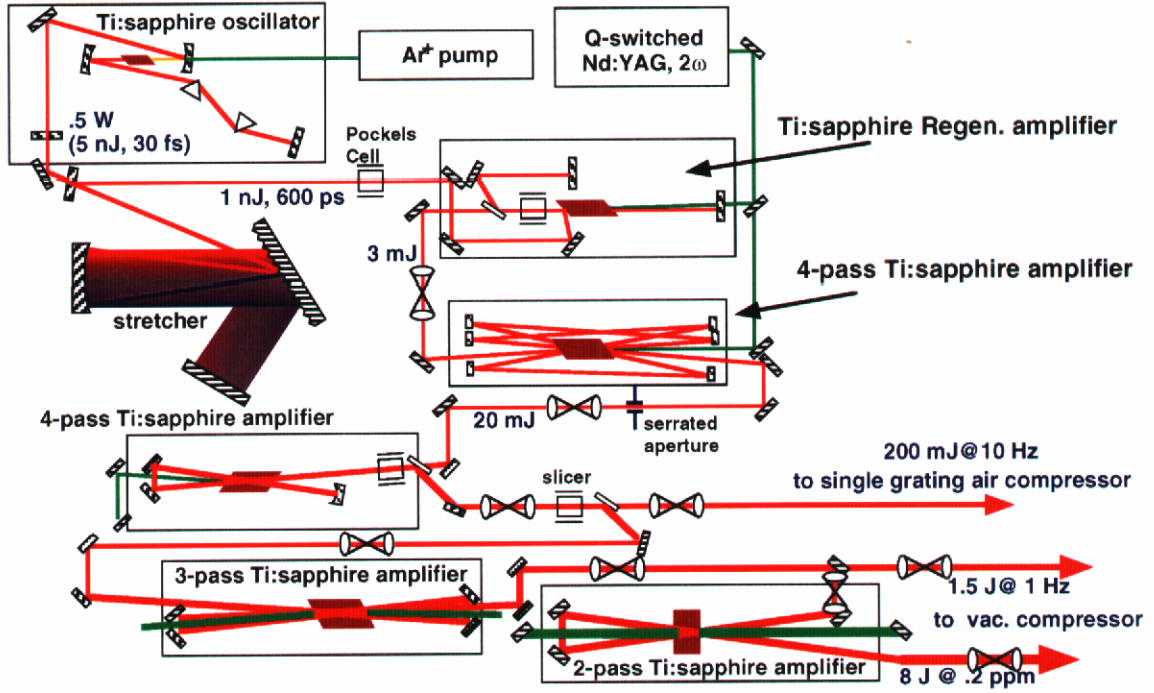


Figure 2.3: Schematic of Ti:sapphire portion of laser.

or amplified further in single shot fashion to 7J to obtain final peak powers of 100 TW. Each of these stages will be described in detail in the following sections.

2.1.1 Master Oscillator and Stretcher

In order to have a 50 fs pulse at the end of the system, one must start with a pulse shorter than 50 fs at the beginning of the system. These seed pulses are produced by a Kerr-lens modelocked Ti:sapphire oscillator (see Fig. 2.4) pumped by a Coherent Innova 310 Argon ion laser. This oscillator (with slight modification) was designed and built by Scott Fochs as part of his Master's thesis.⁴⁸ The output coupler was changed from one with 91% reflectivity to one with 88% reflectivity. This increased the average power output from the laser from about 350 mW to 500 mW at the cost of an increase in pump power from approximately 5.5 W to 6.5 W. Due to a deficiency in the tube pressure stabilization

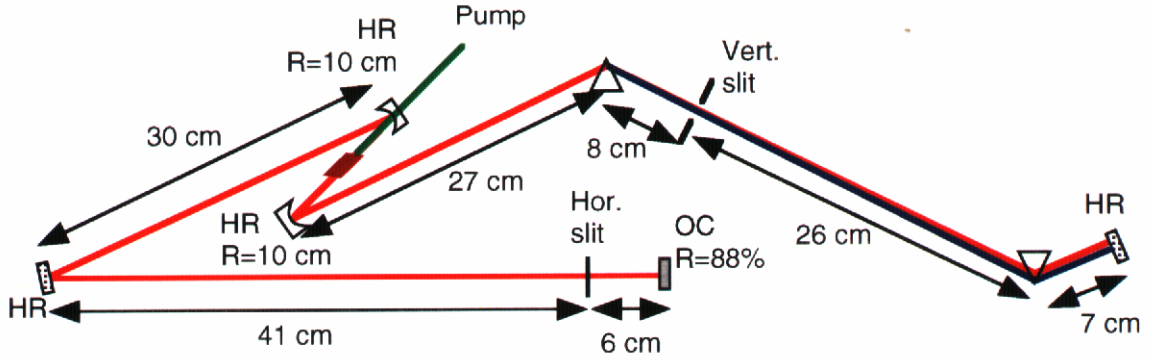


Figure 2.4: 30 fs Kerr-lens modelocked Ti:sapphire oscillator. Ti:sapphire crystal (1 cm long) is placed 5 cm from each curved mirror.

circuitry of the pump laser, it was also found necessary to run the laser at higher than optimum powers ($> 7.5\text{W}$) which resulted in a propensity for CW cavity modes to also lase. It was found empirically that inserting a vertical slit between the two prisms in the dispersion compensation arm of the cavity allowed for the introduction of enough loss to discriminate against the CW modes and improved the stability of cavity operation. It also provided for a simple method of tuning the central frequency of the modelocked spectrum approximately 20 nm in either direction without further cavity adjustment.

The oscillator produces a 92 MHz pulse train of 30 fs (FWHM) pulses with 5 nJ per pulse. These pulses are then stretched to 600 ps using a novel, all-reflective pulse stretcher which will be described in more detail in Chapter 3. Because the beam strikes up to 20 gold reflecting surfaces and 4 grating surfaces (which have a 91% diffraction efficiency) through the stretcher, approximately 80% of the energy is lost. A Pockels cell between crossed polarizers is then used after the stretcher to slice out a 10 Hz pulse train from the 92 MHz train. This serves two purposes: 1) any amplified light coming back from the amplifiers is rejected (the modelocking mechanism of the oscillator is sensitive to even a small amount of feedback) and 2) it reduces the extent to which unwanted pulses leak into the regenerative amplifier. However, the polarizers in this slicer highlight the

fact that the polarizers are the single most critical element in the system in regards to bandwidth limitation. The polarizers used were a broadband, thin-film design from Laser Power Optics. Notwithstanding the designation of broadband, when used in transmission, it was observed that a nominally 32 nm (FWHM) pulse was narrowed to 24 nm by passing through 4 polarizers. Each polarizer used in transmission had the effect of narrowing the pulse spectrum by approximately 7%. The bandwidth passed by each polarizer is also very sensitive to the angle of incidence of the beam striking the polarizer with the shorter wavelengths being affected most by the angle of incidence being too shallow.

The solution to this is to use the polarizers in reflection whenever possible (this is evidenced in the design of the regenerative amplifier which follows). Double polarizers were used in reflection on either side of the Pockels cell and negligible spectral narrowing was observed. This arrangement also provides an improved extinction ratio compared to single polarizers used in transmission.

2.1.2 Broadband Regenerative Amplifier

For the first amplifier stage of the system, it is necessary to achieve total gains on the order of 1–10 million for output energies in the millijoule range. The initial amplifier design for this stage was to pass through the gain medium eight times using a bank of eight 1.2 cm diameter mirrors in a circular pattern on either side of the Ti:sapphire crystal. The advantage of this is that the only material traversed is the gain medium, minimizing material dispersion. The mirrors were used at near normal incidence to maximize the spectral width of their reflectivity curve. This design produced pulses of about 1 mJ, but because the beams were not collinear, the pump beam needed to be larger than 2.0 mm in diameter ($1/e^2$ point). In addition, it was necessary to use high pump fluences in

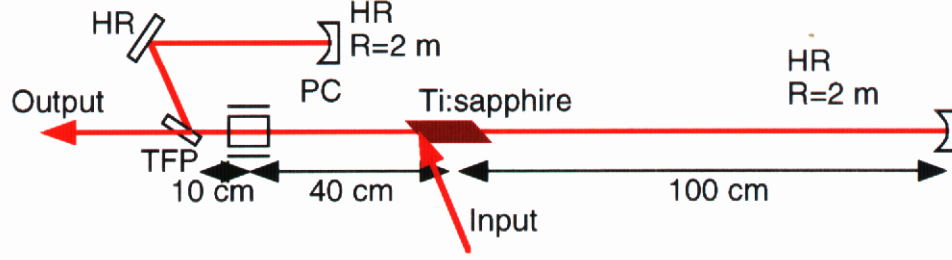


Figure 2.5: Broadband regenerative amplifier design. TFP indicates thin film polarizer, and PC indicates Pockels cell. The flat mirror shown is used as a fold mirror for compactness. The pulse is injected off the face of the Ti:sapphire crystal. The folded leg has a total length of 50 cm from the polarizer to the end mirror.

order to achieve a total gain of 1 million in just 8 passes through the gain medium. This necessitated using 100 mJ of pump energy in order to get 1 mJ out. The final drawback of using this design is that the shot-to-shot energy stability is relatively poor with an rms deviation of 10%.

To improve the shot-to-shot stability of the laser as well as reduce the pump energy required to obtain 1 mJ of output energy, the multipass amplifier was replaced by a regenerative amplifier design. Outside of the increased material dispersion that will be incurred, a regenerative amplifier requires the use of polarizers in conjunction with a Pockels cell in order to switch-in and switch-out the pulse train. Any element within the amplifier cavity will be traversed 20–40 times so its effect will be raised to the 20–40th power. This precludes the use of any polarizer in transmission. It is still necessary to limit the amount of material through which the beam passes. Fig. 2.5 shows a linear cavity design that meets these criteria composed of the end mirrors, the Ti:sapphire crystal, a Pockels cell, and a polarizer used in reflection. The right half of the cavity must be polarized parallel to the page (P polarization) to pass through the Brewster face of the Ti:sapphire crystal, and the left half of the cavity must be polarized perpendicular to the page (S polarization) to be reflected off the polarizer. The beam is injected off the

brewster face of the Ti:sapphire crystal vertically polarized (S polarization) and reflects off the polarizer to the curved end mirror. While the pulse is in this half of the cavity, the Pockels cell is turned on to half-wave voltage, thereby rotating the polarization state to P in the right half of the cavity, passing through the Brewster face of the crystal. The Pockels cell is maintained at half-wave voltage until the pulse is to be switched out of the cavity. It is then turned off while the pulse is in the right half, remains P polarized, and is transmitted through the polarizer out of the cavity.

In order to model the cavity shown in Fig. 2.5, it is important to realize that the transverse spatial gain profile is not flat since we chose to use the frequency-doubled, nearly gaussian output of a Nd:YAG laser. Stuart *et al.*⁴⁹ give a formalism for treating this case by approximating the near gaussian gain profile as a quadratic radial dependence as described by Siegman⁵⁰.

First, the excited state population is calculated based on the absorption of the incident pump beam. The expression for the pump beam fluence $\Gamma_p(r, z)$ as it is absorbed while propagating through the medium is

$$\Gamma_p(r, z) = \Gamma_a \ln \left[1 + e^{-N_0 \sigma_a z} (e^{\Gamma_p(r)/\Gamma_a} - 1) \right]. \quad (2.2)$$

In this equation, N_0 is the initial ground state population density ($5 \times 10^{19} \text{ cm}^{-3}$ for .15% doped Ti:sapphire), $\Gamma_a = h\nu/\sigma_a$ is the absorption saturation fluence, σ_a is the absorption cross section ($5 \times 10^{-20} \text{ cm}^2$ at 532 nm), and $\Gamma_p(r)$ is the initial radially-dependent pump fluence. The ground state population density after absorption is then given by

$$N_0(r, z) = N_0 e^{-\Gamma_p(r, z)/\Gamma_a}, \quad (2.3)$$

and, assuming 100% of the excited population is in the Ti^{3+} state, the excited state

population density (and thus the inversion) becomes

$$\begin{aligned} N(r, z) &= N_0 - N_0(r, z) \\ &= N_0 (1 - \exp(-\Gamma_p(r, z)/\Gamma_a)) . \end{aligned} \quad (2.4)$$

Assuming a gaussian profile for the pump fluence, $\Gamma_p(r) = \Gamma_0 \exp(-2r^2/w_p^2)$ where w_p is the waist ($1/e^2$) of the pulse , the radial dependence of the population inversion at $z = 0$ is

$$N(r, 0) = N_0 (1 - \exp(-\Gamma_0 \exp(-r^2/w_p^2)/\Gamma_a)) . \quad (2.5)$$

In the limit that the absorption is not saturated, i.e. $\Gamma_p \ll \Gamma_a$, this becomes

$$N(r, 0) = N_0 \frac{\Gamma_0}{\Gamma_a} e^{-r^2/w_p^2} \quad (2.6)$$

showing that the inversion also has a gaussian transverse profile as is expected.

The output fluence $\Gamma_{\text{out}}(r)$ is related to a radially varying input fluence $\Gamma_{\text{in}}(r)$ and the longitudinally averaged population inversion

$$\bar{N}(r) = \frac{1}{L} \int_0^L N(r, z) dz \quad (2.7)$$

by

$$\Gamma_{\text{out}}(r) = \Gamma_e \ln [1 + \exp(\bar{N}(r)\sigma_e l)(\exp(\Gamma_{\text{in}}(r)/\Gamma_e) - 1)] \quad (2.8)$$

where l is the length of the gain region in question, $\Gamma_e = h\nu/\sigma_e$ is the stimulated emission saturation fluence, and σ_e is the stimulated emission cross section (e.g. for 820 nm, this is $2.7 \times 10^{-19} \text{ cm}^2$). However, as will be seen later, the peaked transverse gain profile causes the center of the pulse to be amplified more than the wings, spatially, thereby effectively reducing the diameter of the pulse as it is amplified (gain guiding). For this reason, it will be best to break up the Ti:sapphire crystal into several smaller sections in z over which the beam waist can be assumed to be constant.

The average population inversion \overline{N}_j over the j th segment from z_j to z_{j+1} is obtained by substituting Eq. (2.2) into Eq. (2.4) and averaging over the segment

$$\overline{N}_j = \frac{1}{\Delta z} \int_{z_j}^{z_{j+1}} \left[1 - \frac{1}{1 + \exp(-N_0 \sigma_a z) (\exp(\Gamma_p(r)/\Gamma_a) - 1)} \right] dz \quad (2.9)$$

$$= N_0 + \frac{1}{\sigma_a \Delta z} \ln \left[\frac{e^{-N_0 \sigma_a z_j} + e^{\Gamma_p(r)/\Gamma_a} - 1}{e^{-N_0 \sigma_a z_{j+1}} + e^{\Gamma_p(r)/\Gamma_a} - 1} \right]. \quad (2.10)$$

where $\Delta z = z_{j+1} - z_j$. For subsequent passes, the remaining inversion after amplification is, in analogy with Eq. (2.3), given by

$$N^{(n+1)}(r, z) = N^{(n)}(r, z) e^{-\Gamma(r, z)/\Gamma_e} e^{-t/\tau_{se}} \quad (2.11)$$

where the factor $\exp(-t/\tau_{se})$ has been inserted to account for population loss due to spontaneous emission with τ_{se} being the upperstate lifetime of Ti:sapphire. This decoupling of spontaneous emission from the amplification is possible because the amplification takes place in times of the order of 100 ps while the lifetime of Ti:sapphire is approximately 2 μ s. However, the multiple passes in the regenerative amplifier occur over several hundred nanoseconds since the initial excitation by the pump. Thus, the energy loss to spontaneous emission must be accounted for as the pulse builds up in the cavity.

If each segment j is assumed to be small enough such that the population inversion can be taken as constant over the segment (i.e. $N_j^{(n)}(r, z) = \overline{N}_j^{(n)}(r)$), the average population density in the segment for the next pass is given by

$$\overline{N}_j^{(n+1)}(r) = \frac{\overline{N}_j^{(n)}(r) e^{-t/\tau_{se}}}{\Delta z} \int_z^{z+\Delta z} e^{-\Gamma(r, z)/\Gamma_e} dz, \quad (2.12)$$

and integrating,

$$\overline{N}_j^{(n+1)}(r) = \frac{e^{-t/\tau_{se}}}{\sigma_e \Delta z} \ln \left[\frac{e^{-\overline{N}_j^{(n)} \sigma_e z} + e^{\Gamma_{in}(r)/\Gamma_e} - 1}{e^{-\overline{N}_j^{(n)} \sigma_e (z+\Delta z)} + e^{\Gamma_{in}(r)/\Gamma_e} - 1} \right]. \quad (2.13)$$

Now, in order to convert this 2-d problem in r and z to a 1-d problem in z only, it is possible to approximate the gaussian-like radial dependence as a quadratic dependence so

that $\overline{N}(r) \simeq \overline{N}_0(1 - 2r^2/w_p^2)$. This permits the use of the gaussian duct formalism⁵⁰ which also allows for a quadratic transverse dependence of the intensity-dependent refractive index. The refractive index is then $n \simeq n_0 + \gamma I_0(1 - 2r^2/w^2)$, and the propagation over a length Δz is governed by the complex ABCD matrix

$$\begin{bmatrix} A & B \\ C & D \end{bmatrix} = \begin{bmatrix} \cos \eta z & \frac{1}{n_0 \eta} \sin \eta z \\ -n_0 \eta \sin \eta z & \cos \eta z \end{bmatrix} \quad (2.14)$$

where the complex parameter η is given by

$$\eta = \left[\frac{4\gamma I_0}{n_0 w^2} + i \frac{g_0 \lambda}{\pi \Delta z n_0 w_p^2} \right]^{1/2}. \quad (2.15)$$

The additional factors of n_0 in the denominators in Eq. (2.15) take into account the differing sagittal and meridional beam waists inside the gain medium due to the Brewster faces. Thus, by using Eq. (2.14) for propagation inside the Ti:sapphire crystal and standard ABCD matrices elsewhere where the complex beam parameter q is

$$q^{(n)} = \frac{Aq^{(n-1)} + B}{Cq^{(n-1)} + D}, \quad (2.16)$$

and the beam waist obtained from q as

$$w^2 = -\frac{\lambda}{\pi \text{Im}\{1/q\}}, \quad (2.17)$$

the dynamic mode behavior can be calculated throughout the cavity.

Using this procedure, several cavity configurations were modeled in an attempt to determine the optimal cavity design. The results of these are presented in Table 2.1 for two different values of end mirror radii of curvature, 2 m and 4 m. In all cases, both end mirrors are of the same curvature with the crystal being placed at the center. The cavity length was 2 m for all cases except the last line of Table 2.1 for which it was 4 m. The choice of using 2 m mirrors gives a shorter buildup time and lower required pump

Table 2.1: Results of cavity calculations for several design parameters. The fluences are given in J/cm². The cavity round trip time is 13.5 ns in all cases except the last line where it was 26.4 ns. G_1 is the single pass gain for the first pass and τ_{out} is the time that the pulse is in cavity.

R_{mirror} (m)	\mathcal{E}_p (mJ)	$2w_p$ (mm)	Γ_p	G_1	\mathcal{E}_{max}	N_{pass}	τ_{out} (ns)	Γ_{peak}	B
2	20	1.2	3.5	4.5	5.7	16	110	1.2	.34
2	20	1.4	2.6	3.0	3.4	22	150	.64	.26
2	20	1.6	2.0	2.3	1.6	32	215	.28	.23
2	22	1.5	2.5	2.8	2.9	24	161	.48	.26
2	25	1.4	3.3	4.0	5.1	18	121	1.1	.39
2	25	1.6	2.5	2.9	3.1	24	161	.61	.31
2	25	1.8	2.0	2.3	1.5	32	215	.26	.21
2	25	2.0	1.6	2.0	.4	44	296	.06	.09
2	30	1.6	3.0	3.6	4.4	20	135	.83	.40
2	30	1.8	2.4	2.7	2.7	26	175	.48	.32
2	30	2.0	1.9	2.3	1.3	34	229	.22	.21
2	50	1.5	5.7	—	10	10	64	—	—
4	20	1.4	2.6	3.0	5.7	24	161	.5	.37
4	25	1.6	2.5	2.9	5.1	24	161	.44	.26
4	25	1.8	2.0	2.3	2.3	32	215	.19	.16
4	25	2.0	1.6	2.0	.47	44	296	.04	.06
4	30	1.6	3.0	3.6	7.4	20	135	.68	.36
4	30	1.8	2.4	2.7	4.5	26	175	.38	.27
4	30	2.0	1.9	2.3	2.0	36	242	.17	.22
4	30	2.2	1.6	2.0	.43	46	309	.04	.06
4	30	1.8	2.4	2.7	1.4	32	429	.10	.13

energy, but the trade-off is that lower output energies are achieved. It is also important to note that although shorter buildup times can be achieved by decreasing the cavity size, there needs to be sufficient delay between passes to turn on the Pockels cell. It is also important to place the Pockels cell as far away from the beam waist as possible to decrease the B-integral accumulated during amplification, but not close enough to an end mirror to experience counter-propagating beams within the cell.

The final cavity design was a confocal cavity with 2 m mirrors separated by 2 m, the Ti:sapphire crystal was 1 m from either mirror, the Pockels cell was located 40 cm from the crystal, and the polarizer was located 10 cm beyond that (50 cm from the end mirror). For space considerations, the “S” side of the cavity was folded by using a 34° mirror as

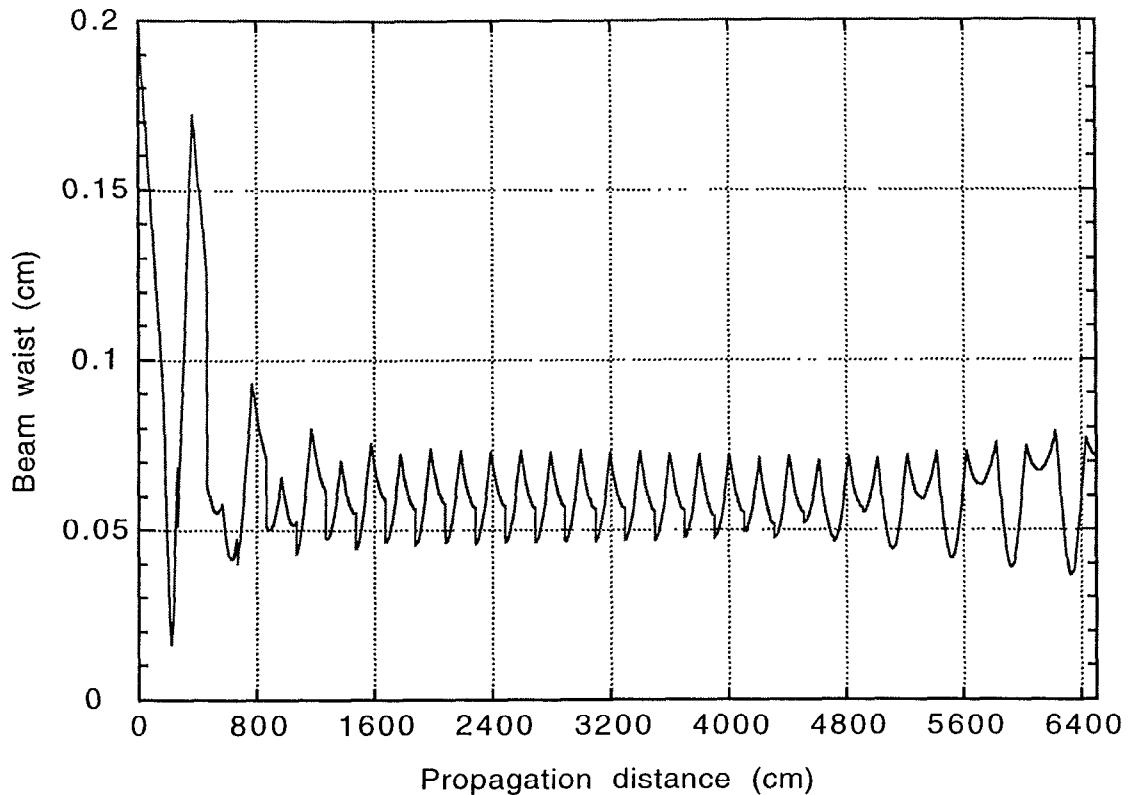


Figure 2.6: Calculated waist of mode in regenerative amplifier. Cavity length is approximately 200 cm.

shown in Fig. 2.5. The evolution of the cavity mode as calculated using the formalism described above is shown in Fig. 2.6 which shows the size of the beam waist as a function of propagation distance. Although the input mode does not match the cavity mode well, the beam quickly assumes the cavity mode profile within 2–3 round trips. The energy buildup of the regenerative amplifier is shown in Fig. 2.7 where each of the peaks is the pulse energy measured by detecting the leak-through of the cavity end mirror with a fast photodiode (ET-2000) calibrated to the energy measured by a pyroelectric energy detector. The pump beam was measured to be 22 mJ with an nominally gaussian spatial profile of 1.5 mm diameter at the $1/e^2$ point. As shown in Table 2.1, higher pump energies will give higher output energies, but at the expense of larger value of B and higher intracavity fluences. The increase in output energy, however, would increase the output energy of the

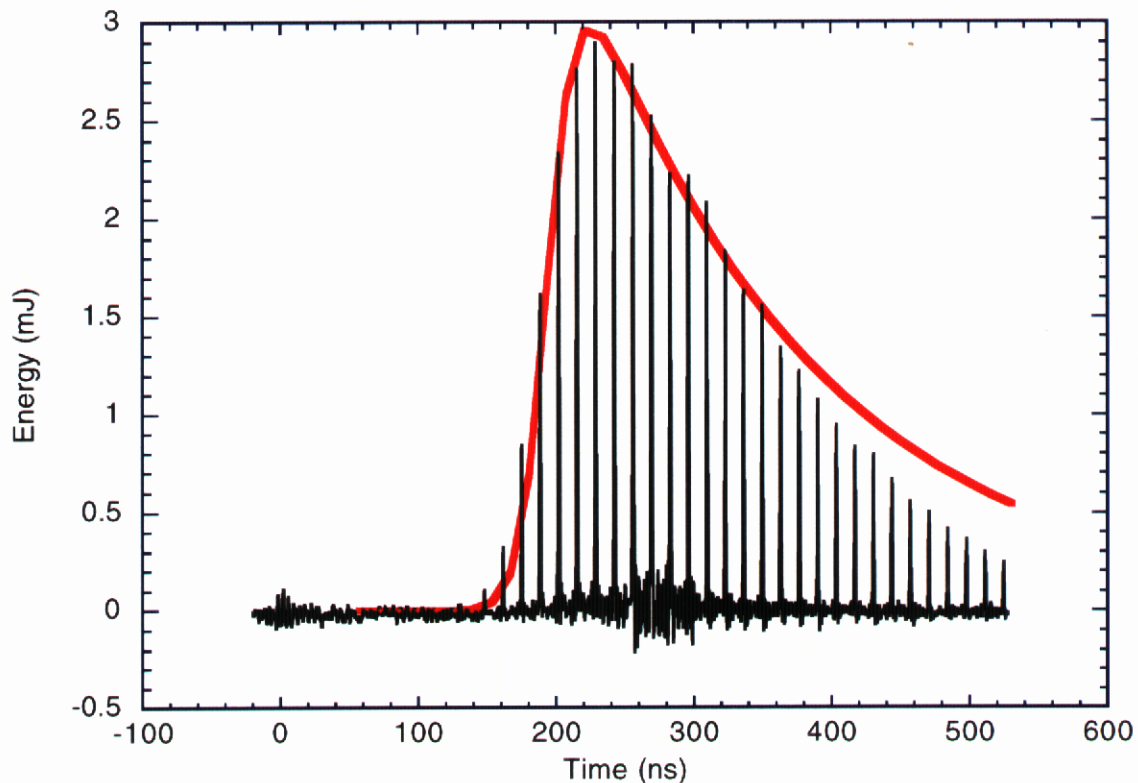


Figure 2.7: Regenerative amplifier buildup. The peaks are the energy buildup in the cavity, and the envelope is that calculated using the model described in the text (shifted 60 ns later).

next amplifier stage only by a small amount. It was decided, therefore, to limit the output energy to approximately 3 mJ.

The energy buildup was calculated using these pump beam parameters and assuming .1 nJ input with 4% loss per pass due to absorption in the crystal⁴⁷ and losses on the polarizer. The result is shown as the gray line in Fig. 2.7 which gives good agreement in maximum energy and qualitative shape with the measured buildup. However, the actual buildup peaks 60 ns later than that calculated and decays faster than calculated. The reasons for this discrepancy are most likely due to the fact that the model assumes a gain volume of infinite transverse extent with a quadratic radial dependence. This is really only valid if the mode size is much less than the pump (and therefore the gain)

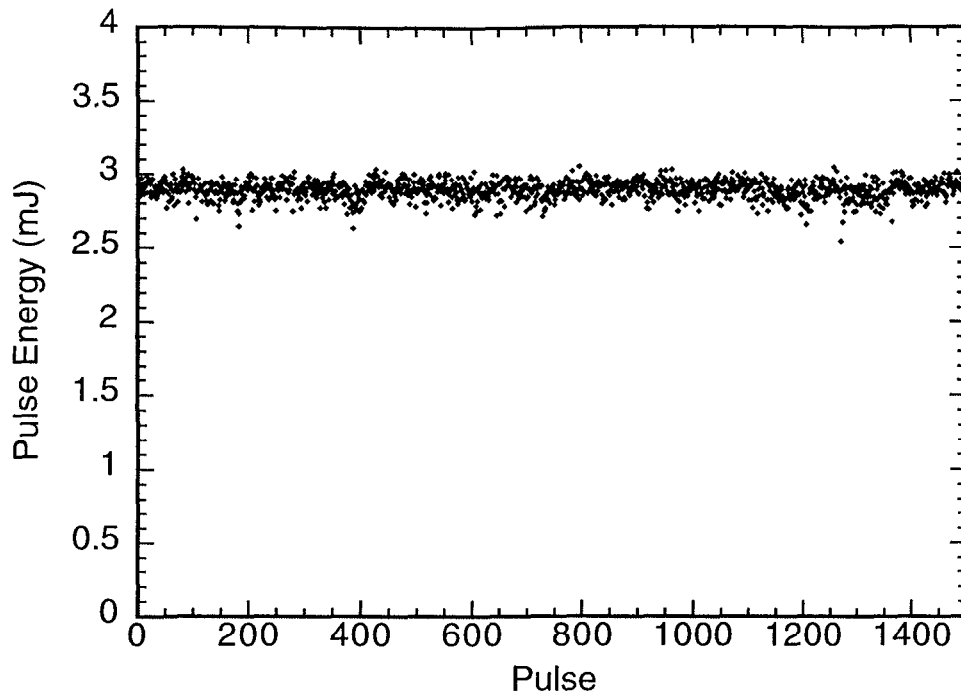


Figure 2.8: Energy stability of the regenerative amplifier over 1000 shots

diameter. Fig. 2.6 shows that for this configuration, the cavity mode is 1–1.1 mm in diameter at the crystal relative to a pump diameter of 1.5 mm and so the accuracy of the quadratic approximation is limited. For the first few passes through the gain medium, the beam waist is larger than the pump diameter, and so much of the energy of the pulse misses the gain volume and is lost. This is not accounted for in the model. Also, as the gain is depleted, the cavity mode begins to change radically, becoming collimated in one propagation direction and focused in the other. This leads to an increased beam waist throughout the cavity so that energy will be lost more rapidly on limiting cavity elements.

The output performance of the regenerative amplifier is shown in Fig. 2.8 where the energy of 1000 consecutive shots were recorded with a pyroelectric detector. The average energy output is 2.9 mJ with a standard deviation of .06 mJ (2%). Fig. 2.9 shows the TEM₀₀ spatial profile of the output of the regenerative amplifier. The spectral effects

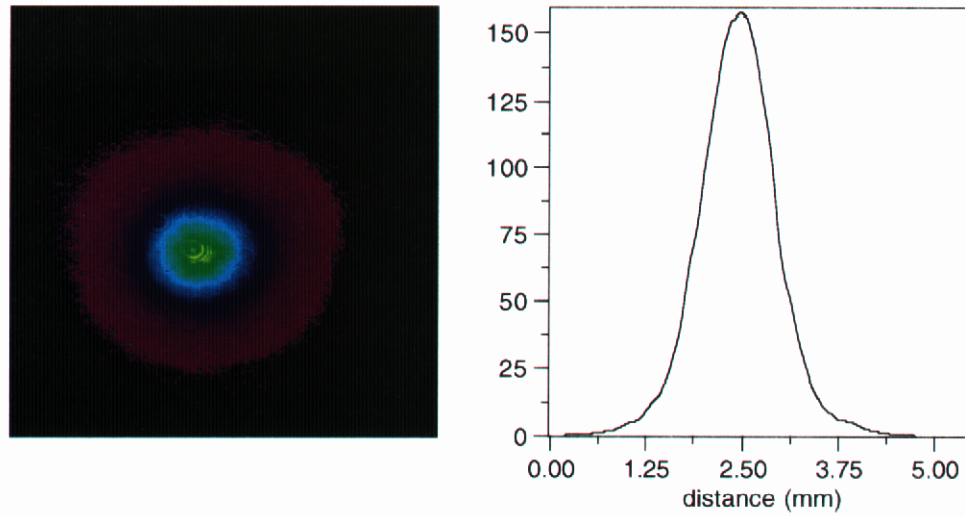


Figure 2.9: Spatial profile of beam output from regenerative amplifier.

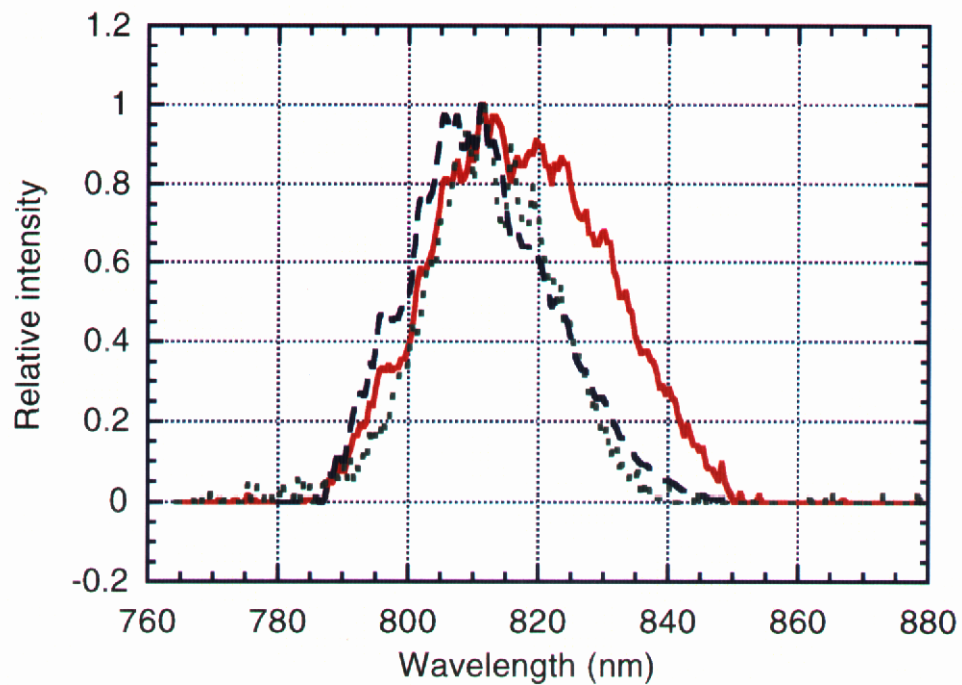


Figure 2.10: Output spectrum of the regenerative amplifier (dotted line). The solid line is the input spectrum and the dashed line is calculated output spectrum given the input spectrum and a gain of 30 million.

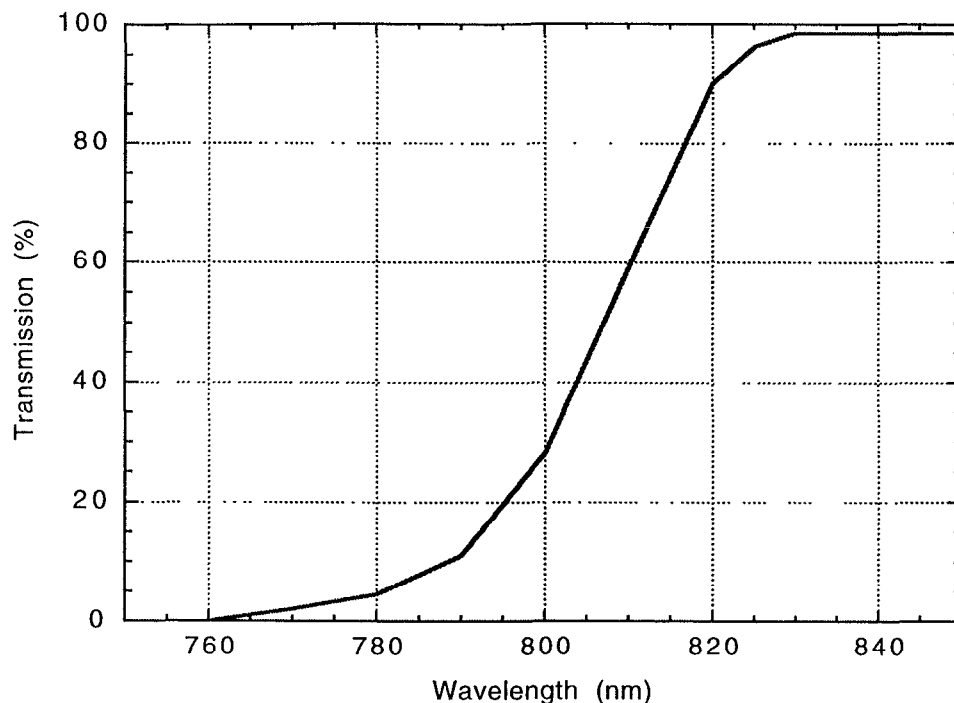


Figure 2.11: Transmission spectrum for P polarization of thin-film polarizer used in regenerative amplifier.⁵¹

of the amplification is shown in Fig. 2.10 where the input spectrum (solid line) and the output spectrum (dotted line) are shown. Also shown is the output spectrum that would be expected simply due to the finite gain spectral profile (see Fig. 2.1) and a gain of 30 million (.1 nJ to 3 mJ) as was discussed at the beginning of this Chapter. The output spectrum is slightly narrower than that expected due solely to gain narrowing. This most likely is due to the poorer transmission of the blue end of the spectrum by the polarizer when it is switched out (see Fig. 2.11). The spectrum is severely pulled toward the blue, but it is not significantly distorted since the regenerative amplifier is not heavily saturated.^{52,53}

2.1.3 4-Pass Power Amplifier

The next stage in the amplifier chain is a geometrically multiplexed 4-pass amplifier pumped by the remainder of the second harmonic output of the Spectra Physics Nd:YAG

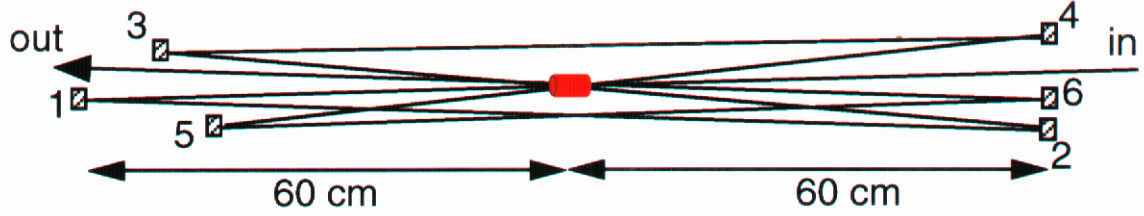


Figure 2.12: Schematic of configuration of first four-pass amplifier. M3 is 10 cm in front of M1 and M5 is 18 cm in front of M1.

laser ($\simeq 200$ mJ). As drawn in Fig. 2.12, the amplifier design is composed of three flat mirrors on either side of the Ti:sapphire crystal. The path followed by the beam is indicated by the line, and the order in which the mirrors are struck is indicated by the numbers next to each mirror. The gaussian radial gain profile again needs to be accounted for in the design of the amplifier. Using the model detailed in Section 2.1.2 to calculate the beam propagation in this design indicates that care must be taken to ensure that on each pass, the beam fills the gain volume as much as possible. The gain guiding previously mentioned effectively reduces the beam waist upon amplification which then must be allowed to diffract back up to a size which will efficiently extract the stored energy. This behavior is shown in Fig. 2.13 where the beam waist is plotted against propagation distance. The 4 dots indicate the actual measured beam waist after each pass (the actual spatial profiles are shown in Fig. 2.14, and highlight where the model being used breaks down. The first pass matches quite well, but on the subsequent passes, several of the approximations do not hold. First, the beam as it expands to fill the gain volume, becomes close to the size of the gain region, and so the quadratic expansion used no longer holds. In addition, to make this a one-dimensional calculation, only the peak fluence is tracked which assumes that the gaussian radial profile of the population inversion is unaffected. This approximation is only valid when the mode size is equal from pass to pass. In any event, the model proved to provide reasonable estimates of the final output energy.

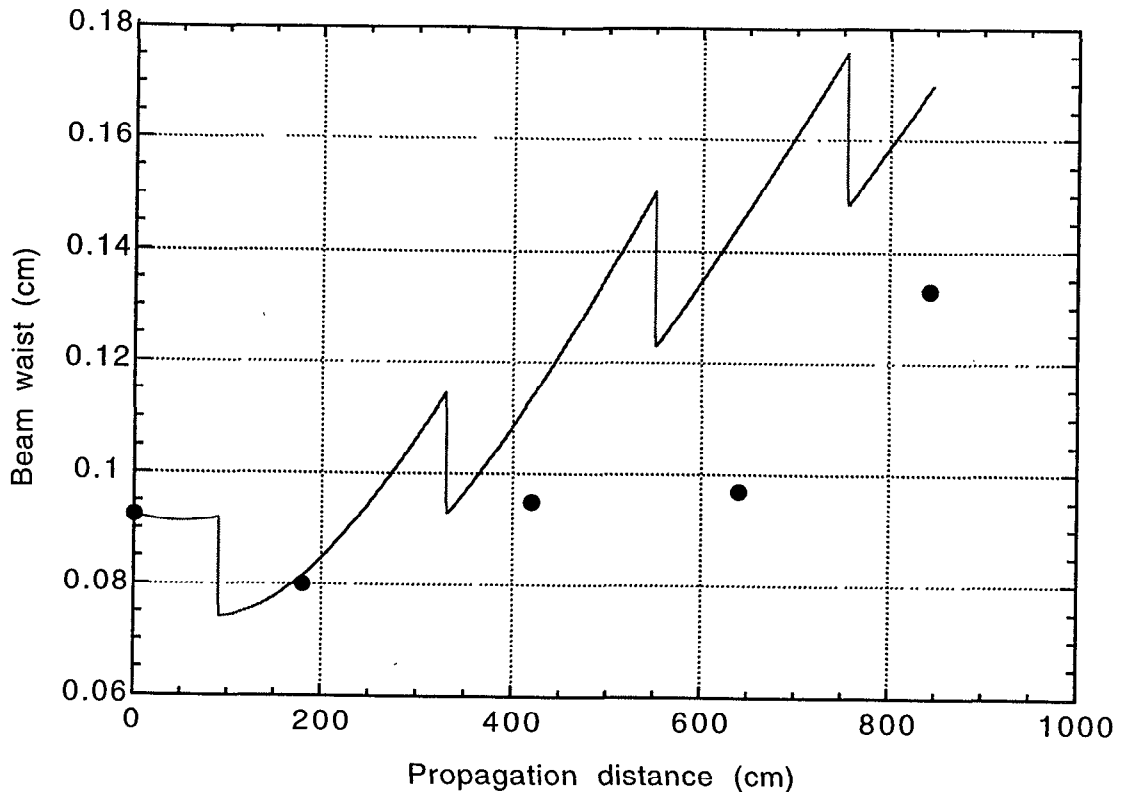


Figure 2.13: The calculated (line) and measured waist (dots) in the first amplifier.

The output of this amplifier stage, when pumped by 180 mJ of green light with a spot size of 2.8 mm, produces an average energy of 40 mJ with a standard deviation of 1 mJ (2.5%). Of interest is the fact that the finite lifetime τ_{SE} of Ti:sapphire has a significant effect on this amplifier because the pump beam arrives $\cong 300$ ns before the beam does (the same laser pumps both regenerative amplifier and this stage). Although the lifetime of Ti:sapphire is 2.3 μ s, calculations show that with no delay, this amplifier should output 50 mJ of energy, but with the 300 ns delay before the first pass, the calculated energy output is only 40 mJ—a loss of 20% in energy output.

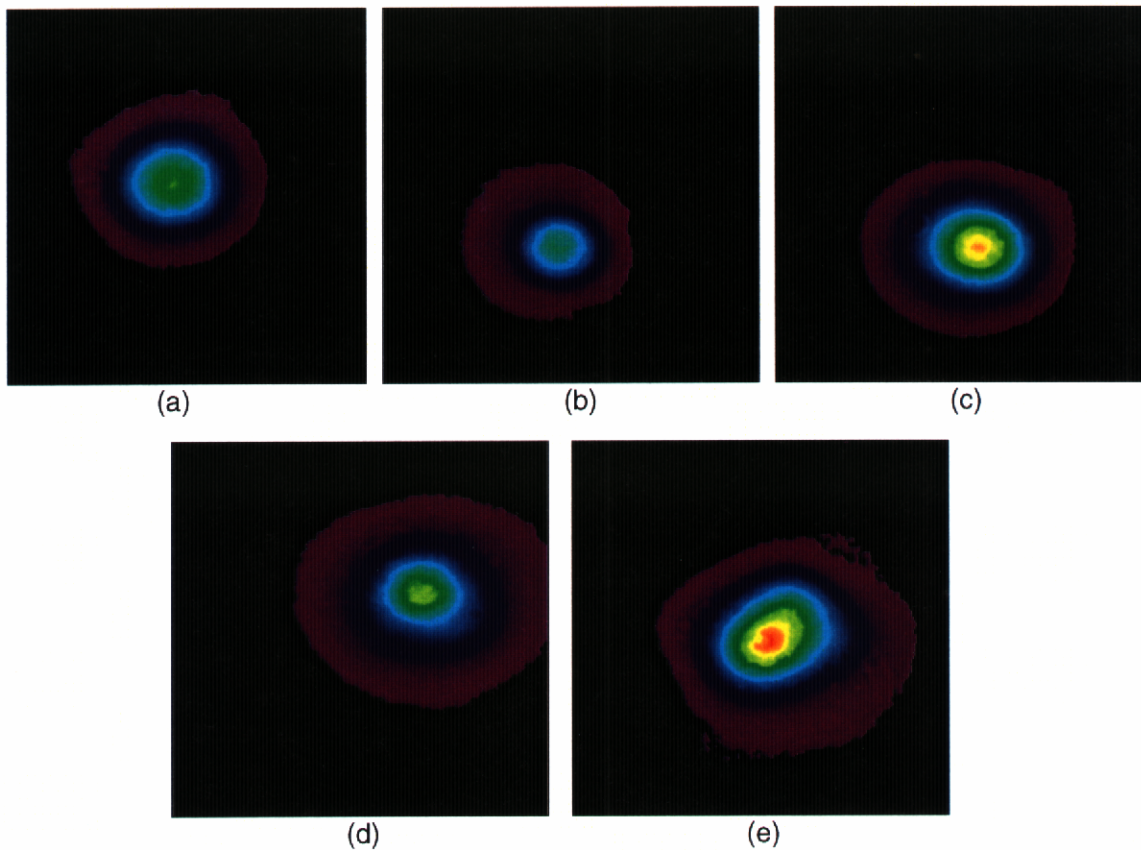


Figure 2.14: The spatial profile of the 820 nm beam 90 cm after each pass through the amplifier. (a) is the free propagating mode (no pump light) and (b)–(e) are passes 1–4 respectively.

2.1.4 Second 4-pass power amplifier

The first four-pass amplifier stage provides 40 mJ in a gaussian spatial mode. For more efficient extraction of the energy in future amplifiers, the spatial profile of the beam is converted into a flattop transverse spatial profile to allow a greater overlap between pump and seed modes without the gain guiding that has been discussed so far. This conversion is accomplished by truncating the gaussian spatial profile using a serrated aperture so that only the relatively flat peak of the gaussian remains. The energy level at which the clipping occurs is determined by a trade-off between the energy loss that is acceptable and the uniformity that is desired. The closer to the peak the beam is clipped, the flatter

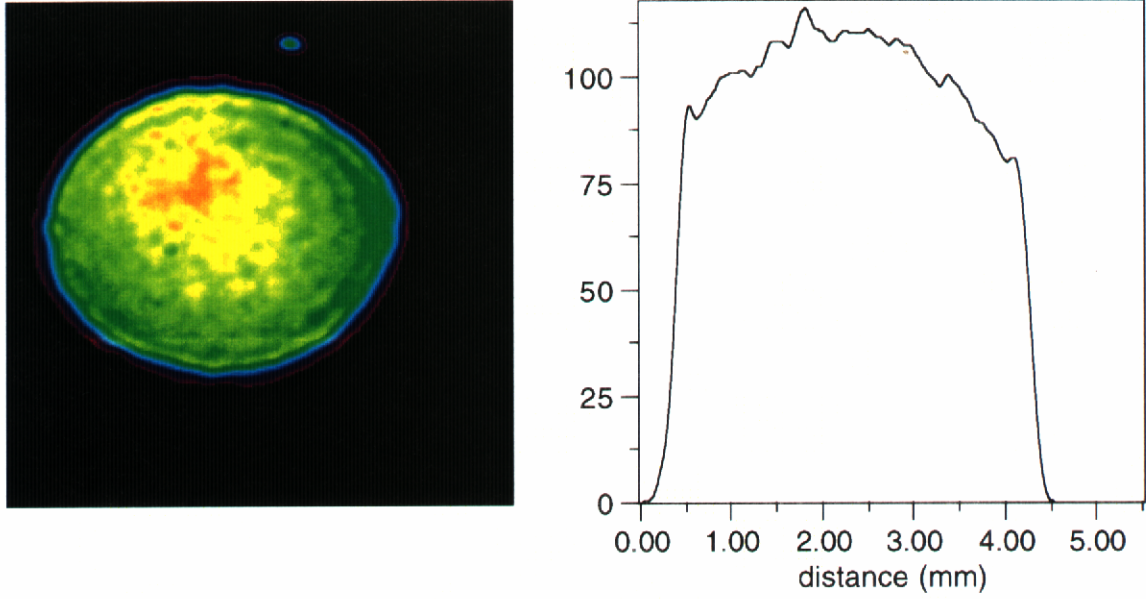


Figure 2.15: The beam as it appears at the image plane (approximately 2/3 of the way through the second amplifier stage).

the beam profile, but the lower the total energy that will be transmitted. Allowing the beam to free propagate for 1.5 m after the first amplifier stage gives a beam waist of 1.8 mm which, for a 2.0 mm diameter aperture, passes 50% of the energy. The high spatial frequencies from the serrates are then removed by sending the beam through a vacuum spatial filter,⁵⁴ which also serves to expand the beam to 4 mm for the next amplifier. The beam at the image plane of the telescope is shown in Fig. 2.15.

Once the beam is clipped, diffraction effects will quickly distort the spatial profile. This can be overcome by using telescopes to relay the image of the aperture to the next amplification stage. In most relay-image systems, the length of the amplifier is comparatively short, and so the system design is mostly determined by optics concerns, e.g. aberrations. However, since each amplification stage in this laser system is multipassed, the effective total amplifier length will reach several meters, e.g. the distance traveled in the first stage is approximately 8 m. Fig. 2.16 shows the beam profile only 1.6 m in front

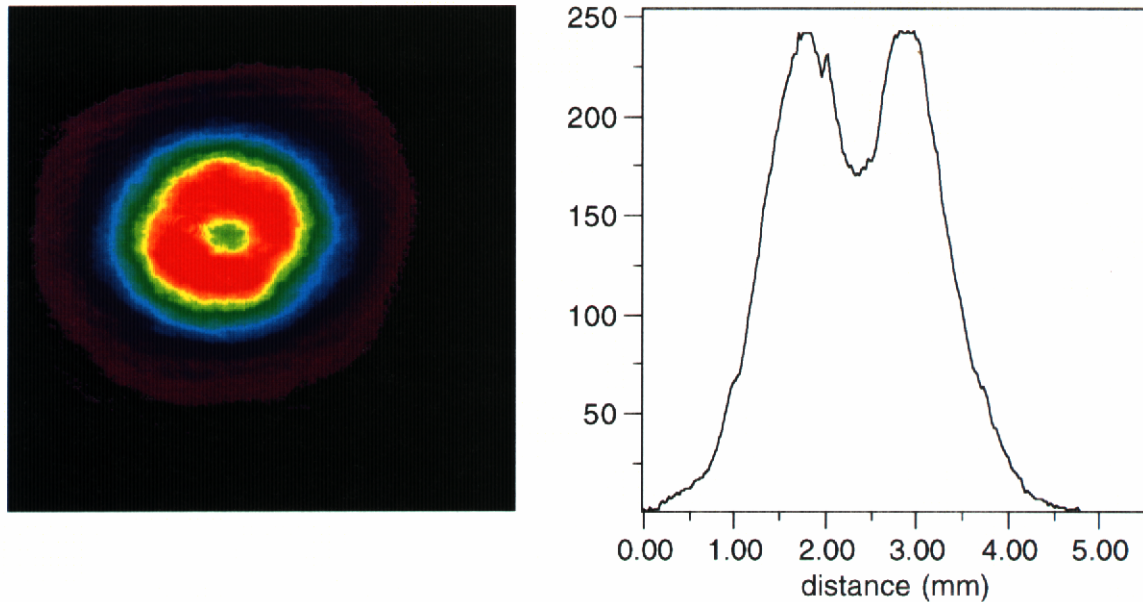


Figure 2.16: The spatial profile of the beam shown in Fig. 2.15 1.6 m in front of focal plane.



Figure 2.17: Schematic of the second amplifier stage. The beam is injected using the Pockels cell and exits reflecting off of the polarizer. The total path length is 3.2 m.

of the focal plane; it is already exhibiting large modulations.

For this reason, it was critical to design the second amplifier stage to be as physically compact as possible while still maintaining small angles between the beam paths of the various passes to minimize distortions caused by the noncollinearity of the pump and seed beams. The solution (Fig. 2.17) was to use a simple double-pass bowtie design so that the mirrors could be pushed as close as possible towards the crystal (40 cm on either side). The beam is then retro-reflected back on itself by a 0° flat mirror to make a third and fourth pass. A Pockels cell slicer placed at the input of the amplifier differentiates between the input and output beams via polarization. For this configuration, then, Fig. 2.16 is the beam profile during its first pass through the Ti:sapphire crystal.

Table 2.2: Output energies for the second amplifier stage. Fluences are in J/cm².

\mathcal{E}_{in} (mJ)	$2w_{\text{in}}$ (mm)	\mathcal{E}_p (mJ)	$2w_p$ (mm)	Γ_p	\mathcal{E}_{out} (mJ)	Γ_{peak}	B
10	4	600	4.5	3.8	240	1.1	.15
10	4	600	5	3.1	170	.8	.10
10	4.5	600	5	3.1	200	.7	.09
10	4	500	4.5	3.1	180	.8	.11
10	4	500	5	2.6	120	.6	.08
10	4.5	500	5	2.6	140	.5	.06
15	4	550	4.5	3.5	230	1.0	.15
15	4.4	500	4.8	2.8	190	.7	.10
15	4.4	550	4.8	3.0	220	.8	.11
15	4.4	600	4.8	3.3	250	.9	.13
20	4	600	4.5	3.8	270	1.2	.20
20	4	600	5	3.1	203	.9	.15
20	4.5	600	5	3.1	240	.9	.13
20	4	500	4.5	3.1	210	1.0	.15
20	4	500	5	2.6	160	.7	.11
20	4.5	500	5	2.6	190	.7	.10

This amplifier stage can be modeled with a simple plane-wave model where the gain is assumed to be transversely uniform as is the beam itself. Table 2.2 gives a range of calculated output energies for several input parameters. The pump energy is provided by the doubled output of one arm of the Nd:YLF laser system that provides the pump light for the remainder of the laser system. There is approximately 550 mJ of green light available. When pumped with approximately 500 mJ, the measured output energy was 160 mJ with an input of 10 mJ.

2.1.5 Final two Ti:sapphire amplifier stages

This process will be repeated again for the final two amplifier stages. However, since the beam will be larger in diameter, a larger distance can be traveled before the same Fresnel number $N_f = w^2/\lambda L$ is reached. The third amplifier stage will use a 20 mm \times 25mm rod pumped with 2.5 J of green light on both sides at 1 Hz. Similar calculations as described in the previous section give that an input of 200 mJ will be amplified to 1.6–2 J in three

passes. This will be injected into a 30 mm diameter disk pumped with 24 J of green light on a single shot basis (every 7 minutes). With 1.6 J input energy, the output energy should be 9-12 J, but heavily saturated. Lower pump energies could be used if spectral effects due to the saturation of the gain should prove to be a problem.

2.2 Hybrid Nd-doped YLF and glass pump system

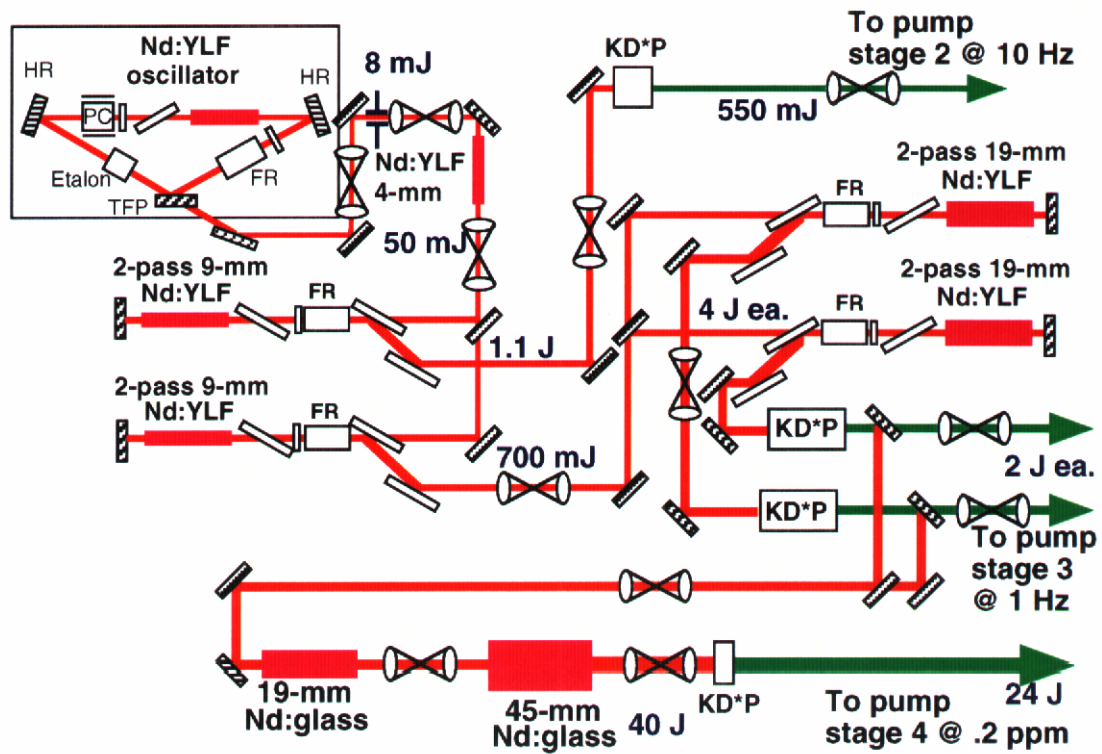


Figure 2.18: Schematic of the YLF-based pump system.

As has been mentioned before, the short upperstate lifetime of Ti:sapphire requires that the population inversion must be established in a very short time. This energy deposition rate can only be achieved via laser pumping of the gain medium. As stated previously, the regenerative amplifier stage and the first power amplifier stage in this system are pumped with 300 mJ total of 532 nm light from a Nd:YAG laser. As seen in Sections 2.1.3 and

2.1.4, only about 25–35% of the pump energy is transferred to the beam at 820 nm. This general trend means that in order to have 200 mJ out of the second stage, pump energies of at least 500 mJ are needed. For a third stage output of 1.5 J, more than 4.5 J of green light are needed, and for 8 J of 820 nm light from the last stage, 24 J of green are needed.

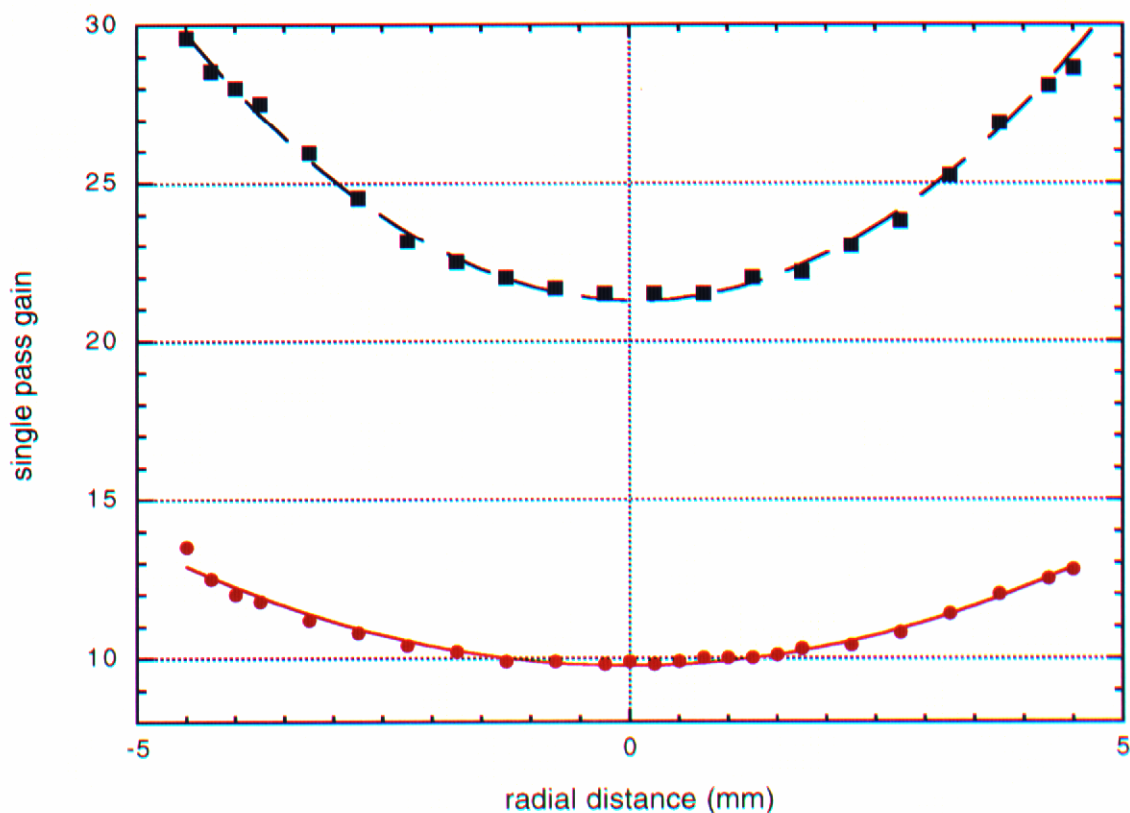


Figure 2.19: The small signal, single pass gain of 9.5 mm aperture Nd:YLF rod as a function of radial position. The squares are the values measured for 160 J of electrical lamp energy and the dots are those for 110 J of lamp energy. The lines are parabolic fits to the data.

It was decided to meet these energy requirements using a single master-oscillator power-amplifier (MOPA) chain. The most common gain material for achieving high pulse energies has been Nd-doped glass. In fact, large aperture phosphate glass rods and heads were available from the 10 TW laser⁵⁵ whose peak laser transition is at 1054 nm. However, glass rods do not efficiently dissipate the thermal energy deposited and so can not

be fired at high repetition rates (usually less than once per second even for intermediate-sized rods). In order to allow for as high a repetition rate as possible (10 Hz) and yet still allow the use of the large aperture glass amplifiers, Nd:YLF was chosen as the gain medium for the remainder of the pump system since it exhibits a laser transition is at 1053 nm. Since YLF is crystalline, its thermal diffusivity is much higher than that of glass, and can be run at higher repetition rates. It also exhibits much less thermal lensing and thermal birefringence (it is naturally birefringent) than Nd:YAG.

As shown in Fig. 2.18, the master oscillator is a unidirectional ring cavity which produces 8 mJ per pulse with approximately 1% rms stability.⁵⁶ The pulse is expanded and clipped by a serrated aperture as described previously except that here the clipping point is determined so that the curvature on the beam will compensate the inverse dependence on radius of the gain profile in the flashlamp-pumped amplifier heads. Fig. 2.19 shows this radial gain profile for the 9.5mm aperture amplifier as well as the calculated profile of the clipped beam needed to produce a flattop profile upon amplification. The calculation is simply done by approximating both profiles by a quadratic form and solving the system of equations to eliminate the second order term.

The energy is then amplified to 50 mJ in a 4 mm \times 68 mm (gain length = 50 mm) rod pre-amplifier so that it can be split into 2 legs; each with a 9.5 mm \times 115 mm (gain length = 100 mm) rod amplifier which is double-passed. Between each amplifier stage, there is a telescope to increase the mode size to best fill the gain volume in the next amplifier. There are two legs so that one can be doubled to pump the second amplifier stage (Section 2.1.4) while the other leg serves as the seed for the rest of the amplifier chain. The output of these 9 mm amplifier heads shows the main disadvantage of Nd:YLF as a laser medium. The heads begin to show severe saturation even for output energies below .5 J; however,

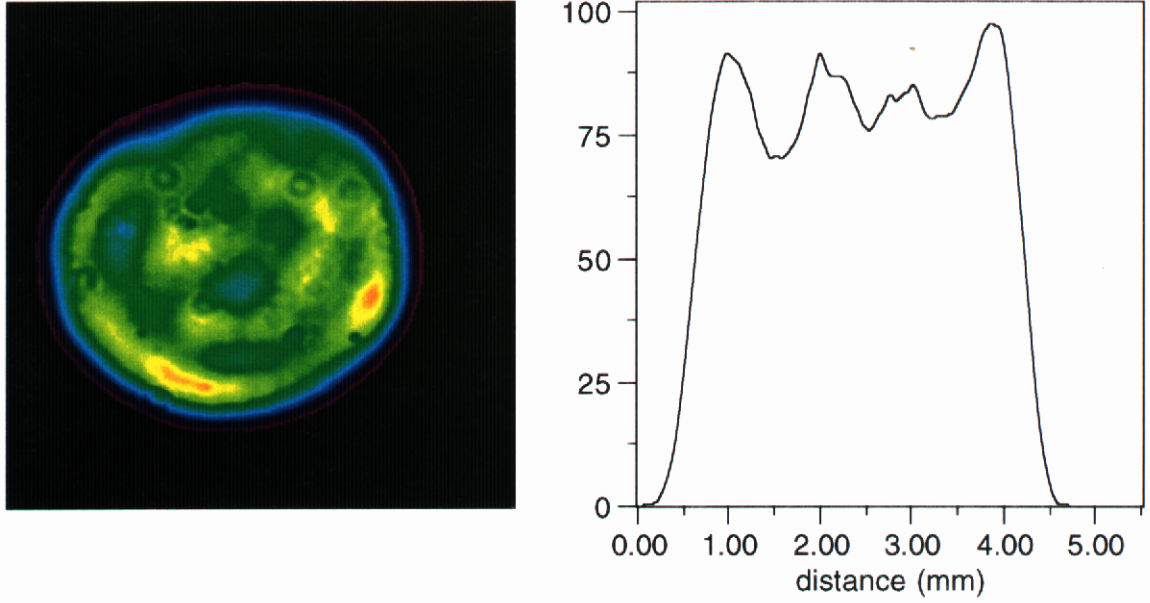


Figure 2.20: The spatial profile of the 10 Hz 9mm amplifier head.

at .5 J, the fluence in the rods is only 1 J/cm^2 which is still below the saturation fluence of $\Gamma_e = h\nu/\sigma_e = 1.6 \text{ J/cm}^2$ ($\sigma_e = 1.2 \times 10^{-19} \text{ cm}^2$ for the 1053 nm laser transition⁵⁷). The main reason behind this is that although Nd:YLF has a very long upperstate lifetime ($480 \mu\text{s}$), its lowerstate lifetime is also comparatively long at 10 ns.⁵⁸ Since the pulse is 16 ns, population accumulates in the lower laser level, producing a bottlenecking effect, making it more difficult to extract the stored energy.

The solution to this problem was to make the seed energy as large as possible to begin saturating by the end of the first pass in order to extract as much energy as possible throughout the length of the rod on the second pass. The most critical leg as far as achieving maximum energy is the leg that will provide the pump light for the second amplifier stage. Therefore 70% of the energy from the 4mm pre-amp was injected into this leg, resulting in 1.1 J out in a 7.5 mm beam; the other leg produces 700 mJ. The rms stability of the output of these two amplifiers is approximately 2.5%, and the tophat

spatial profile is shown in Fig. 2.20.

2.2.1 Second harmonic generation of 1053 nm light

It is critical to be able generate the second harmonic of the 1053 nm light as efficiently as possible since the 527 nm photons are the ones which will produce the population inversion in the Ti:sapphire amplifiers. The one drawback to accomplishing this is that the pulses generated by the ring oscillator are approximately 16 ns long which means that for a given fluence, the intensity of the pulse is low. For example, at a fluence level of 5 J/cm², which is fairly high for damage concerns, the peak intensity is only 300 MW/cm², which is relatively low for frequency conversion. It was decided to down-collimate the output of the 9 mm amplifier to 4 mm in order to have an intensity of 500 MW/cm², but this gives a fluence of 9 J/cm² and even higher on the final window of the vacuum spatial filter used as the relay. Nonetheless, there has been no damage observed after several hours of operation, either on the optics or in the doubling crystal.

The crystal used for frequency conversion is a 12mm × 30mm piece of KD*P from Cleveland Crystals cut for Type II doubling. It is mounted in a temperature-controlled oven set at 30°C to avoid any temperature detuning of the phasematching angle from heat deposited in the crystal because of the slight absorption in KD*P at 1053 nm. It was AR coated with solgel and hermetically sealed with solgel-coated windows to minimize deterioration of the crystal due to exposure to moisture in the air. Fig. 2.21 shows the output this crystal at 527 as a function of the input energy at 1053 nm. In this graph, the line and large squares indicate the output energies calculated for the indicated input energies using a computer code that will be described later in Section 4.5. The spatial profile in Fig. 2.20 was used as the input spatial mode in the calculation, and a temporal pulse

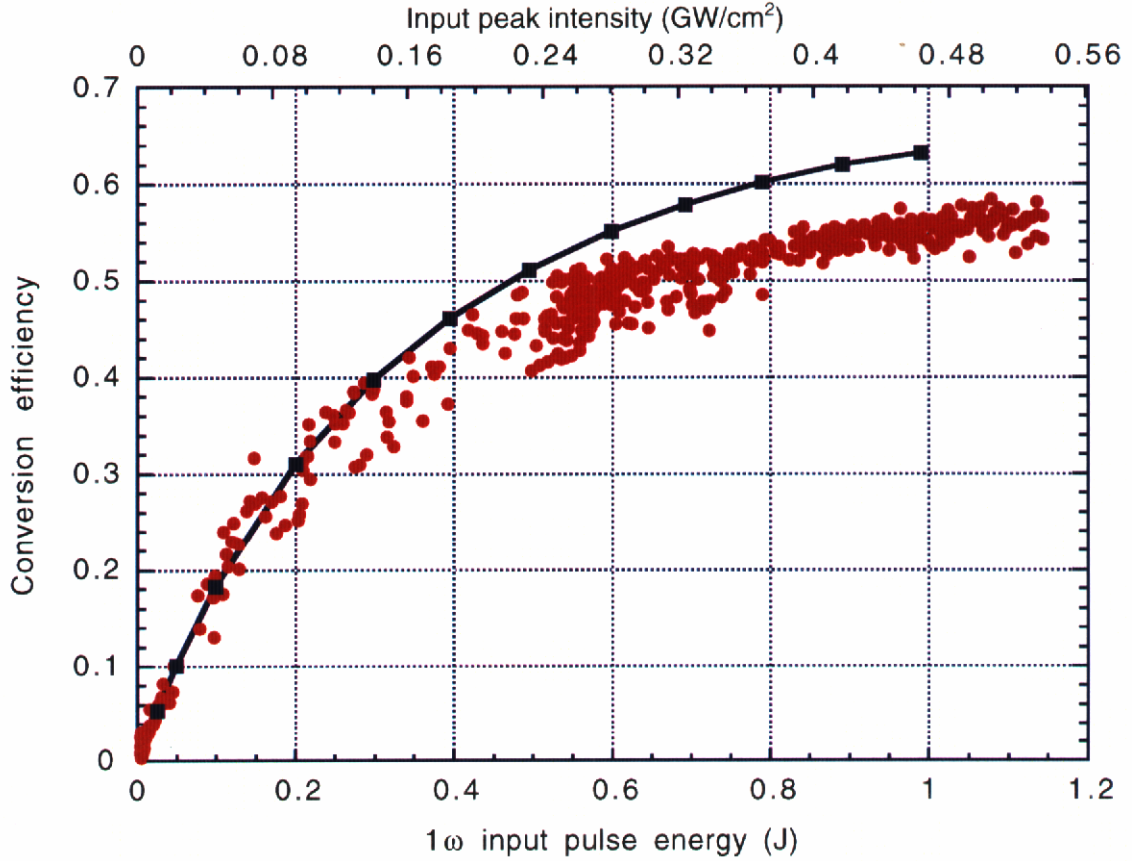


Figure 2.21: The second harmonic generated as a function of input energy of the fundamental. The dots were measured using pyroelectric detectors while the line and squares are the results of a computer calculation

profile simulating the exponential tail evident in the laser pulse with a 16 ns FWHM width. The inclusion of this tail accounted for a reduction in peak efficiency of 3%. Also, the addition of a small temporal amplitude modulation (sinusoidal) to simulate to first order the mode-beating that is present in the pulse resulted in a 5% drop in peak efficiency. The remaining discrepancy between measured and calculated second harmonic efficiency in the high drive regime is likely due to phase modulation on the pulses. Finally, the spatial profile of the green beam at the crystal of the second Ti:sapphire amplifier is shown in Fig. 2.22.

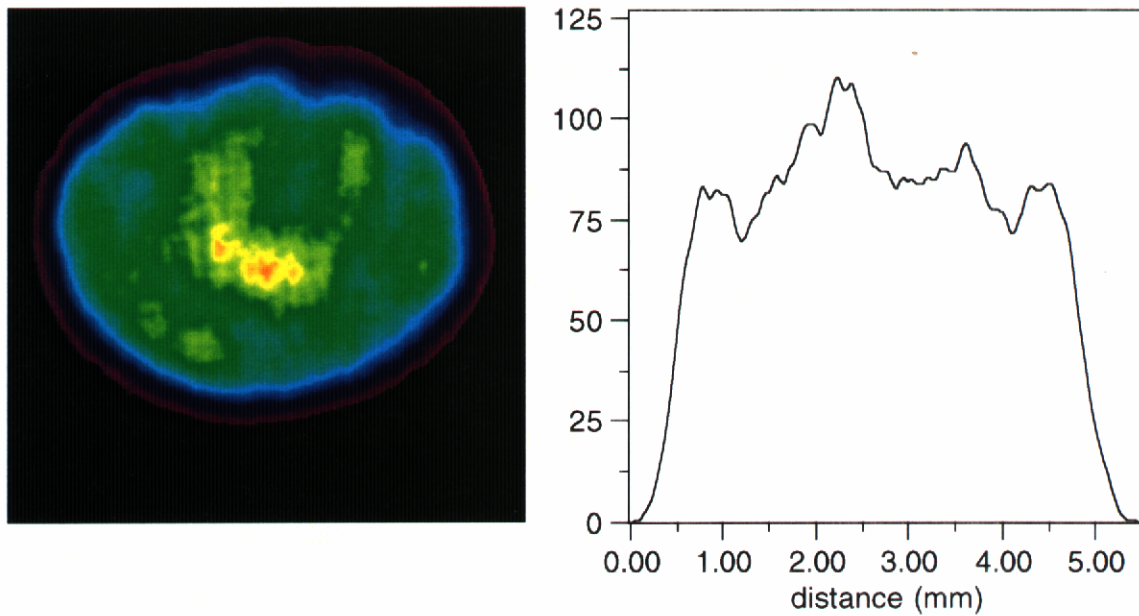


Figure 2.22: The spatial profile and line out of the second harmonic beam at the Ti:sapphire crystal in amplifier #2.

2.2.2 High energy amplifiers

To produce the 5 J of green light needed to pump the third amplifier stage, approximately 8-10 J of IR light will be needed. Doing this with one amplifier stage of reasonable size is not likely to be possible so two will be used in parallel. Nd:YLF can be obtained in rods with 19 mm aperture which can be fired at 1 Hz. Two 19 mm heads were designed with 19 mm \times 120 mm rods giving increase by a factor of four of the gain volume, requiring an increase by a factor of four in electrical energy to achieve the same gain. This would suggest that these amplifiers should be able to output 4-5 J each when double passed, particularly when they will be seeded by 300-350 mJ each. The beam from the second 9 mm leg will be split by a 50/50 beamsplitter so half of the energy from this leg will go into each 19 mm amplifier. The output of these stages will be doubled using two Type I KD*P crystals of 4 cm length which is calculated to provide about 60% conversion to 527 nm. This means that 5-6 J of green light should be available to pump the third amplifier

stage.

After passing through the frequency conversion crystals, there will still be 4–5 J of IR light in two beams. The final pump amplifiers will be a 19 mm and a 45 mm aperture Nd:glass head in series. Since the gain of glass is isotropic in polarization, it is possible to recombine the two beams by making them orthogonal polarizations and reflecting one off the face of a polarizer while transmitting the other through the same polarizer. However, it is necessary to use Type I SHG in order to preserve the polarizations of the two fundamental beams. The 19 mm amplifier will then be seeded with 4–5 J of energy and will be heavily saturated; the stimulated emission cross section for glass is about 4×10^{-20} cm² so the saturation fluence is about three times that of Nd:YLF. The beam will be expanded and further amplified in a 45 mm Nd:glass rod, producing 40 J of light at 1053 nm. Assuming 60% conversion to 527 nm again, this will give 24 J of green light to pump the final amplifier stage.

2.3 Conclusion

In this Chapter, the design of a laser system using Ti:sapphire as its gain medium capable of reaching energies of up to 10 J has been described. When compressed back down to approximately 50 fs, this system will provide peak powers of 100 TW. To date, the system has been completed up to the second multipass amplifier stage—this part alone makes available 2 TW of peak power at 10 Hz in a reasonably user-friendly system.

Chapter 3

All-Reflective Pulse Stretcher for Chirped-Pulse Amplification

As was mentioned in the previous Chapter, the technique of chirped-pulse amplification (CPA) has made possible the production of terawatt and now even petawatt class femtosecond lasers.¹⁵ With CPA, high energy, ultrashort pulses are first stretched in time by using some type of dispersive delay line. It is then possible to amplify the pulse to high energy without damage to the amplifiers. Finally the pulse is recompressed using a dispersive delay line of the opposite sign. Devices used for the purposes of stretching the pulse include optical fibers (both positive and negative chirp depending on the sign of the material dispersion, $\partial^2 n / \partial \omega^2$), diffraction grating pairs, and prism pairs.

As the initial pulse durations in CPA systems decrease, the importance of achieving a high stretching ratio increases for terawatt class systems. This is due to the need to minimize self-phase modulation of the stretched pulse during amplification which will ultimately limit the pulse contrast and the pulse duration achieved upon recompression.⁴⁰ Often before this limit is reached, however, the recompressed pulse is limited by aberrations.

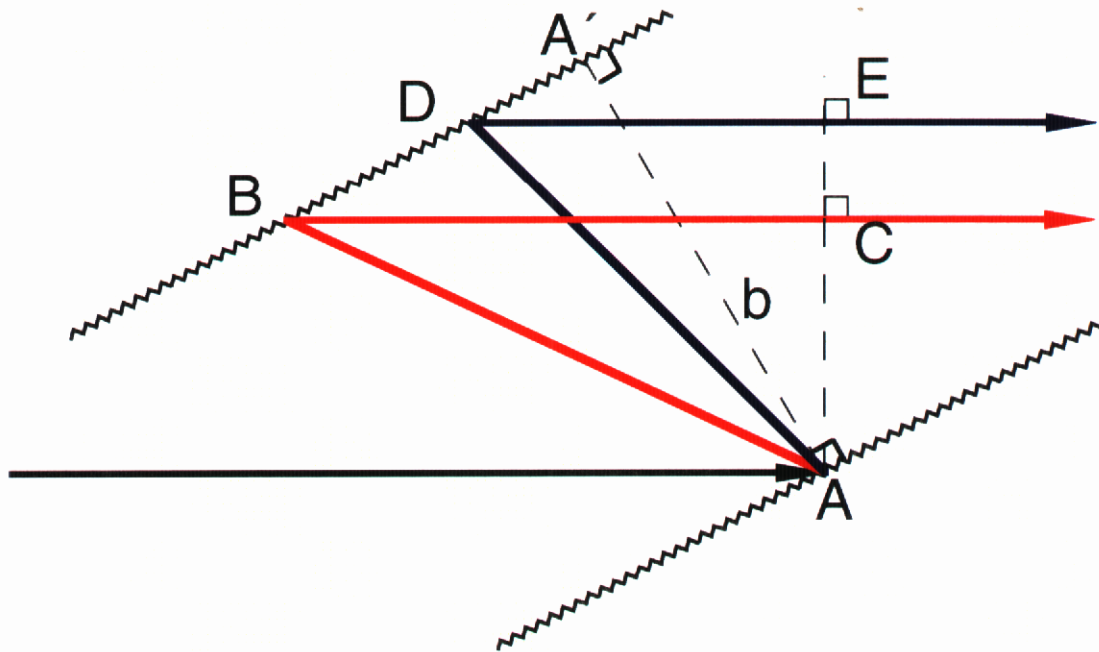


Figure 3.1: A schematic representing dispersion using a pair of diffraction gratings separated by a perpendicular distance b .

tions in the stretcher^{35,44,59} or, as is well known, by the addition of material dispersion which cannot be compensated for in the pulse compressor. In addition to these phase distortions, amplitude modulations such as gain narrowing⁶⁰ and spectral clipping,⁵⁹ while not producing residual chirp, can significantly both degrade contrast and increase the final pulse duration.

The induced chirp is related to first order to the group velocity dispersion (GVD) of the device. Most materials possess a positive GVD in the region of 800 nm where most Ti:sapphire systems operate. In contrast, negative dispersion can be provided by either a grating pair or a prism pair. As an illustration of this, consider a pair of diffraction gratings oriented parallel to each other as shown in Fig. 3.1.^{61,62} They are separated by a distance b defined as the length of the line segment joining the two gratings normal to their faces. The frequency components of a beam incident on one of the gratings with an

angle of incidence θ_i are diffracted into angles $\theta(\omega)$ given by the grating equation

$$\sin \theta(\omega) + \sin \theta_i = \frac{m\lambda}{d} \quad (3.1)$$

where m is the diffraction order and d is the line spacing of the grating (e.g. μm). The dispersed frequency components then strike the second grating with the angles in the reverse order so that they exit the grating pair along a path parallel to that of the input but dispersed spatially. The path length p traveled by each frequency component \overline{ABC} or \overline{ADE} is given by

$$\begin{aligned} \overline{AB} &= \frac{b}{\cos \theta(\omega)} \\ \overline{BC} &= \overline{AB} \cos(\theta_i - \theta(\omega)), \text{ and so} \\ p(\omega) = \overline{ABC} &= \frac{b[1 + \cos(\theta_i - \theta(\omega))]}{\cos \theta(\omega)}. \end{aligned} \quad (3.2)$$

The phase retardation through the grating pair is given by⁶¹

$$\begin{aligned} \phi(\omega) &= k(\omega)p(\omega) \\ &= \frac{\omega p}{c} - \frac{2\pi b}{d} \tan \theta(\omega) \end{aligned} \quad (3.3)$$

where the last term is due to a 2π phase jump between each grating groove (the factor $\frac{b}{d} \tan \theta(\omega)$ gives the number of grooves between the ray position at frequency ω and the point A' on the second grating). It is also convenient to expand the phase ϕ in a Fourier series about the central frequency ω_0 as

$$\phi(\omega) = \phi_0 + \beta_1(\omega - \omega_0) + \frac{\beta_2}{2!}(\omega - \omega_0)^2 + \frac{\beta_3}{3!}(\omega - \omega_0)^3 + \dots \quad (3.4)$$

where

$$\beta_j = \left. \frac{\partial^j \phi}{\partial \omega^j} \right|_{\omega=\omega_0} \quad (3.5)$$

is the j th derivative of ϕ with respect to frequency ω . Now the group delay $\tau = \partial\phi/\partial\omega$ is simply the time taken to propagate the distance $p(\omega)$, i.e. $\tau(\omega) = p(\omega)/c$ where c is the speed of light.

Knowing the path length as a function of frequency enables one to calculate the corresponding coefficients β_j in the phase expansion because $\beta_1 = p/c$. Therefore, the rest of the expansion coefficients are

$$\beta_j = \frac{1}{c} \frac{\partial^{j-1} p(\omega)}{\partial \omega^{j-1}}. \quad (3.6)$$

The first two phase terms β_0 and β_1 simply add a constant phase value to all frequency components and so are unimportant for our purposes. After the constant and linear terms, the second term β_2 corresponds to GVD and a linear chirp added to the pulse and is given by

$$\beta_2 = \frac{b\theta'(\omega)(\sin\theta_i + \sin\theta(\omega))}{c \cos^2 \theta(\omega)}. \quad (3.7)$$

It turns out that for a grating pair such as has been described, $\beta_2 < 0$, which means that the pulse becomes negatively chirped (the higher frequencies lead the lower ones). Finally, the higher order terms describe nonlinear chirp which is added to the pulse. These are

$$\beta_3 = \frac{b}{c \cos^2 \theta(\omega)} \{ \theta'^2(\omega) + [\sin\theta_i + \sin\theta(\omega)][2 \tan \theta(\omega)\theta'^2(\omega) + \theta''(\omega)] \}, \quad (3.8)$$

$$\begin{aligned} \beta_4 = & \frac{b}{c \cos^2 \theta(\omega)} \{ 3[\sin\theta(\omega)\theta'^3(\omega) + \theta'(\omega)\theta''(\omega)] + [\sin\theta_i + \sin\theta(\omega)][2 \sec^2 \theta(\omega) \\ & + 4 \tan^2 \theta(\omega)]\theta'^3(\omega) + 6 \tan \theta(\omega)\theta'(\omega)\theta''(\omega) + \theta'''(\omega) \} \}, \end{aligned} \quad (3.9)$$

and

$$\begin{aligned} \beta_5 = & \frac{b}{c \cos^2 \theta(\omega)} \{ [5 \sec \theta(\omega) + 7 \sin \theta(\omega) \tan \theta(\omega)]\theta'^4(\omega) + 18 \sin \theta(\omega)\theta'^2(\omega)\theta''(\omega) \\ & + 3 \cos \theta(\omega)\theta''^2(\omega) + 4 \cos \theta(\omega)\theta'(\omega)\theta'''(\omega) + [\sin \theta_i + \sin \theta(\omega)] \} \end{aligned}$$

$$\begin{aligned}
& \times \left[[16 \sec^2 \theta(\omega) \tan \theta(\omega) + 8 \tan^3 \theta(\omega)] \theta'^4(\omega) + [12 \sec^2 \theta(\omega) + 24 \tan^2 \theta(\omega)] \right. \\
& \left. \times \theta'^2(\omega) \theta''(\omega) + \tan \theta(\omega) [6 \theta''^2(\omega) + 8 \theta'(\omega) \theta'''(\omega)] + \theta^{(4)}(\omega) \right] \Big\} \quad (3.10)
\end{aligned}$$

Herein lies one of the difficulties of chirped-pulse amplification: a pulse stretcher adds a frequency-dependent phase $\phi(\omega)$ characterized by the coefficients β_j , stretching the pulse in time. These terms, then, must be exactly canceled by the pulse compressor in order to achieve a transform-limited pulse in time. Failure to do this results in degradation of the pulse temporally. As mentioned previously, this is complicated by spectral effects in the amplification chain as well as additional phase acquired by the pulse due to dispersion in the material traversed in the laser system. The degree to which the final pulse is degraded by uncompensated phase terms, as is clear from Eq. (3.4), is determined by the bandwidth of the pulse and so the initial and final pulse lengths. For much of the history of CPA systems, even the third order phase term was often neglected. However, for sub-100 fs pulses, even the fourth order term is important^{63,44} and can significantly broaden the final pulse. A brief study of the effect of various values for the phase terms β_j on the pulse length and shape of a nominally 45 fs pulse is presented in Appendix A. In what follows, the design and characteristics of a novel, user-friendly pulse stretcher will be given that can be used in CPA systems with final pulse durations of less than 50 fs. The two compressor designs mentioned in Chapter 2 will also be presented.

3.1 Pulse Stretcher

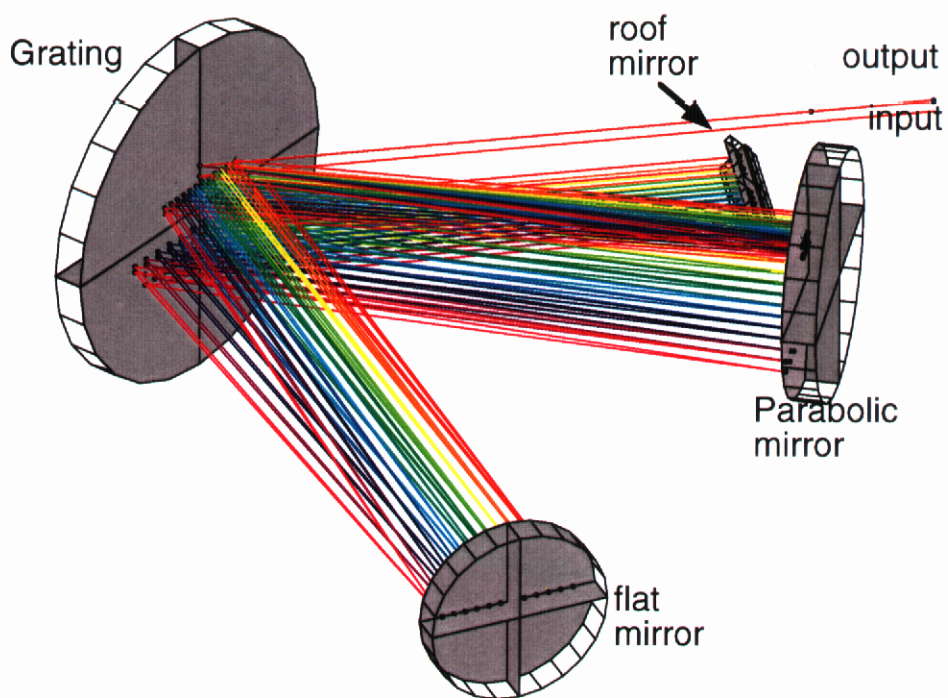
Due to their high dispersion, diffraction gratings have become the most widely used components for stretching and compressing pulses, especially since Martinez⁶⁴ showed that the signs of the phase terms can be inverted by placing a 1-to-1 telescope in between the

grating pair. The typical arrangement in a CPA system, then, is a pulse stretcher (or pulse expander) producing positive delay, and a compressor producing negative delay. Choosing this arrangement allows the use of the more complicated telescope/grating design in the front end of the system where the beam size is small and the energy is low. In early designs, the stretcher was composed of a pair of diffraction gratings separated by a 1-to-1 telescope.^{64,65} Due to the fact that this design was highly sensitive to grating alignment, these double grating designs were replaced with a folded design using a single grating and lens with a mirror at the Fourier plane.⁶⁶ However, the early stretcher designs utilizing refractive optics were limited to pulse lengths above approximately 100 fs due to chromatic and spherical aberration in the telescope which are associated with the extremely large bandwidth required for pulses $\lesssim 80$ fs.

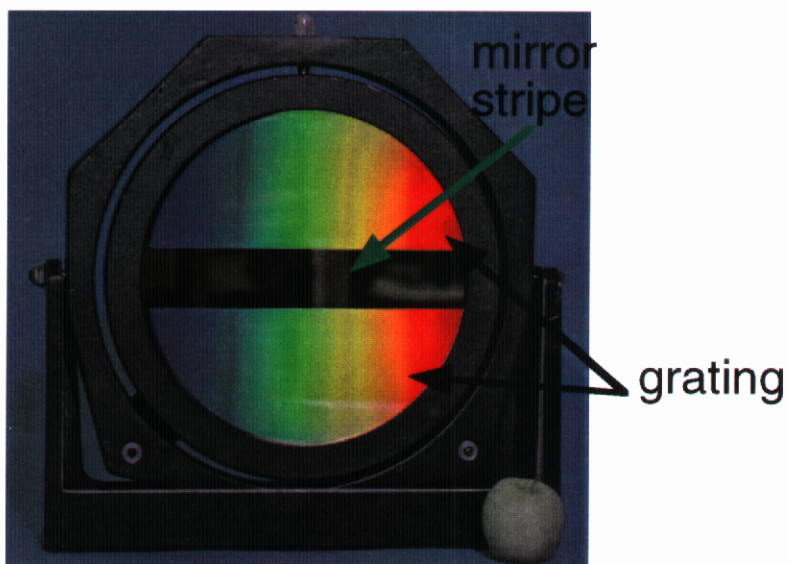
As a result, several groups^{35,44,45,59} have developed all-reflective stretcher designs. These designs either employ large special optics, are limited in the stretching ratio, are used off-axis, or involve a large number of elements which complicate alignment. For our CPA system, we developed an all-reflective, on-axis design containing only four elements which has been used to produce a stretching ratio in excess of 20,000. This pulse stretcher was designed specifically for ease of alignment and insensitivity to slight alignment errors. It was found that off-axis aberrations affected the fourth order phase term, which could be used to compensate for material dispersion in the laser system and to produce sub-50 fs pulses.

3.1.1 Stretcher design

The pulse stretcher design used in this laser system is composed of only four reflective elements as shown in Fig. 3.2. The components are a 6 in. diameter gold mirror (flat) at



(a)



(b)

Figure 3.2: (a) All-reflective stretcher design. The flat mirror is located 63 cm from the centerline of the grating. (b) The face of 12" grating with a 2" wide horizontal mirror stripe

the focal plane, a 113 cm focal length, 8 in. diameter parabolic (or spherical) gold mirror, a 12 in. diameter grating, and a roof mirror which displaces the beam vertically for a second pass through the stretcher. The flat mirror is positioned at the focal plane of the curved mirror, thereby forming a mirror image which allows the use of a single grating and a single curved optic. The stretcher telescope is formed using a parabolic mirror in order to eliminate all on-axis aberrations. The grating itself is a composite where a mirror stripe has been placed horizontally across the center of a holographically-produced, 1480 1/mm, broadband gold grating⁶⁷ (see Fig. 3.2(b)). This stripe acts as the fold mirror necessary to direct the beam to the flat mirror placed in the focal plane of the curved mirror.

The input beam strikes the grating slightly above the mirror stripe and is diffracted to the parabola. The parabolic mirror reflects the dispersed beam at a slight downward angle so that it strikes the mirror stripe in the middle of the grating. The converging beam is reflected from the grating plane to the flat mirror at the focus of the paraboloid. Reflection from the flat mirror repeats this sequence in reverse order, only on the lower half of the optics. The beam exits the stretcher assembly vertically displaced from its incident location. At this point, it is sent back for a second pass through the stretcher by a roof mirror.

The presence of the telescopic system in the stretcher design does not allow for analytic solutions for the path length p traveled as a function of frequency as was possible for a grating pair (Eq. (3.2)). The path length must be determined numerically for a range of frequencies to an accuracy that will enable the determination of the fourth derivative. Simple ABCD matrices do not adequately model the optical system and so it is necessary to do exact raytraces of the system. It was found that the *Mathematica* package *Optica* provided a useful and robust method of raytracing our stretcher design.⁶⁸ A set of rays

of a range of frequencies were traced through the stretcher, giving a set of path lengths as a function of frequency. These were then fit with a sixth order polynomial, which was differentiated four times within *Mathematica* to obtain the phase terms β_j . The number of frequency components used was 12 separated in wavelength by 5 nm. It was verified that increasing this number or decreasing the wavelength spacing did not affect the resultant phase terms. Increasing the order of the fit polynomial also had no effect (as long as the order was less than the number of data points, of course). The values given by *Optica* for the path lengths were also verified by a FORTRAN routine that would raytrace a specific configuration.

3.1.2 Design considerations

For an ideal stretcher design with no aberrations, the phase terms β_j correspond to those calculated for a grating pair with a negative grating separation. The magnitude of this effective grating separation is equal to the distance from the grating surface to the focal plane of the curved optic. Achieving the large stretching ratios needed for amplification to the joule level requires that this distance be made as large as possible. However, another significant requirement is that the design support as large a bandwidth as possible. This second requirement is favored by using shorter focal length optics, but this, in turn, reduces the maximum stretching ratio possible while still maintaining unobstructed beam paths. The accumulated B-integral will become the most significant factor in our laser system so that the stretching ratio will be the overriding factor. As seen in Chapter 2, the spectral bandwidth after amplification will be approximately 20–25 nm FWHM. Using a “rule of thumb” similar to that used in optics where the aperture should be three times the beam diameter to avoid diffraction effects, we need the stretcher to pass roughly 60 nm of

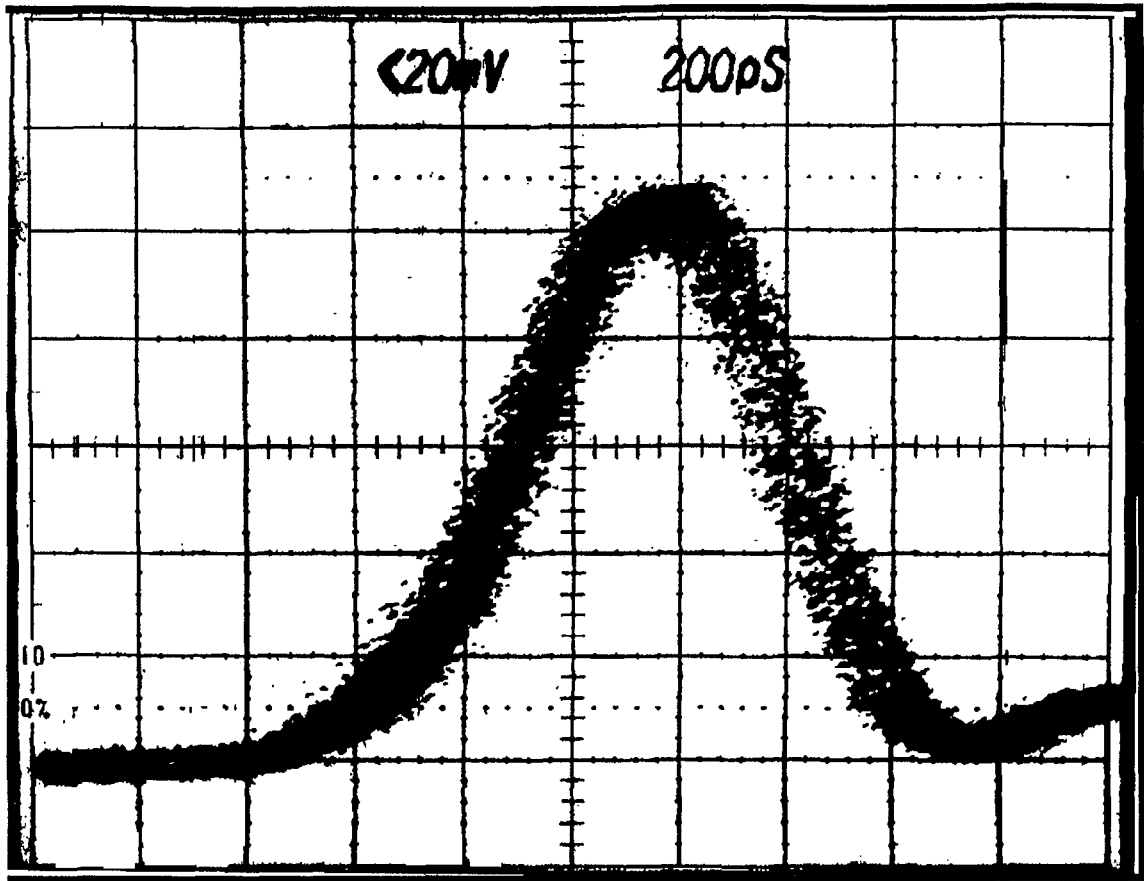


Figure 3.3: Temporal shape of stretched pulse measured with a fast photodiode and sampling head. FWHM ≈ 600 ps (200 ps per division).

bandwidth to avoid pulse distortion due to clipping of the outlying parts of the frequency spectrum.

By choosing to use an 8 in. diameter optic with a focal length of 113 cm, it is possible to stretch 30 fs (FWHM) pulses from the Ti:sapphire oscillator described in Section 2.1.1 to 600 ps (a stretching ratio of 20,000) while still passing 60 nm of bandwidth. Fig. 3.3 shows the stretched pulse as measured using a fast avalanche photodiode. The spectrum of the stretched pulse is shown in Fig. 3.4 and is indeed 60 nm between clipping points (shown by the arrows), the limiting aperture being the parabolic mirror. It should be noted that the 12 in. diameter of the grating is not necessary for the design, but was the size of a standard substrate at LLNL and was used strictly for convenience.

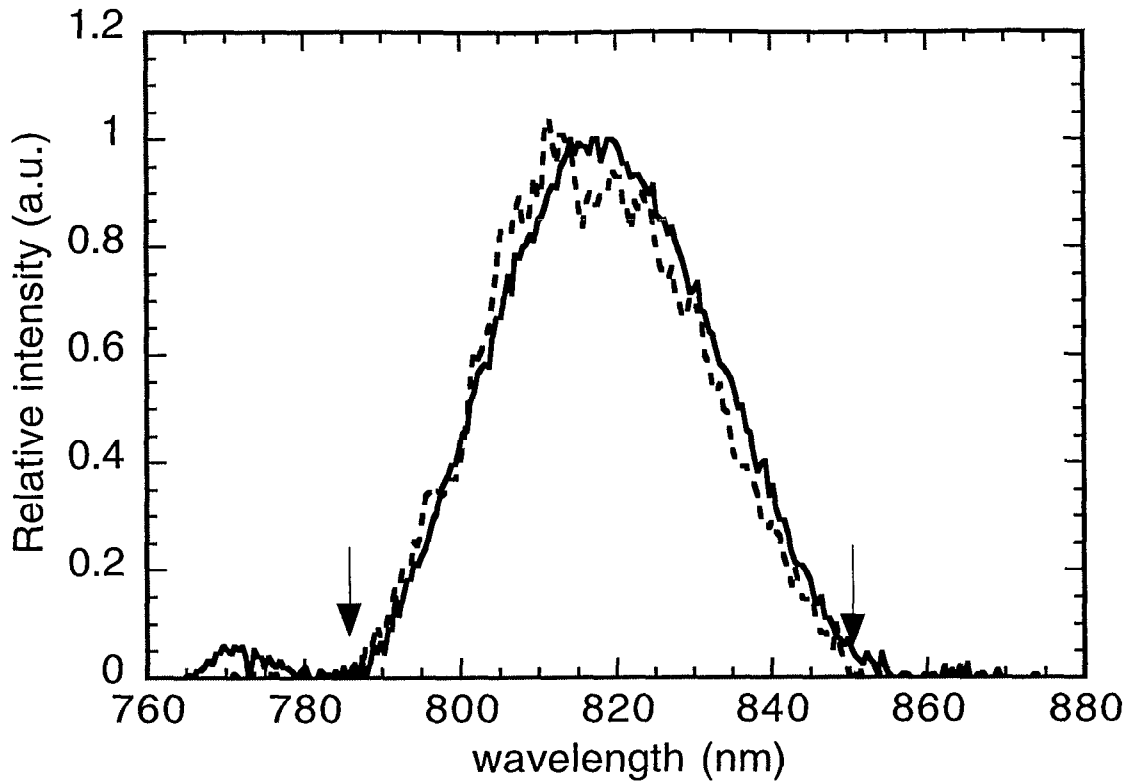


Figure 3.4: Bandpass of stretcher (60 nm indicated by the arrows). The solid line is the spectrum into the stretcher, and the dotted line is the spectrum out of the stretcher.

The stretcher design itself is not limited to this bandpass, however; other choices of optic sizes and focal lengths can be used for different final stretching ratios and bandpasses. In order to increase the spectral throughput of the stretcher while maintaining the stretching ratio, it is possible to simply add two small mirrors at the output to send the beam back into the stretcher for a third and fourth pass. For example, the second pass output beam height could be changed from 4 cm above the center line to 6 cm with the third and fourth passes being at 5 cm and 4 cm, respectively, above the center line. A shorter focal length optic can then be used so that the spectrum is less dispersed on the optics. In fact, raytracing calculations indicate that a spectral throughput in excess of 120 nm is possible by reducing the focal length of the curved mirror to about 80 cm. This indicates that this design can be used for CPA systems that utilize even shorter pulses

Table 3 1 Sensitivity calculations for errors in alignment of stretcher These were all done for a parabolic curved mirror and $\theta_i = 48.19^\circ$ centered at 820 nm Δx is the horizontal displacement (perpendicular to grating grooves) and Δy is vertical displacement of paraboloid center

Δx (cm)	Δy (cm)	$\beta_2 \times (10^6 \text{ fs}^2)$	$\beta_3 (\times 10^7 \text{ fs}^3)$	$\beta_4 (\times 10^7 \text{ fs}^4)$	$\beta_5 (\times 10^8 \text{ fs}^5)$
0 0	0 0	6 909	-1 559	6.467	-3 638
-.5	0 0	6.909	-1 554	6 441	-3 622
-.4	0 0	6 909	-1.555	6.446	-3 625
- 3	0 0	6 909	-1 556	6 451	-3 628
- 2	0 0	6 909	-1 557	6 456	-3 632
- 1	0 0	6 909	-1 558	6 462	-3.635
+ 1	0 0	6.909	-1 560	6 472	-3 641
+ 2	0 0	6 909	-1 561	6.477	-3 644
+ 3	0 0	6 909	-1 562	6 482	-3 648
+ 4	0 0	6 909	-1 563	6 487	-3 651
+ 5	0 0	6 909	-1 564	6 492	-3 654
0 0	+ 5	6 909	-1 559	6 467	-3 638
0 0	- 5	6 909	-1 559	6 467	-3 638

and greater bandwidth

3.1.3 Alignment issues

One of the main advantages of this stretcher design is that is exceptionally simple to align. The input angle was chosen so that the angle from the grating to the parabola would be the Littrow angle for a HeNe alignment laser. This input angle is also just past the edge of the large curved mirror, making it as close to Littrow for 820 nm as possible. It has been shown that operating close to the Littrow angle is advantageous for decreasing the sensitivity to misalignment.⁶⁹

The alignment procedure is as simple as positioning a beamsplitter between the grating and the parabolic mirror such that the HeNe alignment beam is diffracted at Littrow. The zero order reflection from the grating is then used to set the position and angle of the flat focal plane mirror. The first-order beam sets the position and angle of the curved optic. These are the only parameters which need to be adjusted since the fold mirror

and gratings are all on the same optic. Pulse stretchers are extremely sensitive to any relative angle between the gratings which comprise the stretcher (or the fold path in a single grating system). Since “both” gratings and the fold mirror are all fabricated as a single optic, it is impossible to have any relative misalignment between these components. It is, however, difficult to precisely position the center of the paraboloid with certainty so raytrace calculations were performed to determine the effect of placement errors on the order of 1 cm. These results are shown in Table 3.1 which gives the phase terms calculated from raytraces for different horizontal (Δx) and vertical (Δy) parabolic mirror displacement from the center. Calculations for errors in angular positioning of a degree are of similar magnitude (or lower). The size of the phase change due to these alignment errors are negligible, e.g. a phase error of $\beta_4 = 2 \times 10^5 \text{ fs}^4$ broadens a 50 fs pulse by less than .1 fs. By comparison, White *et al.*⁶³ show that changes in alignment in their stretcher optics by 500 μm produce changes in β_4 of up to $4 \times 10^7 \text{ fs}^4$. This indicates that although there are apparently no adjustments that can be made for phase compensation, this design is very immune to phase errors being caused by misalignment.

The one parameter that must be set accurately is the placement of the flat mirror relative to the focal plane. While phase errors are even smaller than those in Table 3.1 for similar displacements, errors in position on the order of 1 mm cause a marked increase in the spectral divergence of the output beam (spectral divergence refers to different frequency components not being collinear). The other parameters that have been discussed have little effect on the spatial characteristics of the beam.

3.1.4 Performance issues

The phase terms for a grating pair separated by -252 cm (the effective separation of the stretcher is -126 cm times two passes) using Eq. (3.2) are

$$\beta_2 = 6.903 \times 10^6 \text{ fs}^2$$

$$\beta_3 = -1.558 \times 10^7 \text{ fs}^3$$

$$\beta_4 = 5.635 \times 10^7 \text{ fs}^4, \text{ and}$$

$$\beta_5 = -2.832 \times 10^8 \text{ fs}^5.$$

When compared with the terms in Table 3.1 for $\Delta x = \Delta y = 0$, i.e. the stretcher is perfectly aligned, the second and third order terms of the phase expansion agree well. The difference is due solely to the fact that the rays travel along a vertically slanted path through the telescope, thus increasing the effective separation between the gratings. When adjusted for this increased distance, the grating pair second and third order terms match those in Table 3.1. However, the fourth order term is still only $5.635 \times 10^7 \text{ fs}^4$ vs. $6.467 \times 10^7 \text{ fs}^4$ for our stretcher design. The fifth order term is similarly much larger than would be expected.

A fourth order residual phase term of this magnitude would broaden a nominally 50 fs pulse by 20-30 fs upon recompression; this was confirmed using an interferometric autocorrelator. Fig. 3.5 shows the autocorrelation trace of the pulse train having been stretched and then compressed using a single-grating compressor designed to produce 50 fs transform-limited pulses. Also shown is the autocorrelation envelope calculated using the pulse spectrum combined with the expected residual phase due to the large fourth order error.

The residual phase term is because, as with the aberration-free stretcher described in

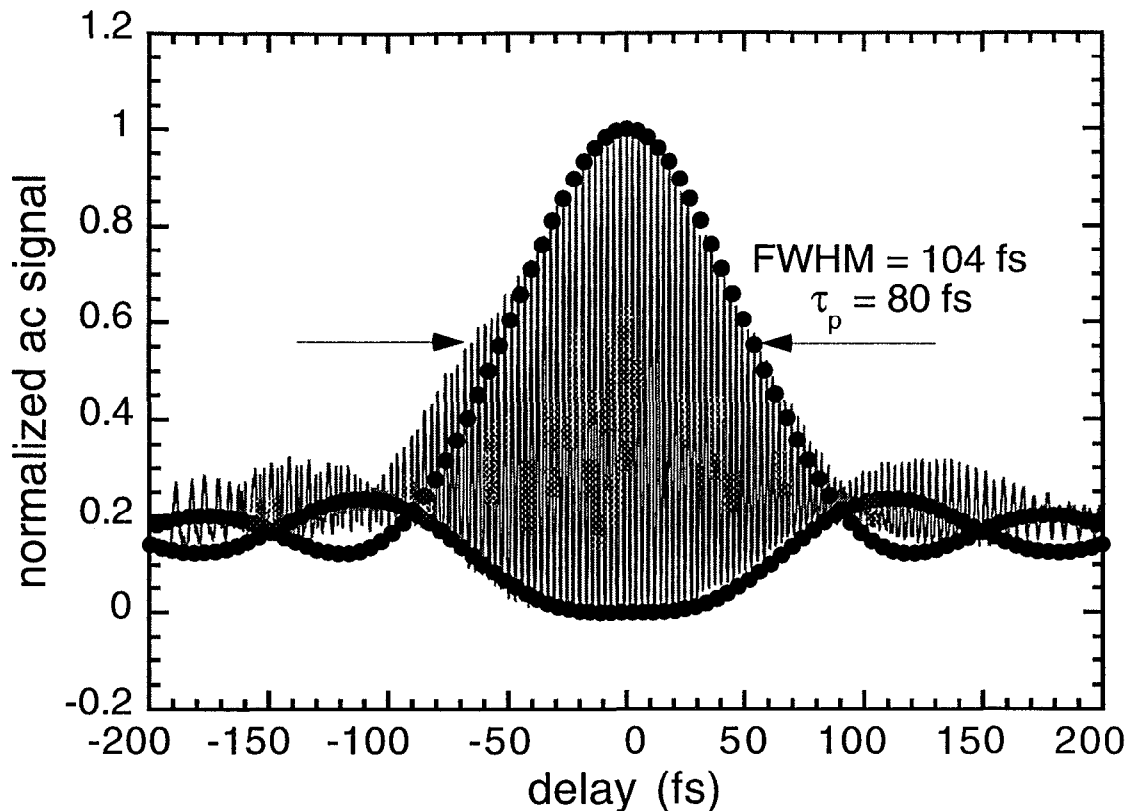


Figure 3.5: Interferometric autocorrelation of pulse stretched using parabolic mirror. Solid circles are the envelope calculated using measured spectral width and predicted uncompensated fourth and fifth order phase. Line is measured autocorrelation trace of compressed pulse.

Ref. 59, this design is only truly aberration-free if the grating is in the focal plane of the parabolic mirror. When the grating is not in the focal plane, the dispersed beam strikes the parabolic mirror as a diverging beam, and thus off-axis. This induces a significant spectral divergence, both horizontal and vertical, where the different frequency components are no longer collinear after striking the grating the 2nd (and 4th) time. This behavior is shown in Fig. 3.6(a) where transverse position of 20 frequency components, evenly spaced from 790 nm to 850 nm, is displayed upon exiting the stretcher. The position is plotted both immediately after (10 cm) striking the grating for the last time and after an additional 150 cm of propagation.

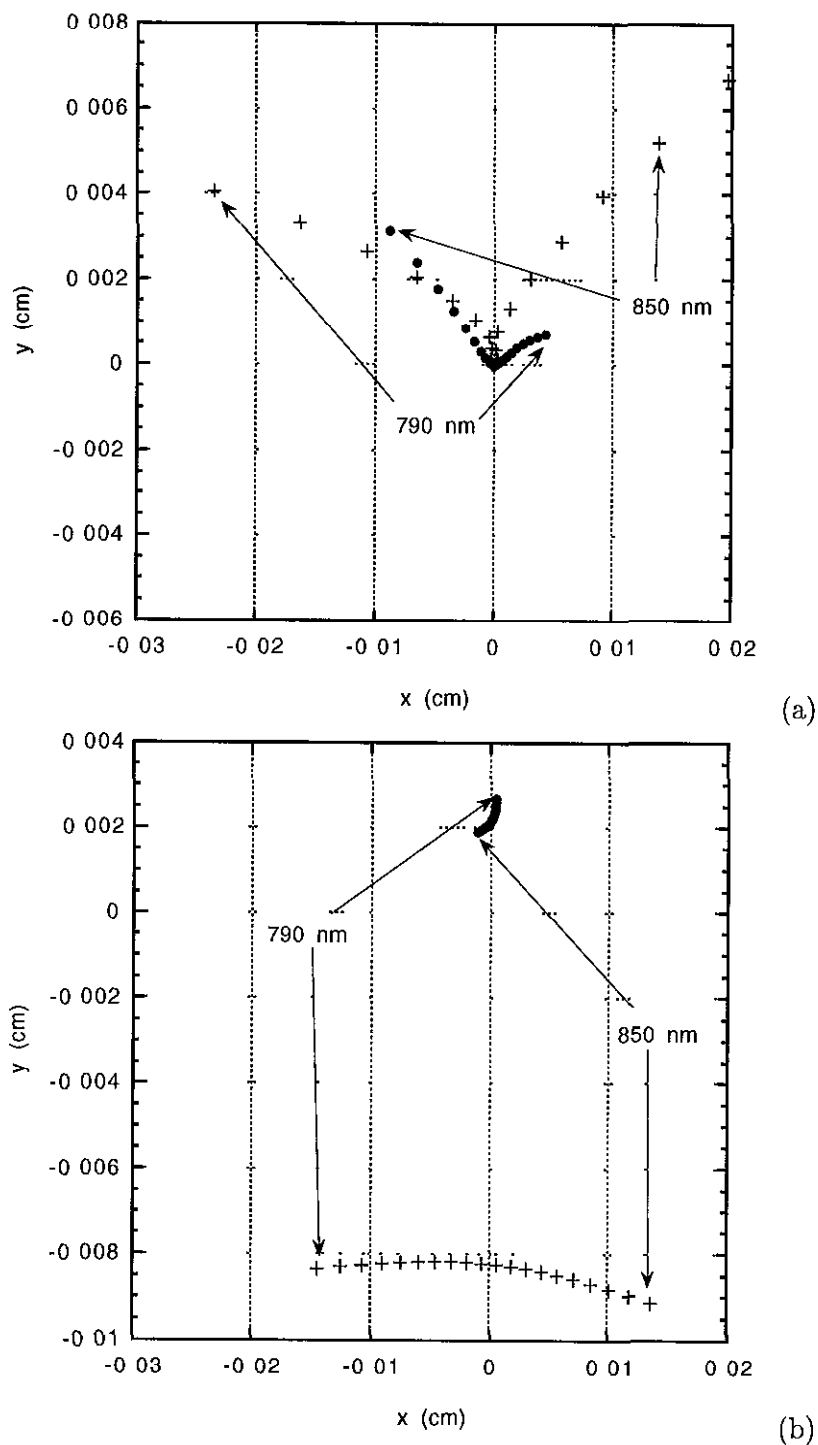


Figure 3.6: The transverse frequency spread of a ray output from our design using a parabolic mirror (a) and from the design of Cheriaux *et al.*⁵⁹(b). The dots show the position of the various frequency components (from 790 nm to 850 nm) 10 cm in front of the grating while the plus signs (+) show the position 150 cm further downstream. The point (0,0) is where all frequency components would be without aberrations.

With no aberrations, this Figure should show a single dot at (0,0), meaning that all frequency components are coincident spatially (i.e. no spectral divergence). This is obviously not the case; the change in the relative positions of the rays as the beam propagates show a divergence among the frequency components. There is approximately a .6 mrad angular spread across the 60 nm of bandwidth. This spatial chirp and spectral divergence, in the plane of grating dispersion in particular, translate directly into changes in the phase expansion terms from the ideal, even though the absolute magnitude of these is on the order of microns and microradians.

For comparison, the transverse spatial position of the frequency components is plotted in Fig. 3.6(b) for the “aberration-free” design presented by Cheriaux *et al.* in Ref. 59 (using the parameters they give in their paper). It can be seen that this design suffers from the same spatial chirp and spectral divergence because the design is only aberration-free on-axis. However, the aberrations do not have a very large effect on the phase terms, with the largest effect being mostly in the third order term ($\Delta\beta_3 = 1.7 \times 10^4$), probably since the frequency components are more evenly spaced in Fig. 3.6(b). It should be noted that the stretching ratio for the parameters that they give in their paper is only 10,000. The effects of aberrations tends to worsen as the stretching ratios increases.

One possible scenario to remove these aberrations would be to deform the roof mirror such that the rays would be redirected back into the stretcher for the second pass along precisely the same trajectories, only in the opposite direction. This would exactly undo all of the imperfect imaging that occurred in the first pass. What such a mirror shape would have to look like is shown in Fig. 3.7 for the stretcher parameters here presented. Only doing this correction in the horizontal plane (the plane of diffraction) causes the output spatial positions of Fig. 3.6(a) to become as in Fig. 3.8. There is no longer any spatial

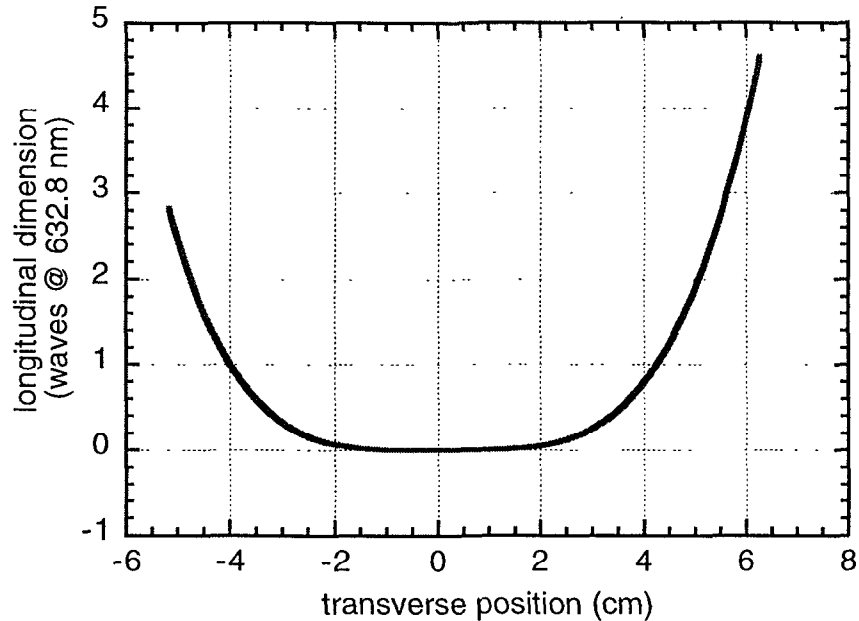


Figure 3.7: Horizontal cross section of retro mirror needed to remove phase aberrations from parabolic stretcher design.

or spectral aberration in this plane. The phase terms from such a configuration exactly match those of a grating pair to fourth order and only differs in fifth order by $5 \times 10^6 \text{ fs}^5$ (which is insignificant). This shows that the aberrations in the plane of dispersion have the most effect on the phase terms, as it to be expected.

Besides using adaptive optics or curved mirrors to eliminate the phase aberrations, it was found via further raytracing calculations that using a spherical surface for the curved mirror instead of a parabolic one reduces the error in β_4 as well. While this is no longer an on-axis aberration-free design, the spherical aberration show up as slightly greater spatial chirp, but the frequency components are much more collinear than for the case with the designs shown in Fig. 3.6 (see Fig. 3.9). For a stretcher using a spherical mirror of the same focal length (113 cm), $\beta_4 = 5.482 \times 10^7 \text{ fs}^4$ and $\beta_5 = -2.683 \times 10^8 \text{ fs}^5$ (β_2 and β_3 are the same). Not only is the resulting error smaller than the previous design, it is of the opposite sign ($-1.53 \times 10^7 \text{ fs}^4$ vs. $8.32 \times 10^7 \text{ fs}^4$ for the parabolic mirror). Because of

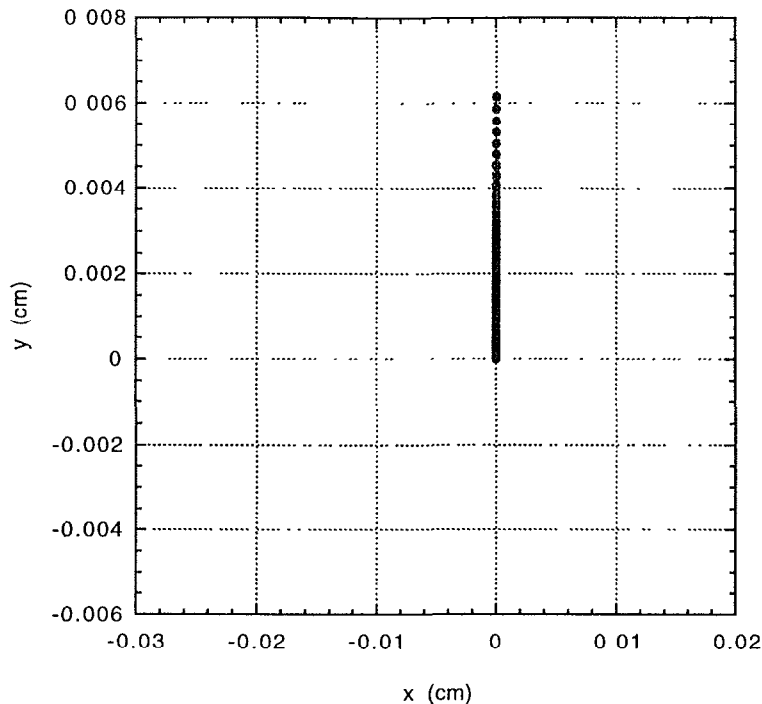


Figure 3.8: The transverse spatial position of the various frequency components (only correcting the imaging aberrations in the horizontal plane).

this, when the material dispersion of the system is added and the compressor is adjusted to zero β_2 and β_3 , $\Delta\beta_4$ is reduced even further. In fact, the dispersion from traversing the amplifiers (88 cm of KD*P and 122 cm of Ti:sapphire) reduces the residual fourth order term to $-2.6 \times 10^5 \text{ fs}^4$, corresponding to less than 1 fs broadening of a 50 fs pulse. Total elimination of the residual fourth order phase term can be accomplished by adding more material (equivalent to 10 cm of Ti:sapphire and 8 cm of KD*P) or by changing the groove spacing of the compressor to 1450 l/mm. This simultaneously reduces the residual fifth order term to approximately 10^5 fs^5 . The effects of various amounts of material on the residual phase are highlighted in Table 3.2. The resulting phase and temporal delay across the pulse spectrum is plotted in Fig. 3.10.

To check these calculations, we replaced the parabolic mirror in the stretcher with a 46 cm diameter spherical mirror that was readily available possessing a radius of curvature

Table 3.2: Table of effects of material dispersion on residual phase using a spherical mirror in the stretcher. For the configuration designations, mat1 is including material from regen. (40 passes) and amplifiers 1 and 2 and FS2 (see Table 3.3). mat2 all amplifiers and all fused silica. (*) indicates changing regen to 44 passes, (†) indicates using a 1448 l/mm grating in compressor, (‡) indicates using a 1450 l/mm grating. l and θ_i are the grating separation and input angle of the compressor that compensate second and third order.

Configuration	l (cm)	θ_i (deg)	$\beta_4^{\text{res}} (\times 10^6 \text{ fs}^4)$	$\beta_5^{\text{res}} (\times 10^7 \text{ fs}^5)$
Grating pair (no mat.)	252	48.2	0.0	0.0
Grating pair w/ regen.	258.6	49.2	1.1	-.99
Grt. pr w/ mat1 (no fs)	259.7	49.4	1.3	-1.1
Grt. pr w/ mat1	259.8	49.4	1.3	-1.2
Parabola w/ mat1	259.8	49.4	9.7	-9.2
Lg. sph w/ mat1	260.6	49.4	-2.5	2.5
Sphere (no mat.)	252.2	48.2	-1.6	1.5
Sphere w/ mat.	260.0	49.4	-.26	.35
Sphere w/ mat2	260.9	49.6	-.13	.23
Sphere w/ mat2*	—	—	-.018	.13
Sphere w/ mat2†	—	—	.00015	.058
Sphere w/ mat2‡	—	—	-.016	.076

Table 3.3: Phase expansion terms for the material dispersion in the various stages of the laser system. The regen is assumed to have 40 passes. FS 1 is the 11.2 cm of fused silica in lenses and windows to the single grating compressor and FS 2 is the additional 16.4 cm of fused silica to the vacuum compressor. Published Sellmeier data for Ti:sapphire (those for sapphire⁷⁰ were used), fused silica,⁷⁰ and KD*P⁷¹ were used in these calculations.

system comp.	β_2 (fs ²)	β_3 (fs ³)	β_4 (fs ⁴)	β_5 (fs ⁵)
regen (40 ps)	81510	73920	-38470	104500
amp 1	5509	4305	-1850	5536
amp 2	6830	5848	-2848	7745
amp 3	4792	4000	-1887	5132
amp 4	2755	2152	-925	2518
FS 1	3871	3159	-1501	4129
FS 2	5668	4626	-2198	6046

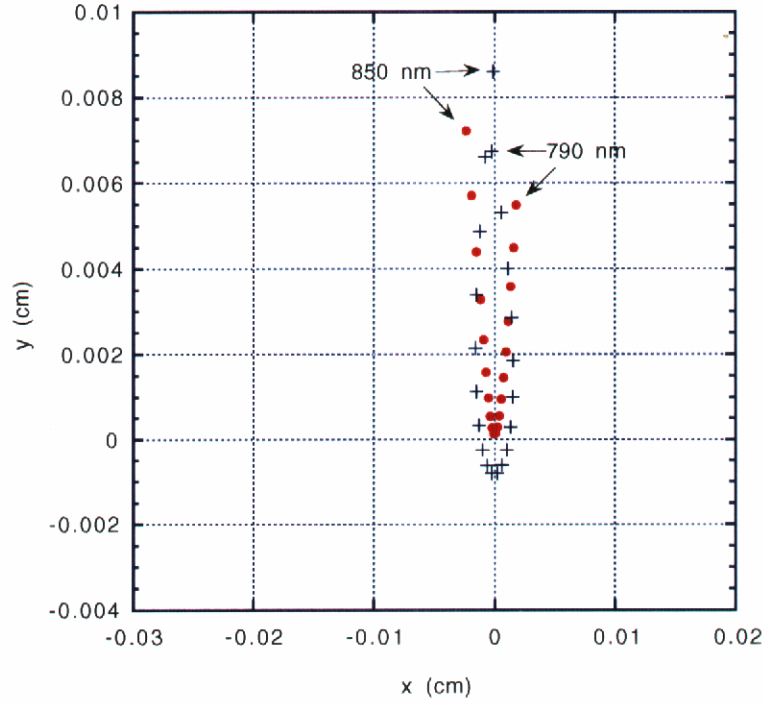


Figure 3.9: The transverse frequency spread of a ray output from this design using 110 cm focal length spherical mirror. The dots show the position of the various frequency components 10 cm in front of the grating while the plus signs (+) show the position 150 cm further downstream. The point (0,0) is where all frequency components would be without aberrations.

of 172 cm. To maintain the same stretching ratio, an additional roof mirror was added, and the beam makes four passes through the stretcher. With the shorter focal length, the bandpass of the stretcher was indeed approximately 90 nm with the limiting aperture now being the 6" flat mirror. The raytrace for this 4-pass configuration gives a smaller fourth order phase term ($5.3 \times 10^7 \text{ fs}^4$) which increases the uncompensated phase, but it is still half the value predicted for the parabolic mirror design. This is confirmed in Fig. 3.11 where the circles are the calculated autocorrelation envelope assuming the measured spectral width and the calculated residual phase and the line is the measured autocorrelation trace of the unamplified pulse. This trace corresponds to a pulse length of approximately 50 fs with a small amount of residual chirp.

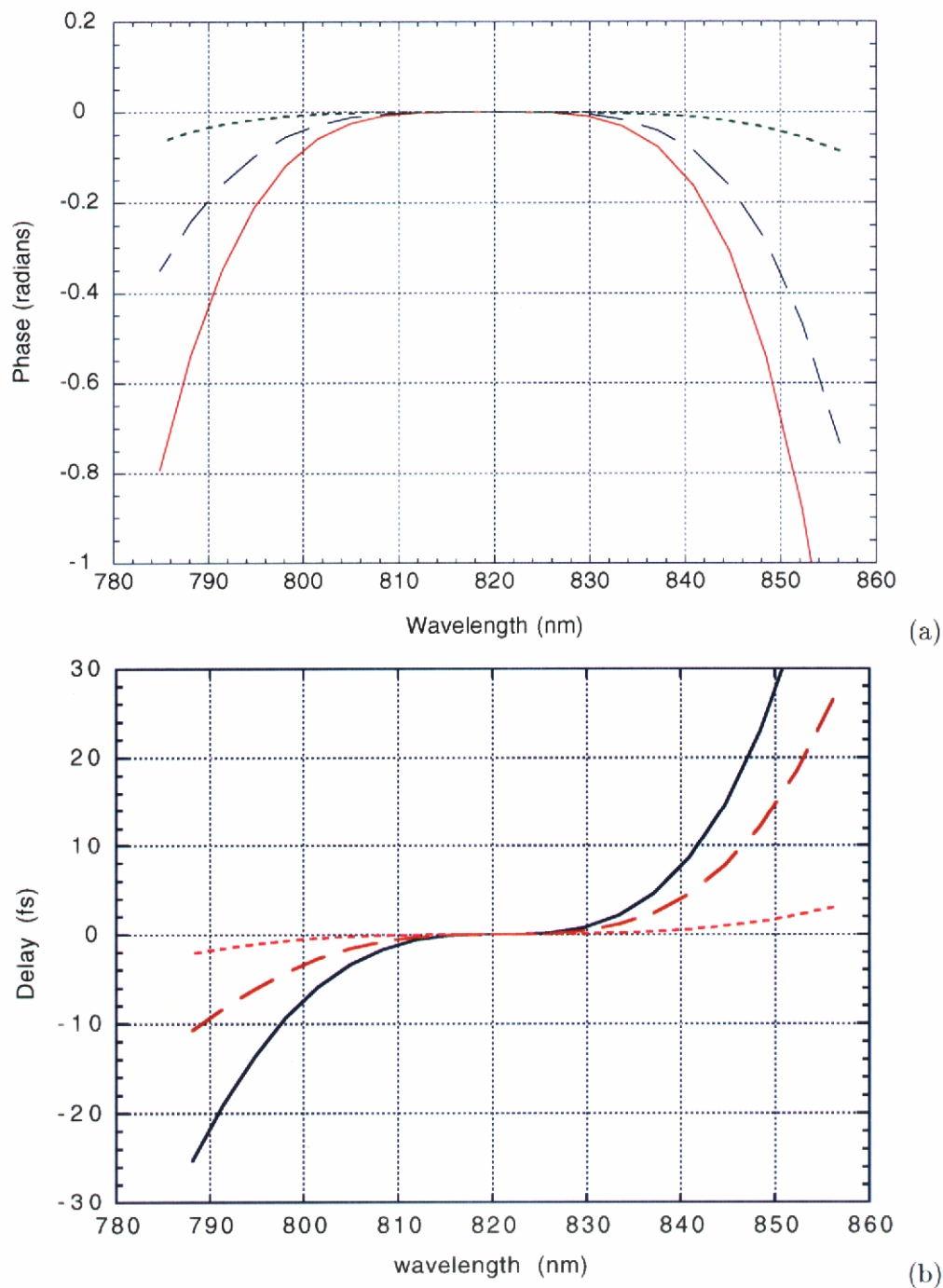


Figure 3.10: Phase (a) and temporal delay (b) as a function of frequency for stretcher with 110 cm focal length spherical mirror: solid line— material through regenerative amplifier only, long-dashed line—all material (mat2 in Table 3.2), and short-dashed line—all material plus four additional passes in regenerative amplifier.

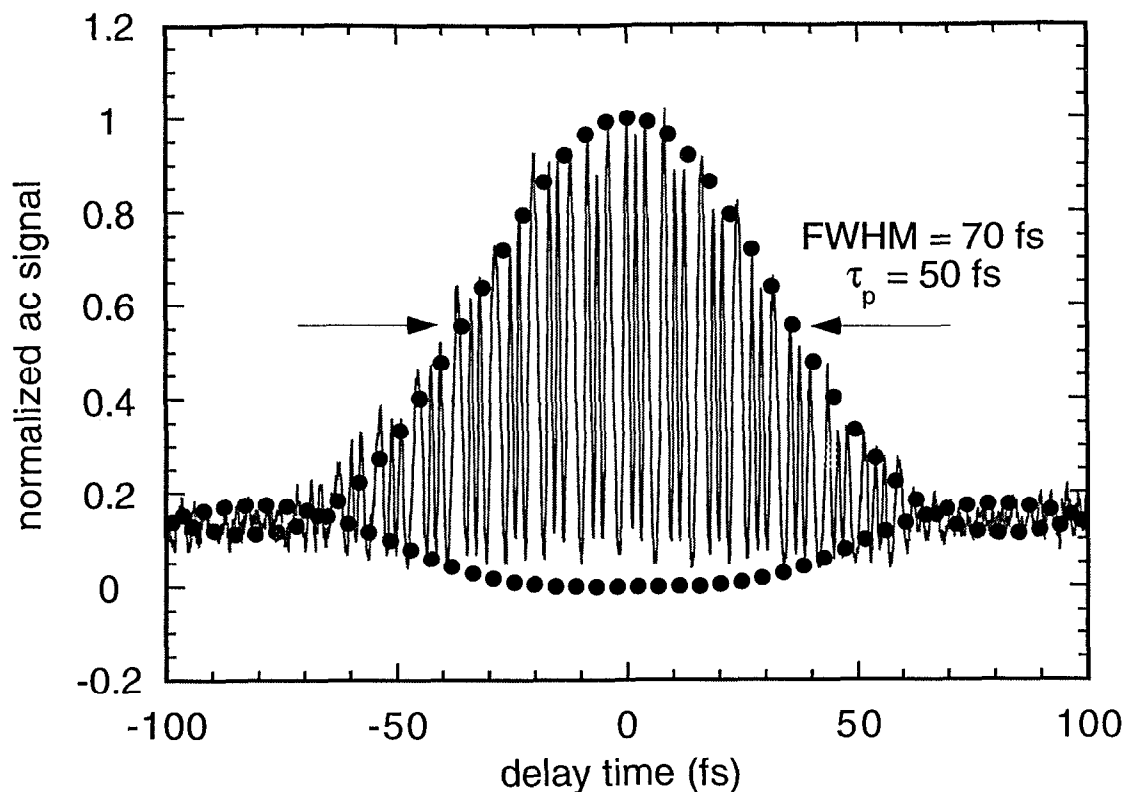


Figure 3.11: Interferometric autocorrelation of pulse stretched using spherical mirror. Solid circles are the envelope calculated using measured spectral width and predicted uncompensated phase. Line is measured autocorrelation trace of compressed pulse.

These calculations were further tested by obtaining a 9 in. diameter spherical mirror with a radius of curvature of 220 cm (110 cm focal length). This was placed in the stretcher and the resulting stretched pulse was amplified to 40 mJ through the amplifier described in Section 2.1.3. This amplified pulse was then compressed and a single shot autocorrelator was used to measure the temporal profile. This is shown in Fig. 3.12(a) and has a FWHM of 65 fs, corresponding to a 45 fs pulse in time (see Fig. 3.12(b)). The theoretical prediction for the autocorrelation for the given spectrum and predicted residual phase is also shown in good agreement. Also shown in Fig. 3.12(b) is the predicted temporal profile for gain-narrowed pulse on a log scale (which is 45 fs FWHM).

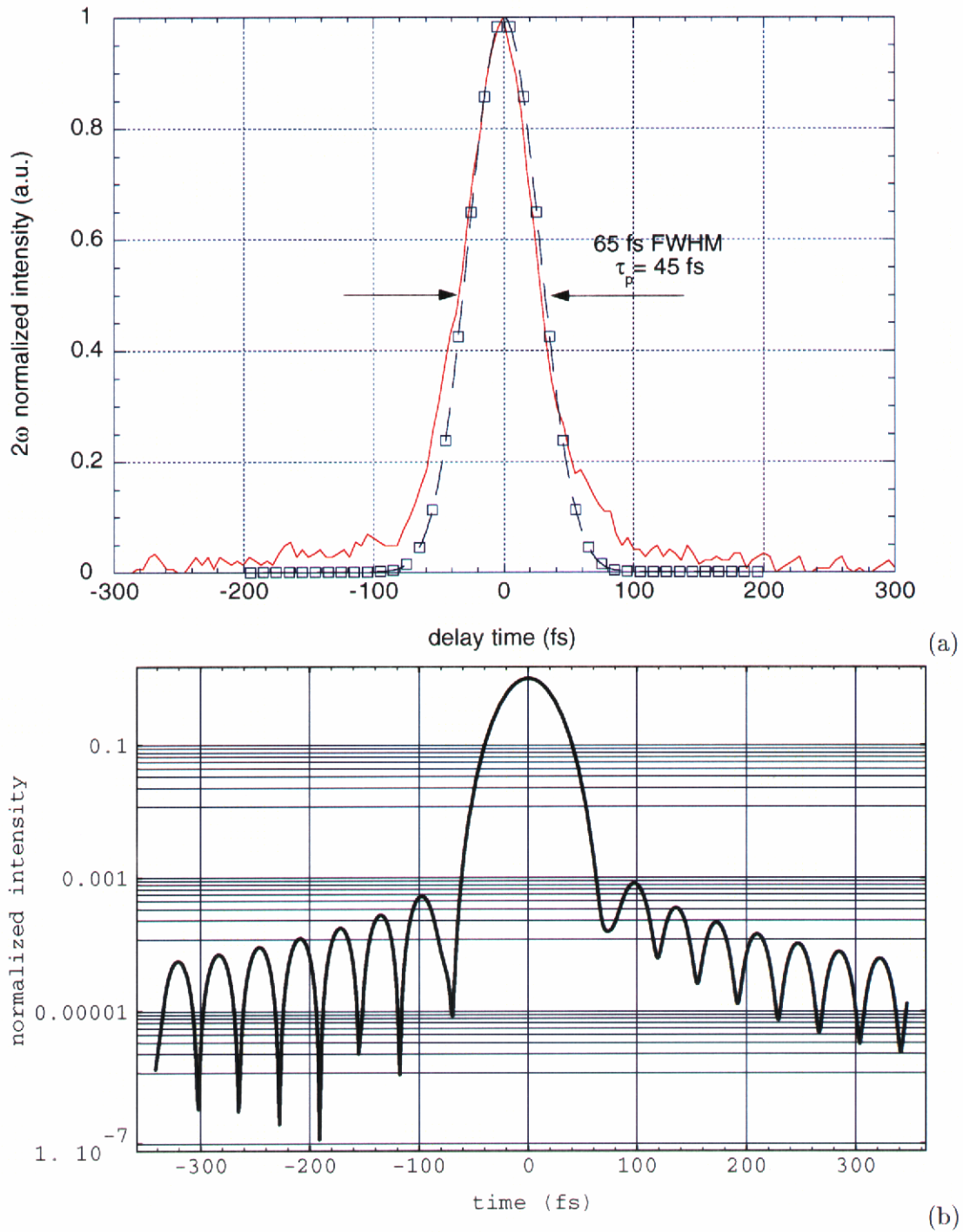


Figure 3.12: (a) Single-shot autocorrelation of pulse with spherical stretcher mirror and material through 1st power amplifier (solid line). Dashed line shows predicted autocorrelation for gain-narrowed spectrum. (b) Temporal profile of predicted pulse.

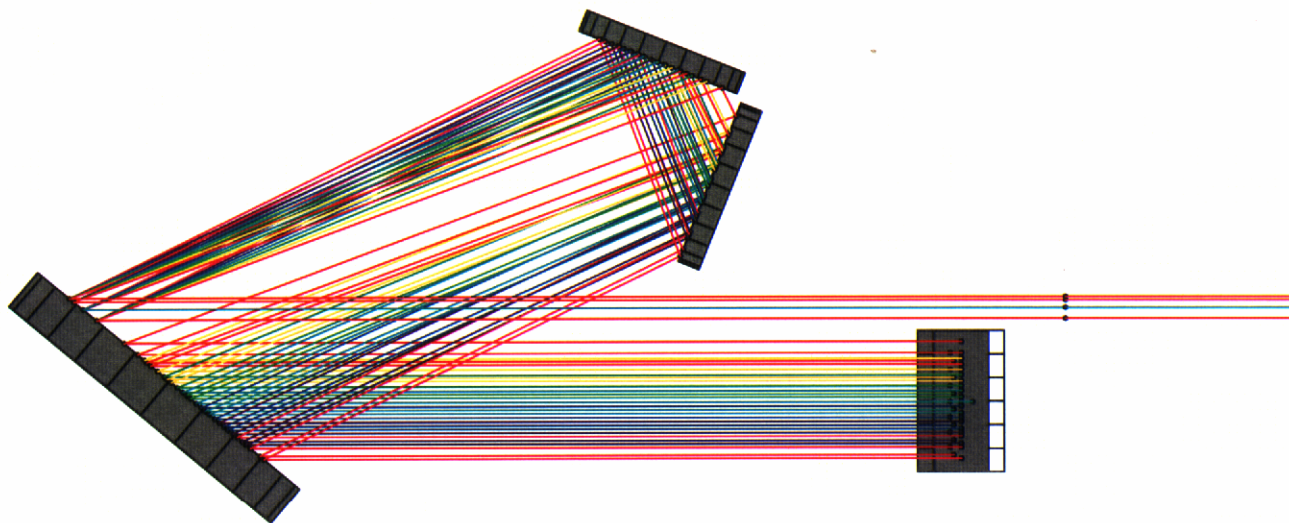


Figure 3.13: Scale drawing of the single-grating compressor to be used for low energy shots. The lines are ray traces assuming a 2 cm diameter beam.

3.2 Compressors

As was mentioned in the previous Chapter, this laser system will have two simultaneously operable beamlines using two separate pulse compressors. The compressor that has been used to this point is a single grating design¹⁷ as shown in Fig. 3.13. This design has the advantage of being easily aligned—no grating/grating misalignment possible—and the output pulse length can be simply adjusted by translating the fold mirrors. However, since it uses gold-coated fold mirrors, the energy throughput possible drops to about 55–65% maximum. Also, as is obvious from Fig. 3.13, there is very little room for the beam to enter and exit between the two sets of fold mirrors. To first order, the effective length of the stretcher determines the distance between the first set of fold mirrors and the grating. Additionally, in order to support the 60 nm necessary to avoid spectral clipping effects, these mirrors must be at least 6 in. wide. The second set of fold mirrors must also be at least 5 in. wide which leaves only slightly more than 1.5 in. between them. There are again the same trade-offs between translation and bandwidth as there are for the stretcher.

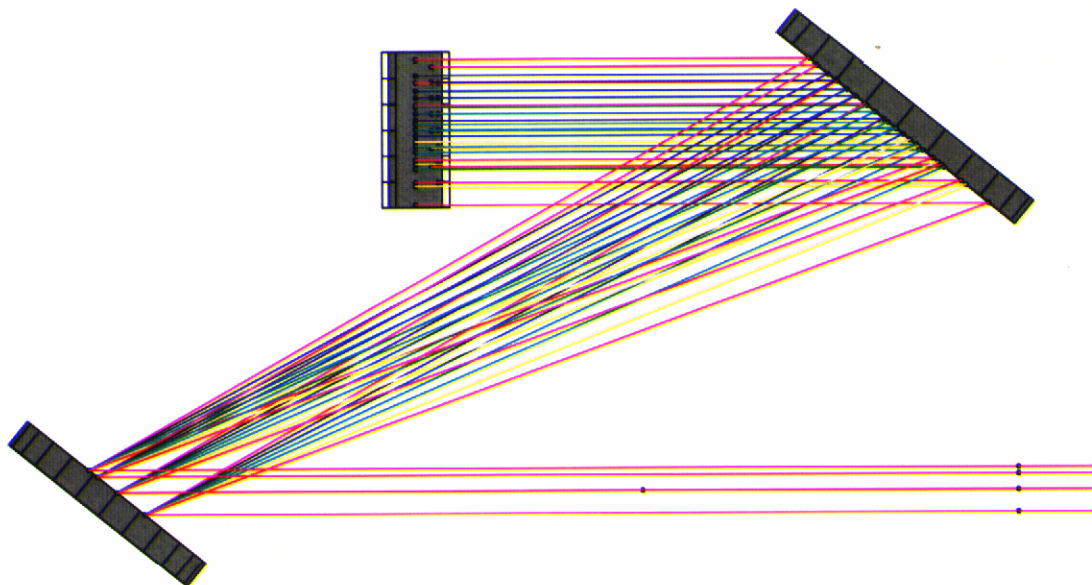


Figure 3.14: Scale raytrace drawing of the compressor design to be used for high energy shots.

The space constraints limit the beam size that can be used with this stretcher to less than 3 cm. There will be approximately 100–120 mJ of energy emerging from this compressor in 50 fs and a 3 cm beam, giving an intensity of 300 GW/cm^2 . Intensities of this magnitude accumulate a B-integral of approximately .75 just by propagating 1 m in air. Propagation through even 1 cm of fused silica (e.g. a window) suffers a B-integral of ten times this.

For this reason, any higher energies must be compressed under vacuum. The vacuum chamber from the 10 TW laser's compressor is available for this purpose. The main consideration for this compressor is material damage constraints, especially the gratings, and optic size. The gold gratings used damage under fluences in the $300\text{--}500 \text{ mJ/cm}^2$ range so in order to safely support 10 J, the beam size must be at least 7 cm and larger if possible. On the other hand, an 8 cm beam is about the largest beam that can still fit on a 16 in. diameter grating and still have 60 nm of spectral throughput. The sizes involved

of course rule out using the single grating design shown in Fig. 3.13 so two gratings will be used, one of 12 in. diameter and one of 16 in. diameter. As before, the 12 in. size is not necessary, but it must be at least 8 in. The final design is then shown in Fig. 3.14 along with the raytrace for an 8 cm beam. As an added bonus, not using the gold fold mirrors increases the maximum energy throughput to approximately 70%.

3.3 Conclusion

In conclusion, we have described a novel design for an all-reflective pulse stretcher for use in CPA systems. The advantages are that it is easily aligned, relatively insensitive to small misalignment, and capable of producing large stretching ratios with a large bandpass. It appears that using a spherical mirror will produce smaller uncompensated phase terms than the on-axis aberration-free design using a parabolic mirror, and it is calculated to be possible to compensate second through fourth order phase terms using a combination of material dispersion in the system and/or changing the line spacing of the compressor grating.

Chapter 4

High intensity nonlinear optics

The interaction of light with matter is described at the macroscopic level by the electric polarization \mathbf{P} of the material through the constitutive relation

$$\mathbf{D} = \mathbf{P} + \epsilon_0 \mathbf{E}. \quad (4.1)$$

For much of the history of the field of optics, the dependence of this term on the applied electric field has been taken to be linear, i.e.

$$\mathbf{P}(t) = \epsilon_0 \int_{-\infty}^{\infty} \chi^{(1)}(t - \tau) : \mathbf{E}(\tau) \, d\tau \quad (4.2)$$

or

$$\mathbf{P}(\omega) = \epsilon_0 \chi^{(1)}(\omega) \mathbf{E}(\omega). \quad (4.3)$$

Here, the terms $\chi^{(1)}(t)$ and $\chi^{(1)}(\omega)$ are known as the electric response function and the electric susceptibility, respectively, and are related via Fourier transforms:

$$\begin{aligned} \hat{\chi}^{(1)}(\mathbf{x}, \omega) &= \int_{-\infty}^{\infty} \chi(\mathbf{x}, t) e^{i\omega t} \, dt \\ &= \mathcal{F}^{-1}[\chi(\mathbf{x}, t)]. \end{aligned} \quad (4.4)$$

However, with the advent of the laser and the high electric fields that it can generate,

it became possible to drive a material hard enough to reach a regime where the material response was no longer purely linear, thus giving rise to the field of nonlinear optics. The nonlinear polarization terms allow for beams of different frequencies to couple with each other giving rise to frequencies not originally present. Phenomena such as second harmonic generation (SHG), sum and difference frequency mixing (SFG and DFG), parametric amplification (OPA) are all due to the second order nonlinearity. The third order nonlinearity gives rise to stimulated Raman scattering (SRS), stimulated Brillouin scattering (SBS), self-phase modulation (SPM), and cross-phase modulation (XPM), among others. Until recently, only the second order processes could be used efficiently except in cases where a resonant enhancement due to the proximity of an electronic transition produces an exceptionally large third order coupling.

Until very recently, the study of nonlinear optical effects at intensities above a few GW/cm^2 and above had been limited to tightly-focused beams in gases and liquids. The focused beams have been able to create fields large enough to ionize atomic gases and excite many high order processes. Nonetheless, this cannot be done in solid materials (more than once, anyway) due to material damage. However, it is known empirically that the intensity damage threshold of solid material increases as roughly $\sqrt{\tau}$ where τ is the temporal pulse length. For example, with a 100 fs pulse, it is possible to propagate $1 \text{ TW}/\text{cm}^2$ or more through some optical materials. The use of CPA lasers with their ability to produce peak powers of terawatts or more in short pulse lengths opens an entire new realm of nonlinear interactions of light with solid-state media.

In this Chapter, the theory of the nonlinear interaction of ultrahigh intensity laser pulses will be presented, focusing primarily on third harmonic generation (THG) in a single crystal. The effects which must be accounted for are basically due to 1) the high irradiance

involved and 2) the short temporal pulse lengths used to create this irradiance. Because of the high intensities, all phasematched third-order processes must be included in the model. Somewhat surprisingly, unphasematched second-order interactions must also be included and can contribute significantly to the overall process. The short temporal pulse length, or alternatively, the large associated spectral bandwidth of the pulse, ultimately limit the coherence length in the nonlinear medium and thereby the achievable conversion efficiency.

After introducing the notation and terminology which will be used, the set of nonlinear wave equations describing the interaction of five distinct waves will be derived. Nonlinear optics is notorious for spurious constant factors which can creep in because of a lack of standardization of many definitions. Formulas for the effective nonlinear coupling coefficients for both second- and third-order processes will be given for all possible polarization combinations, including methods for their determination for biaxial crystals. The material acceptance bandwidths will be presented and discussed. Finally, the numerical method known as the beam propagation method and its implementation will be discussed.

4.1 Preliminaries

Nonlinear optics has suffered from a general lack of consistency of several key quantities, resulting in changes by factors of two as well as inconsistent signs in derivations presented by various authors. I will follow the conventions used by Butcher and Cotter⁷² throughout. The MKS system of units will be used, and absorption effects will be neglected at all levels. In this section, most of the important quantities and relations will be derived in order to carefully account for all relevant coefficients.

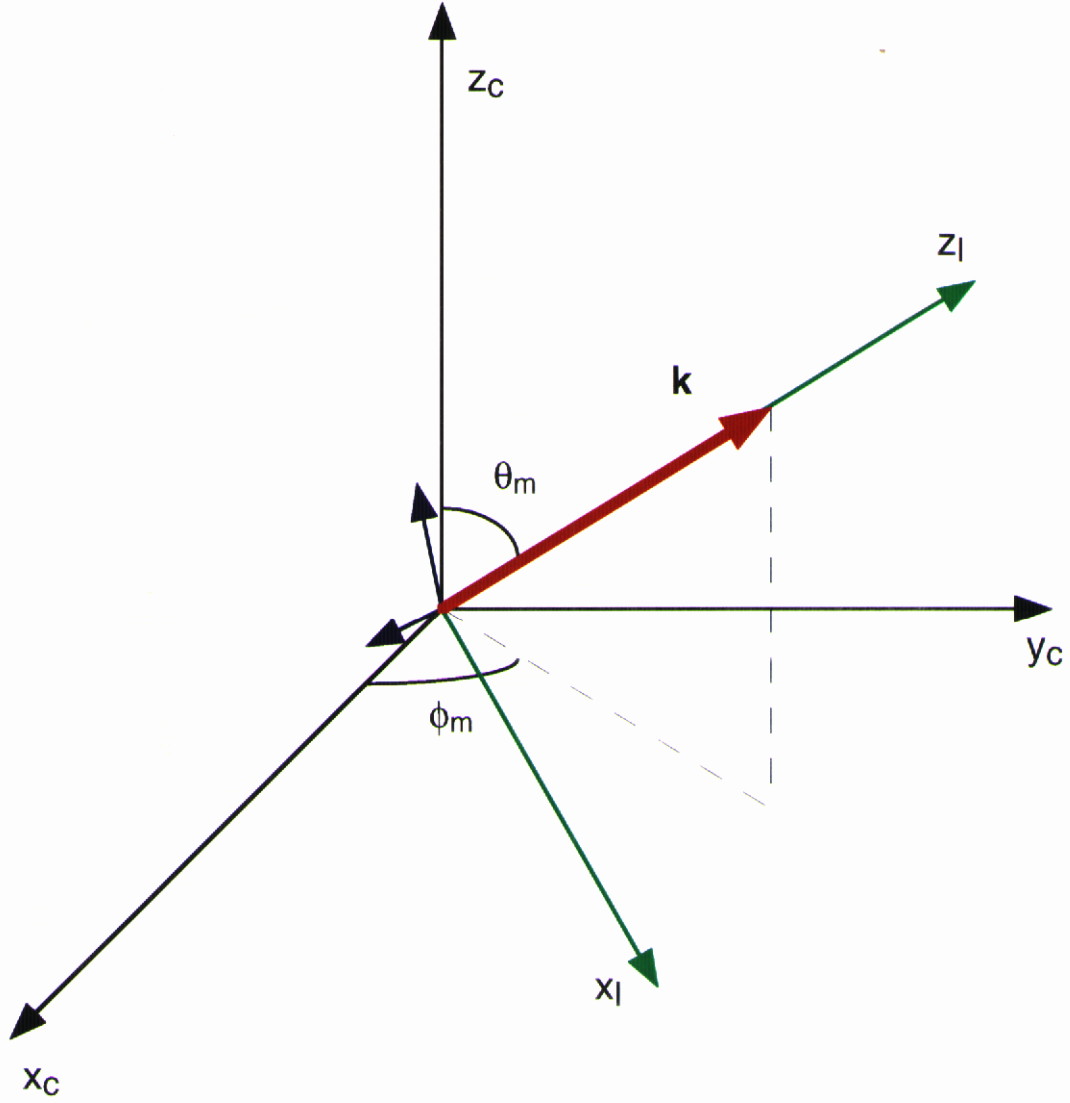


Figure 4.1: The coordinate systems. The crystal dielectric axes are denoted by the subscript c, and the lab axes are denoted by the subscript l. Both are right-handed coordinate systems.

4.1.1 Fourier transform pair

Throughout this work, the definition of the Fourier transform pair will be

$$f(t) = \frac{1}{2\pi} \int_{-\infty}^{\infty} F(\omega) e^{-i\omega t} d\omega = \int_{-\infty}^{\infty} F(2\pi\nu) e^{-i2\pi\nu t} d\nu \text{ and} \quad (4.5)$$

$$F(\omega) = \int_{-\infty}^{\infty} f(t) e^{i\omega t} dt. \quad (4.6)$$

This definition is used in order to be consistent with the standard representation of the rapidly-varying part of the electric field as $\exp(i(kz - \omega t))$. The Fourier transform of a function f will be represented as $\mathcal{F}[f]$ and the inverse transform will be $\mathcal{F}^{-1}[f]$.

4.1.2 Coordinate systems

When dealing with the propagation of beams through a crystalline medium, there are two coordinate systems that are of significance: the lab system which is defined by the beam propagating parallel to the z-axis and the crystal system which is defined by the dielectric axes (those which diagonalize the permeability tensor (see, for example, Nye⁷³)). The relationship between these two systems is shown in Fig. 4.1 where the beam propagates within the crystal at an angle θ_m (the phasematching angle) with respect to the crystal z-axis and an angle ϕ_m from the crystal x-axis. The lab x-axis is defined to lie in the plane containing z_c and \mathbf{k} and to be positive going away from z_c . The transformation from one system (crystal) to another (lab) is governed by the transformation matrix \mathbb{T}

$$\mathbb{T} = \begin{bmatrix} \cos \theta \cos \phi & \cos \theta \sin \phi & -\sin \theta \\ -\sin \phi & \cos \phi & 0 \\ \sin \theta \cos \phi & \sin \theta \sin \phi & \cos \theta \end{bmatrix} \quad (4.7)$$

4.1.3 Derivation of wave equation

The evolution of electromagnetic radiation is described by Maxwell's equations:

$$\nabla \times \mathbf{E}(\mathbf{x}, t) = -\frac{\partial \mathbf{B}(\mathbf{x}, t)}{\partial t} \quad (4.8)$$

$$\nabla \times \mathbf{H}(\mathbf{x}, t) = \frac{\partial \mathbf{D}(\mathbf{x}, t)}{\partial t} + \mathbf{J}(\mathbf{x}, t) \quad (4.9)$$

$$\nabla \cdot \mathbf{D}(\mathbf{x}, t) = \rho(\mathbf{x}, t), \text{ and} \quad (4.10)$$

$$\nabla \cdot \mathbf{B}(\mathbf{x}, t) = 0. \quad (4.11)$$

Here, \mathbf{E} is the electric field, \mathbf{D} is the electric displacement vector, \mathbf{H} is the magnetic field vector, \mathbf{B} is the magnetic induction vector, \mathbf{J} is the current density vector, and ρ is the free charge density. For the purposes of this work, all interactions will assumed to be within a nonmagnetic, dielectric material so that $\rho(\mathbf{x}, t) \equiv 0$, $\mathbf{J}(\mathbf{x}, t) \equiv 0$, and $\mathbf{B} = \mu_0 \mathbf{H}$. Taking the curl of Eq. (4.8) and substituting in Eq. (4.9) gives (using $\mu_0 = 1/(c^2 \epsilon_0)$)

$$\nabla \times \nabla \times \mathbf{E}(\mathbf{x}, t) = -\frac{1}{c^2 \epsilon_0} \frac{\partial^2 \mathbf{D}(\mathbf{x}, t)}{\partial t^2} \quad (4.12)$$

and then, using Eq. (4.1) and the identity $\nabla \times \nabla \times f = \nabla(\nabla \cdot f) - \nabla^2 f$,

$$\nabla^2 \mathbf{E}(\mathbf{x}, t) - \nabla(\nabla \cdot \mathbf{E}(\mathbf{x}, t)) = \frac{1}{c^2} \frac{\partial^2 \mathbf{E}(\mathbf{x}, t)}{\partial t^2} + \frac{1}{c^2 \epsilon_0} \frac{\partial^2 \mathbf{P}(\mathbf{x}, t)}{\partial t^2}. \quad (4.13)$$

The electric polarization can be represented by an expansion

$$\begin{aligned} \mathbf{P}(\mathbf{x}, t) &= \mathbf{P}^{(1)}(\mathbf{x}, t) + \mathbf{P}^{(2)}(\mathbf{x}, t) + \mathbf{P}^{(3)}(\mathbf{x}, t) + \dots \\ &= \mathbf{P}^{(1)}(\mathbf{x}, t) + \mathbf{P}^{\text{NL}}(\mathbf{x}, t) \end{aligned} \quad (4.14)$$

where, in perturbation theory, the terms $\mathbf{P}^{(j)}$ are proportional to the j th power of the electric field. Terms higher than third order will be neglected. Each of the polarization terms are related to the applied electric field $\mathbf{E}(\mathbf{x}, t)$ by higher order material electric response functions in a manner similar to Eq. (4.2). The second order polarization is given by

$$\mathbf{P}^{(2)}(\mathbf{x}, t) = \epsilon_0 \int_{-\infty}^{\infty} \int_{-\infty}^{\infty} \chi^{(2)}(\mathbf{x}, t - \tau_1, t - \tau_2) : \mathbf{E}(\mathbf{x}, \tau_1) \mathbf{E}(\mathbf{x}, \tau_2) d\tau_1 d\tau_2 \quad (4.15)$$

and the third order polarization is given by

$$\mathbf{P}^{(3)}(\mathbf{x}, t) = \epsilon_0 \int_{-\infty}^{\infty} \int_{-\infty}^{\infty} \int_{-\infty}^{\infty} \chi^{(3)}(\mathbf{x}, t - \tau_1, t - \tau_2, t - \tau_3) : \mathbf{E}(\mathbf{x}, \tau_1) \mathbf{E}(\mathbf{x}, \tau_2) \mathbf{E}(\mathbf{x}, \tau_3) d\tau_1 d\tau_2 d\tau_3. \quad (4.16)$$

These expressions can be simplified greatly if the response of the material to the applied field is assumed to be instantaneous as well as uniform throughout the material, i.e.

$$\chi^{(j)}(\mathbf{x}, t_1, \dots, t_j) = \chi^{(j)} \delta(t_1) \dots \delta(t_j). \quad (4.17)$$

The nonlinear polarizations then become simply

$$\mathbf{P}^{(j)}(\mathbf{x}, t) = \epsilon_0 \chi^{(j)} \mathbf{E}(\mathbf{x}, t) \dots \mathbf{E}(\mathbf{x}, t). \quad (4.18)$$

This approximation is equivalent to assuming that there is no dispersion in the electric susceptibilities over the pulse spectrum. While this assumption may begin to break down for pulses shorter than 50 fs, the nonlinear susceptibilities are generally not known accurately enough to begin to account for the dispersion that does exist. With this simplification, Eq. (4.13) becomes

$$\begin{aligned} & \nabla^2 \mathbf{E}(\mathbf{x}, t) - \nabla(\nabla \cdot \mathbf{E}(\mathbf{x}, t)) \\ &= \frac{1}{c^2 \epsilon_0} \frac{\partial^2 (\epsilon_0 \mathbf{E}(\mathbf{x}, t) + \mathbf{P}^{(1)}(\mathbf{x}, t))}{\partial t^2} + \frac{1}{c^2 \epsilon_0} \frac{\partial^2 \mathbf{P}^{\text{NL}}(\mathbf{x}, t)}{\partial t^2} \text{ or} \\ &= \frac{1}{c^2 \epsilon_0} \frac{\partial^2 \mathbf{D}^{(1)}(\mathbf{x}, t)}{\partial t^2} + \frac{1}{c^2 \epsilon_0} \frac{\partial^2 \mathbf{P}^{\text{NL}}(\mathbf{x}, t)}{\partial t^2} \end{aligned} \quad (4.19)$$

where

$$\mathbf{D}^{(1)}(\mathbf{x}, t) = \int_{-\infty}^{\infty} \epsilon_0(\tau) \cdot \mathbf{E}(\mathbf{x}, t - \tau) d\tau. \quad (4.20)$$

is the linear electric displacement.

It is now convenient to make an assumption concerning the fields themselves. All fields $\mathbf{E}(\mathbf{x}, t)$ will be assumed to be of the form

$$\mathbf{E}(\mathbf{x}, t) = \frac{1}{2} \left[\mathbf{A}(\mathbf{x}, t) e^{i(k_0 z - \omega_0 t)} + \text{c.c.} \right] \quad (4.21)$$

where $\mathbf{A}(\mathbf{x}, t)$ is a slowly-varying complex amplitude in time and space with center frequency ω_0 and center k-vector $k_0 \hat{\mathbf{k}}$ (i.e. the wave is propagating in the +z direction). The

same form is assumed for the linear and nonlinear polarizations as well. The laplacian operator on the left-hand side of Eq. (4.19) can be written as

$$\nabla^2 \mathbf{E}(\mathbf{x}, t) = \frac{\partial^2 \mathbf{E}(\mathbf{x}, t)}{\partial z^2} + \nabla_{\perp}^2 \mathbf{E}(\mathbf{x}, t) \quad (4.22)$$

$$= \frac{1}{2} \left[\frac{\partial^2 \mathbf{A}(\mathbf{x}, t)}{\partial z^2} + 2ik_0 \frac{\partial \mathbf{A}(\mathbf{x}, t)}{\partial z} - k_0^2 \mathbf{A}(\mathbf{x}, t) + \nabla_{\perp}^2 \mathbf{A}(\mathbf{x}, t) \right] e^{i(k_0 z - \omega_0 t)} + \text{c.c.} \quad (4.23)$$

Linear dispersion effects

Let us now focus on the linear electric displacement $\mathbf{D}^{(1)}$. First, expand the slowly-varying electric field amplitude as a Fourier series about a point in time τ :

$$\begin{aligned} \mathbf{A}(\mathbf{x}, t) &= \mathbf{A}(\mathbf{x}, t') + \frac{\partial \mathbf{A}(\mathbf{x}, t)}{\partial t} \Big|_{t'} (t - t') + \frac{1}{2!} \frac{\partial^2 \mathbf{A}(\mathbf{x}, t)}{\partial t^2} \Big|_{t'} (t - t')^2 + \dots \text{ or} \\ \mathbf{A}(\mathbf{x}, t' - \tau) &= \mathbf{A}(\mathbf{x}, t') - \frac{\partial \mathbf{A}(\mathbf{x}, \tau)}{\partial \tau} \Big|_{t'} \tau + \frac{1}{2!} \frac{\partial^2 \mathbf{A}(\mathbf{x}, \tau)}{\partial \tau^2} \Big|_{t'} \tau^2 - \dots \end{aligned} \quad (4.24)$$

with t becoming $t' - \tau$. When Eq. (4.24) is substituted into Eq. (4.20), the resulting expression can be separated into parts \mathbf{D}_j such that $\mathbf{D}^{(1)}(\mathbf{x}, t) = \sum_{j=1}^n \mathbf{D}_j$, according to the order of the derivative of $\mathbf{A}(\mathbf{x}, t)$. These parts then become

$$\begin{aligned} \mathbf{D}_1 &= \frac{1}{2} \int_{-\infty}^{\infty} \epsilon(\mathbf{x}, \tau) \cdot \mathbf{A}(\mathbf{x}, t) e^{i(k_0 z - \omega_0(t - \tau))} d\tau + \text{c.c.} \\ &= \frac{1}{2} \int_{-\infty}^{\infty} \epsilon(\mathbf{x}, \tau) e^{i\omega_0 \tau} d\tau \cdot \mathbf{A}(\mathbf{x}, t) e^{i(k_0 z - \omega_0 t)} + \text{c.c.} \\ &= \frac{1}{2} \epsilon(\mathbf{x}, \omega_0) \cdot \mathbf{A}(\mathbf{x}, t) e^{i(k_0 z - \omega_0 t)} + \text{c.c.}, \end{aligned} \quad (4.25)$$

$$\begin{aligned} \mathbf{D}_2 &= -\frac{1}{2} \int_{-\infty}^{\infty} \epsilon(\mathbf{x}, \tau) \cdot \frac{\partial \mathbf{A}(\mathbf{x}, \tau)}{\partial \tau} \Big|_t \tau e^{i(k_0 z - \omega_0(t - \tau))} d\tau + \text{c.c.} \\ &= -\frac{1}{2} \int_{-\infty}^{\infty} \epsilon(\mathbf{x}, \tau) \tau e^{i\omega_0 \tau} d\tau \cdot \frac{\partial \mathbf{A}(\mathbf{x}, \tau)}{\partial \tau} \Big|_t e^{i(k_0 z - \omega_0 t)} + \text{c.c.} \\ &= i \frac{1}{2} \frac{\partial}{\partial \omega_0} \int_{-\infty}^{\infty} \epsilon(\mathbf{x}, \tau) e^{i\omega_0 \tau} d\tau \cdot \frac{\partial \mathbf{A}(\mathbf{x}, \tau)}{\partial \tau} \Big|_t e^{i(k_0 z - \omega_0 t)} + \text{c.c.} \\ &= i \frac{1}{2} \frac{\partial \epsilon(\omega)}{\partial \omega} \Big|_{\omega_0} \cdot \frac{\partial \mathbf{A}(\mathbf{x}, t)}{\partial t} e^{i(k_0 z - \omega_0 t)} + \text{c.c.}, \end{aligned} \quad (4.26)$$

$$\begin{aligned}
\mathbf{D}_3 &= \frac{1}{2} \int_{-\infty}^{\infty} \epsilon(\mathbf{x}, \tau) \cdot \frac{1}{2!} \frac{\partial^2 \mathbf{A}(\mathbf{x}, \tau)}{\partial \tau^2} \Big|_t \tau^2 e^{i(k_0 z - \omega_0(t-\tau))} d\tau + \text{c.c.} \\
&= \frac{1}{2 \cdot 2!} \int_{-\infty}^{\infty} \epsilon(\mathbf{x}, \tau) \tau^2 e^{i\omega_0 \tau} d\tau \cdot \frac{\partial^2 \mathbf{A}(\mathbf{x}, \tau)}{\partial \tau^2} \Big|_t e^{i(k_0 z - \omega_0 t)} + \text{c.c.} \\
&= -\frac{1}{2 \cdot 2!} \frac{\partial^2}{\partial \omega_0^2} \int_{-\infty}^{\infty} \epsilon(\mathbf{x}, \tau) e^{i\omega_0 \tau} d\tau \cdot \frac{\partial^2 \mathbf{A}(\mathbf{x}, t)}{\partial t^2} e^{i(k_0 z - \omega_0 t)} + \text{c.c.} \\
&= -\frac{1}{2 \cdot 2!} \frac{\partial^2 \epsilon(\omega)}{\partial \omega^2} \Big|_{\omega_0} \cdot \frac{\partial^2 \mathbf{A}(\mathbf{x}, t)}{\partial t^2} e^{i(k_0 z - \omega_0 t)} + \text{c.c.}, \tag{4.27}
\end{aligned}$$

and similarly,

$$\mathbf{D}_{n+1} = \frac{i^n}{2n!} \frac{\partial^n \epsilon(\mathbf{x}, \omega)}{\partial \omega^n} \Big|_{\omega_0} \cdot \frac{\partial^n \mathbf{A}(\mathbf{x}, t)}{\partial t^n} e^{i(k_0 z - \omega_0 t)} + \text{c.c.} \tag{4.28}$$

Now let

$$\mathcal{D} = -\mu_0 \frac{\partial^2 \mathbf{D}(\mathbf{x}, t)}{\partial t^2}. \tag{4.29}$$

If one then inserts these expressions for \mathbf{D}_n into \mathcal{D} , one obtains the following:

$$\begin{aligned}
\mathcal{D} &= -\mu_0 \frac{\partial^2}{\partial t^2} (\mathbf{D}_1 + \mathbf{D}_2 + \mathbf{D}_3 + \dots) \\
&= -\frac{\mu_0}{2} \left[\epsilon(\omega_0) \cdot \left\{ \frac{\partial^2 \mathbf{A}(\mathbf{x}, t)}{\partial t^2} - 2i\omega_0 \frac{\partial \mathbf{A}(\mathbf{x}, t)}{\partial t} - \omega_0^2 \mathbf{A}(\mathbf{x}, t) \right\} \right. \\
&\quad + i \frac{\partial \epsilon(\omega)}{\partial \omega} \Big|_{\omega_0} \cdot \left\{ \frac{\partial^3 \mathbf{A}(\mathbf{x}, t)}{\partial t^3} - 2i\omega_0 \frac{\partial^2 \mathbf{A}(\mathbf{x}, t)}{\partial t^2} - \omega_0^2 \frac{\partial \mathbf{A}(\mathbf{x}, t)}{\partial t} \right\} \\
&\quad - \frac{1}{2!} \frac{\partial^2 \epsilon(\omega)}{\partial \omega^2} \Big|_{\omega_0} \cdot \left\{ \frac{\partial^4 \mathbf{A}(\mathbf{x}, t)}{\partial t^4} - 2i\omega_0 \frac{\partial^3 \mathbf{A}(\mathbf{x}, t)}{\partial t^3} - \omega_0^2 \frac{\partial^2 \mathbf{A}(\mathbf{x}, t)}{\partial t^2} \right\} \\
&\quad \left. + \dots \right] e^{i(k_0 z - \omega_0 t)} + \text{c.c.} \tag{4.30}
\end{aligned}$$

Grouping this according to the order of the temporal derivative gives

$$\begin{aligned}
\mathcal{D} &= \frac{\mu_0}{2} \left[-\omega_0^2 \epsilon(\omega_0) \cdot \mathbf{A}(\mathbf{x}, t) - i \left\{ 2\omega_0 \epsilon(\omega_0) + \omega_0^2 \frac{\partial \epsilon(\omega)}{\partial \omega} \Big|_{\omega_0} \right\} \cdot \frac{\partial \mathbf{A}(\mathbf{x}, t)}{\partial t} \right. \\
&\quad + \left\{ \epsilon(\omega_0) + 2\omega_0 \frac{\partial \epsilon(\omega)}{\partial \omega} \Big|_{\omega_0} + \frac{\omega_0^2}{2!} \frac{\partial^2 \epsilon(\omega)}{\partial \omega^2} \Big|_{\omega_0} \right\} \cdot \frac{\partial^2 \mathbf{A}(\mathbf{x}, t)}{\partial t^2} \\
&\quad \left. + \dots \right] e^{i(k_0 z - \omega_0 t)} + \text{c.c.} \tag{4.31}
\end{aligned}$$

For convenience, let us now only work with one of the three fields j at a time as well as transform (4.31) into a scalar equation. This is done by letting $\epsilon_0 n^2(\omega) A(\mathbf{x}, t) =$

$\hat{\mathbf{e}} \cdot (\boldsymbol{\epsilon}(\omega) \cdot \hat{\mathbf{e}} A(\mathbf{x}, t))$ where $\hat{\mathbf{e}}$ is a unit vector in the direction of $\mathbf{A}(\mathbf{x}, t)$, i.e. $\mathbf{A}(\mathbf{x}, t) = \hat{\mathbf{e}} A(\mathbf{x}, t)$.

This gives

$$\begin{aligned} \hat{\mathbf{e}} \cdot \mathcal{D} = & -\frac{1}{2c^2} \left[-\omega_0^2 n^2(\omega_0) A(\mathbf{x}, t) - i \left\{ 2\omega_0 n^2(\omega_0) + \omega_0^2 \frac{\partial n^2(\omega)}{\partial \omega} \Big|_{\omega_0} \right\} \frac{\partial A(\mathbf{x}, t)}{\partial t} \right. \\ & + \left\{ n^2(\omega_0) + 2\omega_0 \frac{\partial n^2(\omega)}{\partial \omega} \Big|_{\omega_0} + \frac{\omega_0^2}{2!} \frac{\partial^2 n^2(\omega)}{\partial \omega^2} \Big|_{\omega_0} \right\} \frac{\partial^2 A(\mathbf{x}, t)}{\partial t^2} \\ & \left. + \dots \right] e^{i(k_0 z - \omega_0 t)} + \text{c.c.} \end{aligned} \quad (4.32)$$

Observing that

$$\frac{n(\omega_0)\omega_0}{c} = k_0, \quad (4.33)$$

$$2\omega_0 n^2(\omega_0) + \omega_0^2 \frac{\partial n^2(\omega)}{\partial \omega} \Big|_{\omega_0} = 2c^2 k_0 \frac{\partial k(\omega)}{\partial \omega} \Big|_{\omega_0}, \text{ and} \quad (4.34)$$

$$n^2(\omega_0) + 2\omega_0 \frac{\partial n^2(\omega)}{\partial \omega} \Big|_{\omega_0} + \frac{\omega_0^2}{2!} \frac{\partial^2 n^2(\omega)}{\partial \omega^2} \Big|_{\omega_0} = c^2 \left[\left(\frac{\partial k(\omega)}{\partial \omega} \Big|_{\omega_0} \right)^2 + k_0 \frac{\partial^2 k(\omega)}{\partial \omega^2} \Big|_{\omega_0} \right], \quad (4.35)$$

one can arrange (4.32) in the following form

$$\begin{aligned} \hat{\mathbf{e}} \cdot \mathcal{D} = & \frac{1}{2} \left[k_0^2 A(\mathbf{x}, t) + 2ik_0 \frac{\partial k(\omega)}{\partial \omega} \Big|_{\omega_0} \frac{\partial A(\mathbf{x}, t)}{\partial t} \right. \\ & \left. - \left[\left(\frac{\partial k(\omega)}{\partial \omega} \Big|_{\omega_0} \right)^2 + k_0 \frac{\partial^2 k(\omega)}{\partial \omega^2} \Big|_{\omega_0} \right] \frac{\partial^2 A(\mathbf{x}, t)}{\partial t^2} \right] e^{i(k_0 z - \omega_0 t)} + \text{c.c.} \end{aligned} \quad (4.36)$$

$$\begin{aligned} = & \frac{1}{2} \left[k_0^2 A(\mathbf{x}, t) + 2ik_0 \beta_1 \frac{\partial A(\mathbf{x}, t)}{\partial t} \right. \\ & \left. - (\beta_1^2 + k_0 \beta_2) \frac{\partial^2 A(\mathbf{x}, t)}{\partial t^2} \right] e^{i(k_0 z - \omega_0 t)} + \text{c.c.} \end{aligned} \quad (4.37)$$

Here, the quantities β_j are defined as

$$\beta_1 = \frac{\partial k(\omega)}{\partial \omega} \Big|_{\omega_0} \text{ and} \quad (4.38)$$

$$\beta_2 = \frac{\partial^2 k(\omega)}{\partial \omega^2} \Big|_{\omega_0}. \quad (4.39)$$

Eqs. (4.37) and (4.23) can then be substituted back into the original wave equation

(4.19), taking the dot product of $\hat{\mathbf{e}}$ with both sides of (4.19). The result is

$$\left(\frac{\partial^2 A(\mathbf{x}, t)}{\partial z^2} - \beta_1^2 \frac{\partial^2 A(\mathbf{x}, t)}{\partial t^2} \right)$$

$$\begin{aligned}
& + 2ik_0 \frac{\partial A(\mathbf{x}, t)}{\partial z} + \nabla_{\perp}^2 A(\mathbf{x}, t) - 2 \left[\hat{\mathbf{e}} \cdot \nabla (\nabla \cdot \mathbf{E}(\mathbf{x}, t)) e^{-i(k_0 z - \omega_0 t)} \right] \\
& = -2ik_0 \beta_1 \frac{\partial A(\mathbf{x}, t)}{\partial t} + k_0 \beta_2 \frac{\partial^2 A(\mathbf{x}, t)}{\partial t^2} - \frac{\omega_0^2}{c^2 \epsilon_0} \hat{\mathbf{e}} \cdot \mathbf{P}_{\omega}^{\text{NL}}(\mathbf{x}, t). \tag{4.40}
\end{aligned}$$

Here, as mentioned before, the nonlinear polarization has been assumed to be of the form

$$\mathbf{P}^{\text{NL}}(\mathbf{x}, t) = \frac{1}{2} (\mathbf{P}_{\omega}^{\text{NL}}(\mathbf{x}, t) e^{i(k_0 z - \omega_0 t)} + \text{c.c.}), \tag{4.41}$$

and that

$$|\omega^2 \mathbf{P}_{\omega}^{\text{NL}}(\mathbf{x}, t)| \gg \left| \omega \frac{\partial \mathbf{P}_{\omega}^{\text{NL}}(\mathbf{x}, t)}{\partial t} \right|, \text{ and } \left| \frac{\partial^2 \mathbf{P}_{\omega}^{\text{NL}}(\mathbf{x}, t)}{\partial t^2} \right|. \tag{4.42}$$

Finally, in the limit that the envelope function $A(\mathbf{x}, t)$ variation is small over a wavelength (slowly-varying envelope approximation), a further simplification can be made. Under this condition, which is the same as neglecting any backward-propagating wave,^{74–77} for a wave traveling at velocity $1/\beta_1$,

$$\frac{\partial A(\mathbf{x}, t)}{\partial z} + \beta_1 \frac{\partial A(\mathbf{x}, t)}{\partial t} \simeq 0 \tag{4.43}$$

or

$$\frac{\partial^2 A(\mathbf{x}, t)}{\partial z^2} - \beta_1^2 \frac{\partial^2 A(\mathbf{x}, t)}{\partial t^2} \simeq 0. \tag{4.44}$$

Eq. (4.40) is then

$$\begin{aligned}
& 2ik_0 \frac{\partial A(\mathbf{x}, t)}{\partial z} + \nabla_{\perp}^2 A(\mathbf{x}, t) - 2 \left[\hat{\mathbf{e}} \cdot \nabla (\nabla \cdot \mathbf{E}(\mathbf{x}, t)) e^{-i(k_0 z - \omega_0 t)} \right] \\
& = -2ik_0 \beta_1 \frac{\partial A(\mathbf{x}, t)}{\partial t} + k_0 \beta_2 \frac{\partial^2 A(\mathbf{x}, t)}{\partial t^2} - \frac{\omega_0^2}{c^2 \epsilon_0} \hat{\mathbf{e}} \cdot \mathbf{P}_{\omega}^{\text{NL}}(\mathbf{x}, t). \tag{4.45}
\end{aligned}$$

For envelope variations on the order of the pulse length τ_p , the slowly-varying envelope approximation will be valid for $c\tau_p \gg \lambda$. Taking 10λ as the threshold,⁷⁸ Eq. (4.45) should hold for pulse lengths longer than approximately 30 fs. It should be also noted that this approximation will also fail if the nonlinear coupling is strong enough to cause significant amplification over the scale of a few wavelengths.

Spatial walkoff

The term involving the divergence of the electric field in Eq. (4.45) is nonzero since the electric displacement and electric field are not, in general, parallel. This also is manifest in the Poynting vector \mathbf{S} and wave vector not being parallel in general. The displacement is perpendicular to \mathbf{k} and has two orthogonal polarizations. The field is perpendicular to \mathbf{S} and its polarizations are not necessarily orthogonal. This is true for extraordinary waves in uniaxial crystals and for any polarization direction in biaxial crystals. This gives rise to the phenomenon of spatial walkoff where the extraordinary waves travel in a different direction than \mathbf{k} . After a long enough distance, the two beams will no longer overlap.

For most crystals, the difference between the propagation directions of ordinary and extraordinary waves is on the order of a few degrees. For nanosecond laser pulses propagating in crystals of lengths of several centimeters, the effect can be significant if the beam sizes (or feature sizes) are of the order of a few millimeters. However, for ultrashort pulses, the crystal lengths will be on the order of a few millimeters or less, and so this effect will be much less important. Nonetheless, it will be included for completeness. For uniaxial crystals, this term becomes approximately⁷⁹

$$\nabla(\nabla \cdot \mathbf{E}(\mathbf{x}, t)) \cong -2i\mathbf{k}_0\rho \frac{\partial \mathbf{E}(\mathbf{x}, t)}{\partial x} \quad (4.46)$$

with

$$\rho = \frac{1}{n_e(\omega, \theta)} \left. \frac{\partial n_e(\omega, \theta)}{\partial \theta} \right|_{\theta=\theta_m} \quad (4.47)$$

being the tangent of the walkoff angle.

Nonlinear polarization

Eq. (4.46) can then be substituted into (4.45) giving

$$\begin{aligned} & 2ik_0 \frac{\partial A(\mathbf{x}, t)}{\partial z} + \nabla_{\perp}^2 A(\mathbf{x}, t) + 2ik_0 \rho \frac{\partial A(\mathbf{x}, t)}{\partial x} \\ &= -2ik_0 \beta_1 \frac{\partial A(\mathbf{x}, t)}{\partial t} + k_0 \beta_2 \frac{\partial^2 A(\mathbf{x}, t)}{\partial t^2} - \frac{\omega_0^2}{c^2 \epsilon_0} \hat{\mathbf{e}} \cdot \mathbf{P}_{\omega}^{\text{NL}}(\mathbf{x}, t). \end{aligned} \quad (4.48)$$

The final part of the puzzle is to determine the form for $\mathbf{P}_{\omega}^{\text{NL}}(\mathbf{x}, t)$, including both second- and third-order contributions. The general process for determining the precise form for this term is to assume that the total electric field in the material is a sum over some set of frequency components, i.e.

$$\mathbf{E}(\mathbf{x}, t) = \frac{1}{2} \sum_{j=1}^n \left[A_j(\mathbf{x}, t) e^{i(k_j z - \omega_j t)} + \text{c.c.} \right] \quad (4.49)$$

with the central frequency of each component field being at ω_j , etc. When this form of $\mathbf{E}(\mathbf{x}, t)$ is inserted into the definitions for $\mathbf{P}^{(j)}$ (Eq. (4.18)), many terms are obtained related to all possible interactions for that set of frequency components. All of the terms involved in THG will be given in the next section.

4.2 Coupled wave equations

The nonlinear partial differential equation shown in Eq. (4.48) describes the evolution of a wave at a given polarization direction with a narrow frequency spread about some central wavelength. In reality, there are n of these equations for each possible polarization direction and central frequency that will be involved in the interaction, and n will usually be a very large number. However, for efficient transfer of energy from one wave to another to take place, the waves must be in phase throughout the interaction region. This phase-matching requirement is normally satisfied by using birefringent crystals to compensate

for the difference in the phase velocities of the different waves in the solid. For second order interactions, there are basically three interaction types, classified as¹⁸

$$\begin{array}{ll} \text{Type I} & \text{slow} + \text{slow} \rightarrow \text{fast} \\ \text{Type II} & \text{fast} + \text{slow} \rightarrow \text{fast} \\ \text{Type III} & \text{slow} + \text{fast} \rightarrow \text{fast} \end{array}$$

where the order is taken to be from the longest wavelength to the shortest. The terms fast and slow refer to a wave polarized along the “fast” axis (lowest refractive index) or “slow” axis (largest index). For example, for negative uniaxial crystals, the fast axis is the extraordinary axis and the opposite for positive uniaxial crystals. The notation using fast (f) or slow (s) to designate the indices of refraction is more general and holds equally well for biaxial crystals.

For third order interactions, there are now seven, i.e. $(2^3 - 1)$, possible combinations. However, our concern will be restricted to harmonic generation (all input waves of same wavelength) so that for third order interactions, the interactions will be specified as

$$\begin{array}{ll} \text{Type I} & \text{slow} + \text{slow} + \text{slow} \rightarrow \text{fast} \\ \text{Type II} & \text{slow} + \text{slow} + \text{fast} \rightarrow \text{fast} \\ \text{Type III} & \text{slow} + \text{fast} + \text{fast} \rightarrow \text{fast} \end{array}$$

where the order on the left side of the arrow is unimportant (the three waves are of the same wavelength).

Assuming that only third harmonic generation is phasematched, the significant waves will be the fundamental (with both possible polarizations) and the third harmonic. It will be seen that the waves at the second harmonic (both polarizations) will also become important and need to be included. These will be denoted using subscripts defined in the following way:

- 1: 1ω (slow polarization),
- 2: 1ω (fast polarization),
- 3: 2ω (slow polarization),
- 4: 2ω (fast polarization), and
- 5: 3ω (fast polarization).

This means that $\omega_5 = 3\omega_0$, $\omega_3 = \omega_4 = 2\omega_0$, and $\omega_1 = \omega_2 = \omega_0$. The set of wave equations governing the total interaction will then be

$$\begin{aligned}
\frac{\partial A_1}{\partial z} = & -\beta_{11} \frac{\partial A_1}{\partial t} - \frac{i}{2} \beta_{21} \frac{\partial^2 A_1}{\partial t^2} + \frac{i}{2k_1} \nabla_{\perp}^2 A_1 - \rho_1(\theta_m) \frac{\partial A_1}{\partial x} \\
& + \frac{i\omega_1}{n_1 c} \left[\frac{3C_1^{\text{SPM}}}{2} |A_1|^2 A_1 + 3C_1^{\text{XPM}} |A_5|^2 A_1 + 3C_2^{\text{XPM}} |A_2|^2 A_1 \right] \\
& + \frac{i\omega_1}{n_1 c} \left[d_1 A_3 A_1^* e^{i\Delta k_1 z} + d_3 A_4 A_1^* e^{i\Delta k_3 z} + d_2 A_3 A_2^* e^{i\Delta k_2 z} + d_4 A_4 A_2^* e^{i\Delta k_4 z} \right. \\
& + d_5 A_5 A_4^* e^{i\Delta k_5 z} + d_7 A_5 A_3^* e^{i\Delta k_7 z} \\
& \left. + 3C_1 A_5 A_2^* A_1^* e^{i\Delta k_9 z} + \frac{3C_2}{2} A_5 A_1^{*2} e^{i\Delta k_{10} z} \right] \tag{4.50}
\end{aligned}$$

$$\begin{aligned}
\frac{\partial A_2}{\partial z} = & -\beta_{12} \frac{\partial A_2}{\partial t} - \frac{i}{2} \beta_{22} \frac{\partial^2 A_2}{\partial t^2} + \frac{i}{2k_2} \nabla_{\perp}^2 A_2 - \rho_2(\theta_m) \frac{\partial A_2}{\partial x} \\
& + \frac{i\omega_2}{n_2 c} \left[\frac{3C_2^{\text{SPM}}}{2} |A_2|^2 A_2 + 3C_3^{\text{XPM}} |A_5|^2 A_2 + 3C_4^{\text{XPM}} |A_1|^2 A_2 \right] \\
& + \frac{i\omega_2}{n_2 c} \left[d_2 A_3 A_1^* e^{i\Delta k_2 z} + d_4 A_4 A_1^* e^{i\Delta k_4 z} + d_6 A_5 A_4^* e^{i\Delta k_6 z} \right. \\
& \left. + d_8 A_5 A_3^* e^{i\Delta k_8 z} + \frac{3C_1}{2} A_5 A_1^{*2} e^{i\Delta k_9 z} \right] \tag{4.51}
\end{aligned}$$

$$\begin{aligned}
\frac{\partial A_3}{\partial z} = & -\beta_{13} \frac{\partial A_3}{\partial t} - \frac{i}{2} \beta_{23} \frac{\partial^2 A_3}{\partial t^2} + \frac{i}{2k_3} \nabla_{\perp}^2 A_3 - \rho_3(\theta_m) \frac{\partial A_3}{\partial x} \\
& + \frac{i\omega_3}{n_3 c} \left[\frac{3C_3^{\text{SPM}}}{2} |A_3|^2 A_3 + 3C_5^{\text{XPM}} |A_5|^2 A_3 + 3C_6^{\text{XPM}} |A_2|^2 A_3 + 3C_7^{\text{XPM}} |A_1|^2 A_3 \right] \\
& + \frac{i\omega_3}{n_3 c} \left[\frac{d_1}{2} A_1^2 e^{-i\Delta k_1 z} + d_2 A_2 A_1 e^{-i\Delta k_2 z} + d_7 A_5 A_1^* e^{i\Delta k_7 z} \right. \\
& \left. + d_8 A_5 A_2^* e^{i\Delta k_8 z} \right] \tag{4.52}
\end{aligned}$$

$$\begin{aligned}
\frac{\partial A_4}{\partial z} = & -\beta_{14} \frac{\partial A_4}{\partial t} - \frac{i}{2} \beta_{24} \frac{\partial^2 A_4}{\partial t^2} + \frac{i}{2k_4} \nabla_{\perp}^2 A_4 - \rho_4(\theta_m) \frac{\partial A_4}{\partial x} \\
& + \frac{i\omega_4}{n_4 c} \left[\frac{3C_3^{\text{SPM}}}{2} |A_4|^2 A_4 + 3C_8^{\text{XPM}} |A_5|^2 A_4 + 3C_9^{\text{XPM}} |A_2|^2 A_4 + 3C_{10}^{\text{XPM}} |A_1|^2 A_4 \right] \\
& + \frac{i\omega_4}{n_4 c} \left[\frac{d_3}{2} A_1^2 e^{-i\Delta k_3 z} + d_4 A_2 A_1 e^{-i\Delta k_4 z} + d_5 A_5 A_1^* e^{i\Delta k_5 z} \right. \\
& \left. + d_6 A_5 A_2^* e^{i\Delta k_6 z} \right] \tag{4.53}
\end{aligned}$$

$$\begin{aligned}
\frac{\partial A_5}{\partial z} = & -\beta_{15} \frac{\partial A_5}{\partial t} - \frac{i}{2} \beta_{25} \frac{\partial^2 A_5}{\partial t^2} + \frac{i}{2k_5} \nabla_{\perp}^2 A_5 - \rho_5(\theta_m) \frac{\partial A_5}{\partial x} \\
& + \frac{i\omega_5}{n_5 c} \left[\frac{3C_5^{\text{SPM}}}{2} |A_5|^2 A_5 + 3C_{11}^{\text{XPM}} |A_2|^2 A_5 + 3C_{12}^{\text{XPM}} |A_1|^2 A_5 \right] \\
& + \frac{i\omega_5}{n_5 c} \left[d_5 A_4 A_1 e^{-i\Delta k_5 z} + d_6 A_4 A_2 e^{-i\Delta k_6 z} + d_7 A_3 A_1 e^{-i\Delta k_7 z} \right]
\end{aligned}$$

$$+ d_8 A_3 A_2 e^{-i\Delta k_8 z} + \frac{3C_1}{2} A_1^2 A_2 e^{-i\Delta k_9 z} + \frac{C_2}{2} A_1^3 e^{-i\Delta k_{10} z} \Big] \quad (4.54)$$

In these equations, Δk_j are defined as

$$\Delta k_1 = k_3 - 2k_1 \quad (4.55)$$

$$\Delta k_2 = k_3 - k_1 - k_2 \quad (4.56)$$

$$\Delta k_3 = k_4 - 2k_1 \quad (4.57)$$

$$\Delta k_4 = k_4 - k_1 - k_2 \quad (4.58)$$

$$\Delta k_5 = k_5 - k_4 - k_1 \quad (4.59)$$

$$\Delta k_6 = k_5 - k_4 - k_2 \quad (4.60)$$

$$\Delta k_7 = k_5 - k_3 - k_1 \quad (4.61)$$

$$\Delta k_8 = k_5 - k_3 - k_2 \quad (4.62)$$

$$\Delta k_9 = k_5 - 2k_1 - k_2 \quad (4.63)$$

$$\Delta k_{10} = k_5 - 3k_1 \quad (4.64)$$

The terms β_{1j} and β_{2j} are simply β_1 and β_2 for the j th wave. The coefficients d_j and C_j are the effective nonlinear coupling coefficients defined in terms of the nonlinear susceptibilities as

$$d = \hat{\mathbf{e}}_1 \cdot \chi^{(2)} : \hat{\mathbf{e}}_2 \hat{\mathbf{e}}_3 / 2 \quad (4.65)$$

and

$$C = \hat{\mathbf{e}}_1 \cdot \chi^{(3)} : \hat{\mathbf{e}}_2 \hat{\mathbf{e}}_3 \hat{\mathbf{e}}_4 / 4 \quad (4.66)$$

where $\hat{\mathbf{e}}_k$ represents a unit vector in the polarization direction of the k th wave in the order given for Δk_j above (see Tables 4.1–4.2). The factors of 1/2 and 3 appearing in Eqs. (4.54–4.50) are due to the degeneracy in polarization and wavelength that appears in some of the terms (see, for example, pg. 26 of Ref. 72). In Eqs. (4.54), (4.51), and

(4.50), the contribution due to cross-phase modulation by the second harmonic wave has been neglected since this wave will never reach appreciable intensities. All interactions are assumed to be collinear, i.e. all waves propagate parallel to z axis in lab frame.

4.2.1 Cascaded third harmonic generation

It is instructive to simplify Eqs. (4.54-4.50) greatly in order to observe the effect of the second harmonic term. Ordinarily, such terms would be neglected because they are unphasematched. However, as has been shown previously,^{28,30,31,80-82} the fact that the third harmonic and fundamental waves are phasematched allows for the possibility of conversion to the third harmonic even with no third order coupling ($C_j = 0$) as illustrated in Fig. 4.2.

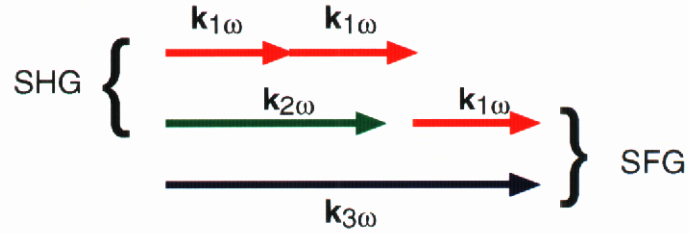


Figure 4.2: Illustration of processes involved in third harmonic generation via cascaded second-order processes. The first process is SHG ($\omega + \omega \rightarrow 2\omega$, indicated by the left brace) followed by sum frequency generation (SFG, $2\omega + \omega \rightarrow 3\omega$, indicated by the right brace). The space between $\mathbf{k}_{2\omega}$ and $\mathbf{k}_{1\omega}$ on the second line indicates a possible phase mismatch for SHG and SFG processes.

For low conversion, the fundamental waves can be assumed to be constant (no pump depletion, i.e. $\partial A_1/\partial z = \partial A_2/\partial z \simeq 0$), and, to a good approximation, the individual interactions can be assumed to be independent of each other. For illustration, let us examine Type I phasematching and consider the interaction oo-o + oo-e. Finally, let us neglect longitudinal and transverse spatial dependence of the pulse as well as self- ($C_j^{\text{SPM}} = 0$) and cross-phase modulation ($C_j^{\text{XPM}} = 0$). for simplicity. Eqs. (4.54-4.50)

reduce to

$$\frac{\partial A_1}{\partial z} = \frac{i\omega_1}{n_1 c} \left[d_1 A_3 A_1^* e^{i\Delta k_1 z} + d_7 A_5 A_3^* e^{i\Delta k_7 z} + \frac{3C_2}{2} A_5 A_1^{*2} e^{i\Delta k_{10} z} \right] \quad (4.67)$$

$$\simeq 0$$

$$\frac{\partial A_3}{\partial z} = \frac{i\omega_3}{n_3 c} \left[\frac{d_1}{2} A_1^2 e^{-i\Delta k_1 z} + d_7 A_5 A_1^* e^{i\Delta k_7 z} \right] \quad (4.68)$$

$$\frac{\partial A_5}{\partial z} = \frac{i\omega_5}{n_5 c} \left[d_7 A_3 A_1 e^{-i\Delta k_7 z} + \frac{C_2}{2} A_1^3 e^{-i\Delta k_{10} z} \right] \quad (4.69)$$

As before, A_3 is the electric field envelope for the second-harmonic wave polarized along the slow-axis, and A_5 is for the third-harmonic wave polarized along the fast-axis (e.g. $\omega_5 = 3\omega$, $\omega_3 = 2\omega$, and $\omega_1 = \omega$). If the third-order interaction is neglected for the moment as a further simplification ($C_2 = 0$) and Δk_{10} is set to 0, these equations can be solved analytically. Differentiating (4.68) and substituting (4.69) and (4.68) into the result gives a second order ODE with constant coefficients which is easily solved. The final solutions are

$$A_3(z) = \frac{i\omega_3}{2n_3 c \zeta} d_1 A_1^2 e^{i\Delta k_7 z/2} \sin \zeta z \quad (4.70)$$

and

$$A_5(z) = \frac{d_1 A_1^2}{2d_7 A_1^*} \left[e^{-i\Delta k_7 z/2} \left(\cos \zeta z + \frac{\Delta k_7}{2\zeta} \sin \zeta z \right) - 1 \right] \quad (4.71)$$

with

$$\zeta^2 = \frac{\omega_5 \omega_3}{n_5 n_3 c^2} d_7^2 |A_1|^2 + \left(\frac{\Delta k_7}{2} \right)^2. \quad (4.72)$$

When converted to intensities ($I = c\epsilon_0 n |A|^2/2$), these become

$$I_3(z) = \left(\frac{\omega_3}{n_1 c \zeta} \right)^2 \frac{d_1 I_1^2}{\epsilon_0 c n_3} \sin^2 \zeta z \quad (4.73)$$

and

$$I_5(z) = \frac{d_1^2 n_5 I_1}{4n_1 d_7^2} \left[1 + \cos^2 \zeta z + \frac{\Delta k_7^2}{4\zeta^2} \sin^2 \zeta z - 2 \cos \zeta z \cos \frac{\Delta k_7 z}{2} - \frac{\Delta k_7}{\zeta} \sin \zeta z \sin \frac{\Delta k_7 z}{2} \right]. \quad (4.74)$$

Although Eq. (4.74) appears to have only a linear dependence on the input fundamental intensity I_1 , a further approximation can be made for most circumstances, i.e. $\zeta \simeq \eta + \Delta k_7/2$ where

$$\eta = \frac{\omega_5 \omega_3}{n_5 n_3 c^2} \frac{d_7^2}{\Delta k_7} |A_1|^2 \quad (4.75)$$

with $\eta \ll \Delta k_7$. Eq. (4.74) then takes on the following form (again, no third-order coupling)

$$I_5(z) = \left(\frac{\omega_3}{n_3 c \Delta k_7} \right)^2 \frac{\omega_5^2 (d_1 d_7)^2}{n_5 n_1^3 \epsilon_0^2 c^4} I_1^3 z^2. \quad (4.76)$$

This compares with the standard solution for THG involving only the third order nonlinear susceptibility of (setting $d_j = 0$ in ((4.68) and 4.69))

$$I_5(z) = \frac{\omega_5^2 C_2^2}{n_5 n_1^3 \epsilon_0^2 c^4} I_1^3 z^2. \quad (4.77)$$

It is clear that these two solutions have the same form if one defines an effective nonlinear coefficient C_{eff} for the cascaded second-order process as

$$C_{\text{eff}} = \frac{\omega_3}{n_3 c \Delta k_7} d_1 d_7. \quad (4.78)$$

With the first term in the parentheses in Eq. (4.76) equal to roughly 15–30 for typical values of ω , n , and Δk and d_j being about 10^{-12} m/V, $C_{\text{eff}} \cong 10^{-23}$ – 10^{-22} m²/V². This is in the same range as is expected for the values of C due solely to the third-order susceptibility. In fact, Bloembergen³¹ states that the contributions from these two processes should be of the same order of magnitude.

Qiu and Penzkofer²⁸ proceed along a somewhat different path to arrive at the conclusion for specifically BBO. They do not assume perfect phasematching and present results indicating that the cascaded second-order process should also have the standard $\text{sinc}^2 \Delta k l / 2$ dependence on the THG phase mismatch. However, there are substantial errors in some of their approximations as well as in the expressions they give for the effective

Table 4.3: Possible interactions for THG. The polarization directions f/s are given in order of longest wavelength to shortest.

Phasematching Type	SHG int.	SFG int.	THG int.
Type I			
	ss→s	ss→f	
	ss→f	sf→f	
			sss →f
Type II			
	ss→s	fs→f	
	sf→s	ss→f	
	ss→f	ff→f	
	sf→f	sf→f	
			ssf→f
Type III			
	sf→s	fs→f	
	ff→s	ss→f	
	sf→f	ff→f	
	ff→f	sf→f	
			sff→f

nonlinear coefficients which invalidate their results. Nonetheless, the errors do not affect the qualitative conclusions which they draw,

4.2.2 Effective nonlinear coupling

It is necessary to account for all possible second order interactions, including ones not typically phase-matchable (Table 4.3). Of course, any of these interactions can take place for any phasematching configuration. However, for each phasematching Type, efficient THG will occur only for the interactions shown as a result of phasematching.

Because all possible polarization combinations can affect high intensity frequency conversion, it is necessary to calculate the effective nonlinear coefficient d_j for each of the crystal classes. For all of these, Kleinman symmetry will be assumed so that the second-order tensor d_{ijk} can be reduced to the standard symbol d_{im} . Here the m is determined as shown in Table 4.4. The numerals 1, 2, and 3 represent the x, y, and z components.

Table 4.4: Relationship between subscripts of d_{ijk} and d_{im} .

m	jk
1	11
2	22
3	33
4	23, 32
5	13, 31
6	12, 21

Table 4.5: Relationship between subscripts of C_{ijkl} and C_{im} .

m	jkl
1	111
2	222
3	333
4	233, 323, 332
5	223, 232, 322
6	133, 313, 331
7	113, 131, 311
8	122, 212, 221
9	112, 121, 211
0	123, 132, 213, 231, 312, 321

The term $\hat{\mathbf{e}}_2\hat{\mathbf{e}}_3$ from Eq. (4.65) is then given by the following matrix

$$\begin{bmatrix} e_{21}e_{31} \\ e_{22}e_{32} \\ e_{23}e_{33} \\ e_{22}e_{33} + e_{23}e_{32} \\ e_{21}e_{33} + e_{23}e_{31} \\ e_{21}e_{32} + e_{22}e_{31} \end{bmatrix} = \begin{bmatrix} e_{2x}e_{3x} \\ e_{2y}e_{3y} \\ e_{2z}e_{3z} \\ e_{2y}e_{3z} + e_{2z}e_{3y} \\ e_{2x}e_{3z} + e_{2z}e_{3x} \\ e_{2x}e_{3y} + e_{2y}e_{3x} \end{bmatrix}. \quad (4.79)$$

(It must be remembered here that the subscripts 2 and 3 in (4.79) only indicate position in Eq. (4.65) and do not directly refer to the five waves.) The third-order tensor C_{ijkl} can be similarly reduced to a 3×10 matrix C_{im} under these conditions following the rules shown in Table 4.5.⁸³ The term $\hat{\mathbf{e}}_2\hat{\mathbf{e}}_3\hat{\mathbf{e}}_4$ in Eq. (4.66) can be written as a 10×1 vector in a fashion similar to (4.79) using Table 4.5 as a guide.

Since the dispersion of even the second-order susceptibility is unknown and has been neglected, only the polarization directions involved will affect the effective coupling for each interaction, independent of wavelength (or order in Table 4.3). Therefore, the effective nonlinear coefficient will need to be calculated for only the following interactions: sss, ssf, sff, fff, sssf, ssff, and sfff. These are presented in Tables 4.6–4.9 for second-order interactions in uniaxial crystals.

Following these are the effective nonlinear coefficients for third order interactions; there are five possible polarization configurations. In Tables 4.10–4.14, Kleinman symmetry is assumed which means that any frequency dependence of the tensor elements has been neglected. In this case, the nonlinear coefficients are the same for any third-order interaction (THG, SPM, or XPM), depending only on the polarizations of the interacting waves.

4.2.3 Self-phase modulation

Recently, there have been several published works^{84–86} that suggest that the effect of SPM on SHG is actually quite dependent upon the dispersion that exists between the nonlinear refractive index n_2 at the fundamental and second harmonic (where n_2 is defined by $n = n_0 + n_2|E|^2 = n_0 + \gamma I$). In fact, the value for γ has been measured to vary from $2\text{--}4 \times 10^{-16} \text{ cm}^2/\text{W}$ from 1064–400 nm,⁸⁷ indicating significant dispersion exists. The nonlinear refractive index is related to C_{eff} by

$$n_2 = \frac{3C_{\text{eff}}^{\text{SPM}}}{2n_0} = \frac{\epsilon_0 c n_0}{2} \gamma, \quad (4.80)$$

and so the dispersion of n_2 in SHG is the same as dispersion between $C_{\text{eff}}^{\text{SPM}}(-\omega; \omega, -\omega, \omega)$ and $C_{\text{eff}}^{\text{SPM}}(-2\omega; 2\omega, -2\omega, 2\omega)$.

There are two points which should be made: first, that as seen in the actual form of C_{eff}

for the various interactions, the actual value for C_{eff} is highly dependent on propagation angle, and since the fundamental and second harmonic waves are typically of different polarizations (e.g. ordinary vs. extraordinary), the angular dependence will be different. Even if there is no actual dispersion in the tensor elements, the effective coupling, and thus the value of n_2 is not equal. For example, we shall assume Type I SHG in KDP (class $\bar{4}2m$) where $\phi = \pi/4$ and $\theta_m = \pi/4$. Then SPM for the fundamental is an oooo interaction, and for the second harmonic, it is an eeee interaction. The effective nonlinear coupling is then proportional to

$$C_{1\omega} = \frac{1}{2} (C_{11} + 3C_{18}) \quad (4.81)$$

for the fundamental and

$$\begin{aligned} C_{2\omega} &= \frac{1}{8} (C_{11} + 3C_{18}) + \frac{C_{33}}{4} + \frac{3C_{16}}{2} \\ &= \frac{1}{4} C_{1\omega} + \frac{C_{33}}{4} + \frac{3C_{16}}{2} \end{aligned} \quad (4.82)$$

for the second harmonic. It is clear that although the tensor elements are assumed to be independent of wavelength, the values for self-phase modulation for the fundamental and second harmonic are formally very different in KDP. The actual difference between Eqs. (4.81) and (4.82) is unknown because the tensor elements C_{16} and C_{33} are unknown.

This complicated angular dependence of C_{eff} for even self-phase modulation (the interaction of a wave with itself) indicates that the nonlinear refractive index must be measured with much greater attention to the crystal orientation than has been done in the literature to this point. It is typically measured for ordinary waves and extraordinary waves at some wavelength, and then this value is used for any crystal orientation. Presumably, this measurement is usually done for $\theta_m = \pi/2$ and $\phi = 0$ (or $\pi/2$). For KDP under these

conditions,

$$C_{\text{ord}} = C_{11} \text{ and} \quad (4.83)$$

$$C_{\text{ext}} = C_{11} + C_{33}. \quad (4.84)$$

Second, SPM and XPM are subject to similar cascaded second order interactions as has been discussed concerning third harmonic generation.^{88–90} DeSalvo *et al.* give a formula for an effective second order nonlinear refractive index of

$$n_{2,\text{eff}} = -\frac{4\pi}{c\epsilon_0\lambda n_{2\omega}n_{\omega}^2} \frac{d_{\text{eff}}^2}{\Delta k} \quad (4.85)$$

for second harmonic generation which is slightly unphasematched ($\Delta kl \lesssim 100$). This effect exists no matter what the phase mismatch is, as long as the process transfers energy to some other frequency or pair of frequencies. This means that the contribution to the effective second-order nonlinear index is the sum of all possible interactions of the form $\omega \rightarrow \omega_1 + \omega_2$ followed by $\omega_1 + \omega_2 \rightarrow \omega$ (keeping in mind that ω_j can be negative as well).

The question as to the effect of SPM and XPM on high intensity frequency conversion is at best a complicated issue. The angular dependence is some mixture of second- and third-order effective coupling coefficients involving an infinite number of unphasematched three-wave interactions. It is unlikely that any “subtle” effects such as dispersion of the third-order susceptibility tensor elements could be separated in any useful way. To effectively model the many interactions and the relative effects of each is beyond the scope of this work, but some concrete examples of the effects will be discussed in the next chapter.

4.2.4 Optimal input intensity

Finally, in order to compare the relative strengths between different phasematching configurations, it is necessary to account for the different initial intensities for each wave. For

Type I phasematching, the input beam is polarized along the slow polarization axis and so $I_1 = I_{\text{in}}$ and $I_2 = 0$. However, for other phasematching types, the input intensity is divided between the fast and slow polarizations.

For Type II SHG, for example, $I_4 \propto I_2 I_1$ and $I_2 + I_1 = I_{\text{in}}$. Maximizing the product $I_2 I_1$ gives $I_2 = I_1 = I_{\text{in}}/2$ as is obvious. In fact, it is a common practice to split the ordinary wave into two waves, each with half the intensity even for Type I phasematching in order to use the same code for either phasematching condition. This is possible because the 1/2 induced in this manner gives the same answer as using a single wave with the factor of 1/2 introduced due to the degeneracy of the waves.

For third order interactions, this ansatz no longer holds. For example, for Type II THG, $I_5 \propto I_2 I_1^2$ which is maximized for $I_2 = I_1/2 = I_{\text{in}}/3$. If one were to treat it as the interaction of three distinguishable waves of a third of the total intensity, it would introduce a factor of 1/27 while the degeneracy factor (or lack thereof) for the third-order interaction of four distinguishable waves would introduce a factor of $6^2 = 36$. It is clear that the apparent symmetry for second-order interactions which permits the arbitrary treatment of a wave as multiple distinguishable waves is not generally valid. Higher order interactions must be treated more carefully.

Thus, for Type I THG, the intensity at the third harmonic is proportional to $I_5^3 = I_{\text{in}}^3$, but for Type II phasematching, the third harmonic intensity is proportional to $I_2 I_1^2 = 4I_{\text{in}}^3/27$. This means that the “effective” input intensity of the fundamental for Type II phasematching is 4/27 times that for Type I phasematching. When comparing, for example, the nonlinear coupling between Type I and Type II THG, this difference in the effective input intensity between the two phasematching configurations must be taken into account.

Table 4.6: Effective nonlinear coefficient for second-order interactions, neglecting dispersion. ooo interactions.

Crystal class	d_{eff}
3	$-d_{11} \sin 3\phi - d_{22} \cos 3\phi$
3m	$-d_{22} \cos 3\phi$
$\bar{6}$	$-d_{11} \sin 3\phi - d_{22} \cos 3\phi$
6 and 4	0
6mm and 4mm	0
622 and 422	0
$\bar{6}m2$	$-d_{22} \cos 3\phi$
$\bar{4}$	0
32	$-d_{11} \sin 3\phi$
$\bar{4}2m, \bar{4}3m$ and 23	0

Table 4.7: Effective nonlinear coefficient for second-order interactions, neglecting dispersion. ooe interactions.

Crystal class	d_{eff}
3	$\cos \theta_m (d_{11} \cos 3\phi - d_{22} \sin 3\phi) + d_{31} \sin \theta_m$
3m	$-d_{22} \cos \theta_m \sin 3\phi + d_{31} \sin \theta_m$
$\bar{6}$	$\cos \theta_m (d_{11} \cos 3\phi - d_{22} \sin 3\phi)$
6 and 4	$d_{31} \sin \theta_m$
6mm and 4mm	$d_{31} \sin \theta_m$
622 and 422	0
$\bar{6}m2$	$-d_{22} \cos \theta_m \sin 3\phi$
$\bar{4}$	$-\sin \theta_m (d_{31} \cos 2\phi + d_{36} \sin 2\phi)$
32	$d_{11} \sin \theta_m \cos 3\phi$
$\bar{4}2m, \bar{4}3m$ and 23	$-d_{36} \sin \theta_m \sin 2\phi$

Table 4.8: Effective nonlinear coefficient for second-order interactions, neglecting dispersion. ooe interactions.

Crystal class	d_{eff}
3	$\cos^2 \theta_m (d_{11} \sin 3\phi + d_{22} \cos 3\phi)$
3m	$d_{22} \cos^2 \theta_m \cos 3\phi$
$\bar{6}$	$\cos^2 \theta_m (d_{11} \sin 3\phi + d_{22} \cos 3\phi)$
6 and 4	0
6mm and 4mm	0
622 and 422	0
$\bar{6}m2$	$d_{22} \cos^2 \theta_m \cos 3\phi$
$\bar{4}$	$\sin 2\theta_m (d_{36} \cos 2\phi - d_{31} \sin 2\phi)$
32	$d_{11} \cos^2 \theta_m \sin 3\phi$
$\bar{4}2m, \bar{4}3m$ and 23	$\sin 2\theta_m d_{36} \cos 2\phi$

Table 4.9: Effective nonlinear coefficient for second-order interactions, neglecting dispersion. eee interactions.

Crystal class	d_{eff}
3	$\cos^3 \theta_m (-d_{11} \cos 3\phi + d_{22} \sin 3\phi) + 3d_{31} \sin \theta_m \cos^2 \theta_m + d_{33} \sin^3 \theta_m$
3m	$d_{22} \cos^3 \theta_m \sin 3\phi + 3d_{31} \sin \theta_m \cos^2 \theta_m + d_{33} \sin^3 \theta_m$
$\bar{6}$	$\cos^3 \theta_m (-d_{11} \cos 3\phi + d_{22} \sin 3\phi)$
6 and 4	$3d_{31} \sin \theta_m \cos^2 \theta_m + d_{33} \sin^3 \theta_m$
6mm and 4mm	$3d_{31} \sin \theta_m \cos^2 \theta_m + d_{33} \sin^3 \theta_m$
622 and 422	0
$\bar{6}m2$	$d_{22} \cos^3 \theta_m \sin 3\phi$
$\bar{4}$	$3 \sin \theta_m \cos^2 \theta_m (d_{36} \sin 2\phi + d_{31} \cos 2\phi)$
32	$-d_{11} \cos^3 \theta_m \cos 3\phi$
$\bar{4}2m, \bar{4}3m$ and 23	$3d_{36} \sin \theta_m \cos^2 \theta_m \sin 2\phi$

Table 4.10: Effective nonlinear coefficient for third-order interactions, neglecting dispersion. oooo interactions.

Crystal Class	C_{eff}
Trigonal (3 and $\bar{3}$)	C_{11}
Trigonal (3m, $\bar{3}m$, and 32)	C_{11}
Hexagonal (6, $\bar{6}$, 6/m, 622, 6mm, 6/mmm, and $\bar{6}m2$)	C_{11}
Tetragonal (4, $\bar{4}$, and 4/m)	$\frac{1}{4} [C_{11}(3 + \cos 4\phi) + 6C_{18} \sin^2 2\phi] + C_{21} \sin 4\phi$
Tetragonal ($\bar{4}2m$, 422, 4mm, and 4/mmm)	$\frac{1}{4} [C_{11}(3 + \cos 4\phi) + 6C_{18} \sin^2 2\phi]$
Cubic (23, m3, 432, $\bar{4}3m$, and m3m)	$\frac{1}{4} [C_{11}(3 + \cos 4\phi) + 6C_{16} \sin^2 2\phi]$
Isotropic	C_{11}

Table 4.11: Effective nonlinear coefficient for third-order interactions, neglecting dispersion. oooo interactions.

Crystal Class	C_{eff}
Trigonal (3 and $\bar{3}$)	$\sin \theta_m (C_{10} \cos 3\phi + C_{15} \sin 3\phi)$
Trigonal (3m, $\bar{3}m$, and 32)	$C_{10} \cos 3\phi \sin \theta_m$
Hexagonal (6, $\bar{6}$, 6/m, 622, 6mm, 6/mmm, and $\bar{6}m2$)	0
Tetragonal (4, $\bar{4}$, and 4/m)	$-\cos \theta_m [C_{21} \cos 4\phi + \frac{1}{4} \sin 4\phi (3C_{18} - C_{11})]$
Tetragonal ($\bar{4}2m$, 422, 4mm and 4/mmm)	$\frac{1}{4} \cos \theta_m \sin 4\phi (C_{11} - 3C_{18})$
Cubic (23, m3, 432, $\bar{4}3m$, and m3m)	$\frac{1}{4} \cos \theta_m \sin 4\phi (C_{11} - 3C_{16})$
Isotropic	0

Table 4.12: Effective nonlinear coefficient for third-order interactions, neglecting dispersion. oooo interactions.

Crystal Class	C_{eff}
Trigonal (3 and $\bar{3}$)	$\frac{1}{3} C_{11} \cos^2 \theta_m + C_{16} \sin^2 \theta_m + \sin 2\theta_m (C_{10} \sin 3\phi - C_{15} \cos 3\phi)$
Trigonal (3m, $\bar{3}m$, and 32)	$\frac{1}{3} C_{11} \cos^2 \theta_m + C_{16} \sin^2 \theta_m + C_{10} \sin 2\theta_m \sin 3\phi$
Hexagonal (6, $\bar{6}$, 6/m, 622, 6mm, 6/mmm, and $\bar{6}m2$)	$\frac{1}{3} C_{11} \cos^2 \theta_m + C_{16} \sin^2 \theta_m$
Tetragonal (4, $\bar{4}$, and 4/m)	$\frac{1}{2} \cos^2 \theta_m [C_{11} \sin^2 2\phi + C_{18} (3 \cos^2 2\phi - 1) - 2C_{21} \sin 4\phi] + C_{16} \sin^2 \theta_m$
Tetragonal ($\bar{4}2m$, 422, 4mm and 4/mmm)	$\frac{1}{2} \cos^2 \theta_m [C_{11} \sin^2 2\phi + C_{18} (3 \cos^2 2\phi - 1) + C_{16} \sin^2 \theta_m]$
Cubic (23, m3, 432, $\bar{4}3m$, and m3m)	$\frac{1}{2} \cos^2 \theta_m [C_{11} \sin^2 2\phi + C_{16} (3 \cos^2 2\phi - 1) + C_{16} \sin^2 \theta_m]$
Isotropic	$\frac{1}{3} C_{11}$

Table 4.13: Effective nonlinear coefficient for third-order interactions, neglecting dispersion. oeee interactions.

Crystal Class	C_{eff}
Trigonal (3 and $\bar{3}$)	$-3 \cos^2 \theta_m \sin \theta_m (C_{10} \cos 3\phi + C_{15} \sin 3\phi)$
Trigonal (3m, $\bar{3}m$, and 32)	$-3C_{10} \cos^2 \theta_m \sin \theta_m \cos 3\phi$
Hexagonal (6, $\bar{6}$, 6/m, 622, 6mm, 6/mmm, and $\bar{6}m2$)	0
Tetragonal (4, $\bar{4}$, and 4/m)	$\cos^3 \theta_m [C_{21} \cos 4\phi + \frac{1}{4} \sin 4\phi (3C_{18} - C_{11})]$
Tetragonal ($\bar{4}2m$, 422, 4mm and 4/mmm)	$\frac{1}{4} (3C_{18} - C_{11}) \cos^3 \theta_m \sin 4\phi$
Cubic (23, m3, 432, $\bar{4}3m$, and m3m)	$\frac{1}{4} (3C_{16} - C_{11}) \cos^3 \theta_m \sin 4\phi$
Isotropic	0

Table 4.14: Effective nonlinear coefficient for third-order interactions, neglecting dispersion. eeee interactions.

Crystal Class	C_{eff}
Trigonal (3 and $\bar{3}$)	$4 \sin \theta_m \cos^3 \theta_m (C_{15} \cos 3\phi - C_{10} \sin 3\phi) + C_{11} \cos^4 \theta_m + \frac{3}{2} C_{16} \sin^2 2\theta_m + C_{33} \sin^4 \theta_m$
Trigonal (3m, $\bar{3}m$, and 32)	$-4C_{10} \sin \theta_m \cos^3 \theta_m \sin 3\phi + C_{11} \cos^4 \theta_m + \frac{3}{2} C_{16} \sin^2 2\theta_m + C_{33} \sin^4 \theta_m$
Hexagonal (6, $\bar{6}$, 6/m, 622, 6mm, 6/mmm, and $\bar{6}m2$)	$C_{11} \cos^4 \theta_m + \frac{3}{2} C_{16} \sin^2 2\theta_m + C_{33} \sin^4 \theta_m$
Tetragonal (4, $\bar{4}$, and 4/m)	$\cos^4 \theta_m [\frac{1}{4} C_{11} (3 + \cos 4\phi) + \frac{3}{2} C_{18} \sin^2 2\phi + 2C_{21} \sin 4\phi] + \frac{3}{2} C_{16} \sin^2 2\theta_m + C_{33} \sin^4 \theta_m$
Tetragonal ($\bar{4}2m$, 422, 4mm and 4/mmm)	$\frac{1}{4} C_{11} \cos^4 \theta_m (3 + \cos 4\phi) + \frac{3}{2} C_{16} \sin^2 2\theta_m + \frac{3}{2} C_{18} \cos^4 \theta_m \sin^2 2\phi + C_{33} \sin^4 \theta_m$
Cubic (23, m3, 432, $\bar{4}3m$, and m3m)	$\frac{1}{4} C_{11} [\cos^4 \theta_m (3 + \cos 4\phi) + \sin^4 \theta_m] + \frac{3}{2} C_{16} [\sin^2 2\theta_m + \cos^4 \theta_m \sin^2 2\phi]$
Isotropic	C_{11}

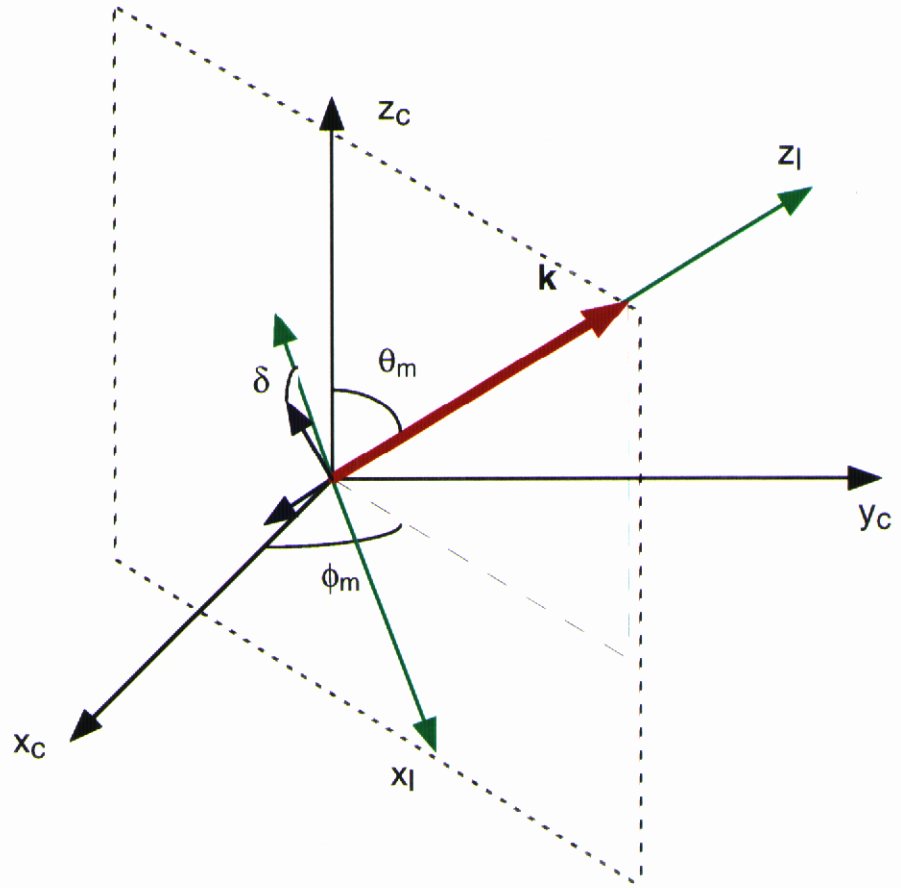


Figure 4.3: Principal axes for a biaxial crystal. For a beam propagating in direction \mathbf{k} at angles θ_m and ϕ , the polarization eigendirections are at an angle δ and $\delta + \pi/2$ with respect to the \mathbf{k} - z plane.

4.3 Biaxial crystals

To this point, everything has been directed at either uniaxial or isotropic crystals. Biaxial crystals are more complicated because the polarization eigendirections are not fixed; they are a function of the propagation direction. Fig. 4.3 shows the principal axes of a biaxial crystal where by convention, $n_z > n_y > n_x$. The two refractive index eigenvalues for a given direction of propagation are given in terms of these principal indices as^{91–95}

$$n_{\pm}(\theta_m, \phi) = \sqrt{\frac{1}{2}(-B \pm \sqrt{B^2 - 4C})} \quad (4.86)$$

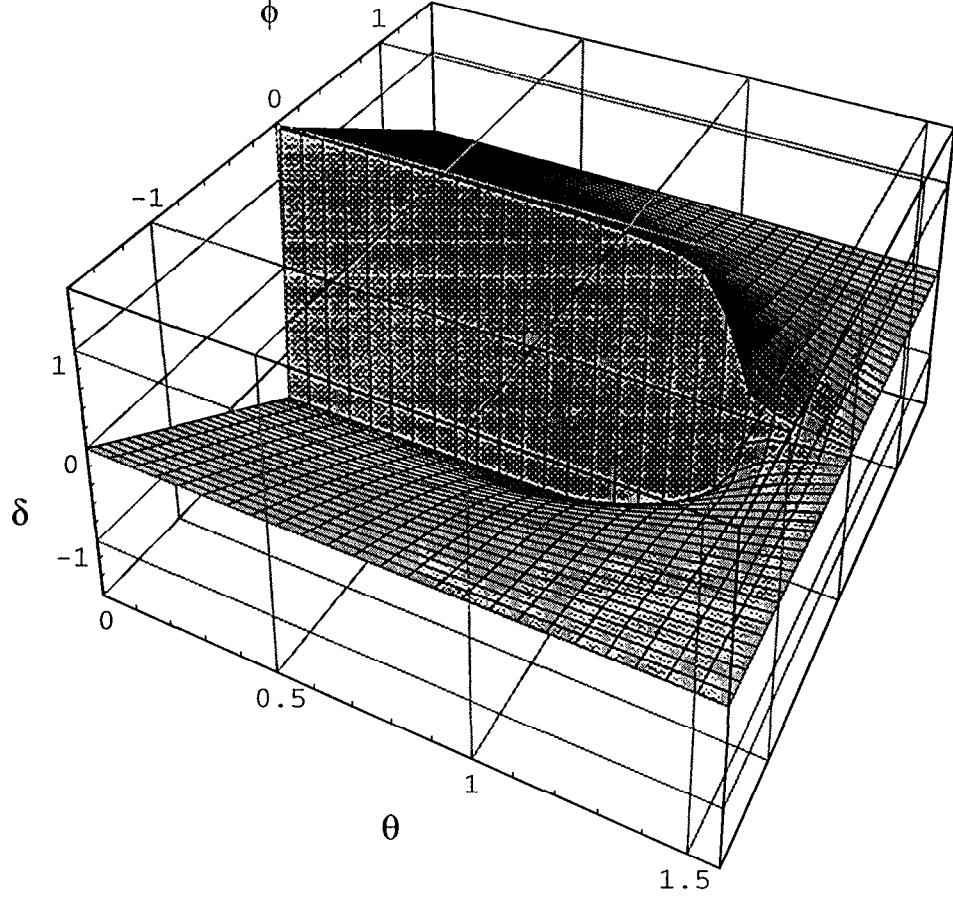


Figure 4.4: Polarization eigendirection angle δ with the k-z plane as a function of polar θ and azimuthal ϕ angle in a biaxial crystal.

with

$$B = -\frac{n_x^2(n_y^2 + n_z^2)s_x^2 + n_y^2(n_x^2 + n_z^2)s_y^2 + n_z^2(n_x^2 + n_y^2)s_z^2}{(s_x n_x)^2 + (s_y n_y)^2 + (s_z n_z)^2} \text{ and} \quad (4.87)$$

$$C = \frac{n_x^2 n_y^2 n_z^2}{(s_x n_x)^2 + (s_y n_y)^2 + (s_z n_z)^2}. \quad (4.88)$$

The terms s_j are the direction cosines given by $s_x = \sin \theta_m \cos \phi$, $s_y = \sin \theta_m \sin \phi$, and $s_z = \cos \theta_m$. Obviously, n_+ denotes the index of refraction of slow wave and n_- denotes the index of the fast wave.

The polarization directions (of the electric displacement \mathbf{D}) of these two eigenindices are orthogonal to \mathbf{k} and make an angle δ and $\delta + \pi/2$ with the k-z plane, respectively. The

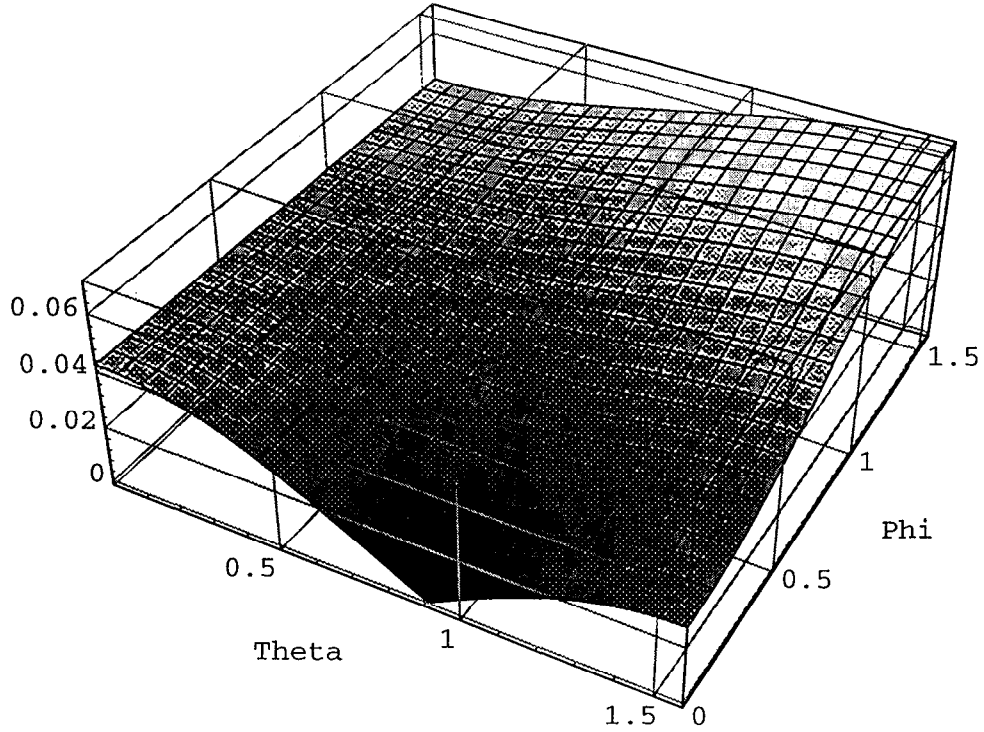


Figure 4.5: The birefringence $\Delta n = n_+ - n_-$ of a biaxial crystal with $n_x = 1.496$, $n_y = 1.538$, and $n_z = 1.566$.

angle δ is given by^{95,94,93}

$$\delta = \frac{1}{2} \cot^{-1} \frac{\cot^2 V \sin^2 \theta_m - \cos^2 \theta_m \cos^2 \phi + \sin^2 \phi}{\cos \theta_m \sin 2\phi}. \quad (4.89)$$

where V is the angle between the optic axes and the z axis,

$$\cot^2 V = \frac{1/n_y^2 - 1/n_z^2}{1/n_x^2 - 1/n_y^2} \quad (4.90)$$

or

$$\sin V = \left(\frac{n_z}{n_y} \right) \frac{n_y^2 - n_x^2}{n_z^2 - n_x^2}. \quad (4.91)$$

Although Eq. (4.89) has a period of only $\pi/2$, the relative signs of the numerator and denominator can be used to extend this to π . This angle δ is plotted in Fig. 4.4 against θ and ϕ . The apparent discontinuity is really the same polarization (rotated by 180°). The optic axis for this crystal (d-LAP) is $\theta = 71^\circ$ and $\phi = 0^\circ$. The birefringence $n_+ - n_-$ of a

representative biaxial crystal is shown in Fig. 4.5 in the first octant. The minimum is the position of the optic axis at an angle $\theta_m = V$.

The polarization eigenvectors in the crystal frame are then

$$\mathbf{E}_j = \mathbb{T}^{-1} \mathbf{E}_j^{(l)} \quad (4.92)$$

so

$$\begin{aligned} \hat{\mathbf{e}}_s &= \mathbb{T}^{-1} \begin{bmatrix} -\cos \delta \\ -\sin \delta \\ 0 \end{bmatrix} \\ &= \begin{bmatrix} -\cos \theta_m \cos \phi \cos \delta + \sin \phi \sin \delta \\ -\cos \theta_m \sin \phi \cos \delta - \cos \phi \sin \delta \\ \sin \theta_m \cos \delta \end{bmatrix} \end{aligned} \quad (4.93)$$

and

$$\begin{aligned} \hat{\mathbf{e}}_f &= \mathbb{T}^{-1} \begin{bmatrix} \sin \delta \\ -\cos \delta \\ 0 \end{bmatrix} \\ &= \begin{bmatrix} \cos \theta_m \cos \phi \sin \delta + \sin \phi \cos \delta \\ \cos \theta_m \sin \phi \sin \delta - \cos \phi \cos \delta \\ -\sin \theta_m \sin \delta \end{bmatrix}. \end{aligned} \quad (4.94)$$

These can then be used to determine the effective nonlinear coupling coefficients as before. However, because of the angular dependence of the polarization eigendirections, the formulas are so complicated that little is gained from writing them out explicitly, even for second-order interactions. Therefore, only those for the sss interactions for the eight biaxial crystal classes will be given in Table 4.15 as an example. The others are simply calculated using the procedure described here.

Table 4.15: Effective nonlinear coefficient for second-order interactions in biaxial crystals, neglecting dispersion. sss interactions. Only 4 of the 10 independent elements are shown for class 1.

Crystal Class	d_{eff}
1	$d_{11}(\sin \phi \sin \delta - \cos \theta_m \cos \phi \cos \delta) + 3d_{12}(\sin \phi \sin \delta - \cos \theta_m \cos \phi \cos \delta) \times$ $(\cos \phi \sin \delta + \cos \theta_m \sin \phi \cos \delta)^2 + 3d_{13} \sin^2 \theta_m \cos^2 \delta (\sin \phi \sin \delta -$ $\cos \theta_m \cos \phi \cos \delta) +$ $6d_{14} \sin \theta_m \cos \delta (\sin \phi \sin \delta - \cos \theta_m \cos \phi \cos \delta) (\cos \phi \sin \delta +$ $\cos \theta_m \sin \phi \cos \delta)$ $+ \dots$
2	$-(\cos \phi \sin \delta + \cos \delta \cos \theta_m \sin \phi) \times$ $\{d_{22}(\cos \phi \sin \delta + \cos \delta \cos \theta_m \sin \phi)^2 +$ $3d_{21}(\cos \delta \cos \theta_m \cos \phi - \sin \delta \sin \phi)^2 -$ $6d_{14} \cos \delta \sin \theta_m (\cos \delta \cos \phi \cos \theta_m - \sin \delta \sin \phi) + 3d_{23} \cos^2 \delta \sin^2 \theta_m\}$
m	$(-\cos \delta \cos \theta_m \cos \phi + \sin \delta \sin \phi) \times$ $\{d_{11}(-\cos \delta \cos \theta_m \cos \phi + \sin \delta \sin \phi)^2 +$ $3d_{31} \cos \delta \sin \theta_m (-\cos \delta \cos \theta_m \cos \phi + \sin \delta \sin \phi) +$ $3d_{12}(\cos \phi \sin \delta + \cos \delta \cos \theta_m \sin \phi)^2 + 3d_{13} \cos^2 \delta \sin^2 \theta_m\} +$ $3d_{32} \cos \delta \sin \theta_m (\cos \phi \sin \delta + \cos \delta \cos \theta_m \sin \phi)^2 + d_{33} \cos^3 \delta \sin^3 \theta_m$
222	$\sin \theta_m \cos \delta [\cos \theta_m \cos 2\phi \sin 2\delta + \sin 2\phi (\cos 2\delta - \sin^2 \theta_m)]$
mm2	$3d_{31}(\sin \phi \sin \delta - \cos \theta_m \cos \phi \cos \delta) +$ $3d_{32} \sin \theta_m \cos \delta (\cos \theta_m \sin \phi \cos \delta - \cos \phi \sin \delta)^2 + d_{33} \sin^3 \theta_m \cos^3 \delta$
$\bar{1}$, 2/m, mmm	0

4.4 Material considerations

One of the main limiting parameters in the frequency conversion of ultrashort pulses is the mismatch of the group velocities of the waves involved in the interaction. Since the dispersion between the group velocities of the fundamental and the generated harmonic increases as the frequency separation increases, this effect will be even more pronounced for third harmonic generation. The same holds for the phase velocities so that achieving phasematching for a given configuration requires more birefringence for the nonlinear medium. For example, KDP phasematches at about 41° for Type I and about 59° for Type II SHG, but phasematches at 65° for Type I THG and Types II and III are not

phase-matchable at all. Also important are the sensitivity to changes in angle (most important for focused-beam geometries) and the sensitivity to the bandwidth of the pulse (since not all frequency components will be phasematched simultaneously).

In Tables 4.16–4.24, several of these material parameters are given for several second- and third-order interactions involving the negative uniaxial crystals potassium dihydrogen phosphate (KDP), potassium di-deuterium phosphate (KD*P), ammonium dihydrogen phosphate (ADP), barium borate (BBO), lithium iodate (LiIO₃), and cesium lithium borate (CLBO) using published Sellmeier and nonlinear tensor element d_{ij} data.^{96,97} The phasematching angle θ_m is the angle which solves the equation $\Delta k = 0$, and it can be found analytically for uniaxial crystals under phasematching configurations for which only one wave is polarized along the extraordinary axis. For example, for Type I phasematching of a second-order process in negative uniaxial crystals, the phasematching equation is

$$\Delta k = \frac{n_4}{\lambda_{2\omega}} - 2\frac{n_1}{\lambda_\omega} = 0 \quad (4.95)$$

which implies that $n_4 = n_1$. The angular dependence of the extraordinary index is

$$n^e(\theta) = \left[\frac{\sin^2 \theta}{(n^e)^2} + \frac{\cos^2 \theta}{(n^o)^2} \right]^{-1} \quad (4.96)$$

where n^o and n^e are the eigenindices for a wave exactly polarized along the ordinary and extraordinary axis, respectively. Eq. (4.96) can be inserted into (4.95) which gives, solving for the angle,

$$\theta_m = \cos^{-1} \left[\frac{\frac{1}{(n_{1\omega}^o)^2} - \frac{1}{(n_{2\omega}^e)^2}}{\frac{1}{(n_{2\omega}^o)^2} - \frac{1}{(n_{2\omega}^e)^2}} \right]^{1/2}. \quad (4.97)$$

Similarly, for Type I direct THG in a negative uniaxial crystal, the phasematching angle is

$$\theta_m = \cos^{-1} \left[\frac{\frac{1}{(n_{1\omega}^o)^2} - \frac{1}{(n_{3\omega}^e)^2}}{\frac{1}{(n_{3\omega}^o)^2} - \frac{1}{(n_{3\omega}^e)^2}} \right]^{1/2}. \quad (4.98)$$

For other phasematching configurations, $\Delta k = 0$ must be solved numerically. In Tables 4.16–4.24, the presence of a dash (–) for θ_m indicates that that particular process cannot be phasematched in that crystal at room temperatures (all calculations are done for room temperature).

The terms $\Delta\lambda l$ and $\Delta\theta l$ are known as the spectral and angular acceptance bandwidths and are defined as

$$\Delta\lambda l = 1.77\pi \left[\left. \frac{\partial\Delta k}{\partial\lambda} \right|_{\lambda_0} \right]^{-1} \quad (4.99)$$

and

$$\Delta\theta l = 1.77\pi \left[\left. \frac{\partial\Delta k}{\partial\theta} \right|_{\theta_m} \right]^{-1}. \quad (4.100)$$

These definitions come from the first order term in Fourier expansions of Δk in terms of λ and θ , respectively, and give the spread in wavelength or angle which reduces the generated irradiance by half of its maximum value.⁹⁶ The angular acceptance will be of lesser interest for our purposes, but because of the large spectral bandwidths associated with short pulses, the spectral acceptance will be critical. Of particular interest is the large spectral acceptance of the KDP isomorphs in Tables 4.18 and 4.19. This is due to the fact that both the indices of refraction and the slopes of the index dispersion for the fundamental and second harmonic can be simultaneously equal (or nearly so) near a fundamental wavelength of 1053 nm.¹⁸ The wavelength position of the near-IR absorption resonance of the material determines the wavelength of the fundamental for which this will occur. However, for most materials, this is further into the infrared, which is seen in the much smaller spectral acceptance bandwidths for interactions at 820 nm.

Related to the spectral acceptance bandwidth for transform-limited pulses is the interaction length due to the group velocity walkoff between two pulses $l_{\text{int}} = \Delta v_g \tau_p$ where τ_p is the temporal pulse length and $\Delta v_g = (1/v_{g1} - 1/v_{g2})^{-1}$ (v_{gj} are the group velocities

of the two waves). For example, for second harmonic generation,

$$\frac{\partial \Delta k}{\partial \omega} = 2 \frac{\partial k_{2\omega}}{\partial (2\omega)} - \frac{\partial k_{\omega}}{\partial \omega} - \frac{\partial k_{\omega}}{\partial \omega} \quad (4.101)$$

$$= \frac{2}{v_{g,2\omega}} - \frac{1}{v_{g,\omega}} - \frac{1}{v_{g,\omega}} \quad (4.102)$$

which implies that l_{int} will be large (as well as $\Delta\lambda l$) if the group velocities match according to Eq. (4.102). In Tables 4.16–4.24, the value for Δv_g is the difference between the ordinary fundamental and the extraordinary second, i.e. $1/v_{g,1\omega}^o - 1/v_{g,2\omega}^e$, (Tables 4.16–4.21) or third, i.e. $1/v_{g,1\omega}^o - 1/v_{g,3\omega}^e$, (Tables 4.22–4.24) harmonic for the given phasematching angle. If Δv_g is given as an ordered pair, the second value is the difference between the ordinary and extraordinary polarizations of the fundamental.

An interesting consequence of this limitation on the interaction length imposed by this group velocity walkoff effect is that, for second-order processes, the conversion becomes dependent upon the input fluence and not the input intensity. For example, it is known that for the non-depleted pump regime, second-harmonic generation is described by $I_{2\omega} \propto I_{\omega}^2 l^2$. If the input pulse is sufficiently short such that $l_{\text{int}} < l_c$ (where l_c is the physical crystal length), the $I_{2\omega} \propto I_{\omega}^2 l_{\text{int}}^2$. Since $I_{\omega} \approx \Gamma/\tau_p$,

$$I_{2\omega} \propto \frac{\Gamma^2}{\tau_p^2} (\Delta v_g)^2 \tau_p^2 = \Gamma^2 (\Delta v_g)^2, \quad (4.103)$$

or the generated intensity is independent of the input pulse length. However, for third-order interactions such as third harmonic generation, $I_{3\omega} \propto I_{\omega}^3 l^2$ so that if $l_{\text{int}} < l_c$,

$$I_{3\omega} \propto \frac{\Gamma^3}{\tau_p^3} (\Delta v_g)^2 \tau_p^2 = \frac{\Gamma^2 (\Delta v_g)^2}{\tau_p}. \quad (4.104)$$

For third-order interactions, higher conversion efficiency can ostensibly be achieved by decreasing the input pulse length.

The final interaction length due to transverse spatial walkoff is given by $l_{\text{int}}^{\text{walkoff}} \cong d/\rho(\theta)$ where d is the beam diameter. As is shown in Tables 4.16–4.24, $\rho \cong 2^\circ$ – 4° which

means that $l_{\text{int}}^{\text{walkoff}}$ is at least several centimeters for beam diameters of a millimeter or larger. Except for the special case of KDP near 1 μm mentioned above, this interaction length is much longer than those due to GVM walkoff/spectral bandwidth for short pulses.

In addition, the effective nonlinear coupling coefficients are given: d_{eff} for the second-order interactions SHG and SFG and $C_{\text{eff}}^{(2)}$ for (single crystal) third harmonic generation. The term $C_{\text{eff}}^{(2)}$ refers to the expected contribution to the coupling to the third harmonic due to the cascaded second order processes, i.e. for Type I phasematching

$$C_{\text{eff}}^{(2)} = \frac{2\pi}{\lambda_{2\omega}} \left[\frac{d_1 d_7}{n_{2\omega}^o \Delta k_7} + \frac{d_3 d_5}{n_{2\omega}^e \Delta k_5} \right] \quad (4.105)$$

and for Type II phasematching

$$C_{\text{eff}}^{(2)} = \frac{2\pi}{\lambda_{2\omega}} \left[\frac{d_2 d_7}{n_{2\omega}^o \Delta k_7} + \frac{d_4 d_5}{n_{2\omega}^e \Delta k_5} + \frac{d_1 d_8}{n_{2\omega}^o \Delta k_8} + \frac{d_3 d_6}{n_{2\omega}^e \Delta k_6} \right]. \quad (4.106)$$

The definitions of Δk_j and d_j are those given in Eqs. (4.55)–(4.62) and Table 4.1, and the ordering of the sets of Δk in Tables 4.22–4.24 is $(\Delta k_7, \Delta k_5)$ for Type I phasematching and $(\Delta k_7, \Delta k_5, \Delta k_8, \Delta k_6)$ for Type II phasematching.

In this section, only parameters for uniaxial crystals have been discussed. Biaxial crystals present greater possibilities since, instead of a single phasematching angle θ_m for a given configuration, there is a loci of angles $\{\theta_m, \phi\}$ which satisfy the phasematching condition. Contour plots of these loci are shown in Appendix B for eight biaxial crystals: lithium triborate (LBO), potassium titanyl phosphate (KTP), LAP, deuterated LAP, potassium lathanum nitrate (KLN), potassium cerium nitrate (KCN), barium magnesium fluoride (BMF), and lithium formate (LFM). It is therefore possible to choose the angle pair which maximizes d_{eff} or perhaps it is possible to choose the phasematching angles such that the group velocity mismatch is minimized or that SPM/XPM are minimized. Several parameters for comparison are given in Table 4.25.

Table 4.16: Interaction lengths and bandwidths for Type I SHG at 820 nm.

Material	θ_m	d_{eff} (pm/V)	ϕ (rad)	$\Delta\lambda l$ (nm cm)	$\Delta\theta l$ (mrad cm)	ρ	Δv_g ($\times 10^{12}$ cm/s)
KDP	44.2°	.27	$\pi/4$	1.4	.82	1.7°	-1.5
KD*P	43.3°	.27	$\pi/4$	1.3	.89	1.6°	-1.3
ADP	44.7°	.27	$\pi/4$	1.3	.76	1.8°	-1.3
BBO	28.3°	1.9	$\pi/6$.56	.33	3.8°	-.57
LiIO ₃	41.1°	4.6	—	.19	.22	5.0°	-1.19
CLBO	34.4°	.54	$\pi/4$.83	.71	2.0°	-.84

Table 4.17: Interaction lengths and bandwidths for Type II SHG at 820 nm.

Material	θ_m	d_{eff} (pm/V)	ϕ (rad)	$\Delta\lambda l$ (nm cm)	$\Delta\theta l$ (mrad cm)	ρ	Δv_g ($\times 10^{12}$ cm/s)
KDP	68.8°	.26	0.0	1.3	2.2	1.1°	(-33,.69)
KD*P	70.7°	.24	0.0	1.4	2.7	.96°	(-8.8,.82)
ADP	71.5°	.23	0.0	1.2	2.3	1.1°	(-100,.62)
BBO	40.9°	1.3	0.0	.60	.54	4.4°	(-1.4,.53)
LiIO ₃	64.5°	0	—	.21	.57	3.6°	(-.40,.23)
CLBO	51.5°	.94	0.0	.88	1.3	2.0°	(-1.7,.9)

Table 4.18: Interaction lengths and bandwidths for Type I SHG at 1053 nm.

Material	θ_m	d_{eff} (pm/V)	ϕ (rad)	$\Delta\lambda l$ (nm cm)	$\Delta\theta l$ (mrad cm)	ρ	Δv_g ($\times 10^{12}$ cm/s)
KDP	41.2°	.26	$\pi/4$	32.6	1.1	1.6°	20
KD*P	38.62°	.24	$\pi/4$	14	1.2	1.5°	-8.7
ADP	41.7°	.26	$\pi/4$	22	1.0	1.7°	13
BBO	23.0°	2.0	$\pi/6$	2.0	.5	3.2°	-1.2
LiIO ₃	30.3°	3.5	—	.61	-.34	4.3°	.37
CLBO	26.1°	.42	$\pi/4$	2.3	1.1	1.6°	-1.4

Table 4.19: Interaction lengths and bandwidths for Type II SHG at 1053 nm.

Material	θ_m	d_{eff} (pm/V)	ϕ (rad)	$\Delta\lambda l$ (nm cm)	$\Delta\theta l$ (mrad cm)	ρ	Δv_g ($\times 10^{12}$ cm/s)
KDP	59.2°	.34	0.0	15	2.2	1.4°	(1.8,.76)
KD*P	59.8°	.34	0.0	16	2.6	1.3°	(2.5,.98)
ADP	61.6°	.33	0.0	22	2.1	1.4°	(1.5,.68)
BBO	32.8°	1.6	0.0	2.0	.77	4.0°	(-6.4,.77)
LiIO ₃	44.6°	0.0	0	.65	.58	4.7°	(-.81,.39)
CLBO	37.8°	.93	0.0	2.4	1.8	2.0	(-3.0,1.5)

Table 4.20: Interaction lengths and bandwidths for Type II SFG, $\omega + 2\omega \rightarrow 3\omega$, (ordinary 2ω and extraordinary 1ω) at 820 nm.

Material	θ_m	d_{eff} (pm/V)	ϕ (rad)	$\Delta\lambda l$ (nm cm)	$\Delta\theta l$ (mrad cm)	ρ	Δv_g ($\times 10^{12}$ cm/s)
KDP	—						
KD*P	—						
ADP	—						
BBO	53.3°	.79	0.0	.93	.59	4.5°	(-.12,.36)
LiIO ₃	—						
CLBO	75.5°	.47	0.0	1.3	2.7	1.0°	(-.30,.60)

Table 4.21: Interaction lengths and bandwidths for Type II SFG, $\omega + 2\omega \rightarrow 3\omega$, (ordinary 2ω and extraordinary 1ω) at 1053 nm. The second line for BBO ($\theta_m = 60.7^\circ$) is for an SFG interaction with extraordinary 2ω and ordinary 1ω waves.

Material	θ_m	d_{eff} (pm/V)	ϕ (rad)	$\Delta\lambda l$ (nm cm)	$\Delta\theta l$ (mrad cm)	ρ	Δv_g ($\times 10^{12}$ cm/s)
KDP	59.1°	.34	0.0	15	2.2	1.5°	(-.85,.76)
KD*P	61.8°	.32	0.0	21	2.7	1.3°	(-.82,.95)
ADP	60.8°	.33	0.0	19	2.1	1.6°	(-.79,.69)
BBO	38.6°	1.3	0.0	2.9	.74	4.4°	(-.36,.59)
BBO	60.7°	.53	0.0	5.4	.92	3.7°	(-1.2,.31)
LiIO ₃	61.9°	0.0	0	1.0	.76	4.1°	(-.12,.25)
CLBO	48.8°	.95	0.0	3.5	1.7	2.1°	(-.54,1.0)

Table 4.22: Interaction lengths and bandwidths for Type I THG of 820 nm.

Material	θ_m	$C_{\text{eff}}^{(2)}$ (pm/V) ²	$\Delta\lambda l$ (nm cm)	$\Delta\theta l$ (mrad cm)	ρ	Δv_g ($\times 10^{12}$ cm/s)	Δk (cm ⁻¹)
KDP	—						
KD*P	—						
ADP	—						
BBO	51.0°	33	.12	.18	4.6°	-.17	(-4670,7320)
LiIO ₃	—						
CLBO	68.6°	6.8	.19	.62	1.5°	-.29	(-2750,4490)

Table 4.23: Interaction lengths and bandwidths for Type I THG at 1053 nm.

Material	θ_m	$C_{\text{eff}}^{(2)}$ (pm/V) ²	$\Delta\lambda l$ (nm cm)	$\Delta\theta l$ (mrad cm)	ρ	Δv_g ($\times 10^{12}$ cm/s)	Δk (cm ⁻¹)
KDP	65.4°	2.2	1.1	.93	1.3°	-.99	(-2230,1950)
KD*P	63.2°	2.3	.92	.94	1.3°	-.85	(-1890,1910)
ADP	66.9°	1.9	.99	.90	1.3°	-.91	(-2500,2190)
BBO	37.7°	77	.38	.24	4.4°	-.35	(-2400,3300)
LiIO ₃	58.1°	0.0	.13	.21	4.5°	-.11	(-5010,8350)
CLBO	46.0°	13	.56	.56	2.1°	-.51	(-1260,2050)

Table 4.24: Interaction lengths and bandwidths for Type II THG. The four phase mismatch parameters are (-12300, 4190, -4670, 11800) cm⁻¹, (-6180, 1870, -2400, 5650) cm⁻¹, and (-3550, 1200, -1260, 3490) cm⁻¹ for lines 1, 2, and 3, respectively.

Material	$\lambda_{1\omega}$ (nm)	θ_m	$C_{\text{eff}}^{(2)}$ (pm/V) ²	$\Delta\lambda l$ (nm cm)	$\Delta\theta l$ (mrad cm)	ρ	Δv_g ($\times 10^{12}$ cm/s)
BBO	820	67.6°	16	.13	.37	3.2°	(-.25,.28)
BBO	1053	47.1°	110	.40	.35	4.4°	(-.51,.43)
CLBO	1053	60.0°	47	.59	.95	1.8°	(-.70,.77)

Table 4.25: Material parameters for 8 uniaxial and 8 biaxial (see Appendix B) crystals. Sellmeier parameters were obtained from Ref. 96 except for CLBO⁹⁷ and KLN and KCN.⁹⁸. The term d^{max} indicates the largest element of d_{ij} in pm/V, γ is the nonlinear refractive index in cm²/W, n gives the ordinary (uniaxial) or smallest (n_x , biaxial) refractive index at 1064 nm, Δn gives $n^e - n^o$ (uniaxial) or $n_z - n_x$ (biaxial), and Phasematch indicates if the material is phase-matchable for Type I THG at 1053 nm.

Material	Class	d^{max}	γ (cm ² /W)	Δn	n	Transpar. range (μm)	Phasematch.
KDP	42m	.39	3×10^{-16}	-.0339	1.4938	.18-1.7	yes
KD*P	42m	.4	—	-.0373	1.4928	.2-2	yes
ADP	42m	.56	—	-.0384	1.5065	.18-1.5	yes
BBO	3m	2.2	5×10^{-16}	-.1125	1.6551	.2-2.6	yes
LiIO ₃	6	7	—	-.1406	1.8571	.3-6	yes
CLBO	42m	.96	—	-.0505	1.4882	.18-1.2	yes
LiNbO ₃	3m	30	—	-.0786	2.2340	.33-4.5	no
Urea	42m	1.3	—	-.1019	1.4811	.2-1.8	yes
LBO	mm2	1.2	—	.0399	1.5656	.16-2.6	yes
KTP	mm2	14	—	.0901	1.7386	.35-4.5	no
RTP	mm2	14	—	.0881	1.7659	.35-4.5	no
LAP	2	.93	—	.0701	1.4973	.25-1.3	yes
d-LAP	2	.93	—	.0695	1.4960	.25-1.3	yes
KLN	mm2	1.1	—	.0617	1.4856	.32- ~1.5	yes
KCN	mm2	1.1	—	.0628	1.4889	.4- ~1.5	yes
BMF	mm2	.04	—	.0238	1.4436	.19-10	no
LFM	mm2	1.7	—	.1442	1.3593	.23-1.2	yes

4.5 Numerical solution of coupled wave equation

The system of equations (4.54–4.50) of course cannot be solved analytically, and so numerical techniques must be used. One such algorithm that is commonly used to solve this sort of system is known as the beam propagation method or the split-step method.^{99–102} The right-hand sides of (4.54–4.50) are separated into a dispersive/diffractive part (all terms involving time and space derivatives) and a nonlinear part. Expressed in operator notation, this means that

$$\frac{\partial A_j}{\partial z} = (\mathbb{D}_j + \mathbb{N}_{1j})A_j + \mathbb{N}_{2j} \quad (4.107)$$

where

$$\mathbb{D}_j = -\beta_{1j} \frac{\partial}{\partial t} - \frac{i}{2} \beta_{2j} \frac{\partial^2}{\partial t^2} + \frac{i}{2k_j} \nabla_{\perp}^2 - \rho_j(\theta_m) \frac{\partial}{\partial x} \quad (4.108)$$

and, for example,

$$\mathbb{N}_{11} = \frac{i\omega_1}{n_1 c} \left[\frac{3C_1^{\text{SPM}}}{2} |A_1|^2 + 3C_1^{\text{XPM}} |A_5|^2 + 3C_2^{\text{XPM}} |A_2|^2 \right] \quad (4.109)$$

and

$$\begin{aligned} \mathbb{N}_{21} = & \frac{i\omega_1}{n_1 c} \left[d_1 A_3 A_1^* e^{i\Delta k_1 z} + d_3 A_4 A_1^* e^{i\Delta k_3 z} + d_2 A_3 A_2^* e^{i\Delta k_2 z} + d_4 A_4 A_2^* e^{i\Delta k_4 z} \right. \\ & + d_5 A_5 A_4^* e^{i\Delta k_5 z} + d_7 A_5 A_3^* e^{i\Delta k_7 z} \\ & \left. + 3C_1 A_5 A_2^* A_1^* e^{i\Delta k_9 z} + \frac{3C_2}{2} A_5 A_1^{*2} e^{i\Delta k_{10} z} \right]. \end{aligned} \quad (4.110)$$

These two classes of operations are assumed to function independently for an appropriate choice of the z -interval Δz . Eq. (4.107) can then be split into three equations which can be solved independently

$$\frac{\partial A_j}{\partial z} = \mathbb{D} A_j, \quad (4.111)$$

$$\frac{\partial A_j}{\partial z} = \mathbb{N}_{1j} A_j, \text{ and} \quad (4.112)$$

$$\frac{\partial A_j}{\partial z} = \mathbb{N}_{2j} \quad (4.113)$$

The dispersive/diffractive step can be solved easily by moving to Fourier space and replacing $\partial/\partial x_j$ with ik_{x_j} and $\partial/\partial t$ with $-i\omega_0$. Then

$$A_j^{(n+1)} = \mathcal{F}^{-1} \left[e^{\mathbb{D}_j(\omega, \mathbf{k})\Delta z} \mathcal{F}[A_j^{(n)}] \right] \quad (4.114)$$

where the superscript (n) in parentheses denotes the step n and the dispersive operator $\mathbb{D}_j(\omega, \mathbf{k})$ in Fourier space is

$$\mathbb{D}_j(\omega, \mathbf{k}) = i\omega\beta_{1j} + \frac{i}{2}\omega^2\beta_{2j} - \frac{i}{2k_j}(k_{jx}^2 + k_{jy}^2) - ik_{jx}\rho_j(\theta_m). \quad (4.115)$$

The nonlinear part is handled in real space with Eq. (4.112) (the phase modulation part \mathbb{N}_{1j} of the nonlinear operator) giving rise to a simple exponential solution $A_j^{(n+1)} = \exp(\mathbb{N}_{1j}\Delta z)A_j^{(n)}$. However, the solution of the coupled set of equations of the form (4.113) must be done using some sort of numerical technique such as Runge-Kutta. It was found that second-order RK was adequate which means the following difference equation

$$y^{(n+1)} = y^{(n)} + \Delta z f(z^{(n)} + \Delta z/2, y^{(n)} + \frac{\Delta z}{2} f(z^{(n)}, y^{(n)})) \quad (4.116)$$

gives the solution to a differential equation of the form

$$\frac{\partial y}{\partial z} = f(z, y). \quad (4.117)$$

The set of difference equations that give the solution to the coupled set of equations involving the operators \mathbb{N}_{2j} is then

$$\begin{aligned} A_1^{(n+1)} = & A_1^{(n)} + \Delta z \frac{i\omega_1}{n_1 c} \left\{ d_1 f_3 f_1^* e^{i\Delta k_1(z^{(n)} + \Delta z/2)} + d_3 f_4 f_1^* e^{i\Delta k_3(z^{(n)} + \Delta z/2)} \right. \\ & + d_2 f_3 f_2^* e^{i\Delta k_2(z^{(n)} + \Delta z/2)} + d_4 f_4 f_2^* e^{i\Delta k_4(z^{(n)} + \Delta z/2)} + d_5 f_5 f_4^* e^{i\Delta k_5(z^{(n)} + \Delta z/2)} \\ & + d_7 f_5 f_3^* e^{i\Delta k_7(z^{(n)} + \Delta z/2)} + 3C_1 f_5 f_2^* f_1^* e^{i\Delta k_9(z^{(n)} + \Delta z/2)} \\ & \left. + \frac{3C_2}{2} f_5 (f_1^*)^2 e^{i\Delta k_{10}(z^{(n)} + \Delta z/2)} \right\}, \end{aligned} \quad (4.118)$$

$$\begin{aligned}
A_2^{(n+1)} = & A_2^{(n)} + \Delta z \frac{i\omega_2}{n_2 c} \left\{ d_2 f_3 f_1^* e^{i\Delta k_2(z^{(n)} + \Delta z/2)} + d_4 f_4 f_1^* e^{i\Delta k_4(z^{(n)} + \Delta z/2)} \right. \\
& + d_6 f_5 f_4^* e^{i\Delta k_6(z^{(n)} + \Delta z/2)} \\
& \left. + d_8 f_5 f_3^* e^{i\Delta k_8(z^{(n)} + \Delta z/2)} + \frac{3C_1}{2} f_5 (f_1^*)^2 e^{i\Delta k_9(z^{(n)} + \Delta z/2)} \right\}, \quad (4.119)
\end{aligned}$$

$$\begin{aligned}
A_3^{(n+1)} = & A_3^{(n)} + \Delta z \frac{i\omega_3}{n_3 c} \left\{ \frac{d_1}{2} (f_1)^2 e^{-i\Delta k_1(z^{(n)} + \Delta z/2)} + d_2 f_2 f_1 e^{-i\Delta k_2(z^{(n)} + \Delta z/2)} \right. \\
& \left. + d_7 f_5 f_1^* e^{i\Delta k_7(z^{(n)} + \Delta z/2)} + d_8 f_5 f_2^* e^{i\Delta k_8(z^{(n)} + \Delta z/2)} \right\}, \quad (4.120)
\end{aligned}$$

$$\begin{aligned}
A_4^{(n+1)} = & A_4^{(n)} + \Delta z \frac{i\omega_4}{n_4 c} \left\{ \frac{d_3}{2} (f_1)^2 e^{-i\Delta k_3(z^{(n)} + \Delta z/2)} + d_4 f_2 f_1 e^{-i\Delta k_4(z^{(n)} + \Delta z/2)} \right. \\
& \left. + d_5 f_5 f_1^* e^{i\Delta k_5(z^{(n)} + \Delta z/2)} + d_6 f_5 f_2^* e^{i\Delta k_6(z^{(n)} + \Delta z/2)} \right\}, \text{ and} \quad (4.121)
\end{aligned}$$

$$\begin{aligned}
A_5^{(n+1)} = & A_5^{(n)} + \Delta z \frac{i\omega_5}{n_5 c} \left\{ d_5 f_4 f_1 e^{-i\Delta k_5(z^{(n)} + \Delta z/2)} + d_6 f_4 f_2 e^{-i\Delta k_6(z^{(n)} + \Delta z/2)} \right. \\
& + d_7 f_3 f_1 e^{-i\Delta k_7(z^{(n)} + \Delta z/2)} + d_8 f_3 f_2 e^{-i\Delta k_8(z^{(n)} + \Delta z/2)} \\
& \left. + \frac{3C_1}{2} f_2 (f_1)^2 e^{-i\Delta k_9(z^{(n)} + \Delta z/2)} + \frac{C_2}{2} (f_1)^3 e^{-i\Delta k_{10}(z^{(n)} + \Delta z/2)} \right\} \quad (4.122)
\end{aligned}$$

where

$$\begin{aligned}
f_1 = & A_1^{(n)} + \frac{i\Delta z \omega_1}{2n_1 c} \left(d_1 A_3^{(n)} A_1^{(n)*} e^{i\Delta k_1 z^{(n)}} + d_3 A_4^{(n)} A_1^{(n)*} e^{i\Delta k_3 z^{(n)}} + d_2 A_3^{(n)} A_2^{(n)*} e^{i\Delta k_2 z^{(n)}} \right. \\
& + d_4 A_4^{(n)} A_2^{(n)*} e^{i\Delta k_4 z^{(n)}} + d_5 A_5^{(n)} A_4^{(n)*} e^{i\Delta k_5 z^{(n)}} + d_7 A_5^{(n)} A_3^{(n)*} e^{i\Delta k_7 z^{(n)}} \\
& \left. + 3C_1 A_5^{(n)} A_2^{(n)*} A_1^{(n)*} e^{i\Delta k_9 z^{(n)}} + \frac{3C_2}{2} A_5^{(n)} (A_1^{(n)*})^2 e^{i\Delta k_{10} z^{(n)}} \right), \quad (4.123)
\end{aligned}$$

$$\begin{aligned}
f_2 = & A_2^{(n)} + \frac{i\Delta z \omega_2}{2n_2 c} \left(d_2 A_3^{(n)} A_1^{(n)*} e^{i\Delta k_2 z^{(n)}} + d_4 A_4^{(n)} A_1^{(n)*} e^{i\Delta k_4 z^{(n)}} + d_6 A_5^{(n)} A_4^{(n)*} e^{i\Delta k_6 z^{(n)}} \right. \\
& \left. + d_8 A_5^{(n)} A_3^{(n)*} e^{i\Delta k_8 z^{(n)}} + \frac{3C_1}{2} A_5^{(n)} (A_1^{(n)*})^2 e^{i\Delta k_9 z^{(n)}} \right), \quad (4.124)
\end{aligned}$$

$$\begin{aligned}
f_3 = & A_3^{(n)} + \frac{i\Delta z \omega_3}{2n_3 c} \left(\frac{d_1}{2} (A_1^{(n)})^2 e^{-i\Delta k_1 z^{(n)}} + d_2 A_2^{(n)} A_1^{(n)} e^{-i\Delta k_2 z^{(n)}} \right. \\
& \left. + d_7 A_5^{(n)} A_1^{(n)*} e^{i\Delta k_7 z^{(n)}} + d_8 A_5^{(n)} A_2^{(n)*} e^{i\Delta k_8 z^{(n)}} \right), \quad (4.125)
\end{aligned}$$

$$\begin{aligned}
f_4 = & A_4^{(n)} + \frac{i\Delta z \omega_4}{2n_4 c} \left(\frac{d_3}{2} (A_1^{(n)})^2 e^{-i\Delta k_3 z^{(n)}} + d_4 A_2^{(n)} A_1^{(n)} e^{-i\Delta k_4 z^{(n)}} \right. \\
& \left. + d_5 A_5^{(n)} A_1^{(n)*} e^{i\Delta k_5 z^{(n)}} + d_6 A_5^{(n)} A_2^{(n)*} e^{i\Delta k_6 z^{(n)}} \right), \text{ and} \quad (4.126)
\end{aligned}$$

$$\begin{aligned}
f_5 = & A_5^{(n)} + \frac{i\Delta z\omega_5}{2n_5c} \left(d_7 A_3^{(n)} A_1^{(n)} e^{-i\Delta k_7 z^{(n)}} + d_5 A_4^{(n)} A_1^{(n)} e^{-i\Delta k_5 z^{(n)}} \right. \\
& + d_8 A_3^{(n)} A_2^{(n)} e^{-i\Delta k_8 z^{(n)}} + d_6 A_4^{(n)} A_2^{(n)} e^{-i\Delta k_6 z^{(n)}} \\
& \left. + \frac{3C_1}{2} (A_1^{(n)})^2 A_2^{(n)} e^{-i\Delta k_9 z^{(n)}} + \frac{C_2}{2} (A_1^{(n)})^3 e^{-i\Delta k_{10} z^{(n)}} \right). \quad (4.127)
\end{aligned}$$

Finally, by splitting the dispersive operation into two half-steps (over an interval $\Delta z/2$), one before the nonlinear operation and one after, the overall operation (dispersive and nonlinear parts) becomes unitary and the accuracy of the method is improved. This is known as the symmetrized or symmetric split-step method.^{103,100}

A FORTRAN code was written to perform these calculations for all three spatial dimensions plus time (or any subset of these). As mentioned previously, the calculations include group-velocity mismatch and group-velocity dispersion effects as well as diffraction and transverse spatial walkoff (for uniaxial crystals). At present, the initial envelope amplitudes $|A_j(x, y, 0, t)|$ can be a super-gaussian of arbitrary order, or the transverse amplitude dependence can be input from an image file from a CCD camera. Providing for the input of initial phase information could be added in a straight-forward manner if so desired. The code can be used to model any second-order frequency conversion process (e.g. SHG, SFG, DFG, OPA) in a single crystal as well as all types of single crystal THG. The effective nonlinear coupling coefficients d_j and C_j are calculated for the given configuration from the reduced nonlinear tensor elements d_{ij} and C_{ij} following Eqs. (4.65) and (4.66). The nonlinear medium can be chosen from the list presented in the previous section, and additional materials can be added by inserting the Sellmeier data and the appropriate values for d_{ij} and C_{ij} .

It was found that even 4-d calculations (with a $64 \times 64 \times 64$ grid and a few tens of z-steps) could be run for a typical crystal in a few minutes on a fast workstation if

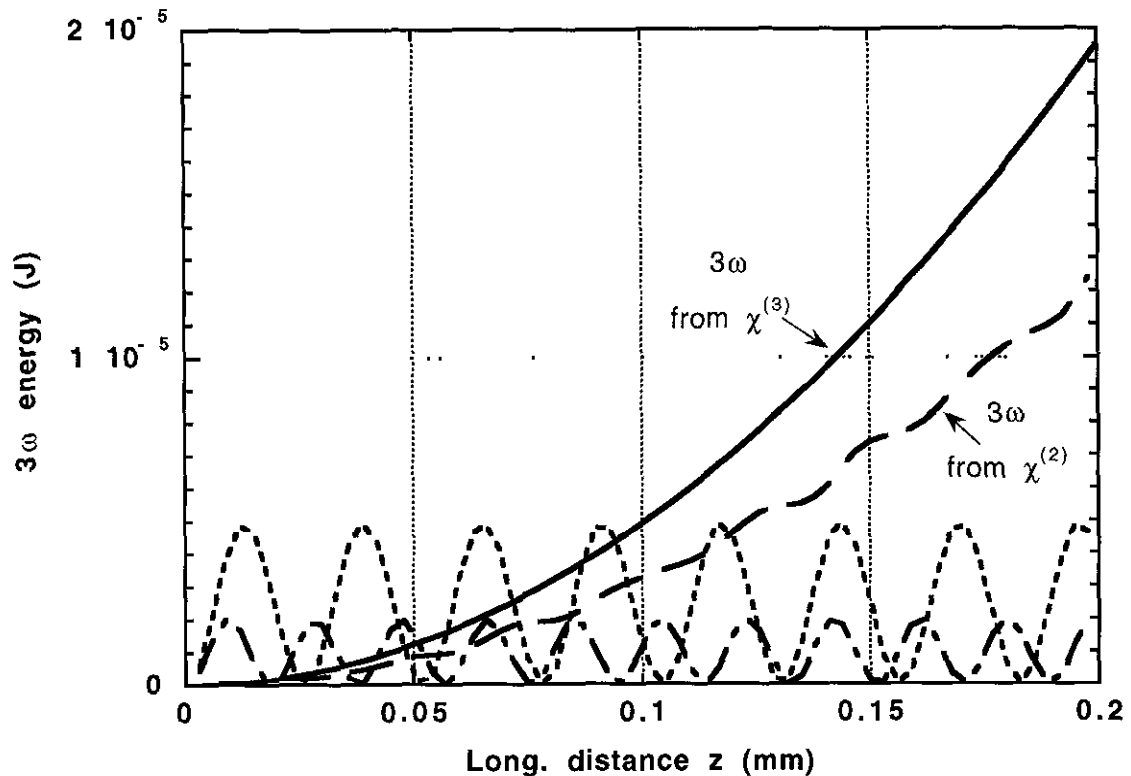


Figure 4.6 Calculated amplitudes of electric field envelope functions A_j as a function of propagation distance in the crystal. The solid line shows what would be expected for third harmonic in presence of $\chi^{(3)}$ only while dashed line shows expected behavior for third harmonic in presence of $\chi^{(2)}$ only. The dotted and dash-dotted lines are the ordinary and extraordinary second harmonic waves, respectively.

the second-order coupling terms were set to 0. However, the inclusion of these terms in THG calculations, because they are unphasematched, introduces a rapidly oscillating component in addition to the slowly varying third harmonic wave, i.e. it becomes a stiff set of equations. This requires the step size in z to be reduced greatly (by as much as a factor of 100). The calculation times correspondingly increase to a few hours for crystals of a few millimeters thickness. An illustration of this in the small signal growth of the second and third harmonic waves is shown in Fig. 4.6. If the interaction is due only to a third-order nonlinearity, the growth with propagation distance is smooth and is simply proportional to z^2 as expected. However, if the THG is due solely to a second-

order nonlinear coupling, the growth of the third harmonic wave is modulated due to the periodic behavior of the intermediate second harmonic waves. The step size used in the calculations must be smaller than this short scale-length variation.

A test of the accuracy of the model for SHG was discussed in Section 2.2.1 for pulses of the nanosecond regime with good results. In addition, second-harmonic conversion of both 1053 nm light at 350 fs (parameters for the front end of the Petawatt laser at LLNL) and 820 nm light at both 350 fs and 100 fs (the latter pulse length is typical of Ti:sapphire amplifier systems) was examined using this code in both KD*P and BBO. For a perfectly uniform transverse spatial profile, the calculated maximum conversion efficiencies are shown in Figs. 4.7, 4.8, and 4.10(a). In Figs. 4.9 and 4.10(b), the propagation distance in the crystal required to reach maximum conversion efficiency is shown.

The behavior of the curves in these graphs illustrate the effects of self-phase modulation and GVM walkoff which are significant in the frequency conversion of sub-picosecond pulse. (For further calculations of the effects of group velocity dispersion effects, see, for example, Sidick *et al.*^{104,105}) First, the decrease in conversion efficiency for higher input intensities for Type I phasematching is due to the induced phase mismatch from the nonlinear refractive index as discussed in Section 4.2.3. Although, as was mentioned, the relevant values for the coefficients C_j^{SPM} and C_j^{XPM} are uncertain, it was assumed that $C_1^{\text{SPM}} = C_2^{\text{SPM}} = 10^{-22} \text{ m}^2/\text{V}^2$, $C_5^{\text{SPM}} = 1.3C_1^{\text{SPM}}$, and that $C_j^{\text{XPM}} = 0$ for purposes of illustration. This effect is also significant for Type II phasematching, but the conversion for low intensities is dominated by group velocity walkoff effects. The effect of the induced phase mismatch is less for BBO because the larger nonlinear susceptibility of BBO cause that the maximum conversion occurs over a shorter distance, thereby lessening the effect of the phase mismatch, i.e. l is smaller so Δkl is also smaller.

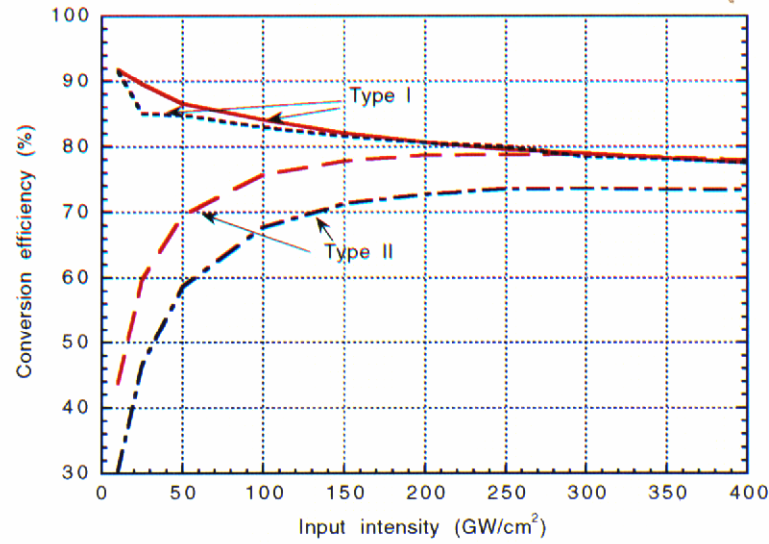


Figure 4.7: Calculated conversion efficiency for SHG of a uniform spatial profile in KD*P as a function of fundamental input intensity. The solid curve is Type I phasematching at 1053 nm (350 fs), the dashed curve is Type II phasematching at 1053 nm (350 fs), the dotted curve is Type I phasematching at 820 nm (350 fs), and the dash-dotted curve is Type II phasematching at 820 nm (350 fs).

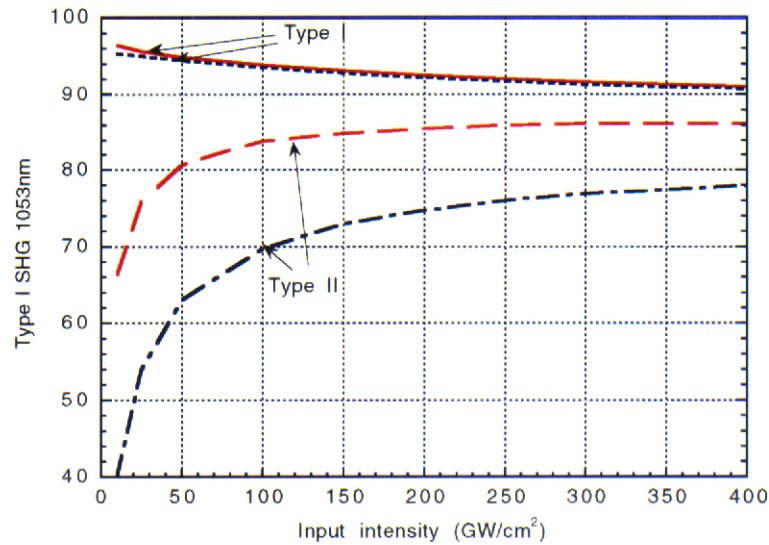


Figure 4.8: Calculated conversion efficiency for SHG of a uniform spatial profile in BBO as a function of fundamental input intensity. The solid curve is Type I phasematching at 1053 nm (350 fs), the dashed curve is Type II phasematching at 1053 nm (350 fs), the dotted curve is Type I phasematching at 820 nm (350 fs), and the dash-dotted curve is Type II phasematching at 820 nm (350 fs).

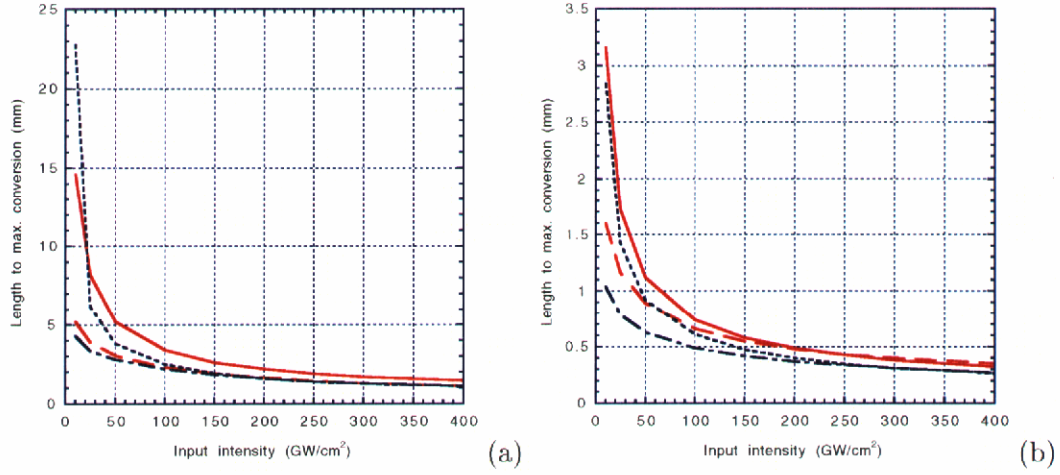


Figure 4.9: Distance in KD*P (a) and BBO (b) crystal required to reach maximum conversion efficiency. The solid curve is Type I phasematching at 1053 nm (350 fs), the dashed curve is Type II phasematching at 1053 nm (350 fs), the dotted curve is Type I phasematching at 820 nm (350 fs), and the dash-dotted curve is Type II phasematching at 820 nm (350 fs).

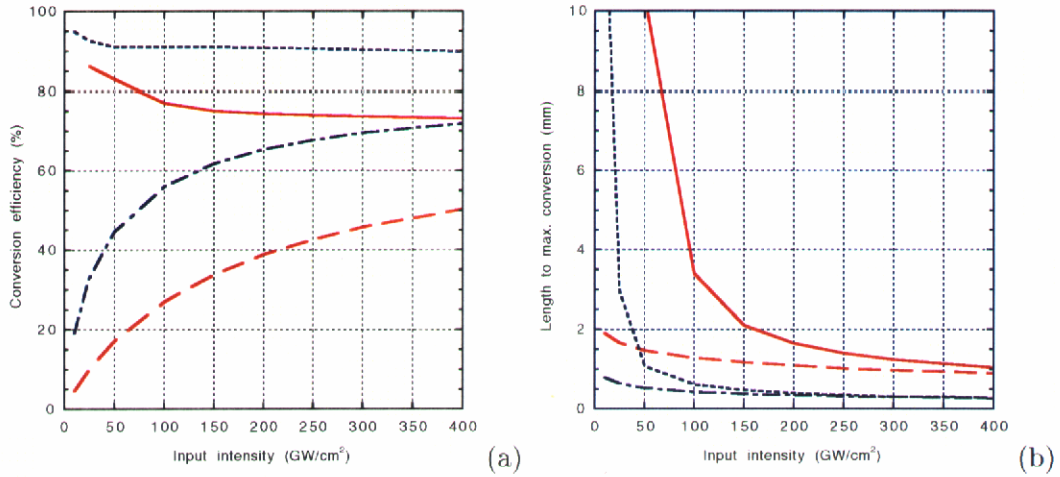


Figure 4.10: Conversion efficiency for SHG of a uniform spatial profile at 820 nm (100 fs) (a) and propagation distance in crystal required to reach maximum conversion efficiency (b) for Type I phasematching in KD*P (solid line), Type II phasematching in KD*P (dashed line), Type I phasematching in BBO (dotted line), and Type II phasematching in BBO.

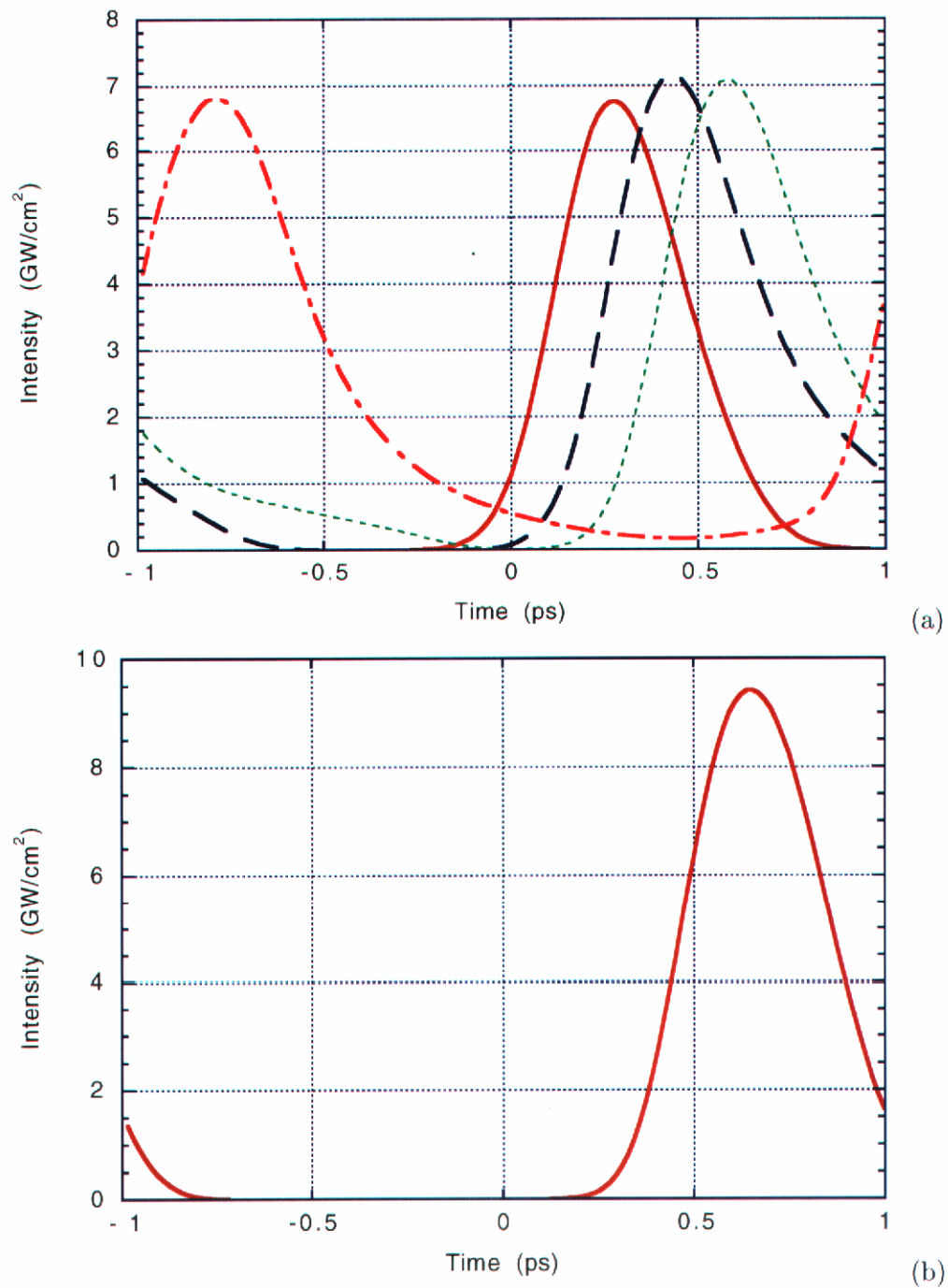


Figure 4.11: Calculated temporal profiles of generated second harmonic pulses for Type I phasematching of 820 nm light (350 fs) (a) and 1053 nm light (350 fs) (b) at 50 GW/cm² input intensity. In (a), the profile is given after 5 mm (solid line), 10 mm (dashed line), 15 mm (dotted line), and 23 mm (dash-dotted line). In (b), the pulse is shown after 14 mm (point of maximum conversion).

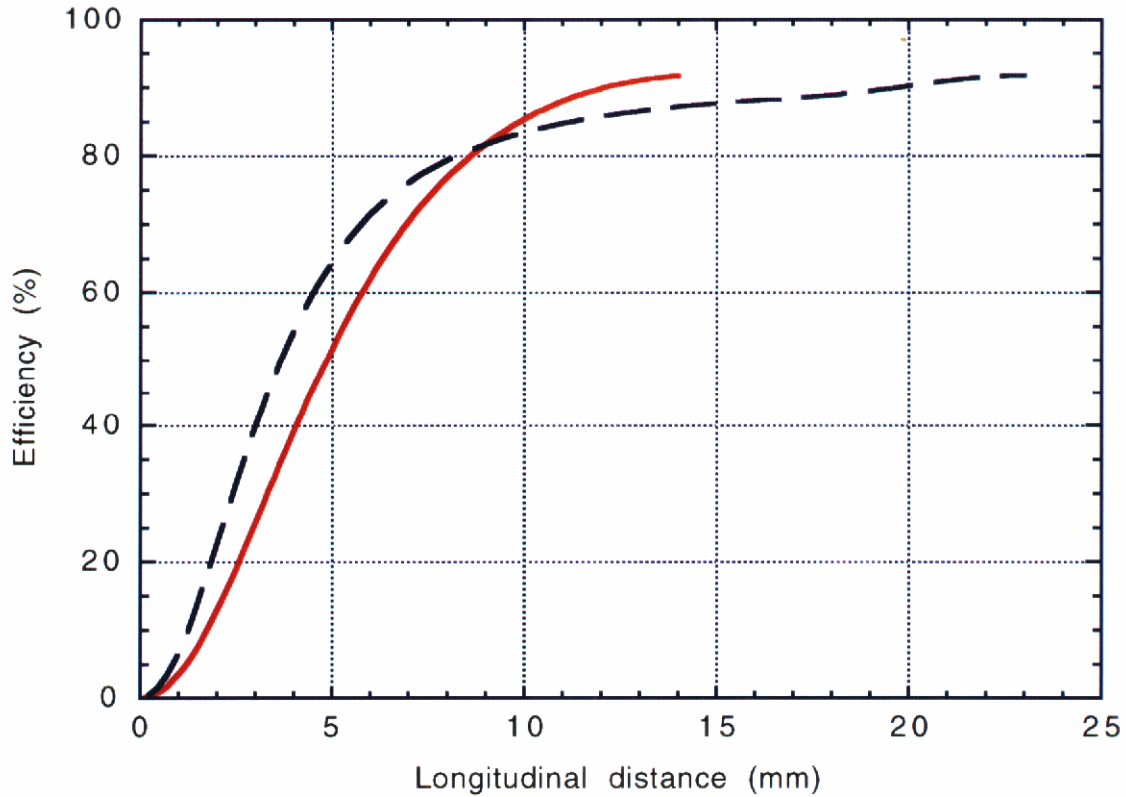


Figure 4.12: Calculated conversion efficiency as a function of longitudinal distance for Type I SHG in KD*P crystal at 1053 nm (solid line) and 820 nm (dashed line) (350 fs).

Type I phasematching in KD*P at 820 nm and 1053 nm provides a good illustration of what can occur as the pulses at different frequencies walk off from each other in time. As seen in Fig. 4.11(a), as the fundamental and second harmonic pulses separate in time, conversion still occurs, adding energy to the foot of the leading edge of the second harmonic pulse. This pulse distortion becomes worse as the pulse propagates in the crystal (the curves in Fig. 4.11(a) are the pulse shapes at .5, 1, 1.5, and 2.3 cm into the crystal). By comparison, because of the linear dispersion properties of KD*P near 1053 nm,¹⁸ the group velocities of the 1053 nm wave and the 527 nm wave are nearly equal. Therefore, (see Table 4.18) the propagation distance required to walk off from each other is 3 cm. The resulting 2ω pulse shown in Fig. 4.11(b) shows no comparable distortion. The slow addition of energy to a leading pedestal because of walkoff can also be seen in Fig. 4.12.

The curves for both wavelengths have a similar initial rise, but for 820 nm light (where walkoff is important), there is a slowly rising tail which is when the conversion is into the second harmonic pedestal. The effect of GVM on single-crystal THG will be discussed in more detail in Chapter 5.

In addition to second harmonic generation calculations, this code was also used to calculate expected efficiencies for two-crystal THG, again for uniform spatial profiles. For two-crystal THG, there is a complex relationship between the SHG efficiency in the first crystal and the SFG (and overall) efficiency in the second crystal. Nonetheless, it was found that for Type I SHG followed by Type II SFG, calculated overall THG efficiencies of approximately 50% were obtained for 200 GW/cm² input in KD*P at 1053 nm and 350 fs (the crystal lengths were 2 mm and 1 mm). Increasing the input intensity to 800 GW/cm² had only a small effect on the maximum efficiency (approximately 55%) but shortened the crystal lengths to 1.2 mm and .5 mm.

There was also an opportunity to parallelize this code for use on the massively parallel Cray T3D using parallel FFT routines written by Tim Williams at NERSC. It was found that it scaled quite well with the number of processors used with the execution time decreasing almost as $1/N$ for large problems, where N is the number of processors utilized. This is true if the overhead required to initialize the job was subtracted. However, the need to coordinate the I/O of N processors on a system level has not yet been adequately addressed which makes the use of MPP machines more complicated than would be desired. And since it has so far been possible to run the problems of interest on a workstation, the effort required to manage the I/O issues made running on the MPP machine less compelling. However, for larger problems, the decrease in computational time possible by using MPP machines with this algorithm will warrant the added effort.

4.6 Conclusion

The number of processes involved in harmonic generation using such high intensity pulses is very large, and they all are likely to have a significant effect. Of particular interest is the contribution to the generation of the third harmonic of unphasematched, cascaded second-order interactions. This shall be examined in more detail in Chapter 5. A computational algorithm for modeling the interaction of these five waves has been developed, and some calculations for second-harmonic generation of short pulses were presented. Maximum efficiencies for two-crystal third harmonic generation were calculated to be approximately 50–60% in KD*P at 1053 nm. The effective nonlinear coefficients have been presented for all possible interactions (if dispersion is neglected) for both second- and third-order processes in uniaxial crystals. Finally, the groundwork was presented for performing the same calculations for biaxial crystals. However, the formulas are so complicated due to the angular dependence of the polarization eigendirections that writing them down is of little use. They can, nonetheless, be easily calculated numerically.

Chapter 5

High intensity third harmonic generation

Generation of the third harmonic (THG) using the third-order susceptibility is an idea that has been around since the inception of nonlinear optics.^{10,11,106,107} However, since the process $\omega + \omega + \omega \rightarrow 3\omega$ is governed by the third order nonlinear electric susceptibility $\chi^{(3)}$, the efficiency of such an interaction is very low unless very high intensity beams are used. To this date, the high intensities needed to drive this process has confined most research into higher order harmonic conversion to highly focused beams in gases or liquids. This is because for nanosecond pulses, material damage thresholds are less than approximately 10 GW/cm². Additionally, even for lasers with pulse energies of 10 J, it is still necessary to focus the beam in order to achieve high irradiance. This reduces the effective interaction lengths because of spatial walkoff with the small beam waist and the spread in **k**-vectors from the focus.

However, it has long been held and recently verified for a wide range of pulse lengths¹⁷ that the damage intensity threshold scales inversely with the square root of the pulse

length. Coupled with the fact that decreasing the pulse length also increases the peak intensity, this makes short pulses attractive for high intensity studies in solids. In addition, the advances in chirped-pulse amplification (CPA) laser design in recent years has made terawatt-class lasers (and beyond) possible with small-scale laser systems. This technology has made it possible to achieve very high intensities ($> 100 \text{ GW/cm}^2$) in collimated beams that will not damage solid material.

CPA laser systems such as the one described in Chapters 2 and 3 can produce peak powers of 1 TW with pulse energies of only 50 mJ. Even with a 2 cm diameter beam, this is a peak intensity of 500 GW/cm^2 for a gaussian spatial mode. At the same time, the surface damage limit is as high as 14 TW/cm^2 (Ref. 17) in fused silica at $1 \mu\text{m}$. Long before such intensities are reached, nonlinear effects of all types will have large impacts on the pulse evolution. The main interest of this work is the generation of the third harmonic in a single crystalline solid.

A few studies of single-crystal THG in solid materials have been done recently, particularly in BBO^{28,29} using pulse lengths from 5 to 45 ps. In fact, Ref. 28 reports a conversion efficiency of 1% with 50 GW/cm^2 input intensity. However, as mentioned previously, there are many errors in that paper, and their calculations of C_{eff} do not match the input parameters which they give. In addition, uncertainties in the value obtained for C_{eff} in either reference are such that the observed effect could be due to either an entirely cascaded second-order nonlinearity, an entirely third-order nonlinearity, or some combination of the two.

Because of these uncertainties, and taking advantage of the higher intensities possible in collimated beams using CPA laser systems, THG in BBO was again examined. Single-crystal THG was also studied in two other materials: KD*P and d-LAP, with the largest

conversion taking place in BBO. As mentioned previously, larger birefringence is needed to phasematch THG than SHG, and this is exacerbated as the third harmonic wavelength becomes shorter. It was, therefore, found most convenient to conduct these experiments at 1053 nm using the CPA system described in Ref. 49. At intensities of 240 GW/cm² we were able to produce up to .6 mJ of third harmonic light in single crystal of BBO with conversion efficiencies above 6%. We were also able to observe the azimuthal angular dependence for both Type I and Type II phasematching configurations and determine the magnitude of the third-order susceptibility tensor elements of BBO relative to the second-order elements. Some slight clouding in the bulk of the BBO crystal was observed at the maximum intensity, probably due to the intense UV light generated. Finally, if this damage can be eliminated, peak conversion efficiencies in the 30–40% range are calculated to be achievable, limited mainly by phase modulation effects.

5.1 BBO

The material BBO (beta-barium borate, β -BaB₂O₄) is of the crystal class 3m. However, there is some discrepancy concerning the choice of x and y axes in the literature (they are occasionally reversed).¹⁰⁸ For all other uniaxial classes, this is unimportant under Kleinman symmetry conditions because both d_{ij} and C_{ij} are isometric on interchange of x and y. However, class 3m is not; the IRE/IEEE standard^{109,110} defines the axes so that $d_{11} = 0$ and $d_{22} \neq 0$ (x is perpendicular to a mirror plane). The matter is also confused with regard to the third-order susceptibility. Butcher¹¹¹ gives the nonzero tensor elements for linear, second-order, and third-order tensor elements due to crystal symmetry requirements. These calculations were later corrected by Zhao¹¹² for classes $\bar{4}2m$, 422, 4mm, 4/mmm, 3, $\bar{3}$, 6, $\bar{6}$, and 6/m, and Shang and Hsu¹¹³ later further corrected 3 and $\bar{3}$

and added corrections for classes 3m, $\bar{3}m$, and 32. These results have been published in many reference works^{114,72,115} along with the forms for d_{ij} which follow the IRE standard.

Unfortunately, the correction Shang and Hsu made to the form for $\chi_{ijkl}^{(3)}$ for classes 3m, etc., was to define the x and y axes such that y is perpendicular to the mirror plane (m) which does not conform to the IRE standard. In fact, this same switch was made by Yang in presenting collapsed forms C_{ij} for all crystal classes,¹¹⁶ and he makes special mention of how the forms in Refs. 72 and 83 are incorrect. It is easy to show that Shang and Hsu and Yang do not use the IRE standard reference frame since, if the x axis is perpendicular to m, exchanging x with -x should have no effect because $\chi^{(3)}$ is a fourth-rank tensor and has even symmetry. This means that all tensor elements with an odd number of subscripts of 1 must be zero. This means, for example, that the element $\chi_{1223}^{(3)} = \chi_{15}^{(3)} \equiv 0$, but Shang and Hsu report this element as nonzero. The original form given by Butcher should then be used. This inconsistency in definition is not critical in and of itself, but when both second- and third-order effects play an important role, it will lead to incorrect forms for the effective nonlinear coupling. It is also confusing to have many texts referring to this form for $\chi^{(3)}$ as complying with the standard definition for the reporting frame for the class 3m. The correct form for $\chi^{(3)}$ for crystal class 3m in the IRE standard reference frame is then given in Table 5.1.

If Kleinman symmetry is assumed, this form also matches that of Midwinter and Warner⁸³ which gives

$$\mathbb{C} = \begin{bmatrix} C_{11} & 0 & 0 & 0 & 0 & C_{16} & 0 & C_{11}/3 & 0 & C_{10} \\ 0 & C_{11} & 0 & C_{16} & -C_{10} & 0 & C_{10} & 0 & C_{11}/3 & 0 \\ 0 & -C_{10} & C_{33} & 0 & C_{16} & 0 & C_{16} & 0 & C_{10} & 0 \end{bmatrix}. \quad (5.1)$$

They state that this form is based on using the nonzero elements of the elasto-optic tensor

Table 5.1: Correct nonzero third-order tensor elements for crystal class 3m.

$$\begin{aligned}
& zzzz \\
& xxyy = yyxx \\
& xxx = yyy = xxy + xyx + yxy \quad xyyx = yxy \\
& xyxy = yxyx \\
& yyzz = xxzz \\
& zzyy = zzzx \quad yyyz = -yxxz = -xyxz = -xxyz \\
& zyyz = zxzx \quad yyzy = -yxzx = -xyzx = -xxzy \\
& yzzz = xzzx \quad yzyy = -yzxx = -xzyx = -xzyy \\
& yzyz = xzxz \quad zyyy = -zyxx = -zxyx = -zxxy \\
& zyzy = zxzx
\end{aligned}$$

p_{ij} given by Nye.⁷³ It is also worth noting that Maker *et al.*⁹ also present the collapsed form C_{ij} for all crystal classes (including biaxials) assuming only THG, but not Kleinman symmetry. They, however, assume the nonstandard reference frame for the class 3m.

The crystal which was used in the experiments was from Cleveland Crystals and was cut at $\theta_m = 39.03^\circ$ and $\phi = 0^\circ$. It has a length of 3.31 mm and was sol-gel AR coated at the input for 1053 nm and 527 nm light and at the output for 351 nm light. The reflections from the input face are in the range of 1–2%, but should be fairly insensitive to input angle within the range of use (<15 – 20° from surface normal).

With a consistent reference frame for second- and third-order interactions, it is now possible to produce an expression for the effective nonlinear coefficient for THG in BBO.

For Type I phasematching,

$$C_{\text{eff}} = \frac{2\pi}{\lambda_{2\omega_0}} d_{22} \left[d_{22} \frac{\sin 6\phi}{2} \left(\frac{\cos \theta_m}{n_3 \Delta k_7} - \frac{\cos^3 \theta_m}{n_4 \Delta k_5} \right) + d_{15} \cos 3\phi \left(\frac{\cos^2 \theta_m \sin \theta_m}{n_4 \Delta k_5} - \frac{\sin \theta_m}{n_3 \Delta k_7} \right) \right]$$

$$+ C_{10} \cos 3\phi \sin \theta_m. \quad (5.2)$$

The equivalent expression for Type II phasematching is

$$\begin{aligned} C_{\text{eff}} = & \frac{2\pi}{\lambda_{2\omega_0}} \left[d_{22}^2 \left(\cos^2 3\phi \left(2 \frac{\cos^4 \theta_m}{n_4 \Delta k_5} - \frac{\cos^2 \theta_m}{n_3 \Delta k_8} \right) + \sin^2 3\phi \left(2 \frac{\cos^2 \theta_m}{n_3 \Delta k_7} - \frac{\cos^4 \theta_m}{n_4 \Delta k_6} \right) \right) \right. \\ & - 2d_{22}d_{15} \sin 3\phi \left(\frac{\sin \theta_m \cos^3 \theta_m}{n_4 \Delta k_6} + \frac{\sin 2\theta_m}{n_3 \Delta k_7} \right) \\ & + d_{15}^2 \sin^2 \theta_m \left(3 \frac{\cos^2 \theta_m}{n_4 \Delta k_6} + \frac{2}{n_4 \Delta k_5} \right) \\ & \left. + \frac{d_{33}}{n_4 \Delta k_6} \left(-d_{22} \sin 3\phi \cos \theta_m \sin^3 \theta_m + d_{15} \sin^4 \theta_m \right) \right] \\ & + 3 \left[\frac{C_{11}}{3} \cos^2 \theta_m + C_{16} \sin^2 \theta_m + C_{10} \sin 2\theta_m \sin 3\phi \right]. \end{aligned} \quad (5.3)$$

Again, Δk_j are defined by Eqs. (4.55)–(4.64) and $n_3 = n_{2\omega_0}^o$ and $n_4 = n_{2\omega_0}^e(\theta_m)$ (BBO is a negative uniaxial crystal so that the slow axis is the ordinary axis). Particularly for Type I phasematching, the difference in azimuthal angular dependence between second-order and third-order interactions is significant. This can be exploited to determine the relative magnitudes of the two types of interactions in single-crystal THG. The situation is somewhat more complicated for Type II phasematching because, first, the angular dependences are not so distinct, and second, the value for d_{33} is unknown since it is not involved in SHG.

5.1.1 Type I phasematching

In any event, the azimuthal angular dependence of C_{eff}^2 , which is proportional to $I_{3\omega}/I_\omega^3$, is shown in Fig. 5.1, separated into the second-order part and the third-order part. The behavior about $\phi = 0$ will easily show the relative magnitudes of the contributions of the different orders. This dependence was measured using the crystal described above and the setup shown in Fig. 5.2. An aperture of 4 mm diameter was placed directly in front of the crystal in order to ensure that the decreasing crystal aperture as the crystal

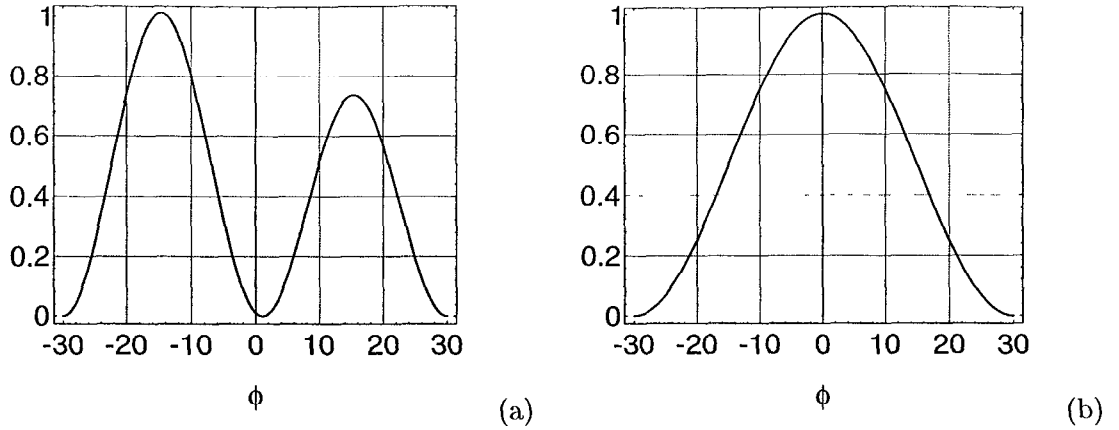


Figure 5.1: Dependence of C_{eff}^2 for Type I phasematching on azimuthal angle ϕ for (a) second-order interactions only and (b) third-order interactions only. The amplitudes are normalized to unity. In (a), $d_{15}/d_{22} = .16/2.2$.¹¹⁷

was rotated had no effect on the measurement. The azimuthal angle was scanned using a goniometer from -22° to $+22^\circ$ in 1° increments, and the energy ratio $\mathcal{E}_{3\omega}/\mathcal{E}_\omega^3 \propto I_{3\omega}/I_\omega^3$ was measured at each step (Fig. 5.3). This was done at both 4 mJ input energy and at 8 mJ input energy with the same results. This indicates that we are still operating in the low drive regime, i.e. $\mathcal{E}_{3\omega} \propto \mathcal{E}_\omega^3$. Approximately 10–20 measurements were taken at each angle at 10 Hz. This was then converted to the internal angle using Snell’s law $\phi_{\text{int}} = \sin^{-1}[(\sin \phi_{\text{ext}})/n_5]$. Because the crystal axis (which is the axis of rotation) is not perpendicular to the surface normal, the change of angle of incidence with change in ϕ_{ext} is fairly involved and using Snell’s law is not exactly true. However, performing the necessary coordinate transformations and rotations shows that using Snell’s law gives the internal angle to within 1% over the range of interest.

The spread in the nonlinear coupling at each value of ϕ is most likely due to small random variations in the pointing of the laser beam. Not only will this change the portion of the beam passing through the limiting aperture, but it will also cause slight fluctuations in the phasematching angle. In addition to systematic errors, there will also be some uncertainty because as ϕ is changed, the refraction at the surface also causes θ_m to change

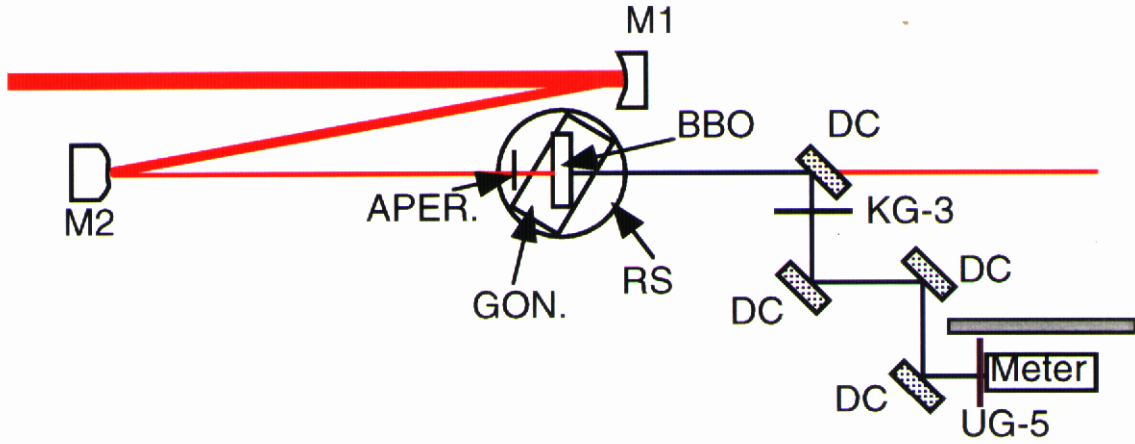


Figure 5.2: Experimental setup for measurement of THG. M1 and M2 are concave/convex mirror pair to down-collimate beam, RS denotes a rotation stage, GON denotes goniometer with axis of rotation parallel to c-axis, APER denotes the 4 mm aperture, KG-3 is KG-3 filter glass, UG-5 is UG-5 filter glass, DC are 4 dichroic mirrors, and Meter is a pyroelectric energy meter.

slightly. At each ϕ , the phasematching angle must be re-optimized which can result in slight random errors at each angle ϕ .

In order to relate the values measured for the effective coupling to C_{eff}^2 directly, precise values of the pulse length and beam size would need to be known as well as the interaction length. The beam sizes were measured on a CCD array and fit to gaussian profiles of 5.4 mm horizontally and 4.6 mm vertically, full width at $1/e^2$. The pulse length was measured using a single shot autocorrelator to be 500 fs. However, the transform limit of the pulses is approximately 350–400 fs indicating that pulses are chirped in some way. This creates an uncertainty in the effective interaction length due to the complicated nature of the way chirped pulses will interact as they walk off from each other temporally and the fact that the actual form of the chirp is unknown.

Fortunately, it is not necessary to know the intensities in order determine the relative contributions to C_{eff} from second- and third-order interactions. The beam sizes, pulse lengths, and interaction lengths simply are an overall multiplicative constant, i.e. $I_5/I_1^3 =$

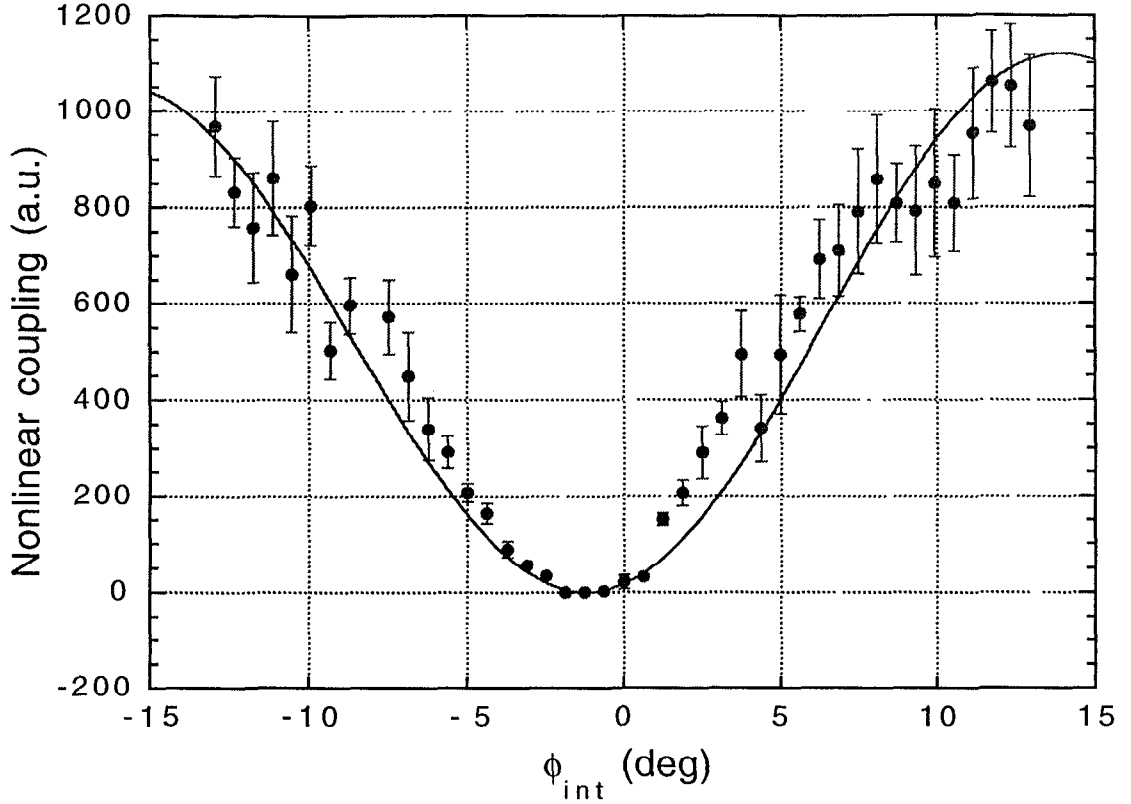


Figure 5.3: Effective nonlinear coupling for internal azimuthal angle ϕ_{int} .

AC_{eff}^2 . Then the nonlinear coupling C_{eff}^2 shown in Fig. 5.3 can be expressed as

$$C_{\text{eff}}^2 = A \left\{ \frac{2\pi}{\lambda_{2\omega_0}} \left[d_{22}^2 \frac{\sin 6\phi}{2} \left(\frac{\cos \theta_m}{n_3 \Delta k_7} - \frac{\cos^3 \theta_m}{n_4 \Delta k_5} \right) + \cos 3\phi \left[d_{22} d_{15} \left(\frac{\cos^2 \theta_m \sin \theta_m}{n_4 \Delta k_5} - \frac{\sin \theta_m}{n_3 \Delta k_7} \right) \right] + C_{10} \sin \theta_m \right] \right\}^2 \quad (5.4)$$

$$= A \left\{ -83.6 \text{ pm}^2/\text{V}^2 \sin 6\phi + (.61 C_{10} + 9.36 \text{ pm}^2/\text{V}^2) \cos 3\phi \right\}^2 \quad (5.5)$$

where $\Delta k_5 = 3300 \text{ cm}^{-1}$, $\Delta k_7 = -2400 \text{ cm}^{-1}$, $n_3 = 1.6755$, and $n_4 = 1.6277$. Here, values of $d_{22} = 2.2 \text{ pm/V}$ and $d_{15} = .16 \text{ pm/V}$ (Ref. 117) are used for the second-order susceptibility. It is possible that the origin for ϕ is slightly off because the crystal c-axis was not oriented precisely parallel to the table surface. Therefore, Eq. 5.5 is an equation with three unknown parameters: A , C_{10} , and ϕ_0 (ϕ in (5.5) becomes $(\phi - \phi_0)$) with A just a scaling factor and ϕ_0 giving the origin. A least squares fit of (5.5) was done on the

data in Fig. 5.3 and is shown as the line. This resulted in values of $A = .4$, $\phi_0 = -1^\circ$, and $.61C_{10} + 9.36 \text{ pm}^2/\text{V}^2 = -1.8 \text{ pm}^2/\text{V}^2$. This then gives a value for C_{10} of $-1.8 \pm .3 \times 10^{-23} \text{ m}^2/\text{V}^2$. The value obtained is sensitive to the value of the zero for ϕ which is the main source of uncertainty in the value. The light generated via the cascaded second-order process at $\phi = 15^\circ$ is 50–60 times that generated from the third order process.

It should be noted that there is some discrepancy in the reported magnitudes for d_{31} for BBO (ranging from .02 to .16 pm/V)^{117–119} and recently, experiments were done indicating that $d_{22}/d_{31} < 0$, i.e. they are of opposite sign.¹²⁰ This range of d_{31} gives a range for C_{10} from $-.4$ to $1.8 \times 10^{-23} \text{ m}^2/\text{V}^2$. Tomov *et al.*²⁹ give a value of $10^{-22} \text{ m}^2/\text{V}^2$ for C_{10} and state that, for Type I phasematching, the third-order nonlinearity is the dominant coupling mechanism. This, of course, is completely inconsistent with the data measured here. The advantage of this technique for measuring the third-order susceptibility tensor elements is that it is not necessary to have an accurate knowledge of the intensity of the beams involved, only an accurate knowledge of the angles. The uncertainty in C_{10} then rests mainly with uncertainty in the values for the second-order susceptibilities.

Finally, the sensitivity of the single-crystal THG process to the phasematching angle θ_m was examined. The generated UV signal was reduced to half of the peak value when the phasematching angle was changed by about $.1^\circ$. The side lobes expected from the sinc^2 functional dependence may be present but could not be clearly distinguished from the noise. Also, the spatial profile of the generated UV beam was measured both at low power (Fig. 5.4(b)) and at maximum intensity (Fig. 5.4(c)). At maximum intensity, the beam was attenuated by passing through 3 filters (about 6–8 mm of glass) which may distort the beam profile somewhat.

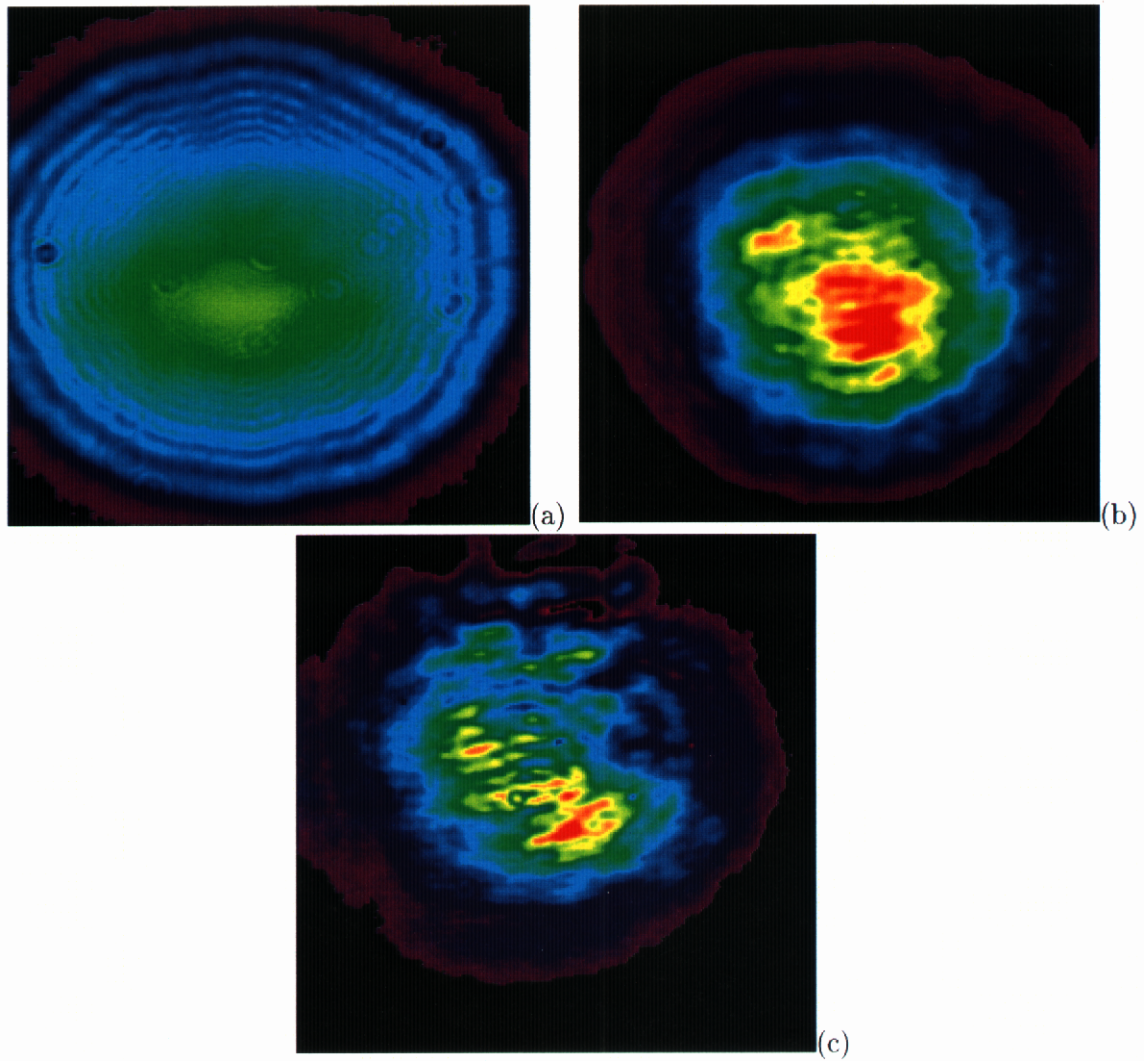


Figure 5.4: The spatial profiles of the incident fundamental beam (a), the generated UV beam at low conversion (b), and the UV beam at high conversion (c). The array is approximately 4 mm square.

5.1.2 Type II phasematching in BBO

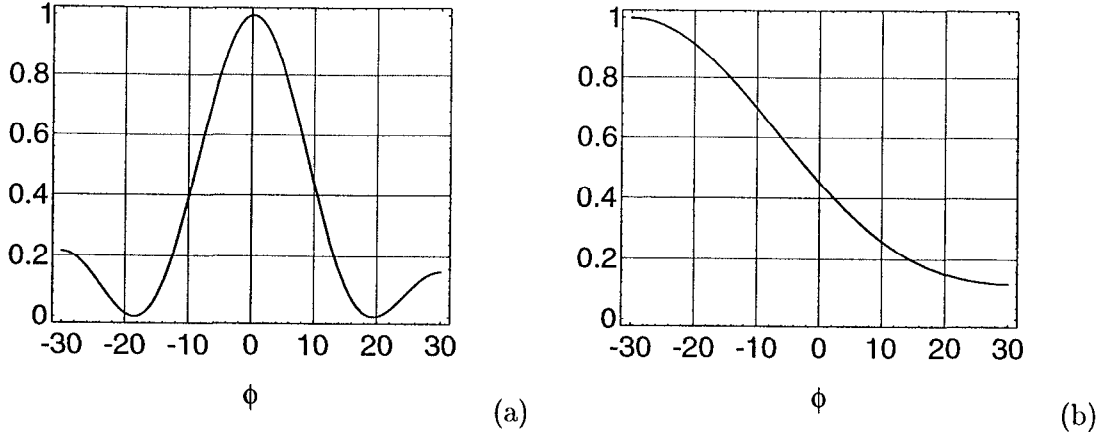


Figure 5.5: Dependence of C_{eff}^2 for Type II phasematching on azimuthal angle ϕ for (a) second-order interactions only and (b) third-order interactions only. The amplitudes are normalized to unity. In (b), it is assumed that $\frac{C_{11}}{3} \cos^2 \theta_m + C_{16} \sin^2 \theta_m = 2C_{10}$ for illustrative purposes.

By rotating the phasematching angle of the BBO crystal by 10° , it was possible to repeat this experiment for Type II phasematching ($\theta_m = 47.1^\circ$). However, as was mentioned before, using the form of C_{eff} (Eq. (5.3)) for Type II configurations is more complex. Nonetheless, the dependence on ϕ for second-order and third-order nonlinearities is quite different as shown in Fig. 5.5. Also, a simplification may be made since it is known that for BBO $d_{31} < .1d_{22}$ so all terms with d_{15}^2 may be neglected. Grouping terms by azimuthal dependence gives

$$\begin{aligned}
 C_{\text{eff}} = & Ad_{22}^2 \cos^2 3\phi + Bd_{22}^2 \sin^2 3\phi \\
 & + \sin 3\phi [Dd_{22}d_{15} + Ed_{22}d_{33} + 3C_{10} \sin 2\theta_m] \\
 & + Fd_{33}d_{15} + 3 \left[\frac{C_{11}}{3} \cos^2 \theta_m + C_{16} \sin^2 \theta_m \right]
 \end{aligned} \tag{5.6}$$

where

$$\begin{aligned}
 A &= \frac{2\pi}{\lambda_{2\omega_0}} \left[2 \frac{\cos^4 \theta_m}{n_4 \Delta k_5} - \frac{\cos^2 \theta_m}{n_3 \Delta k_8} \right] = 10.3, \\
 B &= \frac{2\pi}{\lambda_{2\omega_0}} \left[2 \frac{\cos^2 \theta_m}{n_3 \Delta k_7} - \frac{\cos^4 \theta_m}{n_4 \Delta k_6} \right] = -4.50,
 \end{aligned}$$

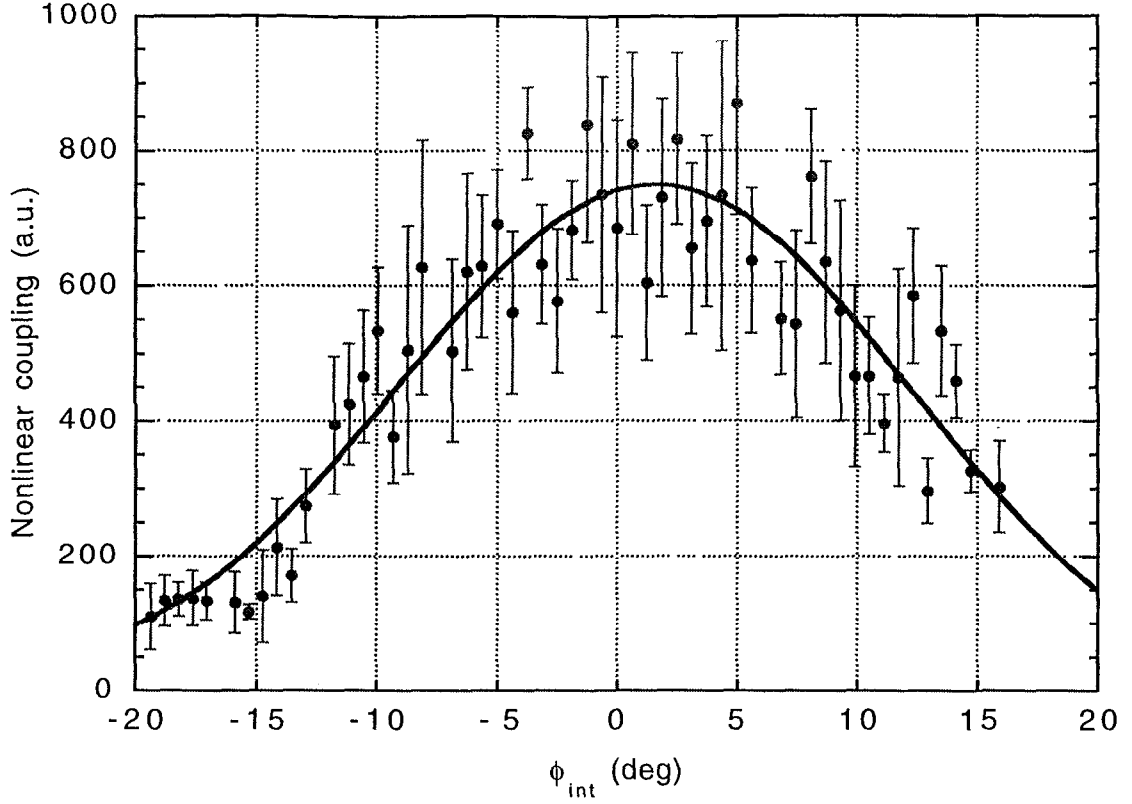


Figure 5.6: Effective nonlinear coupling for internal azimuthal angle ϕ_{int} . The solid line is a fit using known values for second-order coefficients.

$$\begin{aligned}
 D &= -2 \frac{2\pi}{\lambda_{2\omega_0}} \left[\frac{\sin \theta_m \cos^3 \theta_m}{n_4 \Delta k_6} + \frac{\sin 2\theta_m}{n_3 \Delta k_7} \right] = 5.64, \\
 E &= -\frac{2\pi}{\lambda_{2\omega_0}} \frac{\sin^3 \theta_m \cos \theta_m}{n_4 \Delta k_6} = -1.17, \text{ and} \\
 F &= \frac{2\pi}{\lambda_{2\omega_0}} \frac{\sin^4 \theta_m}{n_4 \Delta k_6} = 1.26.
 \end{aligned} \tag{5.7}$$

where $\Delta k_5 = 1870 \text{ cm}^{-1}$, $\Delta k_6 = 5650 \text{ cm}^{-1}$, $\Delta k_7 = -6180 \text{ cm}^{-1}$, $\Delta k_8 = -2400 \text{ cm}^{-1}$, $n_3 = 1.6755$, and $n_4 = 1.6080$.

Now, C_{10} is known from the Type I measurement (same crystal is being used) as is ϕ_0 so the only unknowns in Eq. (5.6) are d_{33} , C_{11} , and C_{16} . There is no way to distinguish between C_{11} and C_{16} . The data obtained are shown in Fig. 5.6 along with the fit obtained using Eq. (5.6). The fit parameters obtained are $A = .10$, $d_{33} = 1.7 \text{ pm/V}$, and $C_{11}(\cos^2 \theta_m)/3 + C_{16} \sin^2 \theta_m = 4.0 \pm .2 \times 10^{-23} \text{ m}^2/\text{V}^2$. The value obtained for d_{33} is

somewhat sensitive to values used for d_{15} and can range from 1 to 5 pm/V. The value for the third-order tensor elements is much less sensitive, thus the confidence interval given. This value agrees with the range given by Tomov *et al.* of $2-8 \times 10^{-23} \text{ m}^2/\text{V}^2$ and is on the low end of that given by Qui and Penzkofer of $6.4 \pm 2.8 \times 10^{-23} \text{ m}^2/\text{V}^2$. However, the level of 1% conversion efficiency is not reached until 80 GW/cm², not 50 GW/cm² as reported by Qiu and Penzkofer.

It should be noted again that the input beam in these measurements was a clipped gaussian spatial profile. Similar measurements without clipping were done and the maximum conversion efficiency achieved dropped to less than 4% for the same range of input intensities. The wings are converted very poorly. This illustrates the pronounced effect that the I^3 dependence on the input intensity has. The response to amplitude variations in space and time is even more pronounced than for SHG. It also indicates that flattop amplitude profiles can dramatically improve conversion efficiency.

The behavior of the THG energy generated as a function of input intensity was also investigated. The energies obtained at the third harmonic are shown in Figs. 5.7 and 5.8 along with cubic fits to the low intensity points (<50 GW/cm²). The corresponding efficiencies are shown in Figs. 5.9 and 5.10. The fit parameters are $5.33 \times 10^{-11} \text{ J}/(\text{GW}/\text{cm}^2)^3$ for Type I phasematching and $4.45 \times 10^{-11} \text{ J}/(\text{GW}/\text{cm}^2)^3$ for Type II phasematching (4 mm beam size). Type I phasematching gives better conversion even though according to the previous calculations, $C_{\text{eff}}^{\text{I}}(-15^\circ) = 8.2 \times 10^{-23} \text{ m}^2/\text{V}^2$ while $C_{\text{eff}}^{\text{II}}(0^\circ) = \sqrt{\frac{4}{3}}(9.0 \times 10^{-23}) \text{ m}^2/\text{V}^2$. The factor $\sqrt{4/3}$ is from the degeneracy factor of 3 for Type II phasematching coupled with the factor of 4/27 from the initial intensities being divided between the two polarizations of the fundamental as discussed in Section 4.2.4.

Higher conversion efficiencies for Type I phasematching is possible because of the dif-

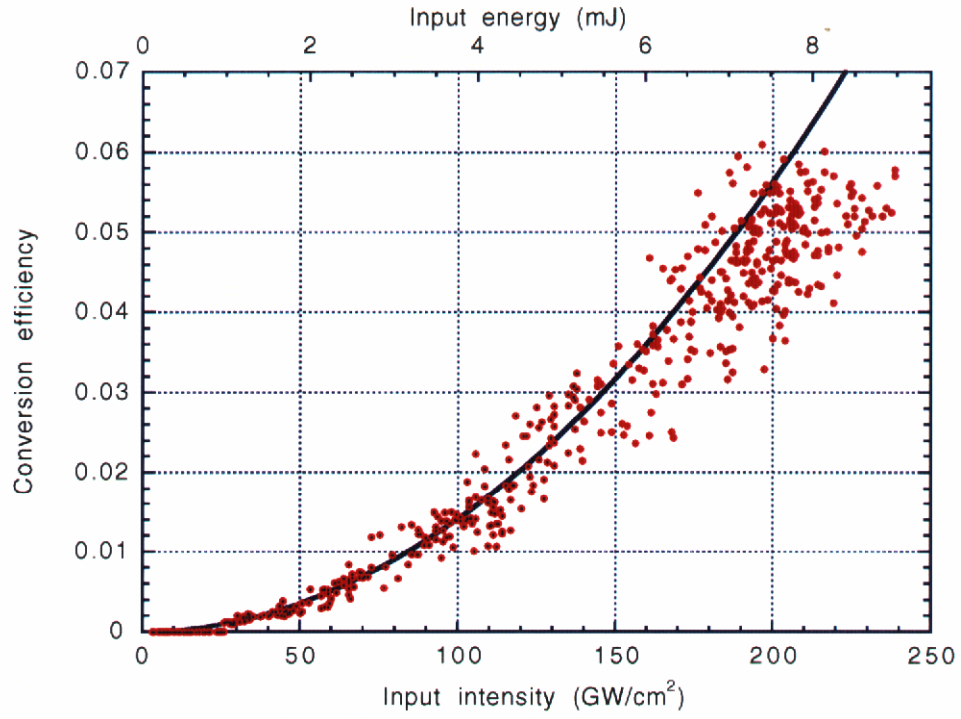


Figure 5.7: Energy output from single BBO crystal at 351 nm along with cubic fit to low drive points. Type I phasematching with $\phi_{\text{int}} = -15^\circ$.

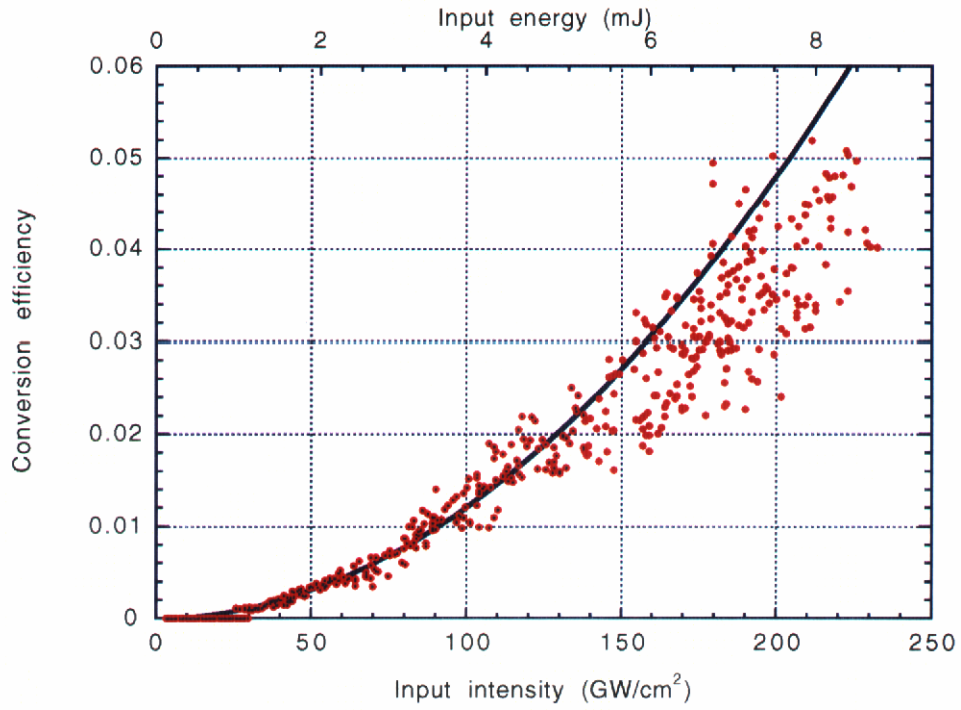


Figure 5.8: Energy output from single BBO crystal at 351 nm along with cubic fit to low drive points. Type II phasematching ($\phi_{\text{int}} = 0^\circ$).

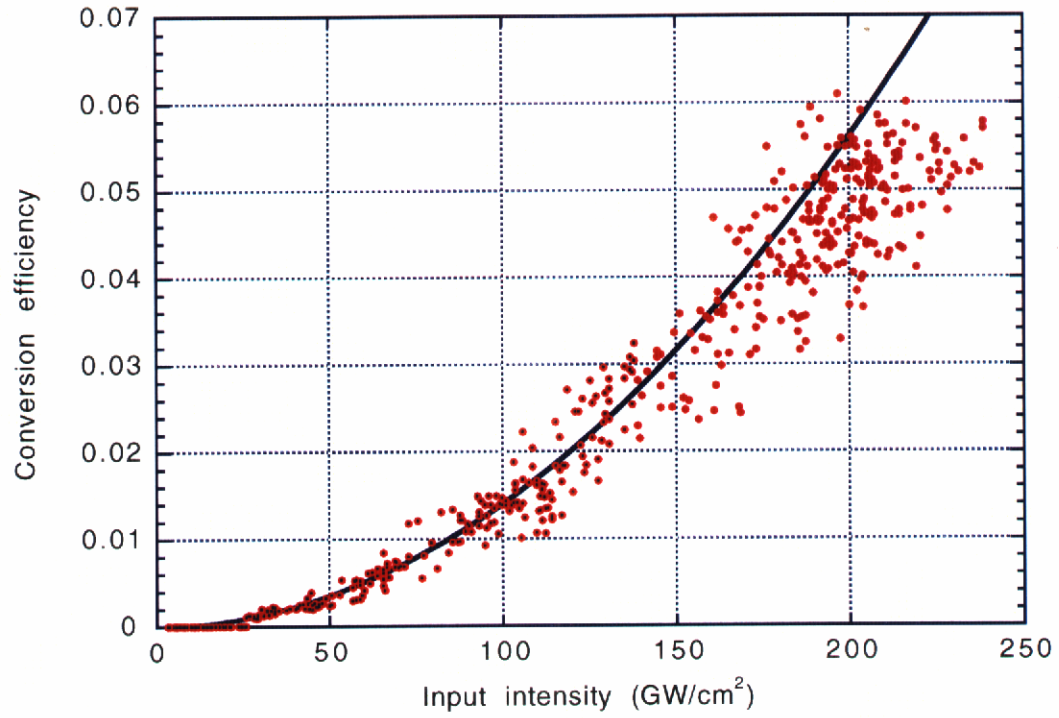


Figure 5.9: Conversion efficiency from single BBO crystal at 351 nm along with quadratic fit to low drive points. Type I phasematching with $\phi_{\text{int}} = -15^\circ$.

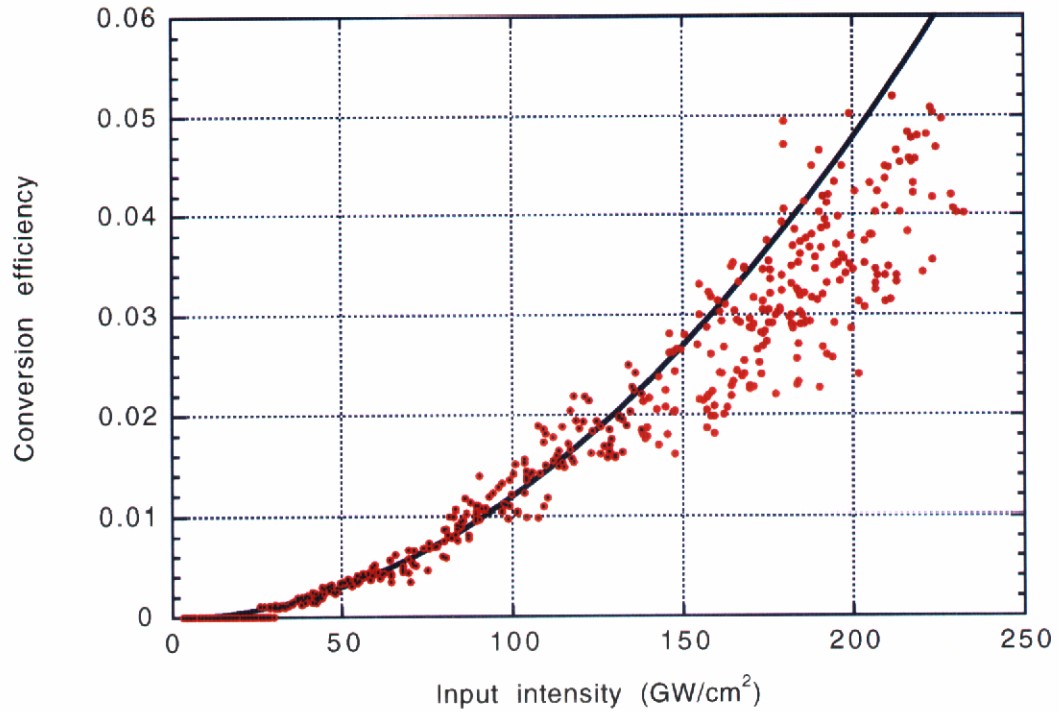


Figure 5.10: Conversion efficiency from single BBO crystal at 351 nm along with quadratic fit to low drive points. Type II phasematching ($\phi_{\text{int}} = 0^\circ$).

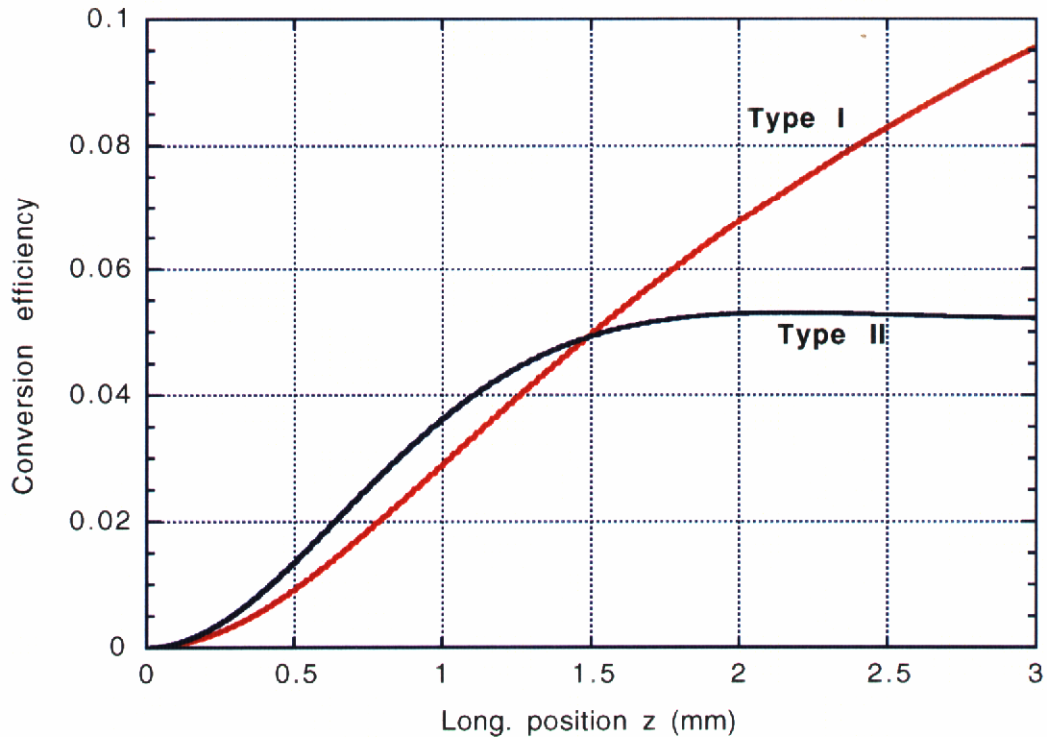


Figure 5.11: Calculated longitudinal growth of Type I (solid line) and Type II (dashed line) 3ω energies. 350 fs pulses, 200 GW/cm² input intensity (8 mJ).

ferent group velocities involved in the two different phasematching configurations. While the interaction length $l_{\text{eff}} = (1/v_{g1} - 1/v_{g2})^{-1}\tau$ due to the group velocity mismatch between the fundamental ordinary wave and the third harmonic extraordinary wave is approximately equal for the two configurations (1.2 mm for Type I vs. 1.7 mm for Type II for a 350 fs pulse), the major limiting factor in Type II phasematching is the walkoff between the two polarizations of the fundamental beam. These two waves walk off in approximately 1.5 mm which is fairly long, but when these waves do not overlap, no further interaction is possible. The resulting temporal effects can be seen more clearly in Figs. 5.11–5.13. For Type I phasematching, conversion continues to proceed even after the pulses walk off from each other with the energy simply being added to the tail of the 3ω pulse (seen in Fig. 5.12). The increased energy comes at the expense of the pulse length of the third

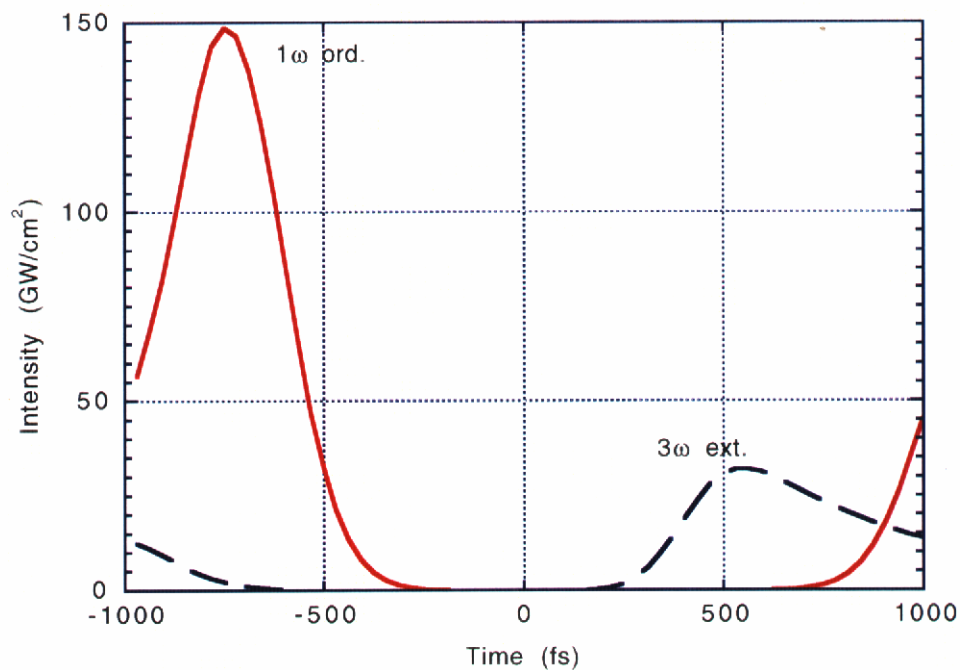


Figure 5.12: Calculated temporal profiles of fundamental (solid line) and third harmonic (dashed line) waves for Type I phasematching. 350 fs pulses, 3 mm crystal, 200 GW/cm² input intensity.

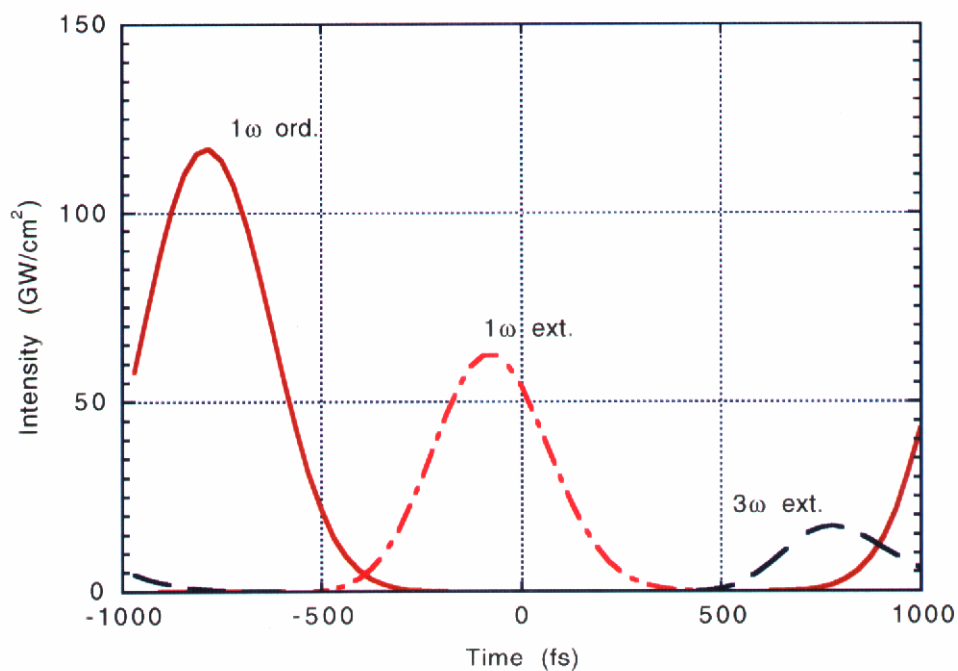
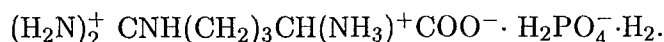


Figure 5.13: Calculated temporal profiles of ordinary fundamental (solid line), extraordinary fundamental (dot-dashed line), and third harmonic (dashed line) waves for Type II phasematching. 350 fs pulses, 3 mm crystal, 200 GW/cm² input intensity.

harmonic with the pulse length (540 fs) being determined to some degree by the crystal length. This does not happen with Type II phasematching since once the fundamental waves walk off from each other, all conversion stops evidenced by the flat line in Fig. 5.11. The third harmonic pulse in this case is essentially gaussian (see Fig. 5.13), and the pulse length (300 fs) is independent of the crystal length. Thus the pulse energy can be greater for Type I phasematching even though the effective nonlinear coefficient is smaller.

5.2 LAP

Similar measurements were done for the deuterated (approximately 95%) organic salt L-arginine phosphate (d-LAP) with formula



This substance is a biaxial (monoclinic) crystal of point group 2 and transparent from 250 nm to 1300 nm. It has a pronounced cleavage plane parallel to the b crystal axis (which is parallel to the y dielectric axis). The x axis makes an angle of 55° with this plane. The $2V$ angle between the two optic axes is wavelength-dependent, but is approximately 142° . This makes the bisector of the acute angle between the optic axes the x axis, defining it to be a “negative” biaxial crystal.

A 1 mm thick piece of d-LAP was cut from a boule of the material at a phasematching angle θ_m of 11° in the x-z plane ($\phi = 0^\circ$), mainly because it was easy to identify this plane (perpendicular to the cleavage plain). It was found that for so thin a crystal, the ease with which d-LAP cleaves caused the cut piece to cleave under the slightest stress. The largest piece intact after polishing was approximately $1.5 \text{ cm} \times 5 \text{ cm} \times 1 \text{ mm}$.

Although it was at first planned to look at 820 nm THG in this crystal (Type I phasematching), this turned out to be impossible. Crystal symmetry of class 2 crystals require that any second-order process involving zero or two waves polarized perpendicular to the x-z plane have zero coupling. This same symmetry requires that any third-order process involving 1 or 3 waves polarized perpendicular to this plane also have zero coupling ($\chi^{(2)}$ (third rank tensor) and $\chi^{(3)}$ (fourth rank tensor) have opposite symmetry). This means that no conversion is possible for Type I phasematching in the x-z plane for phasematching angles $\theta_m < V$. This is because, as shown in Fig. 4.4, the slow polarization is perpendicular to the x-z plane until very near the optic axis.

However, Type II phasematching is not identically zero in this plane and is possible in d-LAP for 1053 nm light although some of the cascaded processes involved are identically zero, again from the same symmetry arguments. The effective, non-zero nonlinear coefficients are

$$d_1 = -d_{22}, \quad (5.8)$$

$$d_4 = d_5 = d_8 = -d_{21} \cos^2 \theta_m + d_{36} \sin 2\theta_m - d_{23} \sin^2 \theta_m, \text{ and} \quad (5.9)$$

$$C_1 = C_{18} \cos^2 \theta_m + C_{24} \sin^2 \theta_m - C_{15} \sin 2\theta_m \quad (5.10)$$

Again, there exists a nonstandard reference frame which is sometimes used for class 2 crystals. This nonstandard frame is used by Singh¹¹⁵ to give the form for C_{ij} . However, C_{ij} in the reference frame following the IRE/IEEE standard is

$$\mathbb{C} = \begin{bmatrix} C_{11} & 0 & C_{13} & 0 & C_{15} & C_{16} & C_{17} & C_{18} & 0 & 0 \\ 0 & C_{22} & 0 & C_{24} & 0 & 0 & 0 & 0 & C_{29} & 0 \\ C_{31} & 0 & C_{33} & 0 & C_{35} & C_{36} & C_{37} & C_{38} & 0 & 0 \end{bmatrix} \quad (5.11)$$

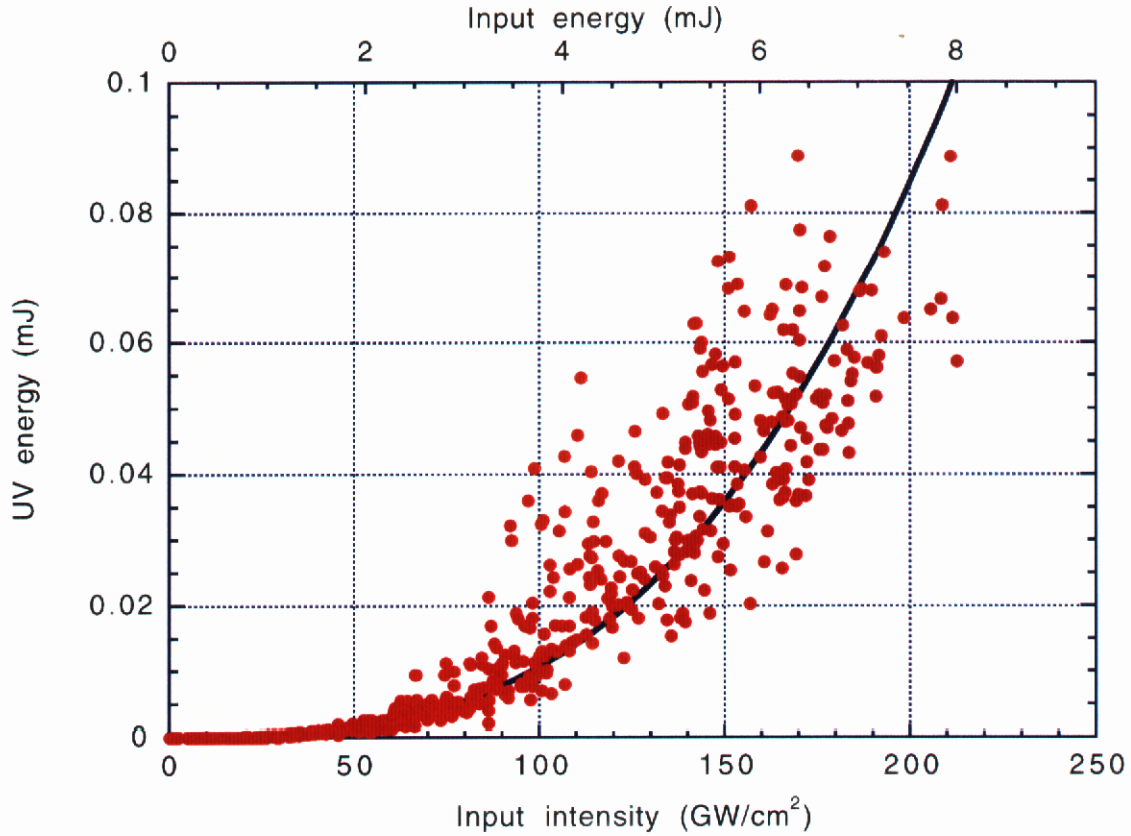


Figure 5.14: Measured energy generated at the third harmonic in 1 mm crystal of d-LAP. The input energy at 200 GW/cm² is 8 mJ. Type II phasematching. The line is a cubic, least-squares fit to data.

and, under Kleinman symmetry conditions,

$$C_{18} = C_{29},$$

$$C_{16} = C_{37},$$

$$C_{24} = C_{35},$$

$$C_{15} = C_{20} = C_{38},$$

$$C_{17} = C_{31}, \text{ and}$$

$$C_{13} = C_{36}.$$

The effective coupling is given by

$$C_{\text{eff}} = \frac{2\pi}{\lambda_{2\omega_0}} \left[\frac{d_1 d_8}{n_3 \Delta k_8} + 2 \frac{d_4 d_5}{n_4 \Delta k_5} \right] + 3C_1. \quad (5.12)$$

For Type II phasematching of 1053 nm light, $\theta_m = 20.2^\circ$, $\Delta k_5 = 1601 \text{ cm}^{-1}$, $\Delta k_8 = -2171 \text{ cm}^{-1}$, $n_4 = 1.5179$, and $n_3 = 1.5768$. For d-LAP, $d_{21} = .40 \text{ pm/V}$, $d_{22} = .39 \text{ pm/V}$, $d_{23} = .83 \text{ pm/V}$, and $d_{36} = -.59 \text{ pm/V}$.¹²¹ The conversion efficiency of d-LAP was measured using the aforementioned crystal (Fig. 5.14) and was found to be about 20% that of Type II BBO.

Comparing the conversion of the two crystals is complicated by the fact that the BBO crystal is longer than the interaction length of BBO so the exact interaction length is unknown, but l_{eff} is calculated to be approximately 1.5 mm (see Fig. 5.11). This introduces a factor of 1.5^2 when comparing C_{eff} of the two substances. Therefore,

$$C_{\text{eff}}^{\text{d-LAP}} \cong \sqrt{\frac{1.5^2}{5}} \cong \frac{2}{\sqrt{5}} C_{\text{eff}}^{\text{BBO}}, \quad (5.13)$$

and $C_{\text{eff}}^{\text{BBO}} = 9 \times 10^{-23} \text{ m}^2/\text{V}^2$ for Type II phasematching. Then substituting the appropriate values into Eq. (5.12) and solving for C_1 in Eq. (5.13) gives a value for C_1 of $4 \times 10^{-23} \text{ m}^2/\text{V}^2$. It is interesting to note that although, after accounting for the different interaction lengths, the conversion efficiency in BBO is two times that in d-LAP, the largest $\chi^{(2)}$ tensor element for d-LAP is less than half the largest element for BBO. The d^4 dependence would indicate a possibility of over 16 times the conversion efficiency. However, the larger phase mismatches involved and larger indices of refraction for BBO substantially reduce the cascaded coupling.

5.3 KD*P

Similar measurements were also made using a 1 mm thick, 1 in. aperture, piece of potassium di-deuterium phosphate (KD*P, 99% deuterated, crystal class $\bar{4}2m$) as the medium. Reported values¹²² of $C_{\text{eff}} \sim 10^{-22} \text{ m}^2/\text{V}^2$ indicated that very efficient single-crystal THG

could be achieved. Only Type I phasematching is possible at 1053 nm (no phasematching is possible at 820 nm), and the relevant effective nonlinear coefficients are given by

$$d_1 = 0, \quad (5.14)$$

$$d_3 = d_7 = -d_{36} \sin 2\phi \sin \theta_m, \quad (5.15)$$

$$d_5 = d_{36} \cos 2\phi \sin 2\theta_m, \text{ and} \quad (5.16)$$

$$C_2 = \frac{1}{4}(C_{11} - 3C_{18}) \sin 4\phi \cos \theta_m. \quad (5.17)$$

The total effective coupling C_{eff} is then

$$C_{\text{eff}} = \frac{2\pi}{\lambda_{2\omega_0}} \frac{d_3 d_5}{n_4 \Delta k_5} + C_2 \quad (5.18)$$

For this configuration, $\theta_m = 61.3^\circ$, $\phi = \pi/4$, $\Delta k_5 = 1906 \text{ cm}^{-1}$, $\Delta k_7 = -1885 \text{ cm}^{-1}$, $n_4 = 1.4771$, $n_3 = 1.5089$, $d_3 = -.315 \text{ pm/V}$, and $d_5 = .285 \text{ pm/V}$.

The value for C_{eff} measured was approximately $6 \pm 2 \times 10^{-24} \text{ m}^2/\text{V}^2$. This is much smaller than that reported in Ref. 122, but is larger than the $8 \times 10^{-25} \text{ m}^2/\text{V}^2$ given in Ref. 26. Again, inserting the various values into Eq. (5.18) gives either $C_2 = 2$ or $10 \times 10^{-24} \text{ m}^2/\text{V}^2$, depending on the relative signs of the second-order and third-order contributions. The resulting value for $C_{11} - 3C_{18}$ is then 1.8 or $9 \times 10^{-23} \text{ m}^2/\text{V}^2$. Because of the very small value for C_{eff} , the efficiency of THG in KD*P is much less—.005% at 50 GW/cm². Scaling to the intensities used for BBO and d-LAP, this would give .08% at 200 GW/cm². Finally, it can be observed from Eqs. (5.14–5.17) that both the second- and third-order parts of C_{eff} have a $\sin 4\phi$ dependence on the azimuthal angle and so there is no way to resolve C_{eff} into its component parts. In any event, it is clear that KD*P is not an ideal material for single-crystal THG.

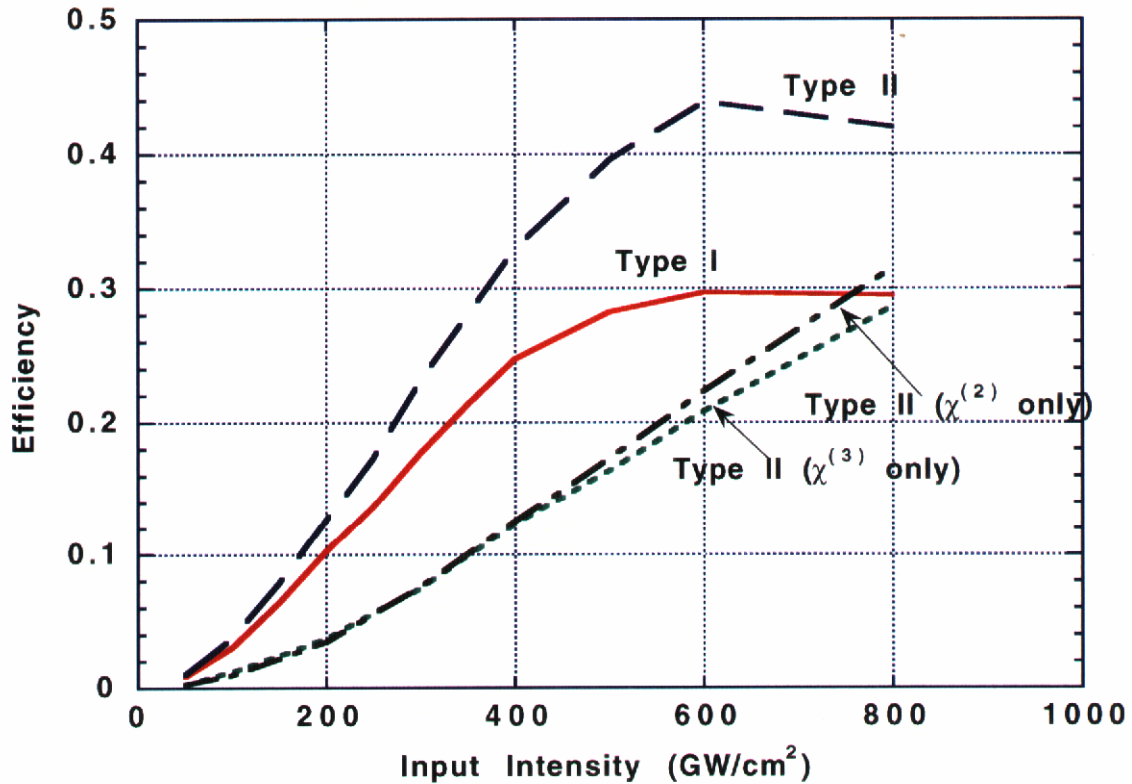


Figure 5.15: Predicted conversion efficiency in 1mm crystal of BBO for both Type I and Type II phasematching.

5.4 Higher intensities and self-phase modulation

It is clear that even at 200 GW/cm² input intensity, the conversion is still in the low drive regime and so higher intensities will increase the conversion efficiency dramatically as the efficiency increases as I^2 . In fact, calculations for BBO using the values for $\chi^{(3)}$ measured in Section 5.1 show that efficiencies of 30–40% can be reached at intensities of 500 GW/cm² (Fig. 5.15). This compares with 50–60% efficiencies calculated to be obtainable via two-crystal THG in Section 4.5. As with the those second-order calculations, the main mechanism limiting the efficiency to the 40% range is self-phase modulation, and its effect is severe at high intensities. With these coefficients set to zero, the calculated efficiency peaks in the 60–70% range. These calculations assume a flattop spatial profile of 5 mm

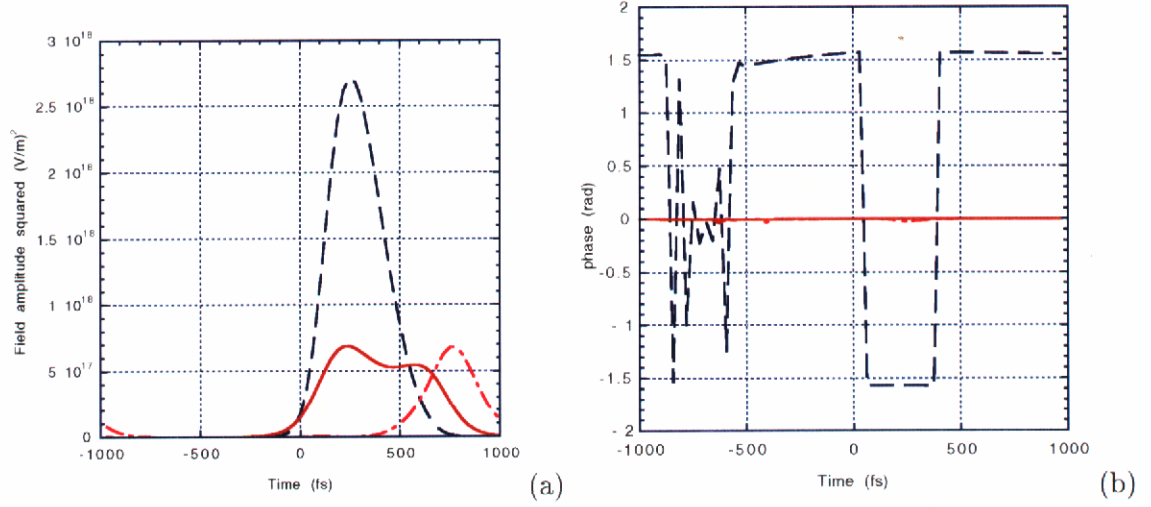


Figure 5.16: Calculated amplitude (a) and phase (b) involving only $\chi^{(3)}$ and no explicit SPM ($C_j^{\text{SPM}} = 0$). Input intensity is 800 GW/cm^2 . Solid line is ordinary fundamental, dash-dotted line is extraordinary fundamental, and dashed line is third harmonic (extraordinary).

diameter and a gaussian temporal profile of 400 fs. They also include values for $C_{2,3,4,5}^{\text{SPM}}$ of $10^{-22} \text{ m}^2/\text{V}^2$ for both fundamental waves and for C_1^{SPM} of $1.3 \times 10^{-22} \text{ m}^2/\text{V}^2$ for the third harmonic wave. The cross-phase modulation terms were assumed to be zero, mainly because there is no reliable data for these terms. The values reported for the nonlinear refractive index γ are about $5 \times 10^{-16} \text{ cm}^2/\text{W}$ at 820 nm,⁸⁸ or about 1.7 times that of KDP.

Using the formulas for class 3m crystals in Tables 4.10 and 4.14, the values for γ for the two possible polarizations can be obtained. For ordinary waves, γ would be $3C_{11}/\epsilon_0 n_o^2$. If dispersion is neglected (which it has been to this point), this tensor element would be the same as that involved in the THG measurements in Section 5.1. However, the angular measurement for Type II phasematching only gives $.154C_{11} + .537C_{16} = .4 \times 10^{-22} \text{ m}^2/\text{V}^2$, and neither element is known. If C_{11} is assumed to be $1.2 \times 10^{-22} \text{ m}^2/\text{V}^2$ (obtained from γ), then $C_{16} = .40 \times 10^{-22} \text{ m}^2/\text{V}^2$ which at least is not unreasonable.

As mentioned in the previous chapter, phase modulation effects at high intensities are

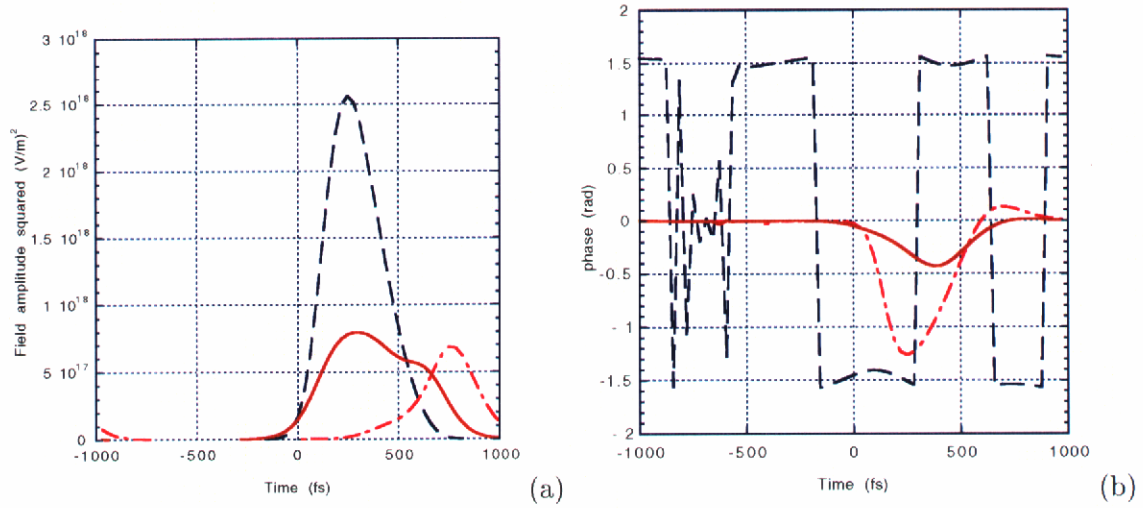


Figure 5.17: Calculated amplitude (a) and phase (b) involving only $\chi^{(2)}$ and $\chi^{(3)}$ with no explicit SPM ($C_j^{\text{SPM}} = 0$). Input intensity is 800 GW/cm². Solid line is ordinary fundamental, dash-dotted line is extraordinary fundamental, and dashed line is third harmonic (extraordinary).

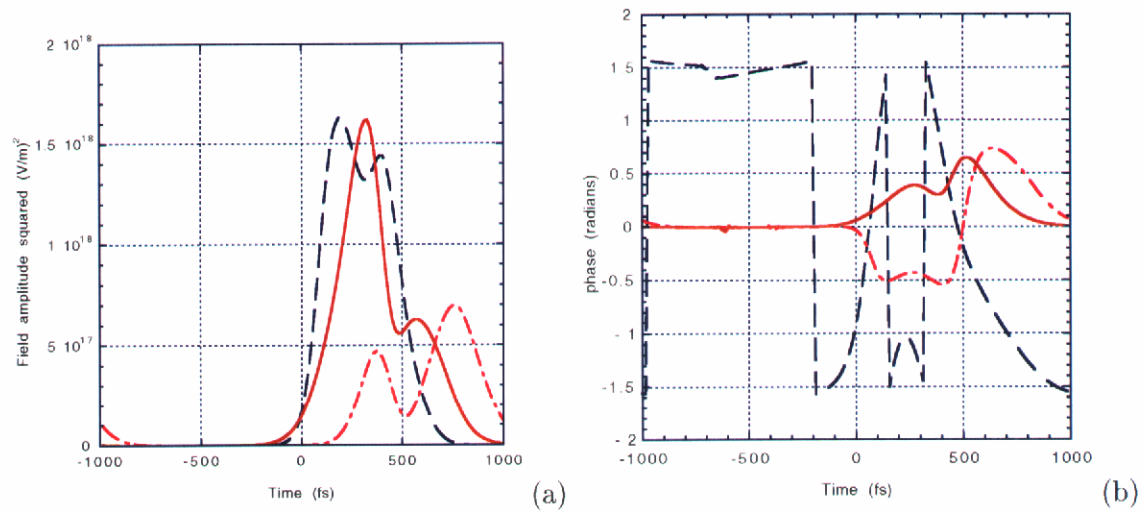


Figure 5.18: Calculated amplitude (a) and phase (b) involving all possible processes. Input intensity is 800 GW/cm². Solid line is ordinary fundamental, dash-dotted line is extraordinary fundamental, and dashed line is third harmonic (extraordinary).

really quite complicated and can occur through many channels. The final amplitudes and phases of the fundamental and third harmonic waves calculated for Type II phasematching in 1 mm of BBO at 800 GW/cm^2 are shown in Figs. 5.16–5.18. Of particular interest is Fig. 5.17 where no third-order interactions are included in the calculation. Even though the overall process is phasematched, the unphasematched intervening second-order processes produce significant modulation of the phase of the fundamental waves (up to 1 radian across the pulse). When SPM is turned on, the phase modulation becomes very large, particularly in the generated wave. Also of interest is that although, for waves at 800 GW/cm^2 , the B-integral is about 1–2 for the fundamental waves and should be even smaller for the generated wave, the accumulated phase at the peak of the 3ω pulse is well over 3 radians. This is the case whether or not the second-order interactions are included suggesting that in the presence of strong phase modulation, the phase of the generated harmonics is strongly modulated by the conversion process. Finally, the existence of the second harmonic channel produces a much more pronounced amplitude modulation on the third harmonic and lowers the maximum achievable intensity.

5.5 Damage and UV absorption

A significant limitation is the damage threshold of the nonlinear medium. As mentioned previously, surface damage thresholds for pulse lengths of 500 fs should be in the range of several TW/cm^2 . Bulk damage mechanisms are more varied and less well understood. In fact, even for operation at 200 GW/cm^2 , some bulk damage in the BBO crystal was observed. The source of this damage is still an open question, but there are some indications that it is triggered by the generated UV light.

After the BBO crystal had been exposed to several thousand shots at full intensity,

it was examined, and a small, sub-millimeter cloudy spot was observed approximately where the center of the beam passed through the crystal. It was difficult to tell where longitudinally the spot was, but it was definitely in the bulk, and it was very faint. Prior to this, another BBO crystal of approximately the same thickness but not phasematched for THG had been exposed to the 1053 nm beam for about 3000 shots at full intensity with no apparent damage.

As the crystal has been used for further experiments, the spot has grown in size to perhaps 1.5–2 mm in transverse diameter. This growth could simply be the result of the peak of the gaussian beam propagating through different parts of the crystal on different days and as the crystal was rotated for the angular dependence measurements, or it could be also due to the exposure time being increased to tens of thousands of shots. The spot is actually just an amorphous region in the center of the crystal which has clouded slightly. There are no tracks or similar morphology visible, and it is still very faint. It requires a very bright light in order to see it in the crystal at all. In addition, there is no obvious change in the wavelength dependence of the linear absorption as measured using a spectrophotometer. Finally, no detectable effect has been observed with regards to conversion efficiency, so it may be that the observed damage morphology has little impact on usability of the crystal.

Damage of similar morphology has been observed in other types of crystals after exposure to short wavelength light, and it has been theorized that it is due to creation of color centers at defect sites in the crystal via nonlinear absorption of the high energy photons. For 3ω pulse energies of .5 mJ, the peak intensities at 351 nm are in the neighborhood of 20–40 GW/cm², depending upon the temporal shape of the generated pulse. This is high enough to begin to have significant absorption of the UV light via 2-photon absorption.

For example, the two-photon absorption coefficient β of BBO at 266 nm is approximately 10^{-9} cm/W.¹²³ Using KD*P as a guide, β at 351 nm is about .02-.1 times its value at 266 nm,^{124,125} so β for BBO at 351 nm will be 10^{-11} – 10^{-10} cm/W. As shown in Fig. 5.11, the generated light reaches its maximum by 1–1.5 mm into the crystal leaving $l \cong 1.5$ mm of free propagation at high intensity. The nonlinear absorption in a material is given by $\exp(-\beta I l)$ which corresponds to a loss at peak intensity of 4%–36% under these conditions. Since the irradiance of the major portion of the pulse is less than the peak, the total percentage lost to two-photon absorption will be less. In any event, this indicates that there could be significant 2-photon absorption occurring and may play a significant role in both the conversion and the damage process. This has not been included in the calculation thus far. Although absorption effects are not explicitly taken into account in the model presented in Chapter 4, it is possible to include such effects via the imaginary parts of the refractive index (linear absorption) and the coefficients C_j^{SPM} and C_j^{XPM} (two-photon absorption), i.e. $\beta = 3\text{Im}[C^{\text{SPM}}]/(\epsilon_0 c n_0)$ (n_0 being the linear real refractive index). In addition, transient UV absorption has also been shown to significantly decrease the conversion efficiency to 266 nm for intensities in the few GW/cm² range,¹²⁴ and so it is possible that it will impact THG for short pulses with intensities in the tens of GW/cm².

In any event, UV bulk damage would appear to be the main limiting factor for increasing intensities to achieve even higher conversion efficiencies. It is currently unclear whether the damage observed is significant from an operational standpoint and at what intensities it will become significant. The effect of two-photon absorption on this process at higher intensities is also unclear. There is also the possibility, if the damage is due to the creation of color centers, to heat the material and anneal out the color centers.

5.6 Conclusion

It has been shown conclusively that cascaded SHG and SFG, even though unphased-matched, can contribute significantly, even play the dominant role, in phasematched single-crystal THG. Up to 6% of the incident light has been converted to the UV in a single crystal of BBO for either Type I or Type II phasematching. The fact that the cascaded second-order coupling has a different azimuthal dependence than the third-order nonlinearity was used to obtain values for tensor elements of $\chi^{(3)}$ of BBO: $C_{10} = 1.8 \times 10^{-23} \text{ m}^2/\text{V}^2$ and $.15C_{11} + .54C_{16} = 4.0 \times 10^{-23} \text{ m}^2/\text{V}^2$, dependent solely on the accuracy of the values used for d_{ij} . LAP can also reach conversion efficiencies in the 1% range, and further exploration of its parameter space is probably worthwhile. KD*P, however, was found to be an unsuitable material for single-crystal THG because of the relatively small values for the second- and third-order susceptibilities. Lastly, if not for material damage limitations, conversion efficiencies of 30–40% are theoretically possible. This is near the calculated theoretical maximum for two-crystal THG discussed in Chapter 4, but the required intensity to reach this is higher.

Chapter 6

Conclusion and future directions

Basically, two things have been accomplished. First, a 50 fs, multi-terawatt Ti:sapphire CPA laser system has been designed and built. It provides 1 W average power at these high peak powers with a very clean beam. To accomplish this, a new all-reflective pulse stretcher has been designed which takes into account the material dispersion of the laser system, thereby eliminating the need for any compensating components which must be precisely aligned. The fact that there are only four elements to the stretcher makes it incredibly robust and easy-to-use. All other components of the laser system function as designed, and the design also includes, for future “growth”, both the pump system and Ti:sapphire amplifiers needed to increase the peak power to the 100 TW level.

Second, relatively high efficiency generation (6%) of the third harmonic in a single crystal has been demonstrated in BBO. Although this appears small, it should be remembered that typical conversion efficiency to the third harmonic using the standard, two-crystal arrangement is only 10–20% for this range of pulse lengths.²⁵ Although the current experimental and calculated maximum conversion efficiencies ($\sim 50\%$ vs. 30–40%) are higher for two-crystal THG, the difference is not that large, and the difference in com-

plexity in implementing the two schemes in an experimental situation is enormous. It is a single crystal vs. two crystals plus dichroic beam splitters, mirrors, and a translation stage or some perfectly matched thickness of material. For applications where the energy at the third harmonic is not too critical, the simplicity of the arrangement makes single-crystal THG extremely attractive if the intensity ($> 100 \text{ GW/cm}^2$) is available.

It was also shown that unphasematched, cascaded SHG and SFG plays an important role in single-crystal THG at these intensities. In fact, it can account for up to 90–95% of the conversion. While this complicates modeling the conversion process, it does have the advantage of allowing one to use the relatively full body of literature dealing with $\chi^{(2)}$ rather than taking shots in the dark, hoping to find a material with a large $\chi^{(3)}$ coupling for THG. It also provides a mechanism, via the angular dependences of the effective nonlinear coefficient of the different orders, to accurately determine the values of the third-order tensor elements in terms of the known elements of $\chi^{(2)}$. For BBO, it was determined that $C_{10} = -1.8 \times 10^{-23} \text{ m}^2/\text{V}^2$ and $.15C_{11} + .54C_{16} = 4 \times 10^{-23} \text{ m}^2/\text{V}^2$.

6.1 Future directions

What has been presented here concerning high intensity THG in a single crystal is by no means an exhaustive treatise on the subject, but rather, it is just the beginning. Even at 200 GW/cm^2 , the conversion is still in the low-drive regime with a quadratic dependence of conversion efficiency on the input intensity. This indicates that even slightly higher intensities will see large gains in efficiency. It is also obvious that using flat-top beams will also produce large gains in efficiency, even within the current range of intensities.

The most immediate issue which needs to be addressed is the crystal greying which was seen in BBO. While the obvious explanation is creation of color centers by the generated

UV light, the exact cause should be more carefully determined. It is also unknown if this damage has some sort of saturation level, above which the effect is slowed or stopped, or whether it can be annealed out by heating the crystal. A simple test would be to down-collimate the beam even further to achieve higher intensities and see what happens. The extent to which two-photon absorption (and other UV absorption mechanisms) affect the generation of the third harmonic needs also to be more carefully examined.

At a more fundamental level, the effect of phase modulation as the ultimate limiting process needs to be fully investigated. To do so, however, a much more complete knowledge and understanding of both the spectral dispersion and the angular dispersion of the nonlinear refractive index needs to be known. Accurate measurements of both temporal amplitude and phase of the generated third harmonic and the fundamental before conversion, perhaps with frequency-resolved optical gating (FROG),¹²⁶ would also be useful.

Then comes the question of whether or not there is a material which is even better than BBO. Since the energy generated goes as $d^4/\Delta k^2$ for the cascaded process, any small improvement in either the effective second-order nonlinear coupling or the phase mismatch for the sum frequency generation part, will dramatically improve the conversion. One possible candidate would be LiIO_3 which can almost be phasematched for 1053 nm. Its cutoff wavelength is approximately 1065 nm which is probably somewhat dependent on how good the Sellmeier parameters are for the near IR. It may be possible to temperature tune the crystal to phasematch it at $\theta_m = 90^\circ$ (noncritically phasematched). LiIO_3 has a very large d and is transparent quite a ways into the UV. How susceptible it is to damage under exposure to high intensity UV light remains to be seen.

Other possible candidates are d-LAP (examine in detail its full range of phasematching angles), CLBO, and lithium formate (LFM). As seen in Section 4.4, the effective

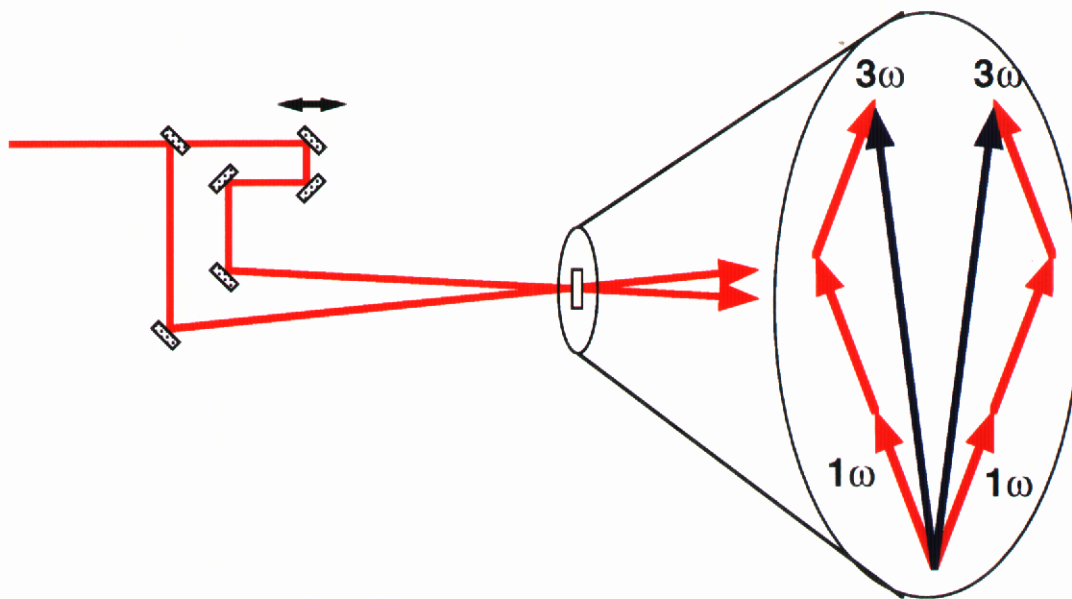


Figure 6.1: Schematic for single-shot third-order autocorrelator

second-order coupling to the third harmonic is roughly the same as d-LAP. It has good transmission properties and supposedly can be grown easily. Xie *et al.*¹²⁷ claim to have seen 1% conversion in LFM at 17 MW/cm^2 . To have that kind of conversion at such low intensities sounds very unlikely, but it deserves further examination. The obvious crystals LBO and KTP cannot be phasematched for even 1053 nm THG, but perhaps one of KTP's isomorphs has a birefringence that is sufficiently different so that it can be phasematched.

Finally, a potential small-scale application of single-crystal THG is its use in a simple single-shot, third-order autocorrelator for diagnosing femtosecond beams (see Fig. 6.1). Because of the third-order process involved (either via $\chi^{(2)}$ or $\chi^{(3)}$), the symmetry in time that is characteristic of SHG autocorrelators is removed, and so information concerning any temporal asymmetries present on the pulse can be obtained. And as a parting thought, in keeping with the current fad of creating useful acronyms like FROG, such a device can be called a Third Order Autocorrelation Device (or TOAD for short).

Appendix A

Effects of residual phase on pulse shapes

As discussed in Chapter 3, the uncompensated phase in a CPA system can significantly effect both the final pulse length as well as the temporal shape of the pulse. In the following graphs, the phase do to uncompensated phase terms according to Eq. (3.4) is added to a 30 nm wide (FWHM) gaussian spectrum. In other words, the spectral intensity is given by

$$E(\omega) = e^{-2 \ln 2 (\omega - \omega_0)^2 / (\Delta\omega)^2} e^{i\phi(\omega)} \quad (\text{A.1})$$

where $\omega_0 = 2\pi c/\lambda_0$ ($\lambda_0 = 820$ nm) and $\Delta\omega = 2\pi c\Delta\lambda/\lambda_0^2$ with $\Delta\lambda = 30$ nm. Both ϕ_0 and β_1 are assumed to be 0. This is then transformed to time ($E(t)$) via Fourier transform giving the resultant pulse shape $I(t) = |E(t)|^2$ in time. By Parseval's theorem, the Fourier transform of $|I(\omega)|^2$ (the Fourier transform of $I(t)$) gives the temporal shape of the second-order intensity autocorrelation.

A.1 Spectral-clipping and gain-narrowing effects

In Section A.1, the effects of truncating the spectrum to a finite width and narrowing the spectrum are shown. Figs. A.1 and A.2 give the temporal profile and autocorrelation of the unmodified pulse. In Figs. A.3, A.4, A.7, and A.8, $E(\omega)$ is changed to

$$E(\omega) = \begin{cases} E(\omega) & \omega_1 \leq \omega \leq \omega_2 \\ 0 & \text{otherwise} \end{cases} \quad (\text{A.2})$$

where $\omega_1 = 2\pi c/(850 \text{ nm})$ and $\omega_2 = 2\pi c/(790 \text{ nm})$. In Figs. A.5–A.8, $E(\omega)$ is modified such that

$$E(\omega) = E(\omega) \times e^{-2 \ln 2 (\omega - \omega_0)^2 / \Omega^2} \quad (\text{A.3})$$

where $\Omega = .084 \text{ fs}^{-1}$. This has the effect of narrowing the spectrum to 20 nm (FWHM).

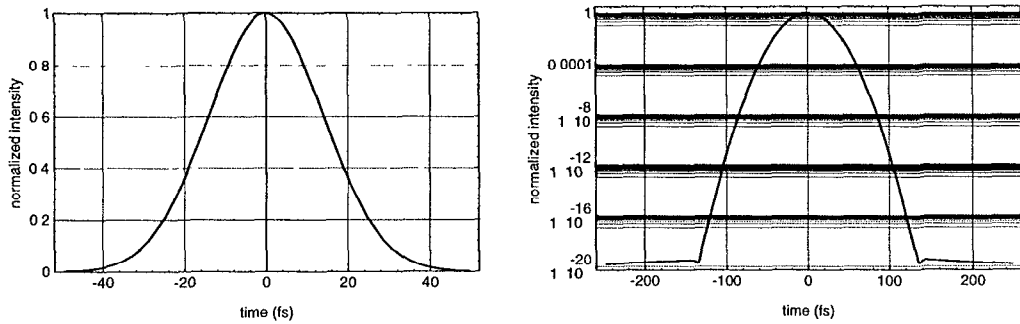


Figure A.1: Temporal pulse shape for no uncompensated phase, no spectral clipping, and no gain-narrowing. FWHM 33.0 fs with peak at 0.

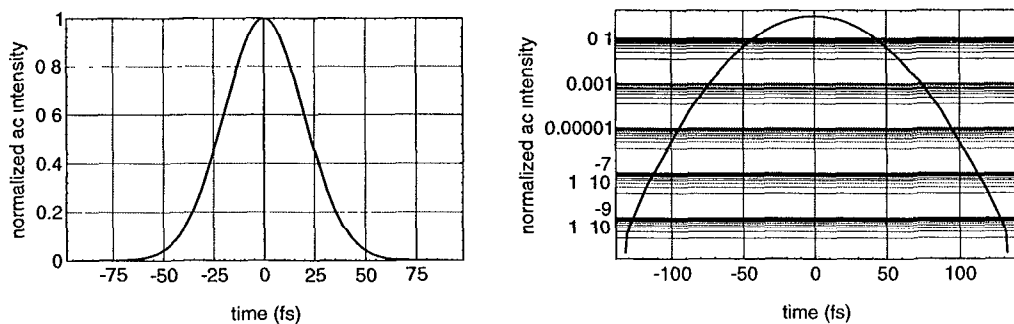


Figure A.2: Second order autocorrelation for no uncompensated phase, no spectral clipping, and no gain-narrowing. FWHM 46.7 fs with peak at 0.

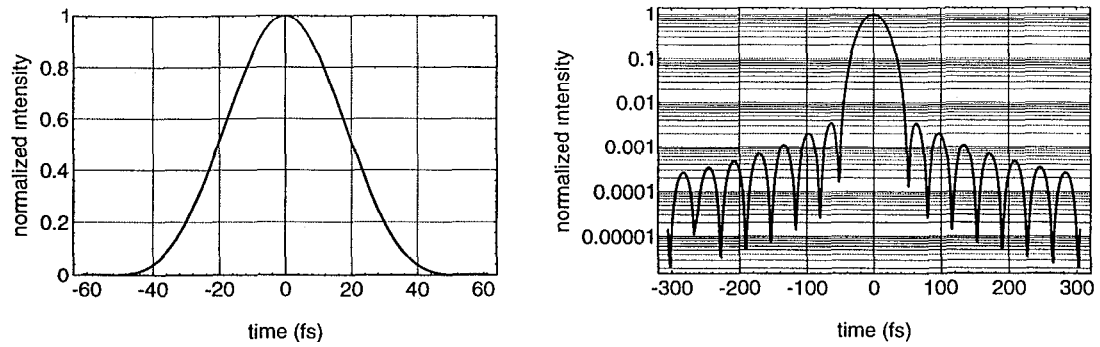


Figure A.3: Temporal pulse shape for no uncompensated phase and no gain-narrowing, but spectrum is truncated at ± 30 nm about center wavelength. FWHM 40.7 fs with peak at 0.

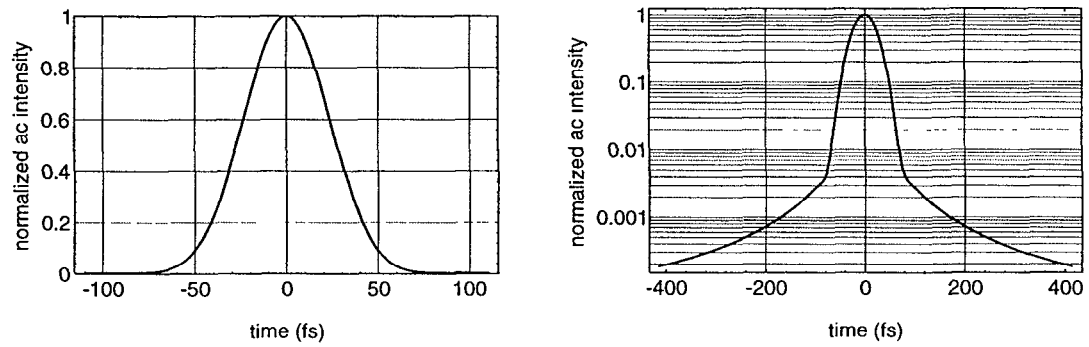


Figure A.4: Second-order autocorrelation for no uncompensated phase and no gain-narrowing, but spectrum is truncated at ± 30 nm about center wavelength. FWHM 55.1 fs with peak at 0.

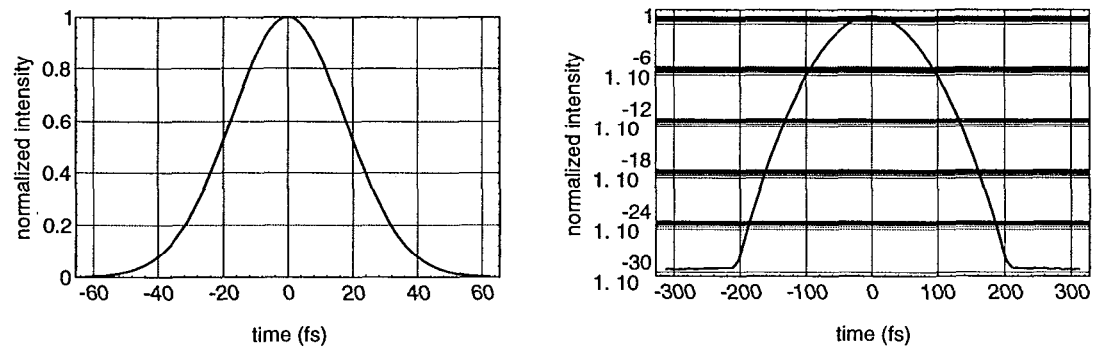


Figure A.5: Temporal pulse shape for no uncompensated phase and no spectral clipping, but spectrum is narrowed to 20 nm. FWHM 41.6 fs with peak at 0.

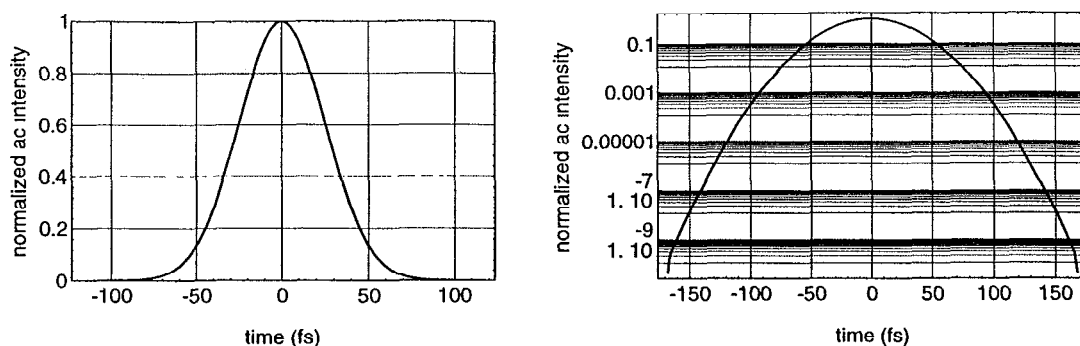


Figure A.6: Second-order autocorrelation for no uncompensated phase and no spectral clipping, but spectrum is narrowed to 20 nm. FWHM 58.8 fs with peak at 0.

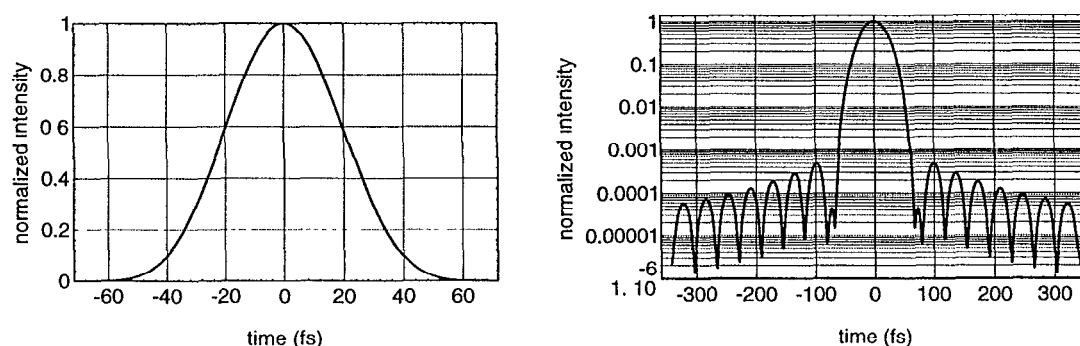


Figure A.7: Temporal pulse shape for no uncompensated phase, but spectrum is truncated at ± 30 nm and spectrum is narrowed to 20 nm. FWHM 45.6 fs with peak at 0.

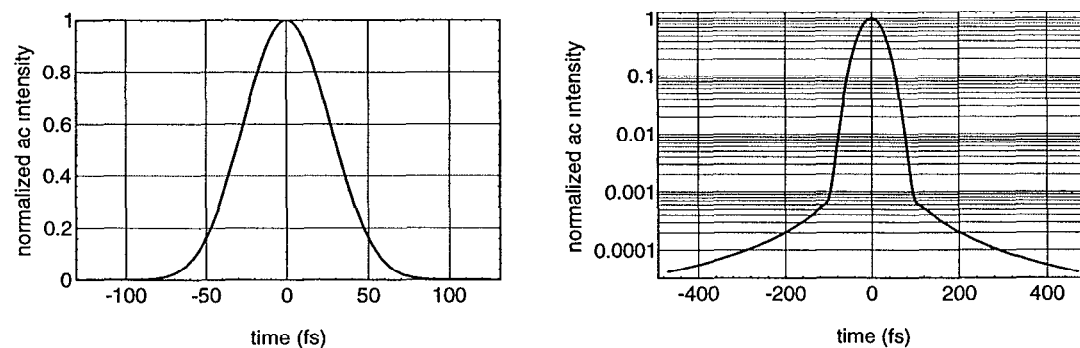


Figure A.8: Second-order autocorrelation for no uncompensated phase, but spectrum is truncated at ± 30 nm and spectrum is narrowed to 20 nm. FWHM 62.6 fs with peak at 0.

A.2 Second-order residual phase effects

For remainder of calculations, the spectrum will be clipped at ± 30 nm and narrowed to 20 nm as in Fig. A.7.

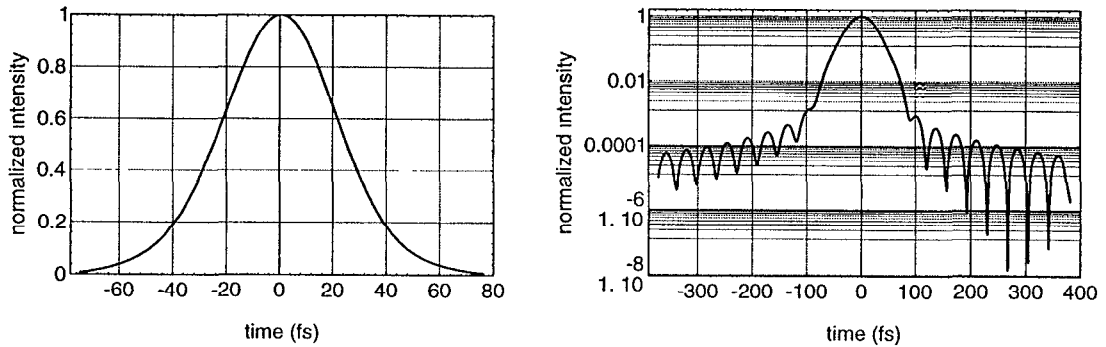


Figure A.9: Temporal pulse shape for clipped, narrowed spectrum with $\Delta\beta_2 = 500$ fs², $\Delta\beta_3 = 0$ fs³, $\Delta\beta_4 = 0$ fs⁴, and $\Delta\beta_5 = 0$ fs⁵. FWHM 50.3 fs with peak at 0.

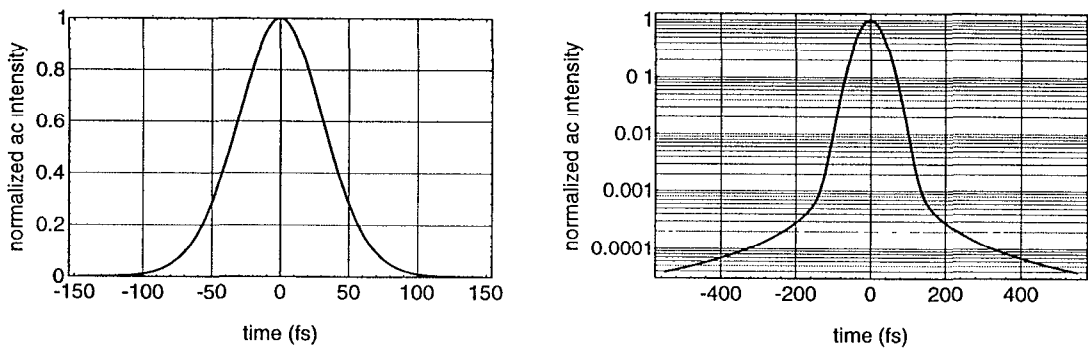


Figure A.10: Second-order autocorrelation for clipped, narrowed spectrum with $\Delta\beta_2 = 500$ fs², $\Delta\beta_3 = 0$ fs³, $\Delta\beta_4 = 0$ fs⁴, and $\Delta\beta_5 = 0$ fs⁵. FWHM 73.3 fs with peak at 0.

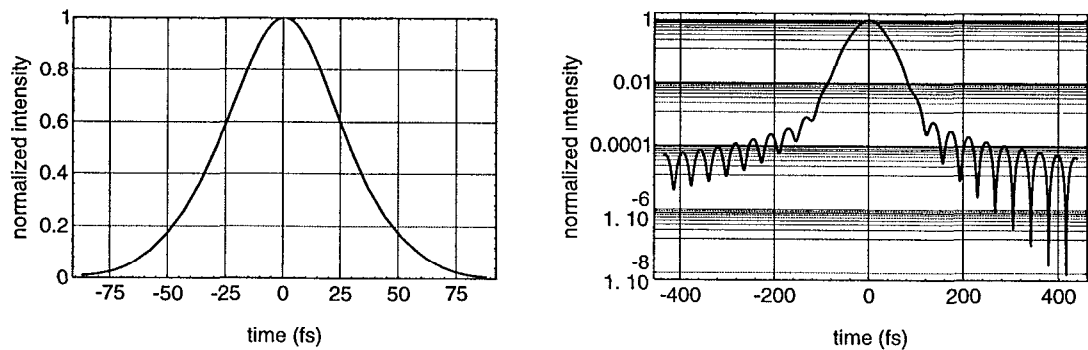


Figure A.11: Temporal pulse shape for clipped, narrowed spectrum with $\Delta\beta_2 = 750$ fs², $\Delta\beta_3 = 0$ fs³, $\Delta\beta_4 = 0$ fs⁴, and $\Delta\beta_5 = 0$ fs⁵. FWHM 58.3 fs with peak at 0.

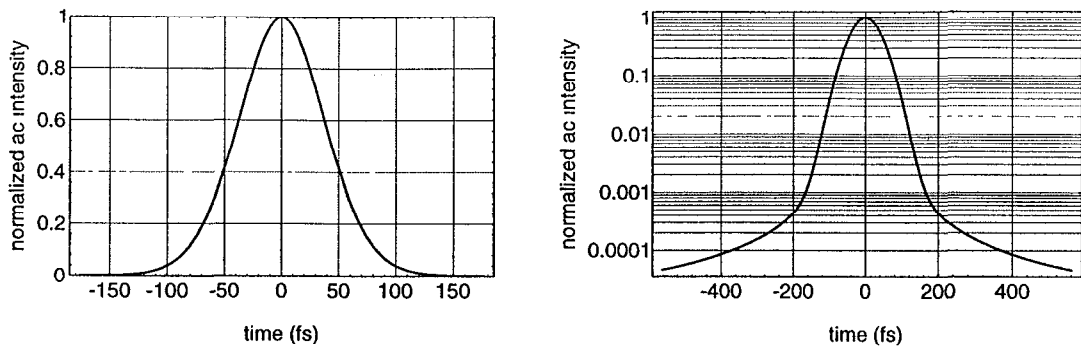


Figure A.12: Second-order autocorrelation for clipped, narrowed spectrum with $\Delta\beta_2 = 750 \text{ fs}^2$, $\Delta\beta_3 = 0 \text{ fs}^3$, $\Delta\beta_4 = 0 \text{ fs}^4$, and $\Delta\beta_5 = 0 \text{ fs}^5$. FWHM 88.1 fs with peak at 0.

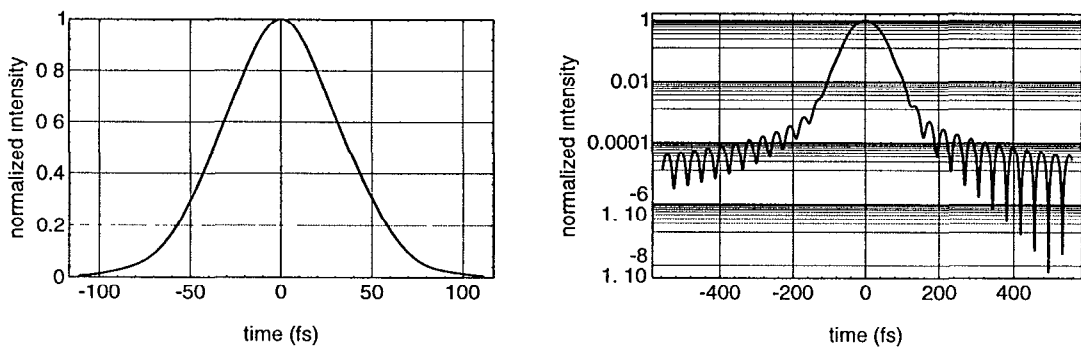


Figure A.13: Temporal pulse shape for clipped, narrowed spectrum with $\Delta\beta_2 = 1000 \text{ fs}^2$, $\Delta\beta_3 = 0 \text{ fs}^3$, $\Delta\beta_4 = 0 \text{ fs}^4$, and $\Delta\beta_5 = 0 \text{ fs}^5$. FWHM 74.1 fs with peak at 0.

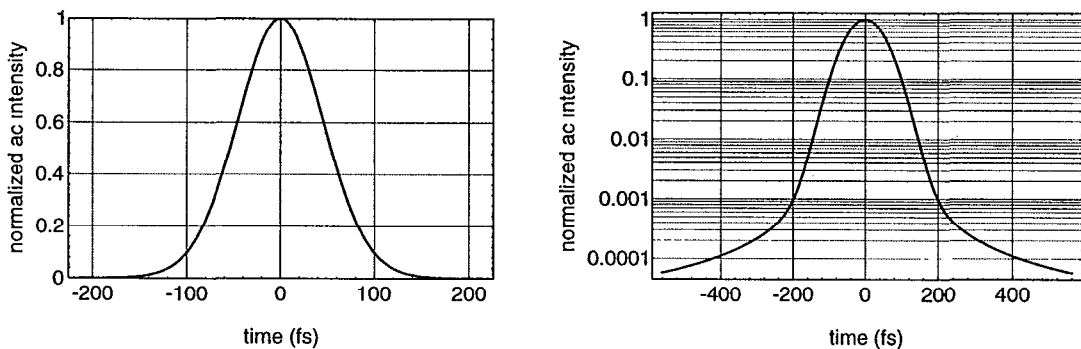


Figure A.14: Second-order autocorrelation for clipped, narrowed spectrum with $\Delta\beta_2 = 1000 \text{ fs}^2$, $\Delta\beta_3 = 0 \text{ fs}^3$, $\Delta\beta_4 = 0 \text{ fs}^4$, and $\Delta\beta_5 = 0 \text{ fs}^5$. FWHM 108 fs with peak at 0.

A.3 Third-order residual phase effects

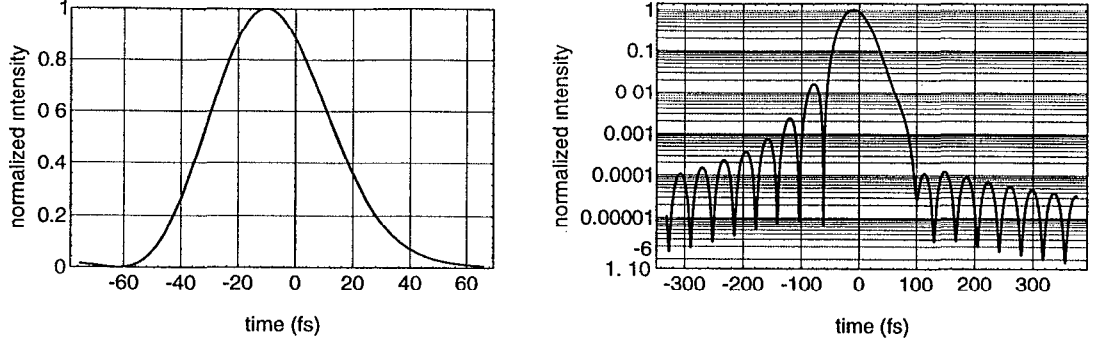


Figure A.15: Temporal pulse shape for clipped, narrowed spectrum with $\Delta\beta_2 = 0 \text{ fs}^2$, $\Delta\beta_3 = -20000 \text{ fs}^3$, $\Delta\beta_4 = 0 \text{ fs}^4$, and $\Delta\beta_5 = 0 \text{ fs}^5$. FWHM 47.0 fs with peak at -11 fs.

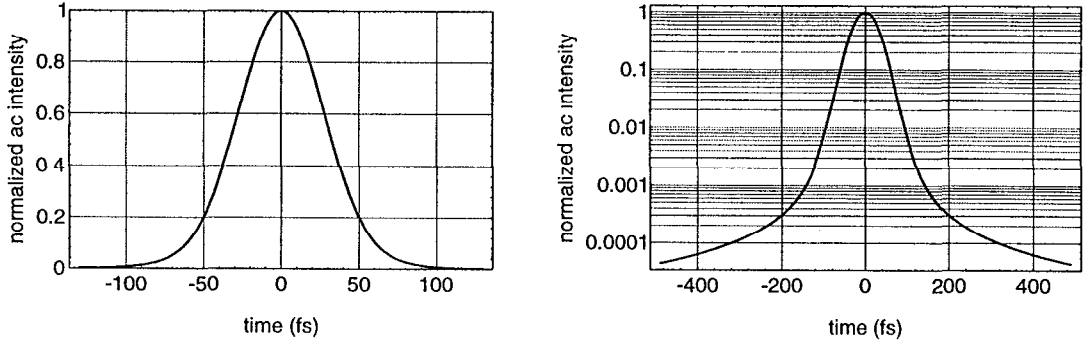


Figure A.16: Second-order autocorrelation for clipped, narrowed spectrum with $\Delta\beta_2 = 0 \text{ fs}^2$, $\Delta\beta_3 = -20000 \text{ fs}^3$, $\Delta\beta_4 = 0 \text{ fs}^4$, and $\Delta\beta_5 = 0 \text{ fs}^5$. FWHM 65.1 fs with peak at 0.

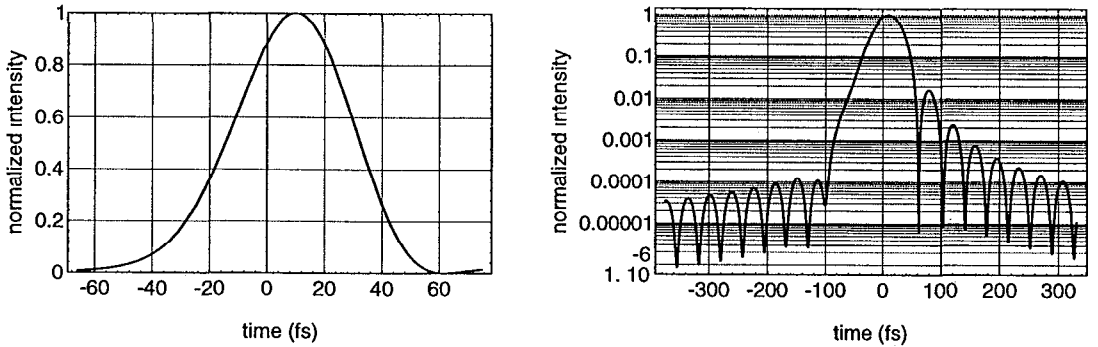


Figure A.17: Temporal pulse shape for clipped, narrowed spectrum with $\Delta\beta_2 = 0 \text{ fs}^2$, $\Delta\beta_3 = 20000 \text{ fs}^3$, $\Delta\beta_4 = 0 \text{ fs}^4$, and $\Delta\beta_5 = 0 \text{ fs}^5$. FWHM 47.0 fs with peak at 11 fs.

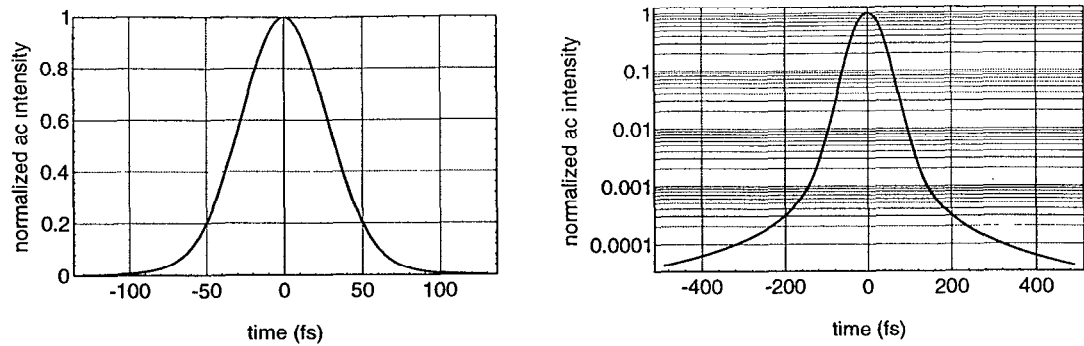


Figure A.18: Second-order autocorrelation for clipped, narrowed spectrum with $\Delta\beta_2 = 0 \text{ fs}^2$, $\Delta\beta_3 = 20000 \text{ fs}^3$, $\Delta\beta_4 = 0 \text{ fs}^4$, and $\Delta\beta_5 = 0 \text{ fs}^5$. FWHM 65.1 fs with peak at 0.

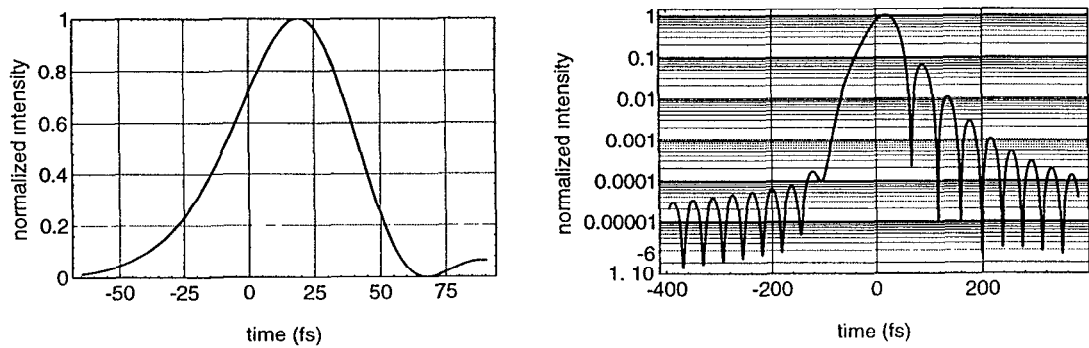


Figure A.19: Temporal pulse shape for clipped, narrowed spectrum with $\Delta\beta_2 = 0 \text{ fs}^2$, $\Delta\beta_3 = 40000 \text{ fs}^3$, $\Delta\beta_4 = 0 \text{ fs}^4$, and $\Delta\beta_5 = 0 \text{ fs}^5$. FWHM 51.6 fs with peak at 18 fs.

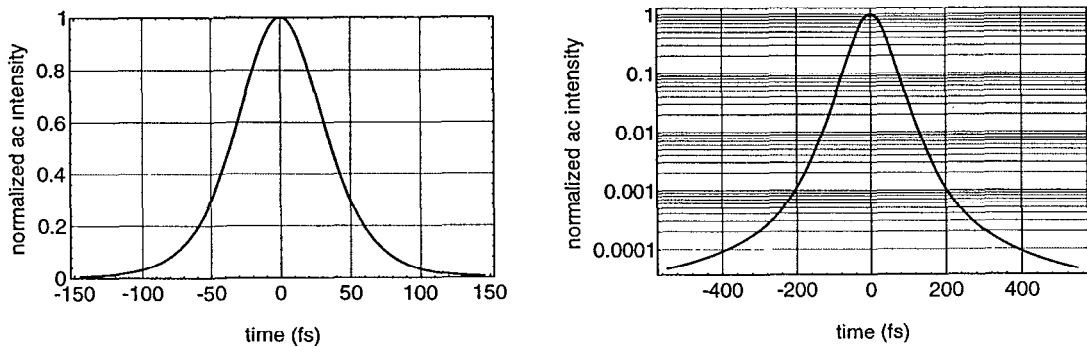


Figure A.20: Second-order autocorrelation for clipped, narrowed spectrum with $\Delta\beta_2 = 0 \text{ fs}^2$, $\Delta\beta_3 = 40000 \text{ fs}^3$, $\Delta\beta_4 = 0 \text{ fs}^4$, and $\Delta\beta_5 = 0 \text{ fs}^5$. FWHM 72.8 fs with peak at 0.

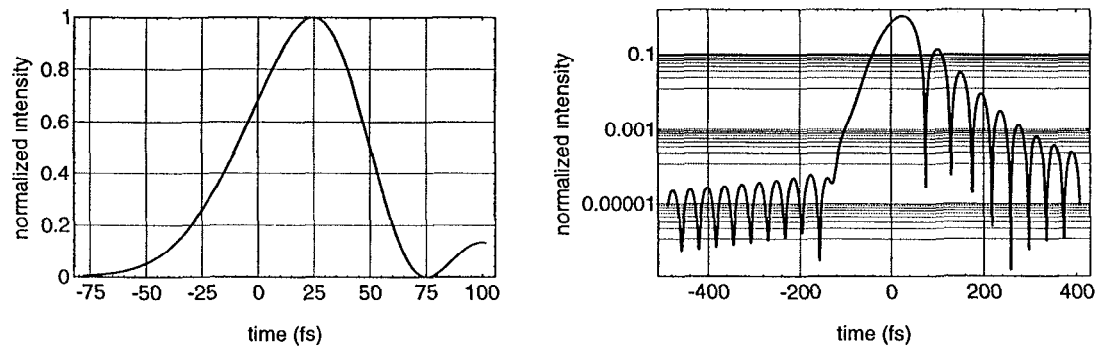


Figure A.21: Temporal pulse shape for clipped, narrowed spectrum with $\Delta\beta_2 = 0 \text{ fs}^2$, $\Delta\beta_3 = 60000 \text{ fs}^3$, $\Delta\beta_4 = 0 \text{ fs}^4$, and $\Delta\beta_5 = 0 \text{ fs}^5$. FWHM 59.7 fs with peak at 25 fs.

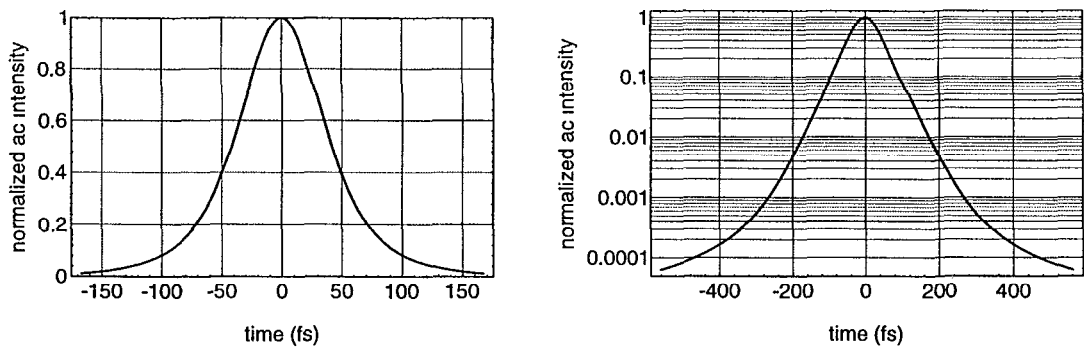


Figure A.22: Second-order autocorrelation for clipped, narrowed spectrum with $\Delta\beta_2 = 0 \text{ fs}^2$, $\Delta\beta_3 = 60000 \text{ fs}^3$, $\Delta\beta_4 = 0 \text{ fs}^4$, and $\Delta\beta_5 = 0 \text{ fs}^5$. FWHM 83.6 fs with peak at 0.

A.4 Fourth-order residual phase effects

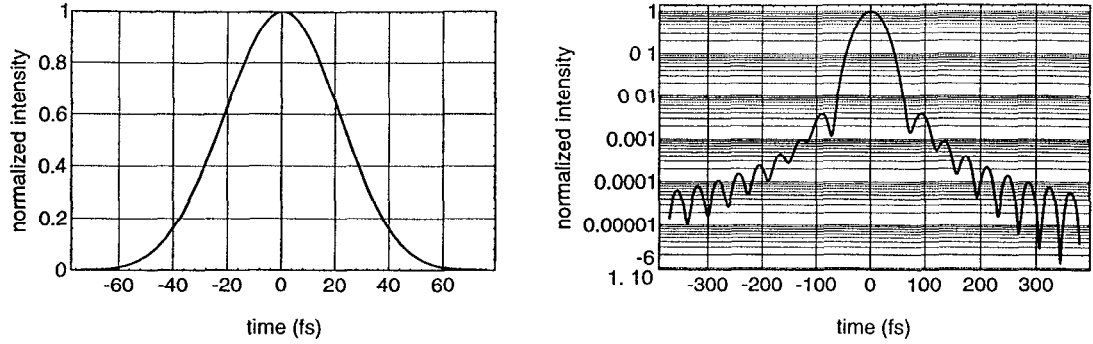


Figure A.23: Temporal pulse shape for clipped, narrowed spectrum with $\Delta\beta_2 = 0 \text{ fs}^2$, $\Delta\beta_3 = 0 \text{ fs}^3$, $\Delta\beta_4 = 10^6 \text{ fs}^4$, and $\Delta\beta_5 = 0 \text{ fs}^5$. FWHM 49.9 fs with peak at 0.

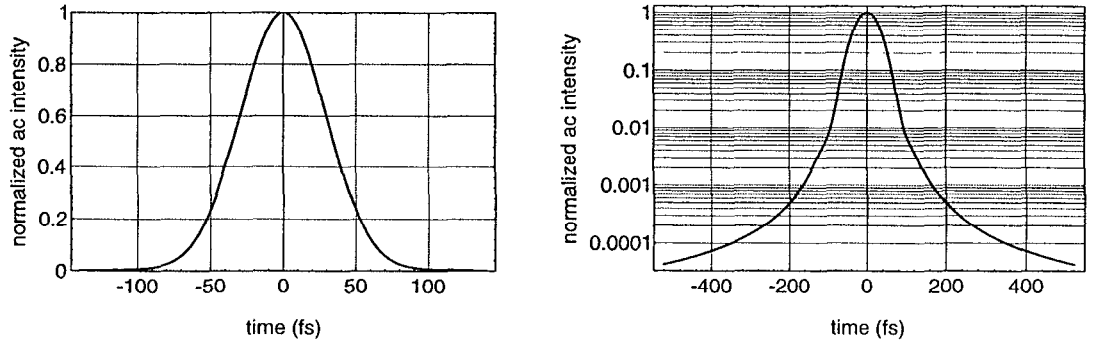


Figure A.24: Second-order autocorrelation for clipped, narrowed spectrum with $\Delta\beta_2 = 0 \text{ fs}^2$, $\Delta\beta_3 = 0 \text{ fs}^3$, $\Delta\beta_4 = 10^6 \text{ fs}^4$, and $\Delta\beta_5 = 0 \text{ fs}^5$. FWHM 69.5 fs with peak at 0.

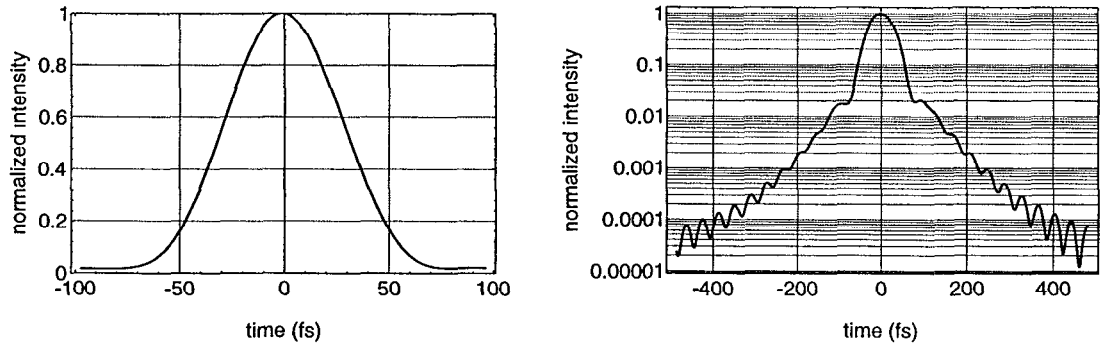


Figure A.25: Temporal pulse shape for clipped, narrowed spectrum with $\Delta\beta_2 = 0 \text{ fs}^2$, $\Delta\beta_3 = 0 \text{ fs}^3$, $\Delta\beta_4 = 2.5 \times 10^6 \text{ fs}^4$, and $\Delta\beta_5 = 0 \text{ fs}^5$. FWHM 64.4 fs with peak at 0.

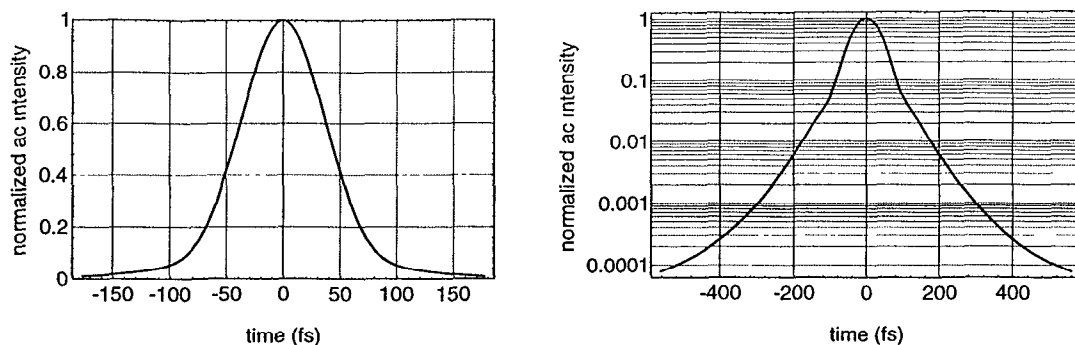


Figure A.26: Second-order autocorrelation for clipped, narrowed spectrum with $\Delta\beta_2 = 0 \text{ fs}^2$, $\Delta\beta_3 = 0 \text{ fs}^3$, $\Delta\beta_4 = 2.5 \times 10^6 \text{ fs}^4$, and $\Delta\beta_5 = 0 \text{ fs}^5$. FWHM 88.4 fs with peak at 0.

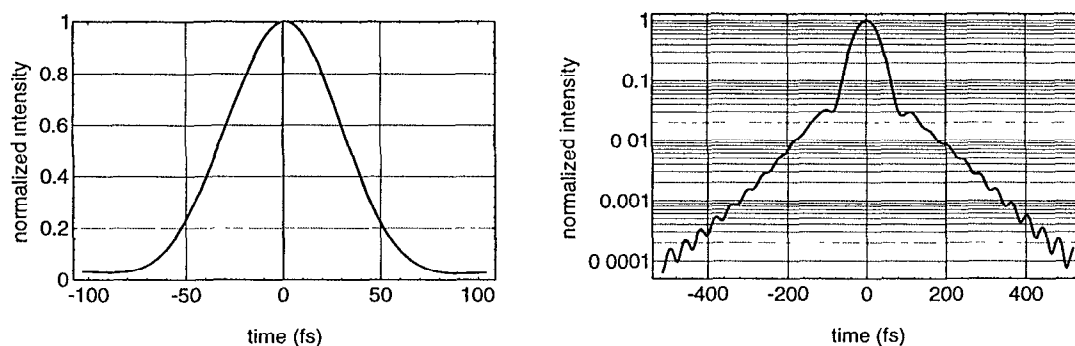


Figure A.27: Temporal pulse shape for clipped, narrowed spectrum with $\Delta\beta_2 = 0 \text{ fs}^2$, $\Delta\beta_3 = 0 \text{ fs}^3$, $\Delta\beta_4 = 4 \times 10^6 \text{ fs}^4$, and $\Delta\beta_5 = 0 \text{ fs}^5$. FWHM 68.8 fs with peak at 0.

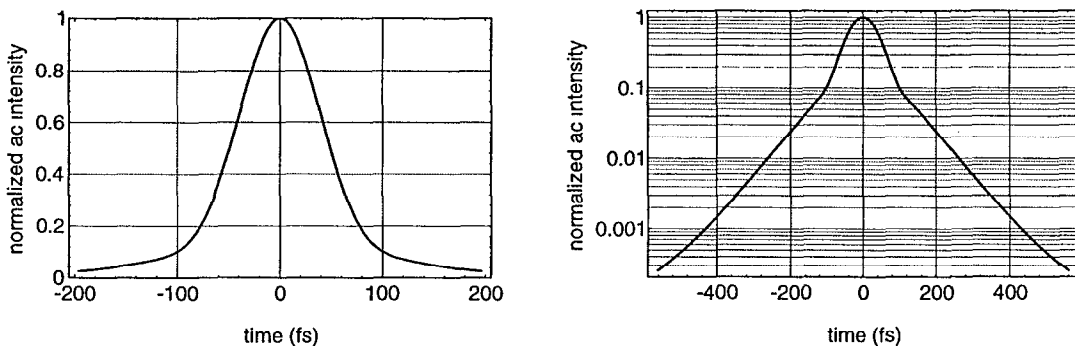


Figure A.28: Second-order autocorrelation for clipped, narrowed spectrum with $\Delta\beta_2 = 0 \text{ fs}^2$, $\Delta\beta_3 = 0 \text{ fs}^3$, $\Delta\beta_4 = 4 \times 10^6 \text{ fs}^4$, and $\Delta\beta_5 = 0 \text{ fs}^5$. FWHM 98.0 fs with peak at 0.

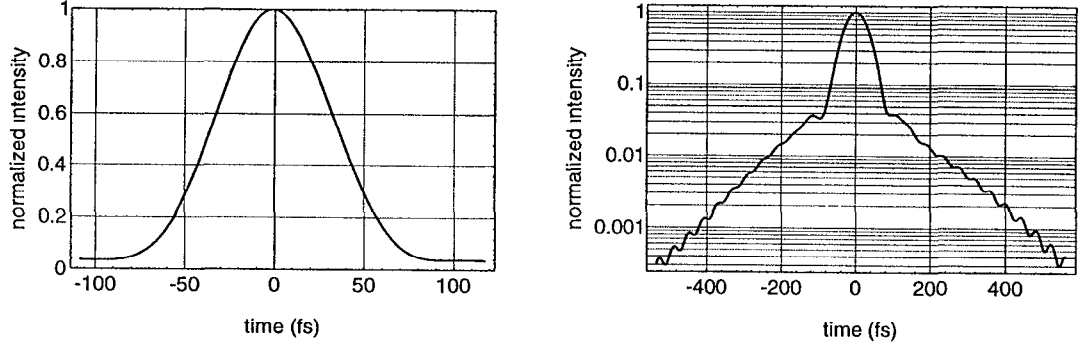


Figure A.29: Temporal pulse shape for clipped, narrowed spectrum with $\Delta\beta_2 = 0 \text{ fs}^2$, $\Delta\beta_3 = 0 \text{ fs}^3$, $\Delta\beta_4 = 5.5 \times 10^6 \text{ fs}^4$, and $\Delta\beta_5 = 0 \text{ fs}^5$. FWHM 75.2 fs with peak at 0.

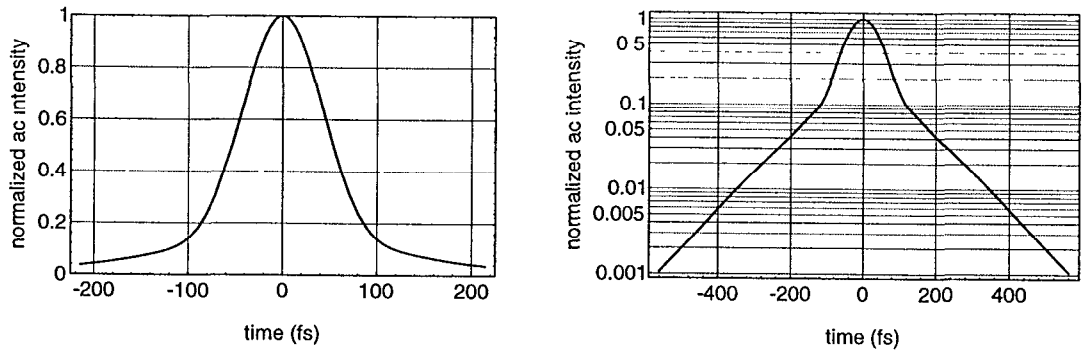


Figure A.30: Second-order autocorrelation for clipped, narrowed spectrum with $\Delta\beta_2 = 0 \text{ fs}^2$, $\Delta\beta_3 = 0 \text{ fs}^3$, $\Delta\beta_4 = 5.5 \times 10^6 \text{ fs}^4$, and $\Delta\beta_5 = 0 \text{ fs}^5$. FWHM 107 fs with peak at 0.

A.5 Fifth-order residual phase effects

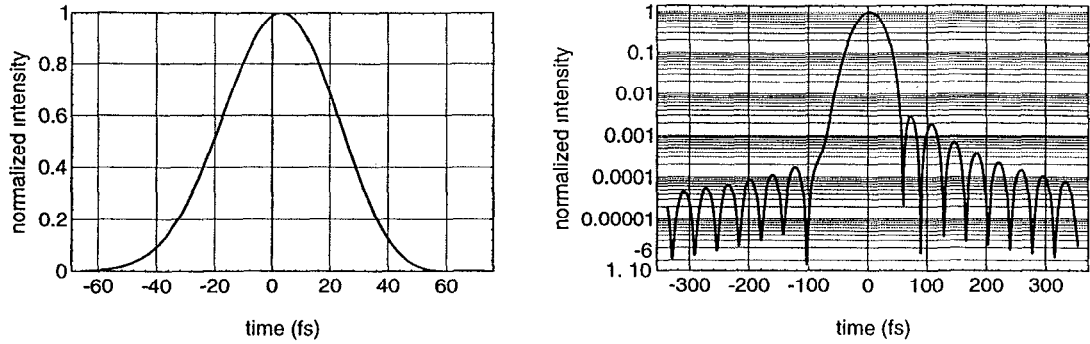


Figure A.31: Temporal pulse shape for clipped, narrowed spectrum with $\Delta\beta_2 = 0 \text{ fs}^2$, $\Delta\beta_3 = 0 \text{ fs}^3$, $\Delta\beta_4 = 0 \text{ fs}^4$, and $\Delta\beta_5 = 3 \times 10^7 \text{ fs}^5$. FWHM 46.1 fs with peak at 2 fs.

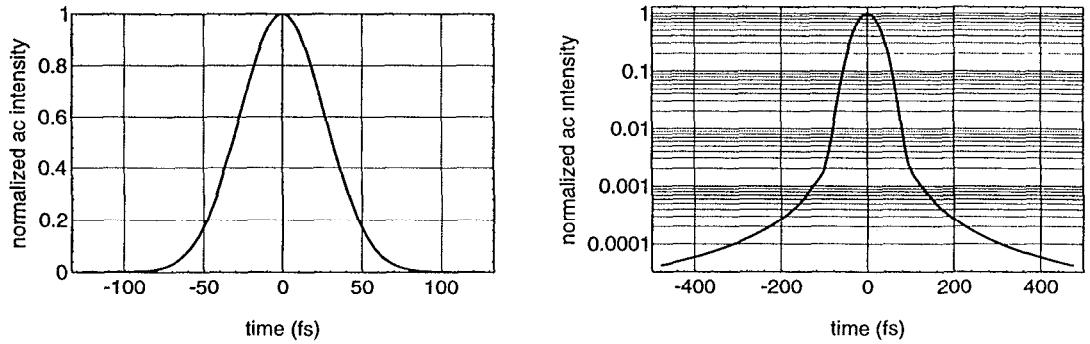


Figure A.32: Second-order autocorrelation for clipped, narrowed spectrum with $\Delta\beta_2 = 0 \text{ fs}^2$, $\Delta\beta_3 = 0 \text{ fs}^3$, $\Delta\beta_4 = 0 \text{ fs}^4$, and $\Delta\beta_5 = 3 \times 10^7 \text{ fs}^5$. FWHM 63.3 fs with peak at 0.

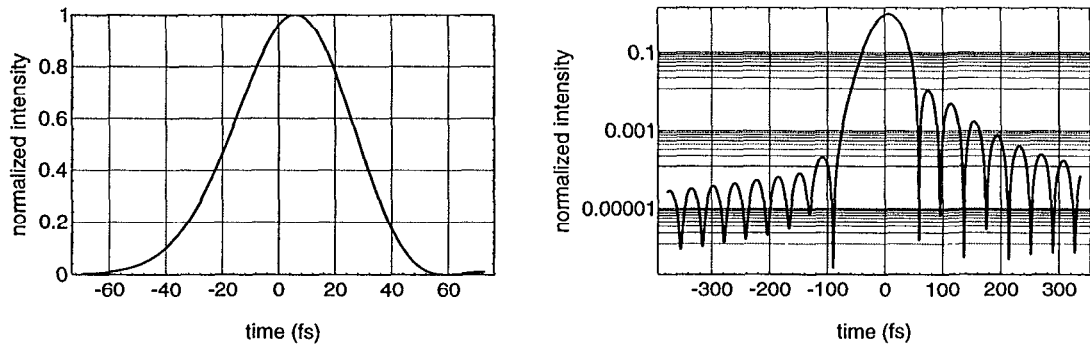


Figure A.33: Temporal pulse shape for clipped, narrowed spectrum with $\Delta\beta_2 = 0 \text{ fs}^2$, $\Delta\beta_3 = 0 \text{ fs}^3$, $\Delta\beta_4 = 0 \text{ fs}^4$, and $\Delta\beta_5 = 6 \times 10^7 \text{ fs}^5$. FWHM 47.5 fs with peak at 7 fs.

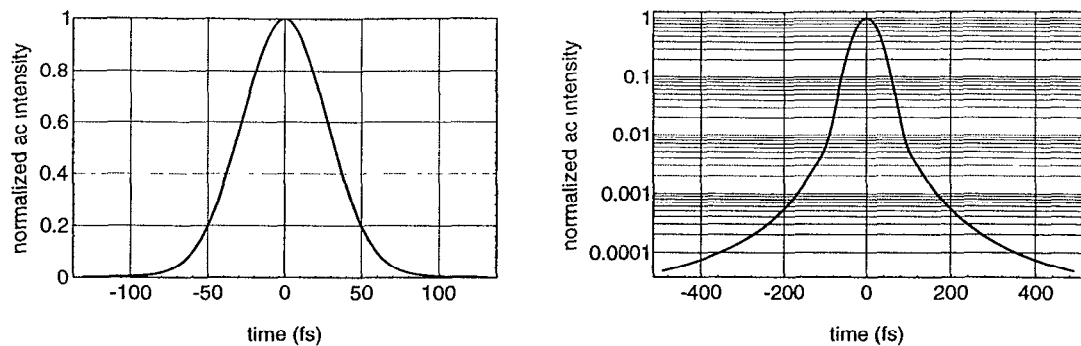


Figure A.34: Second-order autocorrelation for clipped, narrowed spectrum with $\Delta\beta_2 = 0 \text{ fs}^2$, $\Delta\beta_3 = 0 \text{ fs}^3$, $\Delta\beta_4 = 0 \text{ fs}^4$, and $\Delta\beta_5 = 6 \times 10^7 \text{ fs}^5$. FWHM 65.4 fs with peak at 0.

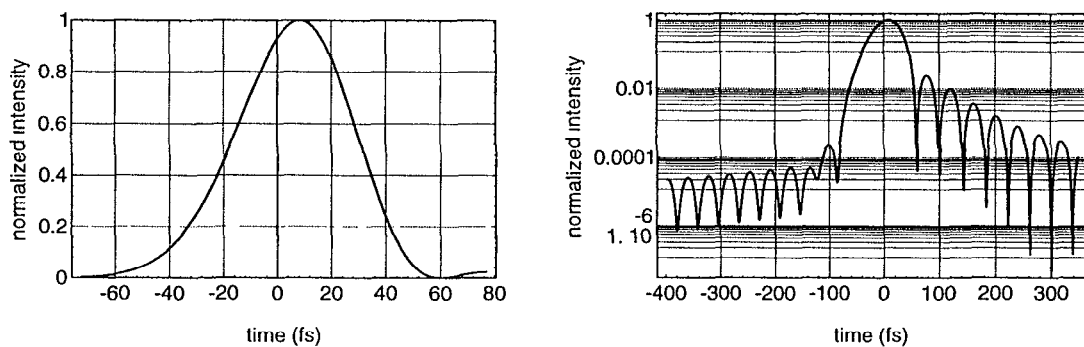


Figure A.35: Temporal pulse shape for clipped, narrowed spectrum with $\Delta\beta_2 = 0 \text{ fs}^2$, $\Delta\beta_3 = 0 \text{ fs}^3$, $\Delta\beta_4 = 0 \text{ fs}^4$, and $\Delta\beta_5 = 9 \times 10^7 \text{ fs}^5$. FWHM 49.7 fs with peak at 9 fs.

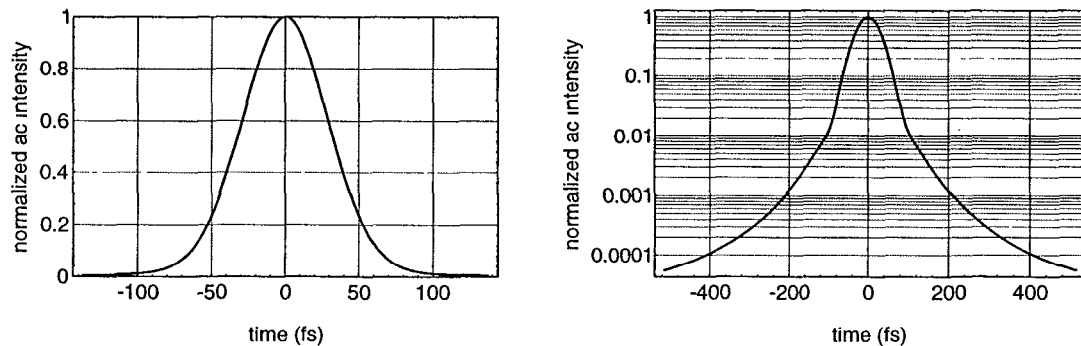


Figure A.36: Second-order autocorrelation for clipped, narrowed spectrum with $\Delta\beta_2 = 0 \text{ fs}^2$, $\Delta\beta_3 = 0 \text{ fs}^3$, $\Delta\beta_4 = 0 \text{ fs}^4$, and $\Delta\beta_5 = 9 \times 10^7 \text{ fs}^5$. FWHM 68.5 fs with peak at 0.

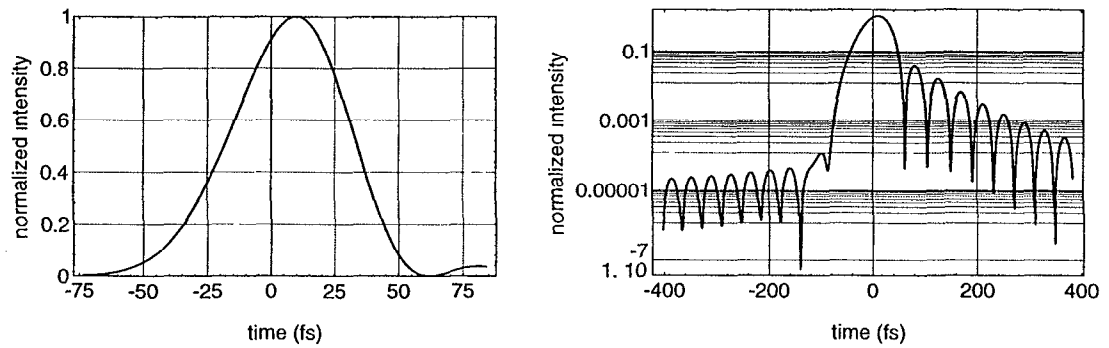


Figure A.37: Temporal pulse shape for clipped, narrowed spectrum with $\Delta\beta_2 = 0 \text{ fs}^2$, $\Delta\beta_3 = 0 \text{ fs}^3$, $\Delta\beta_4 = 0 \text{ fs}^4$, and $\Delta\beta_5 = 1.2 \times 10^8 \text{ fs}^5$. FWHM 52.5 fs with peak at 9 fs.

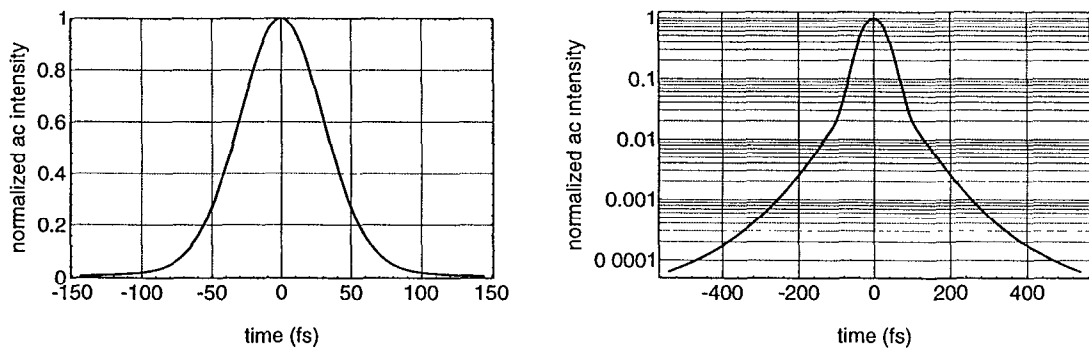


Figure A.38: Second-order autocorrelation for clipped, narrowed spectrum with $\Delta\beta_2 = 0 \text{ fs}^2$, $\Delta\beta_3 = 0 \text{ fs}^3$, $\Delta\beta_4 = 0 \text{ fs}^4$, and $\Delta\beta_5 = 1.2 \times 10^8 \text{ fs}^5$. FWHM 71.9 fs with peak at 0.

Appendix B

Phasematching loci of biaxial crystals

In this appendix, the phasematching loci $\{\theta_m, \phi\}$ are plotted for 8 biaxial crystals: lithium triborate (LBO), potassium titanyl phosphate (KTP), l-arginine phosphate (LAP), deuterated LAP (d-LAP), potassium lathanum nitrate dihydrate (KLN), potassium cerium nitrate dihydrate (KCN), barium magnesium fluoride (BMF), and lithium formate (LFM). The Sellmeier data for each crystal were taken from Ref. 96 with the exception of the nitrates KLN and KCN. The Sellmeier data for these two crystals were taken from Ref. 98. The phasematching loci for Types I and II SHG as well as Types I, II, and III direct THG are shown for fundamental wavelengths of 820 nm and 1053 nm. If no graph is given for a particular configuration, this indicates that it cannot be phasematched. Finally, in addition to the loci of angles for perfect phasematching of direct THG, contours are also shown for $\Delta k = \pm 50$ and 100 cm^{-1} . This will provide some information as to the angular sensitivity of the phase mismatch for direct THG.

B.1 LBO

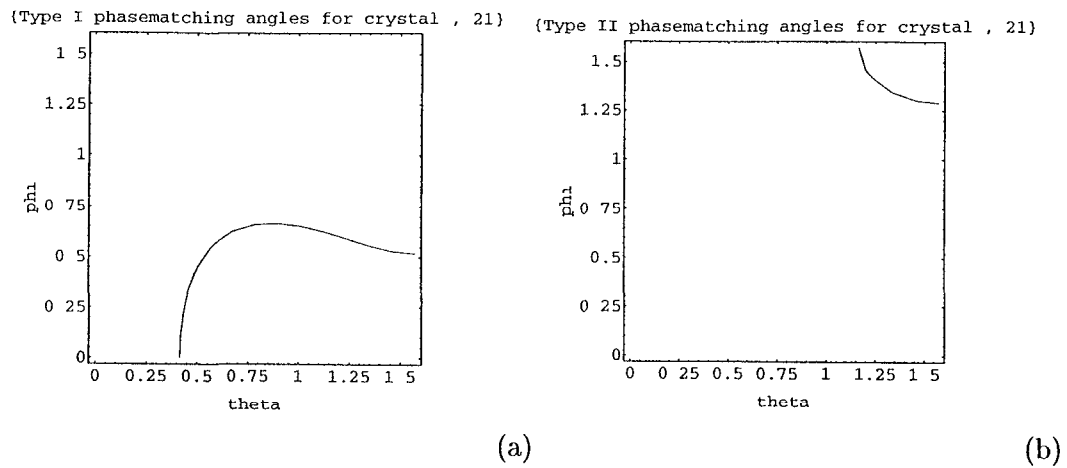


Figure B.1: Phasematching loci for Type I (a) and Type II (b) SHG in LBO at 820 nm.

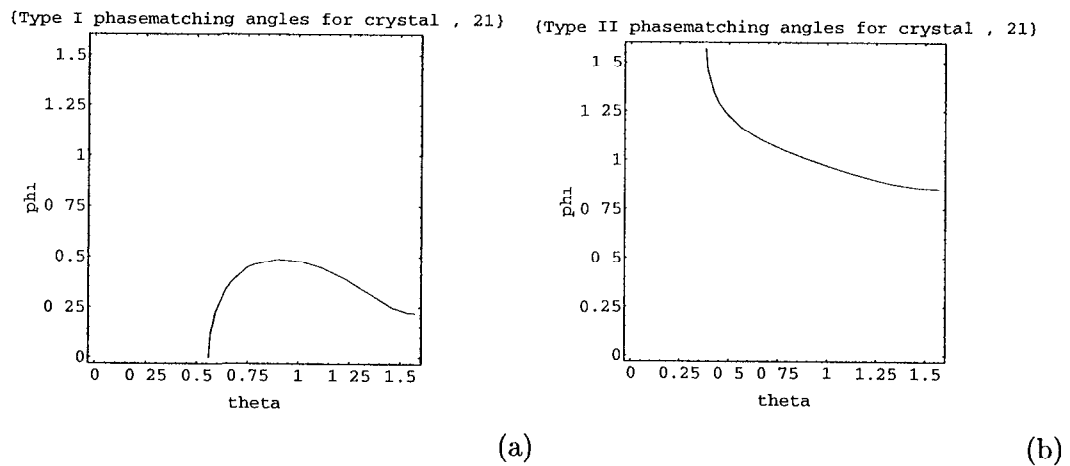


Figure B.2: Phasematching loci for Type I (a) and Type II (b) SHG in LBO at 1053 nm.

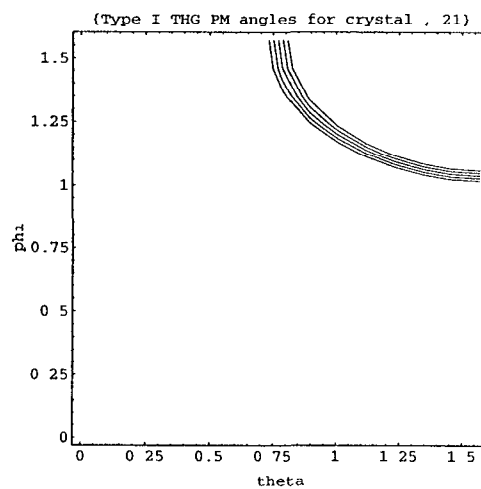


Figure B.3: Phasematching loci for Type I direct THG in LBO at 1053 nm. Contours are drawn for $\Delta k = -100, -50, 0, 50$, and 100 cm^{-1} .

B.2 KTP

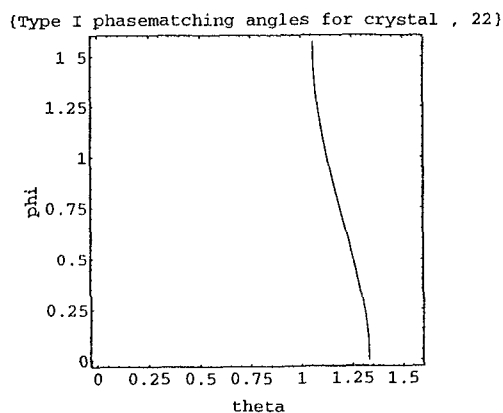


Figure B.4: Phasematching loci for Type I SHG in KTP at 820 nm.

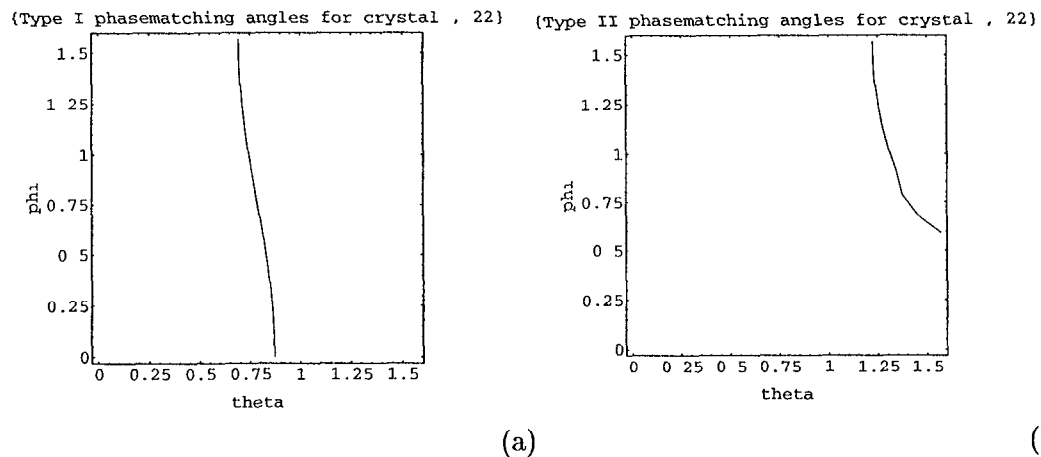


Figure B.5: Phasematching loci for Type I (a) and Type II (b) SHG in KTP at 1053 nm.

B.3 LAP

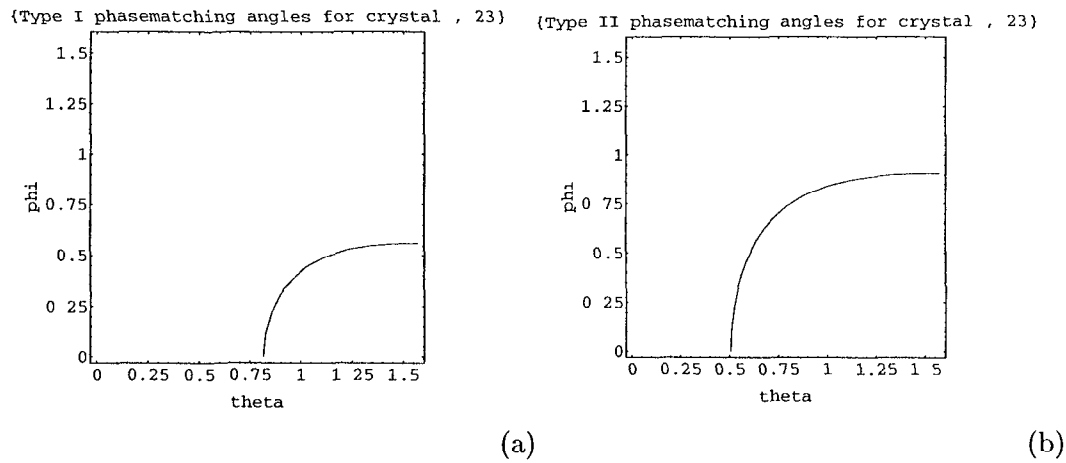


Figure B.6: Phasematching loci for Type I (a) and Type II (b) SHG in LAP at 820 nm.

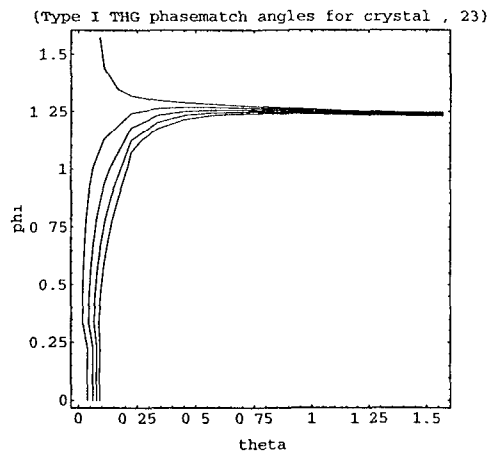


Figure B.7: Phasematching loci for Type I direct THG in LAP at 820 nm. Contours are drawn for $\Delta k = -100, -50, 0, 50$, and 100 cm^{-1} .

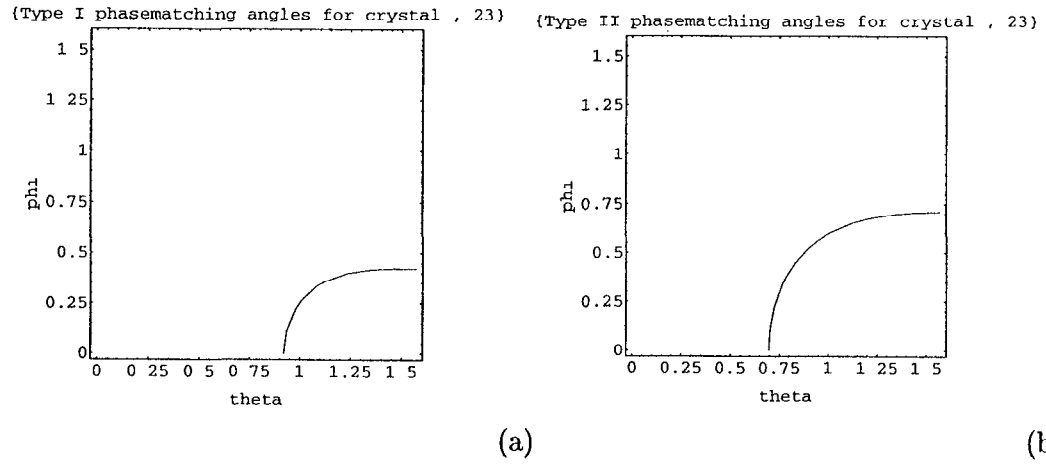


Figure B.8: Phasematching loci for Type I (a) and Type II (b) SHG in LAP at 1053 nm.

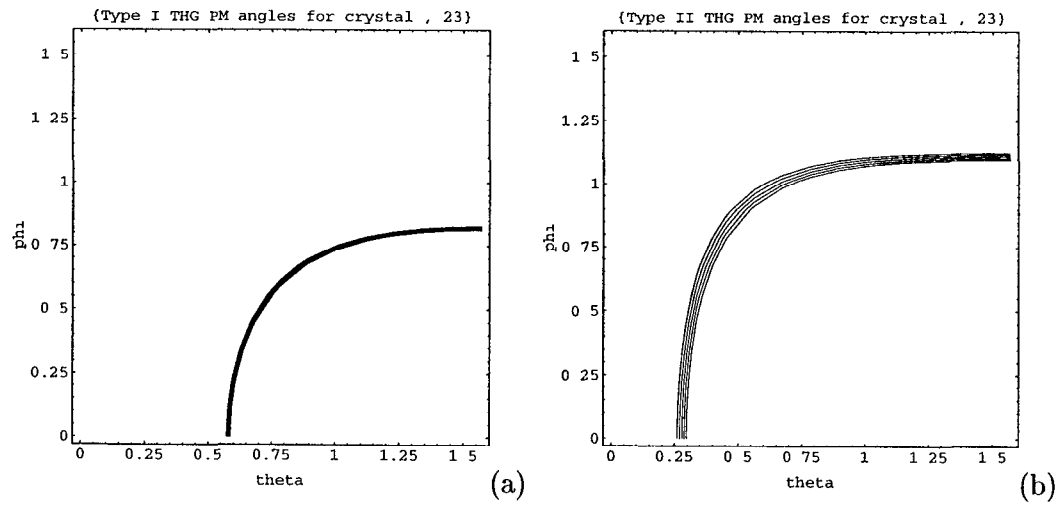


Figure B.9: Phasematching loci for Type I (a) and Type II (b) direct THG in LAP at 1053 nm. Contours are drawn for $\Delta k = -100, -50, 0, 50$, and 100 cm^{-1} .

B.4 d-LAP

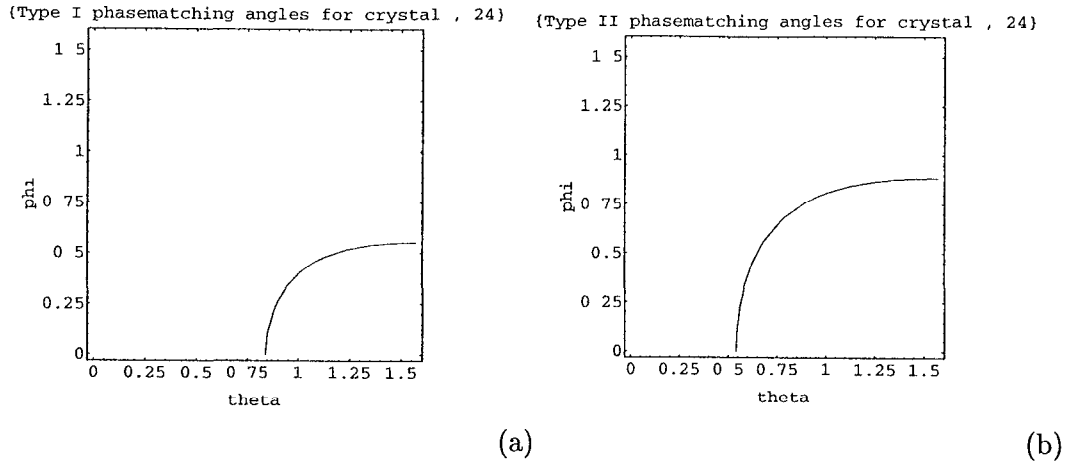


Figure B.10: Phasematching loci for Type I (a) and Type II (b) SHG in d-LAP at 820 nm.

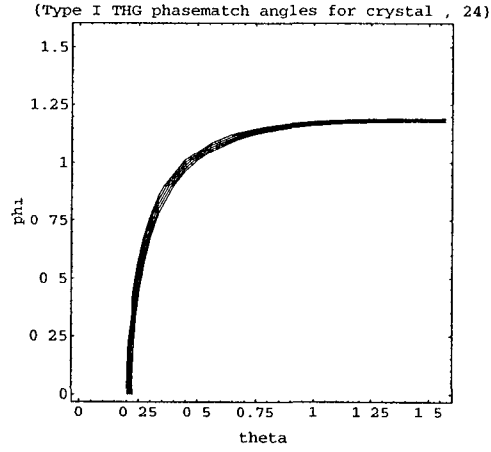


Figure B.11: Phasematching loci for Type I direct THG in d-LAP at 820 nm. Contours are drawn for $\Delta k = -100, -50, 0, 50,$ and 100 cm^{-1} .

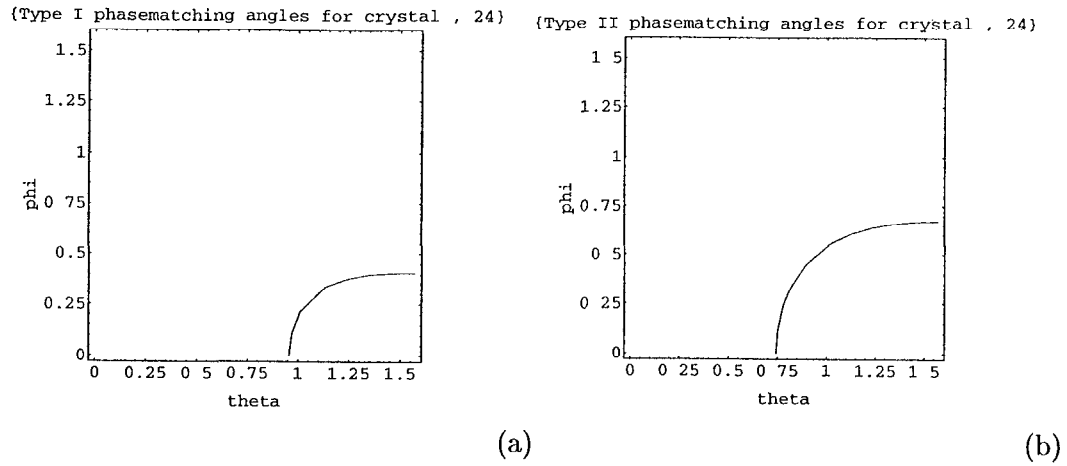


Figure B.12: Phasematching loci for Type I (a) and Type II (b) SHG in d-LAP at 1053 nm.

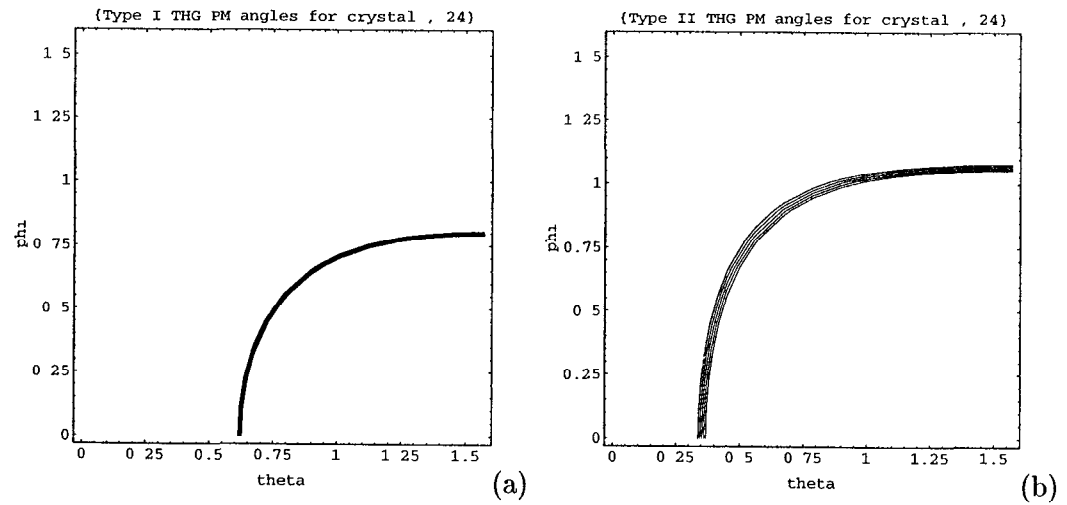


Figure B.13: Phasematching loci for Type I (a) and Type II (b) direct THG in d-LAP at 1053 nm. Contours are drawn for $\Delta k = -100, -50, 0, 50, \text{ and } 100 \text{ cm}^{-1}$.

B.5 KLN

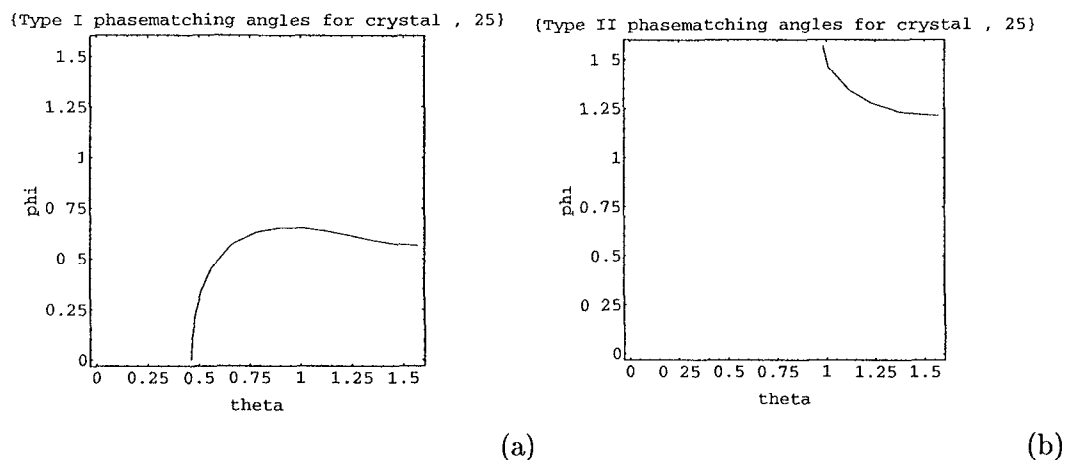


Figure B.14: Phasematching loci for Type I (a) and Type II (b) SHG in KLN at 820 nm.

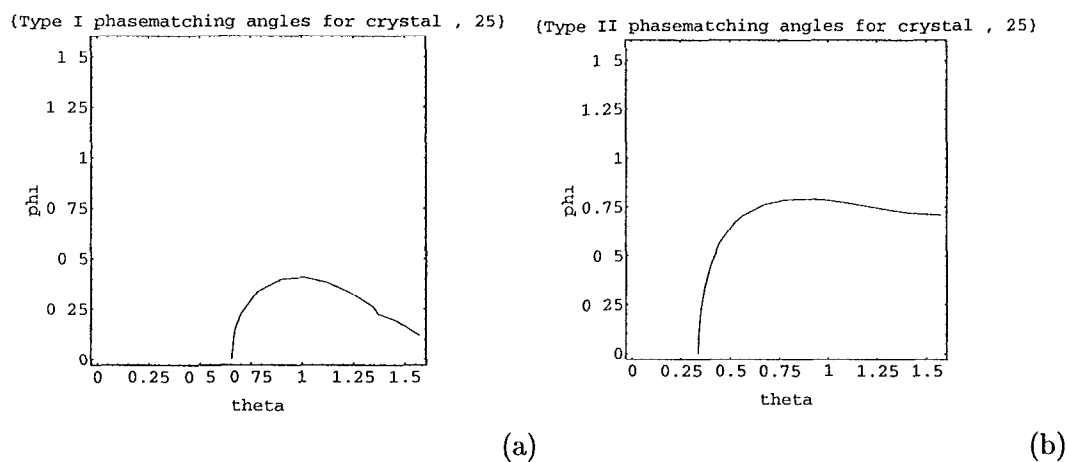


Figure B.15: Phasematching loci for Type I (a) and Type II (b) SHG in KLN at 1053 nm.

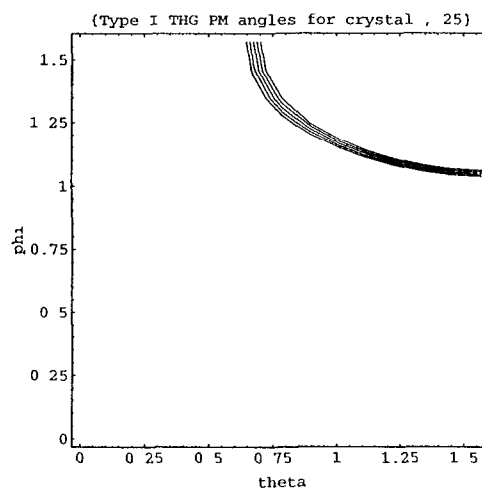


Figure B.16: Phasematching loci for Type I direct THG in KLN at 1053 nm. Contours are drawn for $\Delta k = -100, -50, 0, 50$, and 100 cm^{-1} .

B.6 KCN

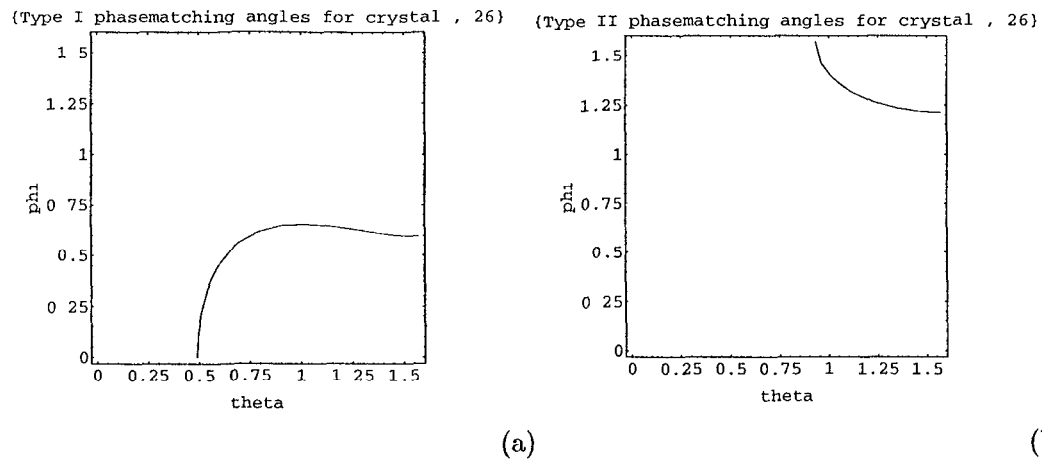


Figure B.17: Phasematching loci for Type I (a) and Type II (b) SHG in KCN at 820 nm.

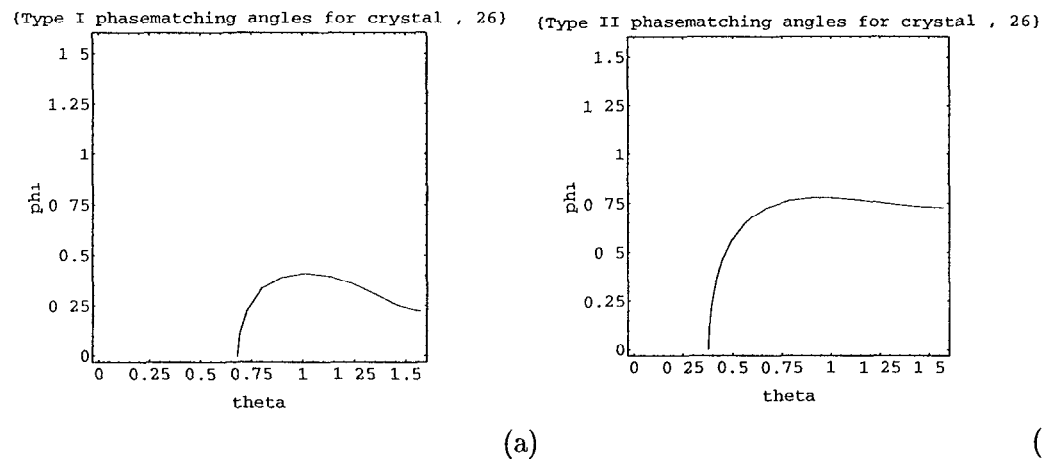


Figure B.18: Phasematching loci for Type I (a) and Type II (b) SHG in KCN at 1053 nm.

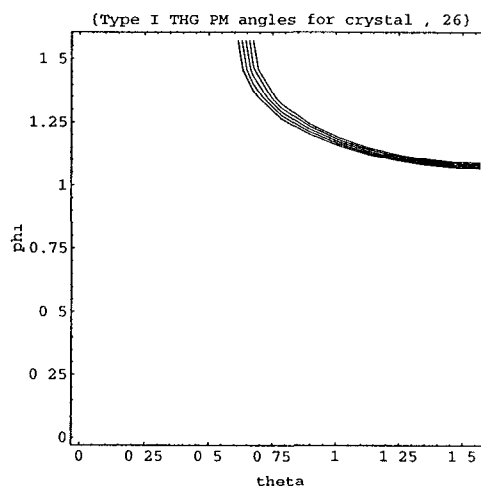


Figure B.19: Phasematching loci for Type I direct THG in KCN at 1053 nm. Contours are drawn for $\Delta k = -100, -50, 0, 50$, and 100 cm^{-1} .

B.7 BMF

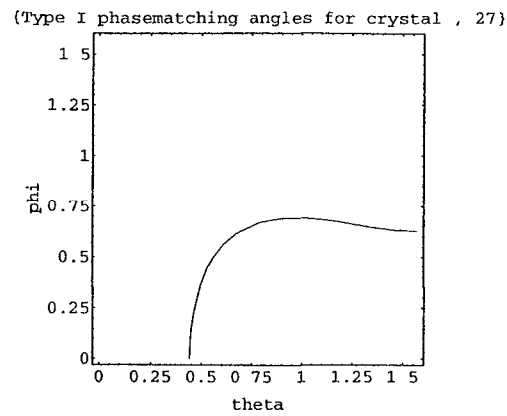


Figure B.20: Phasematching loci for Type I SHG in BMF at 820 nm.

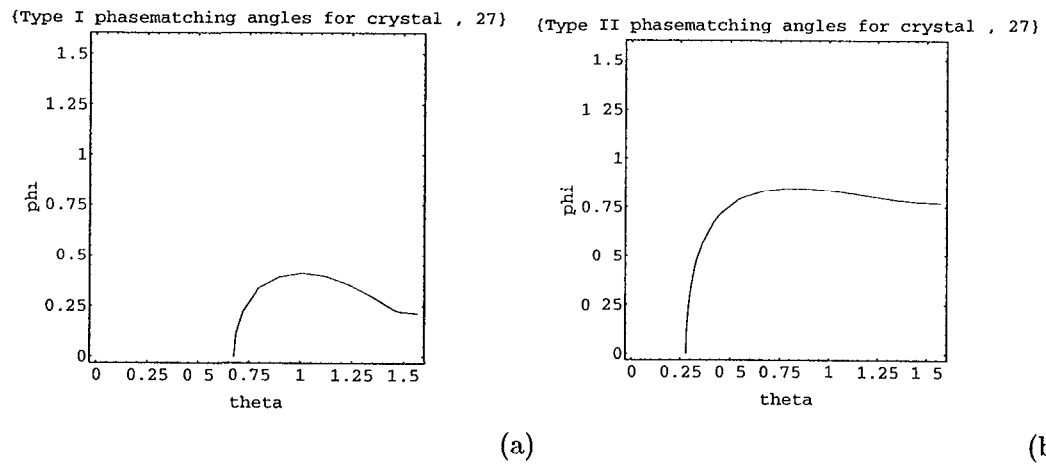


Figure B.21: Phasematching loci for Type I (a) and Type II (b) SHG in BMF at 1053 nm.

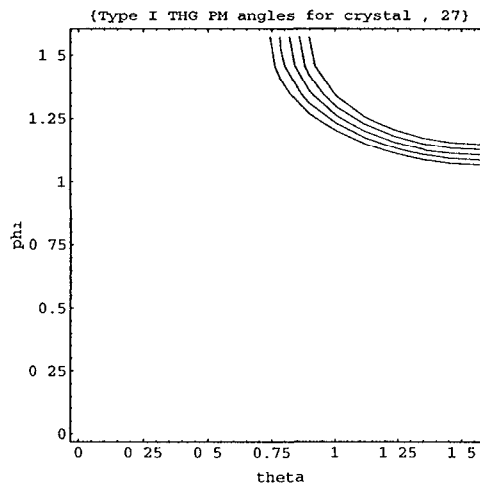


Figure B.22: Phasematching loci for Type I direct THG in BMF at 1053 nm. Contours are drawn for $\Delta k = -100, -50, 0, 50,$ and 100 cm^{-1} .

B.8 LFM

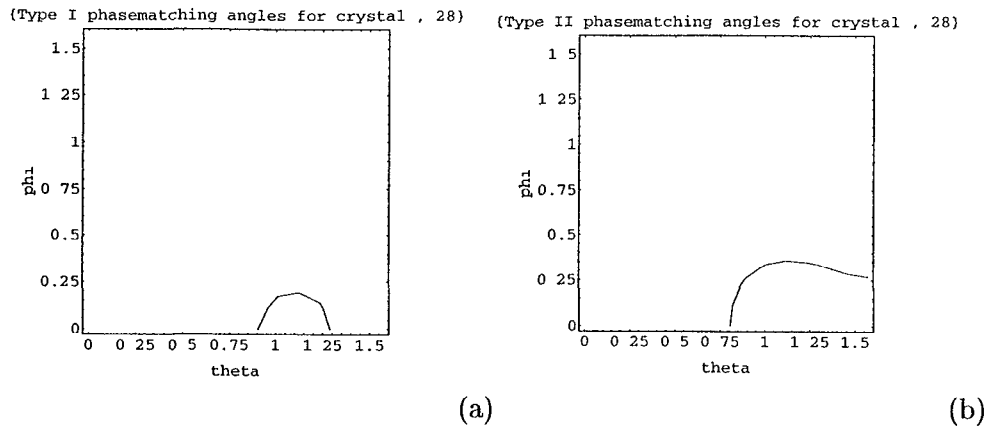


Figure B.23: Phasematching loci for Type I (a) and Type II (b) SHG in LFM at 820 nm.

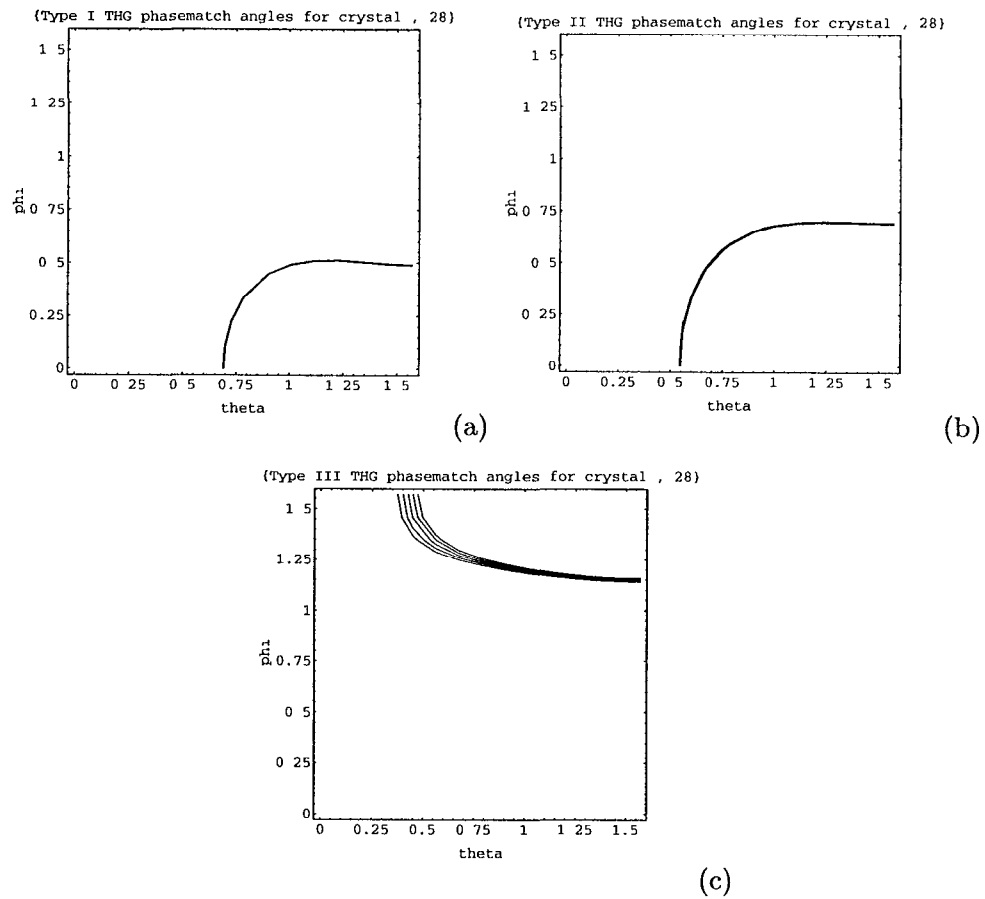


Figure B.24: Phasematching loci for Type I (a), Type II (b), and Type III (c) direct THG in LFM at 820 nm. Contours are drawn for $\Delta k = -100, -50, 0, 50$, and 100 cm^{-1} .

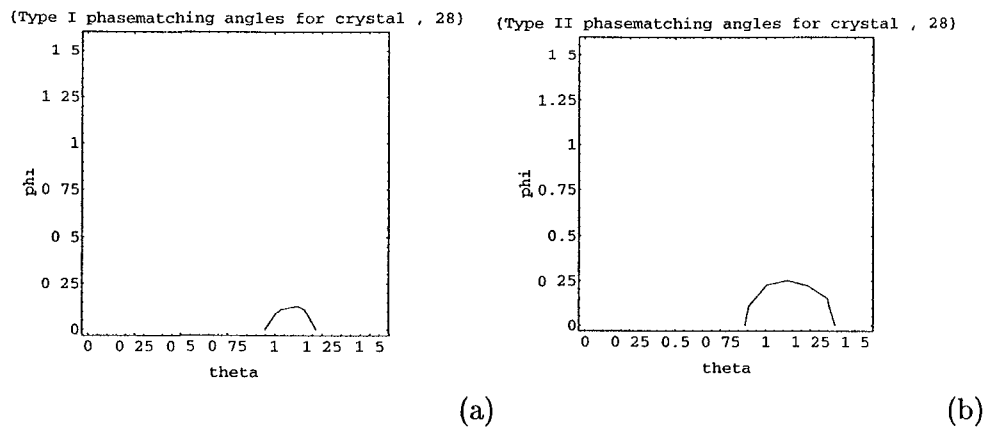


Figure B.25: Phasematching loci for Type I (a) and Type II (b) SHG in LFM at 1053 nm.

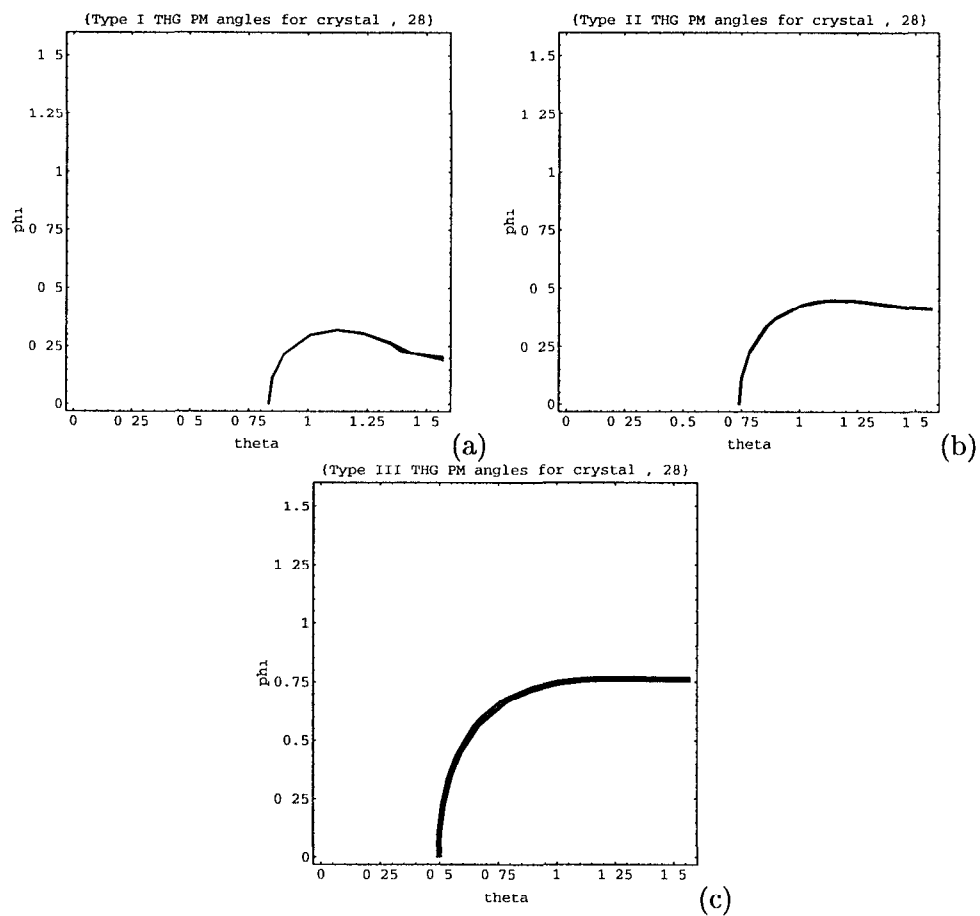


Figure B.26: Phasematching loci for Type I (a), Type II (b), and Type III (c) direct THG in LFM at 1053 nm. Contours are drawn for $\Delta k = -100, -50, 0, 50$, and 100 cm^{-1} .

Bibliography

1. R. J. Collins, D. F. Nelson, A. L. Schawlow, W. Bond, C. G. B. Garrett, and W. Kaiser, "Coherence, narrowing, directionality, and relaxation oscillations in the light emission from ruby," *Phys. Rev. Lett.* **5**, 303–305 (1960).
2. T. H. Maiman, "Stimulated optical radiation in ruby," *Nature* **187**, 493 (1960).
3. P. A. Franken, A. E. Hill, C. W. Peters, and G. Weinrich, "Generation of optical harmonics," *Phys. Rev. Lett.* **7**, 118–119 (1961).
4. D. A. Kleinman, "Theory of second harmonic generation of light," *Phys. Rev.* **128**, 1761–1775 (1962).
5. J. A. Armstrong, N. Bloembergen, J. Ducuing, and P. S. Pershan, "Interactions between light waves in a nonlinear dielectric," *Phys. Rev.* **127**, 1918–1939 (1962).
6. J. A. Giordmaine, "Mixing of light beams in crystals," *Phys. Rev. Lett.* **8**, 19–20 (1962).
7. P. D. Maker, R. W. Terhune, M. Nisenoff, and C. M. Savage, "Effects of dispersion and focusing on the production of optical harmonics," *Phys. Rev. Lett.* **8**, 21–22 (1962).
8. R. W. Terhune, P. D. Maker, and C. M. Savage, "Optical harmonic generation in calcite," *Phys. Rev. Lett.* **8**, 404–406 (1962).
9. P. D. Maker, R. W. Terhune, and C. M. Savage, "Optical third harmonic generation," In *Quantum Electronics*, P. Grivet and N. Bloembergen, eds.,² (Columbia University Press, New York, 1964).
10. R. W. Terhune, P. D. Maker, and C. M. Savage, "Observation of saturation effects in optical harmonic generation," *Appl. Phys. Lett.* **2**, 54–55 (1963).
11. P. D. Maker and R. W. Terhune, "Study of optical effects due to an induced polarization third order in the electric field strength," *Phys. Rev.* **137**, A801–A818 (1965).
12. R. B. Miles, "Optical third harmonic generation in metal vapors," Technical Report No. 2069, Microwave Laboratory, Stanford Univ. (1972) .

13. D. Strickland and G. Mourou, "Compression of amplified chirped optical pulses," *Opt. Commun.* **56**, 219–221 (1985).
14. P. Maine, D. Strickland, P. Bado, M. Pessot, and G. Mourou, "Generation of ultra-high peak power pulses by chirped pulse amplification," *IEEE J. Quantum Electron.* **QE-24**, 398 (1988).
15. M. D. Perry and G. Mourou, "Terawatt to petawatt subpicosecond lasers," *Science* **264**, 917–924 (1994).
16. B. C. Stuart, M. D. Feit, A. M. Rubenchik, B. W. Shore, and M. D. Perry, "Laser-induced damage in dielectrics with nanosecond to subpicosecond pulses," *Phys. Rev. Lett.* **74**, 2248–2251 (1995).
17. B. C. Stuart, M. D. Feit, S. Herman, A. M. Rubenchik, B. W. Shore, and M. D. Perry, "Nanosecond-to-femtosecond laser-induced breakdown in dielectrics," *Phys. Rev. B* **53**, 1749–1761 (1996).
18. M. S. Webb, D. Eimerl, and S. P. Velsko, "Wavelength insensitive phase-matched second-harmonic generation in partially deuterated KDP," *J. Opt. Soc. Am. B* **9**, 1118–1127 (1992).
19. G. Szabo and Z. Bor, "Frequency conversion of ultrashort pulses," *Appl. Phys. B* **58**, 237–241 (1994).
20. E. Sidick, A. Knoessen, and A. Dienes, "Ultrashort-pulse second-harmonic generation. I. Transform-limited fundamental pulses," *J. Opt. Soc. Am. B* **12**, 1704–1712, 1713–1722 (1995).
21. P. Di Trapani, A. Andreoni, C. Colcia, P. Foggi, R. Danielus, A. Dubietis, and A. Piskarskas, "Matching of group velocities in three-wave parametric interaction with femtosecond pulses and application to traveling-wave generators," *J. Opt. Soc. Am. B* **12**, 2237–2244 (1995).
22. I. V. Tomov, R. Fedosejevs, and A. A. Offenberger, "Up-conversion of subpicosecond light pulses," *IEEE J. Quantum Electron.* **QE-18**, 2048–2056 (1982).
23. V. Krylov, A. Rebane, A. G. Kalintsev, H. Schworer, and U. P. Wild, "Second-harmonic generation of amplified Ti:sapphire laser pulses," *Opt. Lett.* **20**, 198–200 (1995).
24. R. S. Craxton, "High efficiency frequency tripling schemes for high-power Nd:glass lasers," *IEEE J. Quantum Electron.* **QE-17**, 1771–1782 (1981).
25. V. Krylov, A. Kalintsev, A. Rebane, D. Erni, and U. Wild, "Second, third and fourth harmonic generation of amplified femtosecond Ti:sapphire laser pulses," In *Generation, Amplification, and Measurement of Ultrashort Laser Pulses II*, Proceedings of the SPIE **2701**, 24–30 (San Jose, CA, 1996).
26. S. A. Akhmanov, L. B. Meisner, S. T. Parinov, S. M. Saltiel, and V. G. Tunkin, "Cubic nonlinear susceptibilities of crystals in the optical band; the signs and magnitudes of the susceptibilities of crystals with and without centers of inversion," *Sov. Phys. JETP* **46**, 898–907 (1977).

27. A. Penzkofer, F. Ossig, and P. Qiu, "Picosecond third-harmonic light generation in calcite," *Appl. Phys. B* **47**, 71–81 (1988).
28. P. Qiu and A. Penzkofer, "Picosecond third-harmonic light generation in β -BaB₂O₄," *Appl. Phys. B* **45**, 225–236 (1988).
29. I. V. Tomov, B. Van Wenterghem, and P. M. Rentzepis, "Third-harmonic generation in barium borate," *Appl. Opt.* **31**, 4172–4174 (1992).
30. C. Flytzanis, in *Quantum Electronics*, H. Rabin and C. L. Tang, eds., (Academic Press, New York, 1975), Vol. I, Part A, Chap. 2.
31. C. Flytzanis and N. Bloembergen, "Infrared dispersion of third-order susceptibilities in dielectrics: retardation effects," *Prog. Quant. Electr.* **4**, 271–300 (1976).
32. C. P. J. Barty, C. L. Gordon III, and B. E. Lemoff, "Multiterawatt 30-fs Ti:sapphire laser system," *Opt. Lett.* **19**, 1442–1444 (1994).
33. C. P. J. Barty, T. Guo, C. Le Blanc, F. Raksi, C. Rose-Petruck, J. Squier, K. Wilson, V. V. Yakovlev, and K. Yamakawa, "Generation of 18-fs, multiterawatt pulses by regenerative pulse shaping and chirped-pulse amplification," *Opt. Lett.* **21**, 668–670 (1996).
34. F. G. Patterson, M. D. Perry, and J. T. Hunt, "Design and performance of a multi-terawatt, subpicosecond neodymium:glass laser," *J. Opt. Soc. Am. B* **8**, 2384–2391 (1991).
35. D. Du, J. Squier, S. Kane, G. Korn, G. Mourou, C. Bogusch, and C. T. Cotton, "Terawatt Ti:sapphire laser with a spherical reflective-optic pulse expander," *Opt. Lett.* **20**, 2114–2116 (1995).
36. J. Zhou, C. P. Huang, M. M. Murnane, and H. C. Kapteyn, "Amplification of 26-fs, 2-TW pulses near the gain-narrowing limit in Ti:sapphire," *Opt. Lett.* **20**, 64–66 (1995).
37. A. Sullivan, J. Bonlie, D. F. Price, and W. E. White, "1.1-J, 120-fs laser system based on Nd:glass-pumped Ti:sapphire," *Opt. Lett.* **21**, 603–605 (1996).
38. B. C. Stuart, M. D. Perry, J. Miller, G. Tietbohl, S. Herman, J. A. Britten, C. Brown, D. Pennington, V. Yanovsky, and K. Wharton, "125-TW Ti:sapphire/Nd:glass laser system," *Opt. Lett.* (1997), to be published Feb. 15, 1997.
39. M. D. Perry *et al.*, "Petawatt Laser Final Report," Technical Report No. UCRL-ID-124933, Lawrence Livermore National Laboratory (1996) .
40. M. D. Perry, T. Ditmire, and B. C. Stuart, "Self-phase modulation in chirped-pulse amplification," *Opt. Lett.* **19**, 2149–2151 (1994).
41. J. M. Eggleston, L. G. DeShazer, and K. W. Kangas, "Characteristics and kinetics of laser-pumped Ti:sapphire oscillators," *IEEE J. Quantum Electron.* **24**, 1009–1015 (1988).

42. T. Ditmire and M. D. Perry, "Terawatt Cr:LiSrAlF₆ laser system," *Opt. Lett.* **18**, 426–428 (1993).
43. P. A. Beaud, M. Richardson, and E. J. Miesak, "Multi-terawatt femtosecond Cr:LiSAF laser," *IEEE J. Quantum Electron.* **31**, 317–325 (1995).
44. B. E. Lemoff and C. P. J. Barty, "Quintic-phase-limited, spatially uniform expansion and recompression of ultrashort optical pulses," *Opt. Lett.* **18**, 1651–1653 (1993).
45. J. Zhou, C. P. Huang, M. M. Murnane, and H. C. Kapteyn, "Generation of 21-fs millijoule-energy pulses by use of Ti:sapphire," *Opt. Lett.* **19**, 126–128 (1994).
46. W. E. White, J. R. Hunter, L. Van Woerkom, T. Ditmire, and M. D. Perry, "120-fs terawatt Ti:Al₂O₃/Cr:LiSrAlF₆ laser system.,", *Opt. Lett.* **17**, 1069–1071 (1992).
47. P. F. Moulton, "Spectroscopic and laser characteristics of Ti:Al₂O₃," *J. Opt. Soc. Am. B* **3**, 125–132 (1986).
48. S. N. Fochs, Master's thesis, UCLA, 1995.
49. B. C. Stuart, S. Herman, and M. D. Perry, "Chirped-pulse amplification in Ti:sapphire beyond 1 μ m," *IEEE J. Quantum Electron.* **31**, 528–538 (1995).
50. A. E. Siegman, *Lasers* (University Science Books, Mill Valley, CA, 1986).
51. *Laser Power Optics*, 1995.
52. J. R. Houliston, M. H. Kay, and I. N. Ross, "Modelling of saturated chirped-pulse amplification and recompression," *Opt. Commun.* **108**, 111–116 (1994).
53. C. L. Blanc, P. Curley, and F. Salin, "Gain-narrowing and gain-shifting of ultrashort pulses in Ti:sapphire amplifiers," *Opt. Commun.* **131**, 391–398 (1996).
54. J. T. Hunt, P. A. Renard, and W. W. Simmons, "Improved performance of fusion lasers using the imaging properties of multiple spatial filters," *Appl. Opt.* **16**, 779–782 (1977).
55. F. G. Patterson, R. Gonzales, and M. D. Perry, "Compact 10-TW, 800-fs Nd: glass system," *Opt. Lett.* **16**, 1107–1109 (1991).
56. C. B. Dane, personal communication.
57. W. Koechner, *Solid-State Laser Engineering* (Springer-Verlag, Berlin, 1996).
58. C. Bibeau, S. A. Payne, and H. T. Powell, "Direct measurements of the terminal laser level lifetime in Neodymium-doped crystals and glasses," *J. Opt. Soc. Am. B* **12**, 1981–1992 (1995).
59. G. Cheriaux, P. Rousseau, J. P. Chambaret, B. Walker, and L. F. Dimauro, "Aberration-free stretcher design for ultrashort-pulse amplification," *Opt. Lett.* **21**, 414–416 (1996).
60. M. D. Perry, F. G. Patterson, and J. Weston, "Spectral shaping in chirped-pulse amplification," *Opt. Lett.* **15**, 381–383 (1990).

61. E. B. Treacy, "Optical pulse compression with diffraction gratings," *IEEE J. Quantum Electron.* **QE-5**, 454–458 (1969).
62. J. D. McMullen, "Analysis of compression of frequency chirped optical pulses by a strongly dispersive grating pair," *Appl. Opt.* **18**, 737–741 (1979).
63. W. E. White, F. G. Patterson, R. L. Combs, D. F. Price, and R. L. Shepherd, "Compensation of higher-order frequency-dependent phase terms in chirped-pulse amplification systems," *Opt. Lett.* **18**, 1343–1345 (1993).
64. O. E. Martinez, "3000 times grating compressor with positive group velocity dispersion: application to fiber compensation in 1.3–1.6 μm region," *IEEE J. Quantum Electron.* **QE-23**, 59–64 (1987).
65. M. Pessot, P. Maine, and G. Mourou, "1000 times expansion/compression of optical pulses for chirped pulse amplification," *Opt. Commun.* **62**, 419–421 (1987).
66. M. D. Perry and F. G. Patterson, "Multiterawatt subpicosecond Nd:glass laser system," In *Conference on Lasers and Electro-Optics*, (1990), paper JMA3.
67. J. A. Britten, M. D. Perry, B. W. Shore, and R. D. Boyd, "A universal grating design for pulse stretching and compression in the 800 to 1000 nm range," *Opt. Lett.* **21**, 540 (1996).
68. *Optica*, v1 (Wolfram Research, Inc., Champaign, IL, 1995).
69. C. Fiorini, C. Sauteret, C. Rouyer, N. Blanchot, S. Seznec, and A. Migus, "Temporal aberrations due to misalignments of a stretcher-compressor system and compensation," *IEEE J. Quantum Electron.* **30**, 1662–1670 (1994).
70. CVI Laser Corporation, "Optics and Coatings Catalog," 1994–1995.
71. K. W. Kirby and L. G. DeShazer, "Refractive indices of 14 nonlinear crystals isomorphic to KH_2PO_4 ," *J. Opt. Soc. Am. B* **4**, 1072–1078 (1987).
72. P. N. Butcher and D. Cotter, *The Elements of Nonlinear Optics, Cambridge Studies in Modern Optics* (Cambridge University Press, Cambridge, 1990).
73. J. F. Nye, *Physical Properties of Crystals* (Oxford Univ., London, 1957).
74. Y. R. Shen, *The Principles of Nonlinear Optics* (John Wiley and Sons, New York, 1984).
75. A. D. Boardman and G. S. Cooper, "Power-dependent polarization of optical pulses," *J. Opt. Soc. Am. B* **5**, 403–418 (1988).
76. N. Tzoar and M. Jain, "Self-phase modulation in long-geometry optical waveguides," *Phys. Rev. A* **23**, 1266–1270 (1981).
77. S. Chi and S. Wen, "Derivation of a wave equation for pulse propagation beyond a slowly varying envelope approximation," *Opt. Quantum Electron.* **28**, 1351–1357 (1996).

78. S. A. Akhmanov, V. A. Vysloukh, and A. S. Chirkin, *Optics of Femtosecond Laser Pulses* (AIP, New York, 1992).
79. D. Eimerl, J. M. Auerbach, and P. W. Milonni, "Paraxial wave theory of second and third harmonic generation in uniaxial crystals. I. Narrowband pump fields," *J. Mod. Opt.* **42**, 1037–1067 (1995).
80. G. R. Meredith, "Lower order effects in nonlinear two- and three-photon resonance spectroscopies," *J. Chem. Phys.* **75**, 4317–4325 (1981).
81. G. R. Meredith, "Cascading in optical third-harmonic generation by crystalline quartz," *Phys. Rev. B* **24**, 5522–5532 (1981).
82. G. R. Meredith, "Second-order cascading in third-order nonlinear optical processes," *J. Chem. Phys.* **77**, 5863–5871 (1982).
83. J. E. Midwinter and J. Warner, "The effects of phase matching method and of crystal symmetry on the polar dependence of third-order non-linear optical polarization," *Brit. J. Appl. Phys.* **16**, 1667–1674 (1965).
84. T. Ditmire, A. M. Rubenchik, D. Eimerl, and M. D. Perry, "Effects of cubic non-linearity on frequency doubling of high-power laser pulses," *J. Opt. Soc. Am. B* **13**, 649–655 (1996).
85. C. Y. Chien, G. Korn, J. S. Coe, J. Squier, G. Mourou, and R. S. Craxton, "Highly efficient second-harmonic generation of ultraintense Nd:glass laser pulses," *Opt. Lett.* **20**, 353–355 (1995).
86. C. Schwan, A. Penzkofer, N. J. Marx, and K. H. Drexhage, "Phase-matched third-harmonic generation of Nd:glass-laser picosecond pulses in a new cyanine-dye solution," *Appl. Phys. B* **57**, 203–211 (1993).
87. A. J. Taylor, G. Rodriguez, and T. S. Clement, "Determination of n_2 by direct measurement of the optical phase," *Opt. Lett.* **21**, 1812–1814 (1996).
88. F. Hache, A. Zeboulon, G. Gallot, and G. M. Gale, "Cascaded second-order effects in the femtosecond regime in β -barium borate: self-compression in a visible femtosecond optical parametric oscillator," *Opt. Lett.* **20**, 1556–1558 (1995).
89. R. DeSalvo, D. J. Hagan, M. Sheik-Bahae, G. Stegeman, and E. W. V. Stryland, "Self-focusing and self-defocusing by cascaded second-order effects in KTP," *Opt. Lett.* **17**, 28–30 (1992).
90. R. Danielus, P. Di Trapani, A. Dubietis, A. Piskarskas, D. Podenas, and G. P. Banfi, "Self-diffraction through cascaded second-order frequency-mixing effects in β -barium borate," *Opt. Lett.* **18**, 574–576 (1993).
91. J. T. Murray, N. Peyghambarian, R. C. Powell, R. A. Stolzenberger, S. Jie, and B. Jassemejnad, "Phase-matching techniques and frequency-conversion efficiency in optically active crystals," *Phys. Rev. A* **49**, 4066–4076 (1994).
92. J. Q. Yao and T. S. Fahlen, "Calculations of optimum phase match parameters for the biaxial crystal KTiOPO_4 ," *J. Appl. Phys.* **55**, 65–68 (1984).

93. H. Ito, H. Naito, and H. Inaba, "Generalized study on angular dependence of induced second-order nonlinear optical polarizations and phase matching in biaxial crystals," *J. Appl. Phys.* **46**, 3992–3998 (1975).
94. J. Yao, W. Sheng, and W. Shi, "Accurate calculation of the optimum phase-matching parameters in three-wave interactions with biaxial nonlinear-optical crystals," *J. Opt. Soc. Am. B* **9**, 891–902 (1992).
95. M. A. Dreger and J. H. Erkkila, "Improved method for calculating phase-matching criteria in biaxial nonlinear materials," *Opt. Lett.* **17**, 787–788 (1992).
96. V. G. Dmitriev, G. G. Gurzadyan, and D. N. Nikogosyan, *Handbook of Nonlinear Crystals* (Springer-Verlag, Berlin, 1991).
97. Y. Mori and T. Sasaki, "CsLiB₆O₁₀ crystal: growth and properties," In *Conference on Lasers and Electro-Optics*, 1996 OSA Technical Digest Series **9**, 234–235 (Optical Society of America, Washington, D. C., 1996).
98. C. A. Ebbers, L. D. DeLoach, M. Webb, D. Eimerl, S. P. Velsko, and D. A. Keszler, "Nonlinear optical properties of K₂La(NO₃)₅·2H₂O and K₂Ce(NO₃)₅·2H₂O," *IEEE J. Quantum Electron.* **29**, 497–507 (1993).
99. M. D. Feit and J. A. Fleck, Jr., "Computation of mode properties in optical fiber waveguides by a propagating beam method," *Appl. Opt.* **19**, 1154–1164 (1980).
100. G. P. Agrawal, *Nonlinear Fiber Optics* (Academic Press, San Diego, 1989).
101. J. M. Burzler, S. Hughes, and B. S. Wherrett, "Split-step Fourier methods applied to model nonlinear refractive effects in optically thick media," *Appl. Phys. B* **62**, 389–397 (1996).
102. R. E. Bridges, R. W. Boyd, and G. P. Agrawal, "Multidimensional coupling owing to optical nonlinearities. I. General formulation," *J. Opt. Soc. Am. B* **13**, 553–559, 560–569 (1996).
103. J. A. Fleck Jr., J. R. Morris, and M. D. Feit, "Time-dependent propagation of high energy laser beams through the atmosphere," *Appl. Phys. B* **10**, 129–160 (1976).
104. E. Sidick, A. Knoesen, and A. Dienes, "Ultrashort-pulse second-harmonic generation. I. Transform-limited fundamental pulses," *J. Opt. Soc. Am. B* **12**, 1704–1712 (1995).
105. E. Sidick, A. Dienes, and A. Knoesen, "Ultrashort-pulse second-harmonic generation. II. Non-transform-limited fundamental pulses," *J. Opt. Soc. Am. B* **12**, 1713–1722 (1995).
106. R. C. Eckardt and C. H. Lee, "Optical third harmonic measurements of subpicosecond light pulses," *Appl. Phys. Lett.* **15**, 425–427 (1969).
107. C. C. Wang and E. L. Baardsen, "Optical third harmonic generation using mode-locked and nonmode-locked lasers," *Appl. Phys. Lett.* **15**, 396–397 (1969).

108. D. A. Roberts, "Simplified characterization of uniaxial and biaxial nonlinear optical crystals: a plea for standardization of nomenclature and conventions," *IEEE J. Quantum Electron.* **28**, 2057–2074 (1992).
109. "Standards on piezoelectric crystals," *Proc. IRE* **37**, 1378–1395 (1949).
110. "IEEE standards on piezoelectricity," *IEEE/ANSI Std.* 176-1987 (1987).
111. P. N. Butcher, "Nonlinear Optical Phenomena," Technical Report No. Bull. 200, Eng. Exp. Station, Ohio State Univ., Columbus (1965) .
112. Y. Zhao, "The spatial symmetry of the third-order susceptibility tensor," *IEEE J. Quantum Electron.* **QE-22**, 1012 (1986).
113. C. C. Shang and H. Hsu, "The spatial symmetric forms of third-order nonlinear susceptibility," *IEEE J. Quantum Electron.* **QE-23**, 177–179 (1987).
114. R. W. Boyd, *Nonlinear Optics* (Academic Press, San Diego, 1992).
115. S. Singh, in *CRC Handbook of Laser Science and Technology*, M. J. Weber, ed., (CRC Press, 1986), Vol. III, Part 1.
116. X. Yang and S. Xie, "Expression of third-order effective nonlinear susceptibility for third-harmonic generation in crystals," *Appl. Opt.* **34**, 6130–6135 (1995).
117. Y. X. Fan, R. C. Eckardt, R. L. Byer, C. Chen, and A. D. Jiang, "Barium borate optical parametric oscillator," *IEEE J. Quantum Electron.* **25**, 1196–1199 (1989).
118. R. C. Eckardt, H. Masuda, Y. X. Fan, and R. L. Byer, "Absolute and relative nonlinear optical coefficients of KDP, KD*P, BaB₂O₄, LiIO₃, MgO:LiNbO₃, and KTP measured by phase-matched second-harmonic generation," *IEEE J. Quantum Electron.* **26**, 922–933 (1990).
119. D. Eimerl, L. Davis, S. Velsko, E. K. Graham, and A. Zalkin, "Optical, mechanical, and thermal properties of barium borate," *J. Appl. Phys.* **62**, 1968–1983 (1987).
120. D. H. Jundt, personal communication.
121. D. Eimerl, S. Velsko, L. Davis, F. Wang, G. Loiacono, and G. Kennedy, "Deuterated L-arginine phosphate: a new efficient nonlinear crystal," *IEEE J. Quantum Electron.* **25**, 179–193 (1989).
122. M. Okada, "Third-order nonlinear optical coefficients of LiIO₃," *Appl. Phys. Lett.* **18**, 451–452 (1971).
123. C. A. Ebbers, personal communication.
124. C. D. Marshall, S. A. Payne, M. A. Hennesian, J. A. Speth, and H. T. Powell, "Ultraviolet-induced transient absorption in potassium dihydrogen phosphate and its influence on frequency conversion," *J. Opt. Soc. Am. B* **11**, 774–785 (1994).
125. P. Liu, W. L. Smith, H. Lotem, J. H. Bechtel, N. Bloembergen, and R. S. Adhav, "Absolute two-photon absorption coefficients at 355 and 266 nm," *Phys. Rev. B* **17**, 4620–4632 (1978).

126. R. Trebino and D. J. Kane, "Using phase retrieval to measure the intensity and phase of ultrashort pulses: frequency-resolved optical gating," *J. Opt. Soc. Am. A* **10**, 1101–1111 (1993).
127. S. Xie, X. Yang, W. Jia, and Y. Chen, "Phase matched third-harmonic generation in biaxial crystals," *Opt. Commun.* **118**, 648–656 (1995).